Particle systems characterization by inversion of critical light scattering patterns

Mariusz Krzysiek

To cite this version:

Mariusz Krzysiek. Particle systems characterization by inversion of critical light scattering patterns. Engineering Sciences [physics]. Université de Provence - Aix-Marseille I, 2009. English. NNT : . tel-00443983

HAL Id: tel-00443983
https://theses.hal.science/tel-00443983
Submitted on 5 Jan 2010

AIX-MARSEILLE UNIVERSITY
Université de Provence*

WROCLAW UNIVERSITY
OF TECHNOLOGY
Politechnika Wrocławska**

Doctoral schools
* " Sciences pour l'Ingénieur : Mécanique, Physique, Micro et Nanoélectronique "
** "Electronics"

PH. D. THESIS COMPLETED IN "CO-TUTELLE"
Fields: Mechanical-Engineering & Electronics

"Particle systems characterization by inversion of critical light scattering patterns"

Presented the 8th December 2009 by

Mariusz KRZYSIEK

Composition of the jury

Kuan-Fang REN	Professor at University of Rouen	France	Referee & President
Fabrice ONOFRI	Director of Research at CNRS -University of Provence	France	Supervisor
Tadeusz PUSTELNY	Professor at Technical University of Silesia	Poland	Referee
Janusz MROCZKA	Professor at Wroclaw University of Technology	Poland	Supervisor

ACKNOWLEDGMENTS

This Ph.D. thesis was completed in "cotutelle" between the laboratory IUSTI UMR CNRS n° 6595* and the Chair of Electronics and Photonics (CEPM), the Aix-Marseille University and the Wroclaw University of Technology, France and Poland. This work was supported by a Ph.D. grant from the French Embassy in Poland, by the Wroclaw University of Technology, as well as a PHC-Polonium project n°17801XJ. So, I want to express here my gratitude to all of these entities and agencies for their support to my work.

I would like to thanks the members of the jury who have accepted to evaluate this work, and more particularly the two referees: Pr. K-F. Ren and Pr. T. Pustelny.

I would like to thanks my two supervisors for all support in this Ph.D. work. Additionally:

Prof. Janusz Mroczka for help while my stay in Poland (scientifically and administrative) also for introducing me to Dr Fabrice Onofri being person that starts this "cotutelle" Ph.D. work.

Dr. Fabrice Onofri for welcome me in France, supporting me scientifically, but also for introducing me to French culture.

Sharing my time between France and Poland I met many people. I would like to thanks all of them and above all those which help me too much to complete my work and, namely: Ireneusz Jabłoński, Grzegorz Świrniak, Damien Serret, Ben Sobac, Jean-Baptiste Merlière, Jean-Philippe Bonnet, Sebastian Hoffer and Sebastian Linden and all my colleagues from both universities I did not mention.

The members of the « Ambassade France en Pologne », and more particularly Mr. Gilles Carasso, « conseiller de coopération et d'action culturelle » ; M. Guillaume Giraudet, « adjoint de l'attaché pour la science et la technologie » and his assistant Mrs. Elzbieta Gieraltowska.

P. Cervetti, from IUSTI's mechanical workshop, who build for us many mechanical components for the CARS setup,

S. Martinez, from IUSTI's electronical workshop, who build for us useful systems to trig the CARS system or the piezo-jet contolling device,

P. Campion, from the French doctorial school, which us for all French administrative documents to prepare a PhD thesis in "cotutelle",

S. Barbosa, from IUSTI, G. Świrniak from KMEiF, A. Sabat who help us to find out and correct bugs in this manuscript,

Mrs. Anna Nowak, secretary of the KMEiF, who helps me to complete all Polish administrative document, and keeping all things to be on time.

I want thanks my parents and two sisters for all support and believing in me.

At the end I want to give my special thanks for my girlfriend Ilona S. for supporting me every day.

*IUSTI - UMR CNRS n°6595 - Univ. de Provence - Polytech'Marseille-Dept. ME
Technopôle Château Gombert - 5. r. Enrico Fermi - 13453 Marseille cedex 13, France
T:(+33) 4 91 10 68 92 F:(+33) 4 91 10 69 69 Email: Fabrice.Onofri@polytech.univ-mrs.fr
http://iusti.polytech.univ-mrs.fr/~tcm/dom/dom.html

Table of contents

LIST OF SYMBOLS AND ABBREVIATIONS

Symbols

C(x), S(x)	Fresnel's integrals,
D,	particle diameter,
$H(\alpha)$	This function describe the diffraction angular pattern versus the dimensionless parameter α,
$S_2.S_2^*$	scattered light intensity for parallel polarization,
a,	particle radius,
i	complex number,
j, p, q	index of the $j^{th,}$ p^{th} , q^{th} diffraction fringes observed in the critical scattering pattern,
m_b	refractive index of the particle material for the laser wavelength,
m_s	refractive index of the surrounding medium for the laser wavelength,
m	particle relative refractive index, $m = m_b / m_s$,
α_j	solutions of function $H(\alpha)$,
λ_0	laser wavelength in air,
θ	scattering angle ,
θ_c	critical angle position predicted by geometrical optics,
θ_r	rainbow angle position predicted by geometrical optics,
θ_j	angular position of the j^{th} diffraction fringe,
x	size parameter,
d	equivalent spherical diameter,
ξ	aspect ratio,
Eo	Eotvos's number,
g	gravitational acceleration ,
Mo	Morton's number,
Re	Reynolds's number,
Ta	Tadaki's number,
V	velocity,
We	Weber number,

μ	dynamic viscosity,
ρ	density,
σ	surface tension.

Abbreviations and acronyms

BSD	Bubble size distribution
CAM	Complex Angular Momentum theory
CARS	Critical Angle Refractometry and Sizing technique
CSP	Critical Scattering Pattern(s)
GO	Geometrical optics
GLMT	Generalized Lorenz-Mie Theory
ILIDS	Interferometric Laser Imaging for Droplet Sizing
LDV	Laser Doppler Velocimetry
Log.-Norm.	Log-normal size distribution
LSQ	Least Square method
LMT	Lorenz-Mie Theory
MVIS	Micro-video imaging system
NNLSQ	Least Square Method with Non Negative solutions
PDA	Phase Doppler Anemometry
PIV	Particle Image Velocimetry
POA	Physical Optics Approximation
FGO	Full Geometrical Optics

CAPTIONS OF CHAPTERS' THUMBNAILS

At the beginning of each chapter there is a thumbnail that illustrates the chapter contain, the thumbnails' captions are:

Chapter 1, page 11, intensity of the external and internal electromagnetic fields at the vicinity of the impact parameter corresponding to the critical-angle of a D=100µm air bubble in water.

Chapter 2, page 15, experimental far-field critical scattering pattern produced by a cloud of air bubbles in water.

Chapter 3, page 37, amplitude of the correlation estimator between the experimental and experimental critical scattering intensity profiles (LSQ-LMT-Log. Norm. inversion method).

Chapter 4, page 55, schematic of the collection optics of the critical scattering setup.

Chapter 5, page 90, image of water and dye-water bubbles sinking in silicon oil.

Chapter 6, page 118, micro-video image of spherical and ellipsoidal bubbles.

Chapter 7, page 139, intensity profile of the laser beam of the CARS system.

Chapter 8, page 155, laterally compressed image of the critical scattering pattern recorded for bubbles lighted by a white-light beam.

Chapter 9, page 161, schematic of the newly proposed technique: it analyzes far-field critical scattering patterns to recover the size distribution and composition of bubble clouds.

Chapter 1

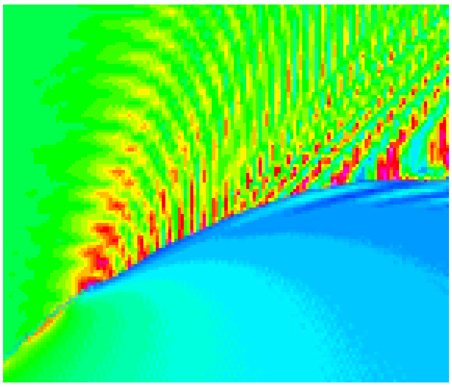

INTRODUCTION

Light is a powerful tool to investigate: at distance, complex, unstable and reactive systems. It is by itself a subject of researches and especially when it interacts with matter, and more particularly particles transported, produced or consumed in multiphase flows. The scattering of light by small particles is a wonderful research domain but it is a rather complex one as it mixes sophisticated physical theories and mathematic tools (e.g. Van de Huslt 1957, Bohren and Huffman 1998), and interdisciplinary applications (e.g. Xu 2001)

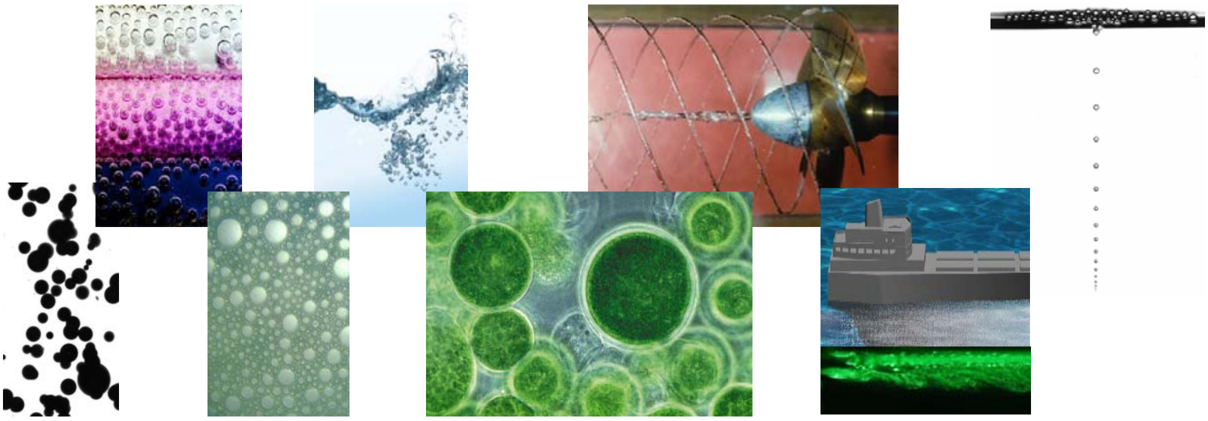

Figure 1.1 Bubbles in Nature (foam, desaturation), laboratory (propeller cavitation, coalescence) and industry (bioreactor, reduction of hydrodynamic drag of ships, calibrated particles).

In Fluid Mechanics, as well as in the day to day life, a bubble is defined as “small particle” which density is lower than the one of the surrounding medium. It rises up in the surrounding fluid because its net buoyancy forces balance is positive. Indeed, it can be either an air bubble in water or an oil droplet in water. So now, what is a bubble from the electromagnetic point of view? To answer such question let first point out the parallel between the mass density of an object and its refractive index. Obviously, the link is not direct and it can be totally contrary for some specific material or wavelengths. However, in the optical domain, a bubble is defined as a “small particle” which has a refractive index with a real part smaller than the one of the surrounding fluid. It can be either an air bubble in water or a water droplet in oil. So that, both definitions of a bubble does not always match.

Bubbles and bubbly flows occur in a wide range of natural systems and industrial processes, including, for example, boiling heat transfer, cloud cavitation, biological or chemical reactors, ship drag reduction systems. Therefore both the understanding of the properties of bubbly flows and controlling their evolution are of great technological and scientific interests (Sommerfeld 2003). In recent years computational fluid dynamics modelling of bubbly flows based on Euler–Lagrange and the Euler–Euler models has become a viable technique of good predictive capabilities (Dhotre et al. 2007). However, this requires a suitable approach as well as closure laws for mass, momentum and energy transfers between the phases and for modelling turbulence effects for instance. Direct numerical simulations can generate a good insight to the basic behaviour of bubbly flows, but they are mostly limited to relatively low Reynolds numbers (Tryggvason et al. 2006). Consequently, experimental data and diagnoses are still required to validate closure laws, as well as to control and monitor real bubbly flows.

Various optical techniques have been developed for the characterization of a single bubble size (Phase Doppler anemometry, critical scattering, optical probes, defocusing PIV…) and the size distribution of a bubble cloud (laser diffractometry, shadowgraphy …). It should be noted that a technique like the Phase Doppler anemometry (e.g. Qiu and Hsu 2004, Albrecht et al. 2003) allows characterizing the concentration and the velocity of the bubbles. In the same manner, the defocusing PIV (David et al. 2003) is able to determine simultaneously the size distribution and dynamics of an ensemble of bubbles. Nevertheless, except the critical scattering technique, none of all the aforementioned techniques is able to recognize the composition of the bubbles or the one of the surrounding fluid. This is particularly frustrating as the characterization of the bubble composition could be a key factor for bubble mixing and coalescence investigations, multiphase flows characterization. In fact, with elastic light scattering techniques the only way to determine the composition of a particle is to measure its relative refractive index.

The Critical Angle Refractometry was developed originally for the characterization of the size of a single bubble of known composition (Marston 1979, Marston and Kingsbury 1981;) and afterwards, to determine simultaneously the size and relative refractive index of a flowing bubble (Onofri F., 1999a). These information are obtained from the analysis of the angular spacing of the fringes observed near the critical angle, when a bubble is passing through an optical probe volume whose dimensions are comparable to the mean size of the studied bubbles. In some aspects this technique shows great similarities with the forward diffraction (e.g. Xu 2001) and the rainbow techniques (e.g. Van Beeck 1997), see Figure 1.2. To obtain the size distribution and the statistical moments, temporal integration is required, which may be a limiting point for some applications. In addition, the critical scattering diagrams can be noisy and difficult to analyse.

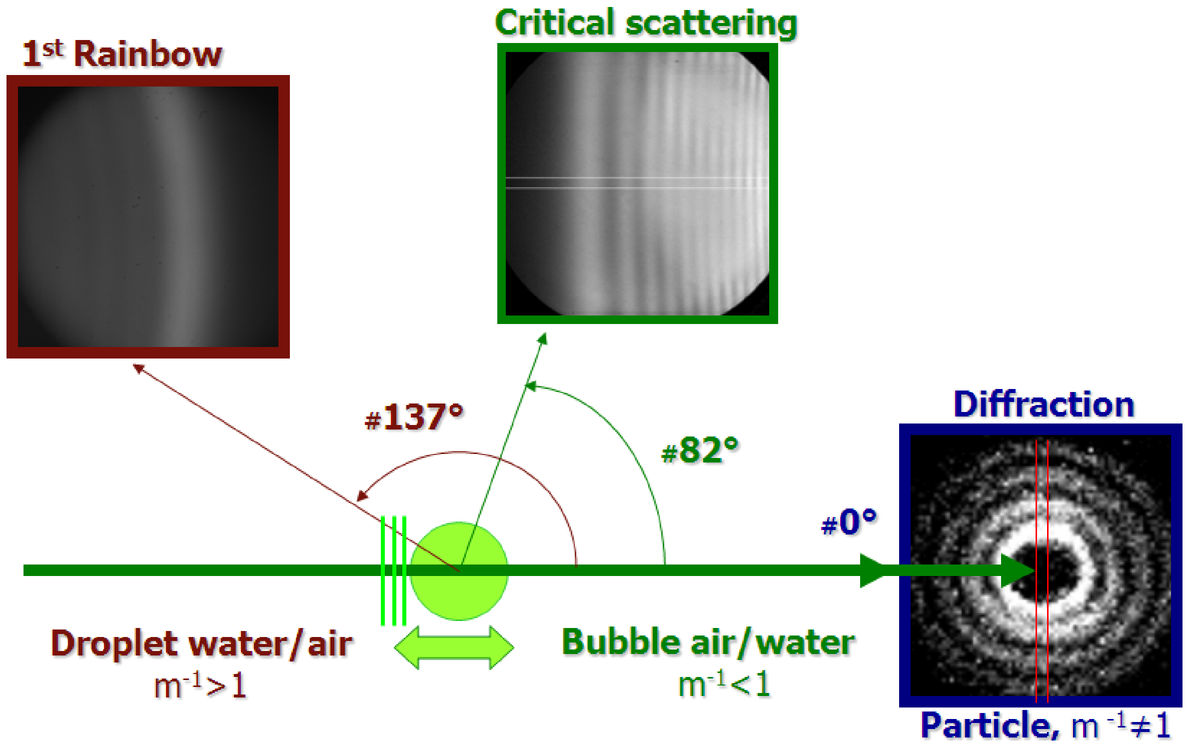

Figure 1.2 This chart point out the similarities that exist between the scattering patterns produced by three diffraction or pseudo-diffraction phenomena: forward diffraction (refractive index discontinuity on the particle edges, i.e. Fraunhofer diffraction), the rainbow (maximum deviation angle and an internal caustic for the second order refracted rays, Airy's theory) and the critical scattering (pseudo-discontinuity of the amplitude of the reflected rays at the vicinity of the critical angle, Marston's theory). Each of these phenomena produce a cone of fringes (rings pattern) with well defined cone angle.

The aim of this Ph. D. thesis is to solve the aforementioned problems, by analysing the critical scattering of bubbles ensemble rather than the scattering of individual bubbles. Our objectives are also to test the limits and advantages of this technique for fluid mechanics applications (Onofri et al. 2007a). This requires the development of dedicated light scattering models, inversion methods as well as experimental validations (Onofri et al. 2009a).

Before the plan of manuscript is detailed it is important to recall that this work was completed in "cotutelle" between the laboratory IUSTI UMR CNRS n° 6595 and the Chair of Electronics and Photonics (CEPM), the Aix-Marseille university and the Wroclaw University of Technology, France and Poland.

The manuscript is organized as follows:

Chapter 2 recalls the various models to predict the scattering of a single bubble, and the principle of the critical angle refractometry and sizing technique (CARS),

Chapter 3 presents various methods we have developed to inverse experimental critical scattering patterns,

Chapter 4 presents the various experimental setups, software and procedures that we have built and developed to investigate and validate the proposed technique, to analyze bubbly flows,

Chapter 5 reports various experiments for the measurement of spherical bubbles (diameters below 1 mm).

Chapter 6 deals with the sizing of large non spherical bubbles,

Chapter 7 details the work done to study two particular effects: trajectory effects induced by the laser beam intensity profile and spatial filter effects induced by the collection optics,

Chapter 8 reports numerical and preliminary experimental results of the bows of color that can produce by air-bubbles in water around the critical scattering angle,

Chapter 9 is an overall conclusion on the work done with perspectives for future.

Chapter 2

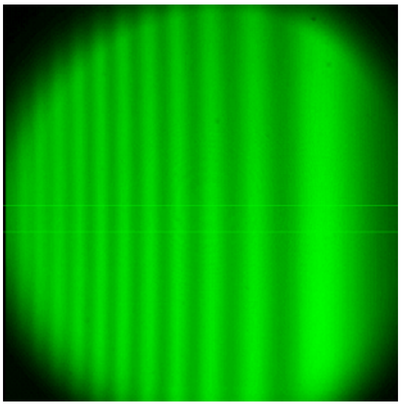

NEAR-CRITICAL-ANGLE SCATTERING OF LIGHT BY A SPHERICAL BUBBLE

2.1 Geometrical optics model

From Snell-Descartes' refraction optics laws we know that in the case of light rays passing from a medium of higher refractive index m_s to a medium with a lower refractive m, $m = m_b / m_s < 1$, there exists an angle of incidence $\phi_c = \sin^{-1}(m)$ leading to an abrupt transition to total reflection for $\phi > \phi_c$, see Figure 2.1. In the case of light rays incident on a spherical bubble, with radius *a,* the same phenomenon occurs but for a curved surface (Fiedler-Ferrari et al., 1991), giving rise to a complex scattering pattern around the critical scattering angle $\theta_c = \pi - 2\phi_c$. The scattering pattern of an air bubble in water $(m = 1/1.332)$ with diameter $D = 100\mu m$, illuminated by a plane wave with parallel polarization and wavelength $\lambda = 0.488\mu m$, is shown in Figure 2.2. Different approaches are used to predict this pattern: i) the Lorenz-Mie Theory (LMT), which is perfectly rigorous (Bohren and Huffman, 1998; Gouesbet et al., 1988; Onofri et al., 1995); ii) Geometrical Optics (GO) when only reflected (p=0) and refracted (p=1) processes are considered (Davis G.E., 1955; van de Hulst, 1957), iii) the Physical Optics Approximation (POA, §2.2) with the reflected light only (p=0) or the reflected and the refracted light (p=0 and p=1). LMT predicts a scattering diagram which is characterized by strong oscillations: a coarse structure (large 'bright' and 'dark' fringes) superimposed on a fine structure (small amplitude and high frequency fringes, that are due to the interference of rays p=0, 1 with rays p=2'). Note that the critical scattering is highly sensitive to

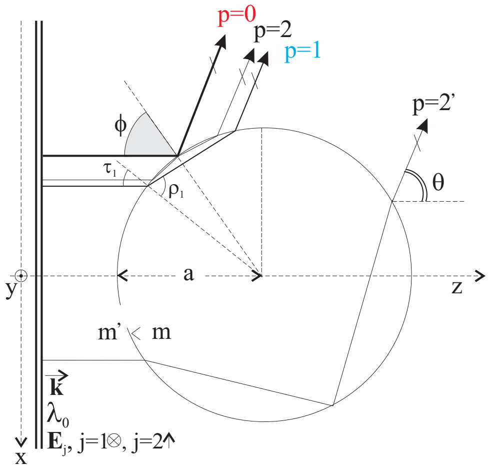

Figure 2.1 Sckematic of the rays scattered at the vicinity of the critical scattering angle.

the polarization of the incident wave. The parallel polarization is the one that gives the most contrasted scattering patterns (see Figure 2.11). So that, in the following, most results are given for this polarization state.

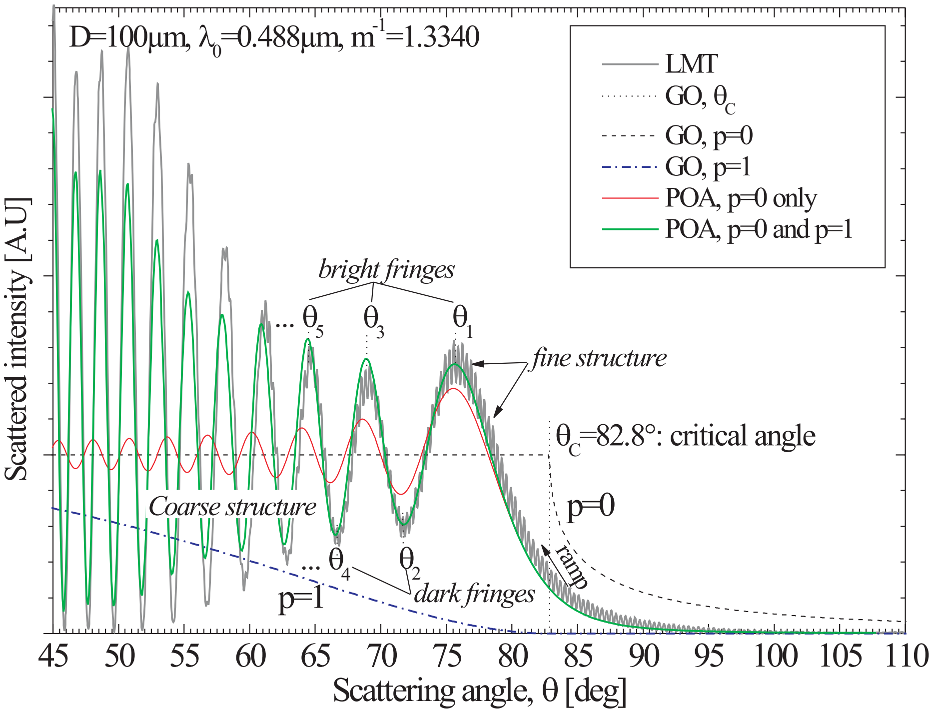

Figure 2.2 Near-critical-angle light scattering pattern produced by a single air bubble in water, according to the Lorenz-Mie Theory (LMT), the Physical Optics Approximation (POA, p=0 for reflection and diffraction, p=1 for first order refraction) and the Geometrical Optics (GO).

2.2 Physical optics approximation (POA)

2.2.1 Background

Marston (1979), Marston and Kingsbury (1981) have developed a physical optics approximation (POA) for the critical scattering phenomena. In the framework of the POA, the contribution of surface reflection is treated by a procedure similar to the Airy's theory of the rainbow (Airy 1838): a Kirchhoff-type approximation is applied to the amplitude distribution along a virtual reflected wave front. The amplitude of the reflection contribution ($p=0$) is approximated as a step function. In the far field, this "edge reflectivity" (Fiedler-Ferrari et al. 1991) gives rise to a diffraction scattering pattern allowing to account for the coarse fringes observed in the CSP. In the same time, the fine structure in CSP is due to interferences phenomena between near side and far side refracted rays (p=0-2 with p=2', see Figure 2.1).

In fact, the total scattering can be considered as the contribution of all orders of interaction between the bubble surface and the incident light:

$$S = \sum_{p} S_p = S_0 + S_1 + S_2 + S_{2'} + S_3 + ... \tag{1}$$

The complex amplitude functions read as:

$$S_p = \frac{-ika}{2} F_p \exp\left[i\gamma_p\right] \tag{2}$$

where $k = 2\pi/\lambda$ is the wave number, with $\lambda = \lambda_0 / m_s$. The total scattered intensity is then given by $I \propto |S|^2 / (kr)^2$ (Bohren and Huffman 1998). Only the reflection (*p*=0) and refraction (*p*=1) will be taken into account in what follows for the scattering amplitude function near the critical-angle.

2.2.2 Reflected contribution (p=0)

The reflection process is treated with Fresnel integrals (Goodman 1996) and leads, for the amplitude of the scattering function, to:

$$F_0 = \left|F(\omega) - F(-\infty)\right| \exp\left[-i\pi/4\right] / \sqrt{2} \tag{3}$$

where parameter $\omega = \sin(\eta)\sqrt{(a/\lambda)\cos\phi_c}$ depends on the bubble's radius a, its relative refractive index and the incident wavelength (Langley and Marston 1984). The angle $\eta = \theta_c - \theta$ is a deviation from the position of the critical angle predicted by geometrical optics, with

$$\theta = \sin^{-1}\left(\omega / \sqrt{(a/\lambda)\cos\phi_c}\right) + \theta_c \tag{4}$$

The oscillatory function $F(\omega)$ is defined with the Fresnel's cosine $C(\omega)$ and sine $S(\omega)$ integrals (Chang et al. 1996):

$$F(\omega) = C(\omega) + iS(\omega) = \int_0^{\omega} \cos\left(\frac{\pi}{2}\varsigma^2\right) d\varsigma + i\int_0^{\omega} \sin\left(\frac{\pi}{2}\varsigma^2\right) d\varsigma \tag{5}$$

where ς is an integral variable. The phase term in Eq. (2) can be deduced from geometrical and physical considerations (Marston and Kingsbury, 1981):

$$\gamma_0 = -2ka\cos(\tau_0) - \Lambda\left[\theta_0 - \theta_c\right]\delta_0 \tag{6}$$

where Λ is the Heaviside function with

$$\begin{cases} \Lambda\left[\theta_0 - \theta_C\right] = 0 \\ \Lambda\left[\theta_0 - \theta_c\right] = 1 \end{cases} \text{for} \begin{cases} \theta > \theta_c \\ \theta \le \theta_c \end{cases} \tag{7}$$

In Eq. (6) the first term comes from the classical phase delay due to the path of geometrical rays with $\tau_0 = (\pi - \theta_0)/2$ and $\rho_0 = \tau_0$ (van de Hulst 1957, Bultynck 1998). The second term δ_0 is a phase delay due to the tunneling effect (Lötsch 1971, Nussenzweig 1992, see also Figure 2.5):

$$\tan(\delta_0 / 2) = m^{-2}\sqrt{\sin^2\tau_0 - m^2} / \cos\tau_0 \tag{8}$$

If only the reflected/diffracted process is taken into account in Eq. (1), the intensity scattered near the critical scattering angle is of the following form:

$$I_0(\theta, D, m, \lambda) \propto \left[C(\omega) + 1/2\right]^2 + \left[S(\omega) + 1/2\right]^2 \equiv H(\omega) \tag{9}$$

The angular positions of the bright and dark fringes in the coarse structure of the CSP are determined by the zeros ω_n of the first derivative of the oscillating function $H(\omega)$ (Onofri, 1999a).

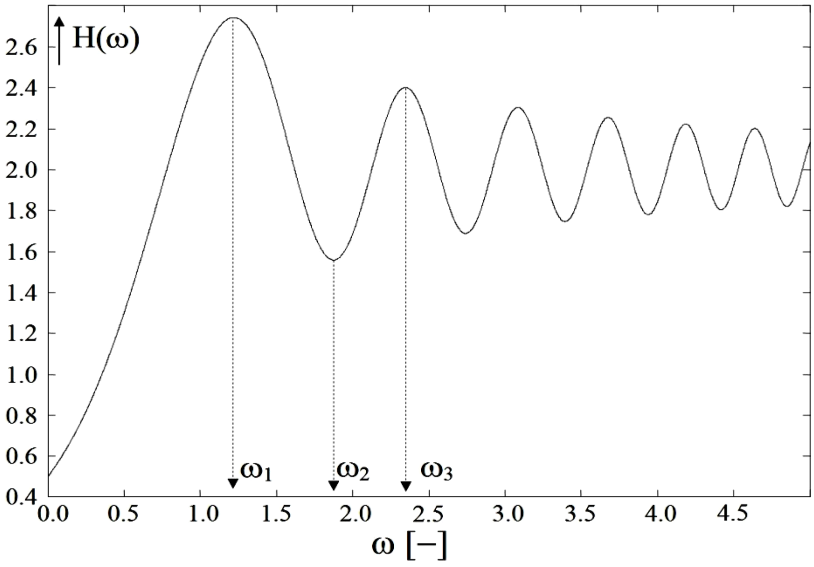

Figure 2.3 Evolution of Fresnel's integral based funct

n	Location of the nth extremes ω_n
1	1.2171982507
2	1.8725190624
3	2.3448538242
4	2.7390080864
5	3.0881958234
6	3.3913355077
7	3.6741104772

Table 2.1 Tabulation of the location of nth extremum

They can be found numerically with an iterative scheme. The seven first zeros are shown in Table 2.1. Depending on the bubble radius and relative refractive index, the angular position θ_n of the n^{th} fringes is

$$\theta_n(a_n, m) = \sin^{-1}\left(\omega_n / \sqrt{(a_n/\lambda)\cos\phi_c}\right) + \theta_c \tag{10}$$

where the subscript n refers to a quantity that can be obtained from the n^{th} fringe. If the relative refractive index m (i.e. the bubble and the surrounding medium compositions) is known, the bubble radius can be deduced directly from the measurement of the angular position of the n^{th} fringe:

$$a_n = \frac{\lambda_0 m \omega_n^2}{\sin^2\left(\theta_c - \theta_n\right)\cos\phi_c} \tag{11}$$

If neither the bubble relative index nor radius is known, they can be determined by measuring the angular position of two fringes of the CSP (Onofri 1999a) that are denoted $n = \upsilon,\ \kappa\ \left(\kappa > \upsilon\right)$:

$$m \approx m_{\upsilon\kappa} = \sin\left[\left(\pi - \theta_\upsilon - \Omega_{\upsilon\kappa}\right)/2\right] \tag{12}$$

$$a \approx a_{\upsilon\kappa} = \lambda_0 m_{\upsilon\kappa} \frac{\omega_\upsilon^2 + \omega_\kappa^2 - 2\omega_\upsilon\omega_\kappa\cos\Delta_{\upsilon\kappa}}{\sin^2\left(\Delta_{\upsilon\kappa}\right)\sin\left[\left(\theta_\upsilon - \Omega_{\upsilon\kappa}\right)/2\right]} \tag{13}$$

where

$$\Omega_{\upsilon\kappa} = \tan^{-1}\left[\sin\Delta_{\upsilon\kappa} / \left(\cos\Delta_{\upsilon\kappa} - \omega_\kappa / \omega_\upsilon\right)\right] \tag{14}$$

$$\Delta_{\upsilon\kappa} = \theta_\kappa - \theta_\upsilon \tag{15}$$

Compared with GO predictions, the first term of the POA provides a significant improvement in the description of the near-critical-scattering pattern, see Figure 2.2. However, the first term of the POA gives a very poor estimation of the angular position of the other fringes ($\theta_n \geq \theta_2$) and of their relative amplitude, Figure 2.2. The angular position of the first two extremes (i.e. $\theta_1,\ \theta_2$) are in rather good agreement with the ones predicted by LMT. This is confirmed by Figure 2.4 which presents POA and LMT's predictions for θ_1, for various bubble sizes and bubble relative refractive indices.

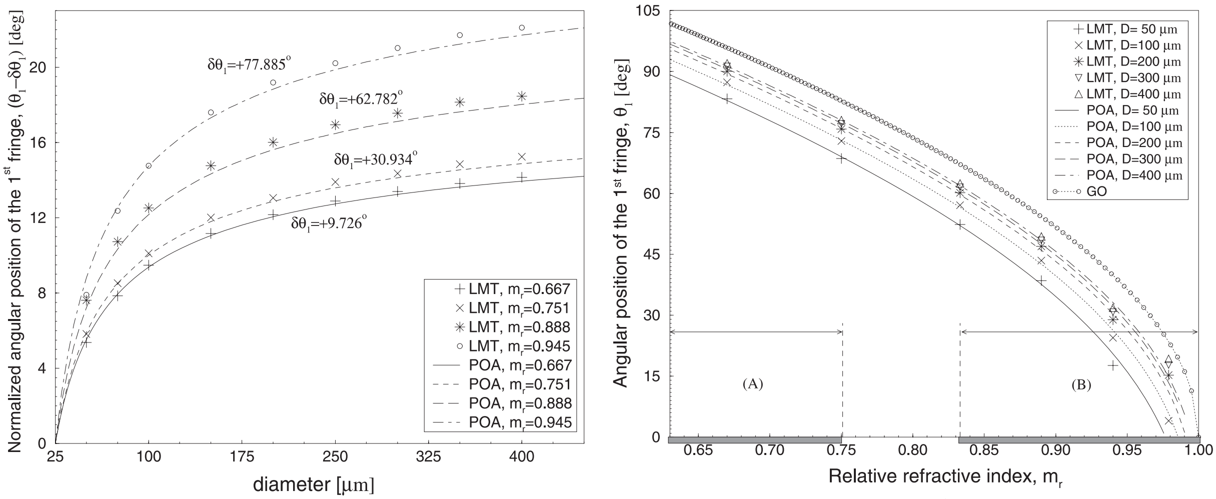

(a) (b)

Figure 2.4 Angular position of the first critical fringe according to the Lorenz-Mie Theory and the Physical Optics Approximation (p=0 only): a) versus the bubble size and b) the relative refractive index.

2.2.3 Refracted contribution (p=1)

According to van de Hulst (1957), the phase and amplitude of the contribution of the refracted process (*p*=1) read as:

$$\gamma_1 = 2ka\left(m\cos\rho_1 - \cos\theta_1\right) \tag{16}$$

$$F_1 = 2\left(1 - r_{\|}^2\right)\sqrt{D_1}\Lambda\left[\theta_1 - \theta_c\right] \tag{17}$$

where $r_{\|} = \tan\left(\tau_1 - \rho_1\right) / \tan\left(\tau_1 + \rho_1\right)$ is the Fresnel amplitude coefficient for parallel polarization. Note that in Eq. (16) the phase shifts due to the focal lines (van de Hulst 1957) are not taken into account. D_1 is a divergence function which takes into account the effect of the particle surface curvature in the Fresnel coefficients :

$$D_1 = \sin\tau_1 \cos\tau_1 / \left(2\sin\theta\left|1 - m^{-1}\cos\tau_1 / \cos\rho_1\right|\right) \tag{18}$$

where τ_1 and ρ_1 are respectively the angles made by the bubble surface with the incident ray and the internally refracted ray (van de Hulst 1957). They can be expressed as functions of the scattering angle of the refracted rays (*p*=1):

$$\tau_1 = -\frac{\theta_1}{2} + \tan^{-1}\left(\frac{m^{-1}\sin\left(\theta_1/2\right)}{m^{-1}\cos\left(\theta_1/2\right) - 1}\right), \quad \rho_1 = \sin^{-1}\left(m^{-1}\sin\tau_1\right). \tag{19}$$

Without doubt the predictions of the POA are significantly improved by taking into account the refracted term, as earlier shown in Figure 2.2. The positions of the fringes are always in good agreement to those of LMT. The prediction of the relative amplitude is also greatly improved although the results are not as good for smaller bubbles (see Figure 2.9).

2.3 Lorenz-Mie's and Debye's theories

2.3.1 Lorenz-Mie's theory

The « Mie » or « Lorenz-Mie » theory (LMT; Mie, 1908) is a reference for all particle light scattering techniques. It solves in an exact manner the problem of the scattering of a monochromatic plane wave by a spherical particle whose material is homogeneous, isotropic and linear (a so-called "Mie scatter"). The external medium must be transparent. Basically, LMT solves the wave equation with a separation variable method and appropriate boundary conditions. Expressions for electrical and the magnetic fields are then related through the Maxwell equations. Note that Debye has proposed a quite different formulation for this problem (see §2.3.2).

2.3.1.1 Wave equation and the separation variable method

To be a solution of Maxwell's equations an electromagnetic wave has to satisfy the following equations, with $k^2 = \omega^2 \varepsilon \mu$:

$$\begin{cases} \nabla^2 \mathbf{E} + k^2 \mathbf{E} = 0 \\ \nabla^2 \mathbf{H} + k^2 \mathbf{H} = 0 \end{cases} \tag{20}$$

This problem can be reduce to the solving of the scalar wave equation :

$$\nabla^2 \psi + k^2 \psi = 0 \tag{21}$$

where ψ is a function connected to the spherical harmonics by $\mathbf{M} = \nabla \times (\mathbf{r}\psi)$ and $\mathbf{N} = (\nabla \times \mathbf{M})/k$. In the spherical coordinates system the scalar wave equation reads as:

$$\frac{1}{r}\frac{\partial}{\partial r}\left(r^2 \frac{\partial \psi}{\partial r}\right) + \frac{1}{r^2 \sin\theta}\frac{\partial}{\partial \theta}\left(\sin\theta \frac{\partial \psi}{\partial \theta}\right) + \frac{1}{r^2 \sin\theta}\frac{\partial^2 \psi}{\partial \phi^2} + k\psi^2 = 0 \tag{22}$$

The Lorenz-Mie theory uses a separation variable method (SVM) to solve the previous equation:

$$\psi(r,\theta,\phi) = R(r)\Theta(\theta)\Phi(\phi) \tag{23}$$

This procedure allows obtaining three equations (where m and n are separation constants):

$$\begin{cases} \dfrac{d^2\Phi}{d\phi^2} + m\phi^2 = 0 & \text{(a)} \\ \dfrac{1}{\sin\theta}\dfrac{d}{d\theta}\left(\sin\theta \dfrac{d\Theta}{d\theta}\right) + \left[n(n+1) - \dfrac{m^2}{\sin^2\theta}\right] = 0 & \text{(b)} \\ \dfrac{d}{dr}\left(r^2 \dfrac{dR}{dr}\right) + \left[k^2 r^2 - n(n+1)\right]R = 0 & \text{(c)} \end{cases} \tag{24}$$

The solutions of Eq. (24) a) are of the following type:

$$\begin{cases} \Phi_e = \cos(m\phi) \\ \Phi_o = \sin(m\phi) \end{cases} \tag{25}$$

The solutions of Eq. (24)-(b) are the Legendre's polynomials $P_n^m(\cos\theta)$ and the associated Legendre's functions. The solutions of Eq. (24)-(c) are obtained by introducing the change of variable $\rho = kr$ and by introducing the function $Z = R\sqrt{\rho}$, Eq. (24)-(c) can then be written as:

$$\rho \frac{d}{d\rho}\left(\rho \frac{dZ}{d\rho}\right) + \left[\rho^2 - \left(n - \frac{1}{2}\right)^2\right] Z = 0 \tag{26}$$

We are looking for linearly independents solutions which are combinations of spherical Bessel's functions $j_n, y_n, k_n^{(1)}, k_n^{(2)}$ (e.g. Bohren and Huffamn 1998). So that the solutions of Eq. (23) are of the following form :

$$\begin{aligned} \psi_{emn} &= \cos(m\phi)P_n^m\left(\cos\theta\right)z_n\left(kr\right) \\ \psi_{omn} &= \sin(m\phi)P_n^m\left(\cos\theta\right)z_n\left(kr\right) \end{aligned} \tag{27}$$

Note that for a plane wave illumination only the terms with $|m|=1$ are not null.

2.3.1.2 Fields formula and continuity criteria

The different spherical Bessel functions $j_n, y_n, k_n^{(1)}, k_n^{(2)}$ do not exist for all point of space. For instance, $y_n \to \infty$ when $r \to 0$. Then the later function cannot be used to describe the internal electrical and magnetic fields (i.e. inside the particle). In opposite, it can be used to describe the scattered fields (i.e. $y_n \to 1/r$ when $r \to \infty$).

Similar considerations allow obtaining the following formula for the internal fields (subscript p) and the scattered ones (subscript s) :

$$\begin{cases} \mathbf{E}_p = \sum_{n=1}^{\infty} E_n\left(c_n\mathbf{M}_{o1n}^{(1)} - id_n\mathbf{N}_{e1n}^{(1)}\right) \\ \mathbf{H}_p = \dfrac{-k_p}{\omega\mu_p}\sum_{n=1}^{\infty} E_n\left(d_n\mathbf{M}_{e1n}^{(1)} - ic_n\mathbf{N}_{o1n}^{(1)}\right) \end{cases} \quad \begin{cases} \mathbf{E}_s = \sum_{n=1}^{\infty} E_n\left(ia_n\mathbf{N}_{e1n}^{(3)} - b_n\mathbf{M}_{o1n}^{(3)}\right) \\ \mathbf{H}_s = \dfrac{k}{\omega\mu}\sum_{n=1}^{\infty} E_n\left(ib_n\mathbf{N}_{o1n}^{(3)} - a_n\mathbf{M}_{e1n}^{(3)}\right) \end{cases} \tag{28}$$

with $E_n = i^n E_0\left(2n+1\right)/n\left(n+1\right)$.

In Eq. (28) the electric and magnetic fields are described by a linear combination of an infinite number of spherical harmonics with complexes coefficients. The coefficients a_n, b_n are the so-called "external scattering coefficients", c_n, d_n are the "internal scattering coefficients"

Tangential components of the electromagnetic fields' have to fulfill boundary conditions onto the particle surface:

$$\begin{cases} \left[\mathbf{E}_p\left(\mathbf{X}\right) - \mathbf{E}_e\left(\mathbf{X}\right)\right]\times\hat{\mathbf{n}} = 0 \\ \left[\mathbf{H}_p\left(\mathbf{X}\right) - \mathbf{H}_e\left(\mathbf{X}\right)\right]\times\hat{\mathbf{n}} = 0 \end{cases} \tag{29}$$

which gives for $r = D/2$:

$$\begin{cases} E_{i\theta} + E_{s\theta} = E_{p\theta} \\ H_{i\theta} + H_{s\theta} = H_{p\theta} \end{cases} \quad \begin{cases} E_{i\phi} + E_{s\phi} = E_{p\phi} \\ H_{i\phi} + H_{s\phi} = H_{p\phi} \end{cases} \tag{30}$$

These relations permit to obtain the following relations for the external scattering coefficients :

$$\begin{aligned} a_n &= \frac{m\psi_n(mx)\psi'_n(x)-\psi_n(x)\psi'_n(mx)}{m\psi_n(mx)\xi'_n(x)-\xi_n(x)\psi'_n(mx)} \\ b_n &= \frac{\psi_n(mx)\psi'_n(x)-m\psi_n(x)\psi'_n(mx)}{\psi_n(mx)\xi'_n(x)-m\xi_n(x)\psi'_n(mx)} \end{aligned} \tag{31}$$

where the Ricatti-Bessel functions are defined by $\psi_n(\rho)=\rho j_n(x), \quad \xi_n(x)=\rho h_n^{(1)}(x)$

To compute efficiently the a_n, b_n coefficients, it is necessary to introduce the logarithmic derivatives of the Riccati-Bessel functions:

$$\begin{aligned} a_n &= D_n^{(3)}\frac{mD_n^{(1)}(x)-D_n^{(1)}(mx)}{mD_n^{(2)}(x)-D_n^{(1)}(mx)} \\ b_n &= D_n^{(3)}\frac{D_n^{(1)}(x)-mD_n^{(1)}(mx)}{D_n^{(2)}(x)-mD_n^{(1)}(mx)} \end{aligned} \tag{32}$$

where

$$D_n^{(1)}(z)=\frac{\psi_n^{'}(z)}{\psi_n(z)}, \quad D_n^{(2)}(z)=\frac{\xi_n^{'}(z)}{\xi_n(z)}, \quad D_n^{(3)}(z)=\frac{\psi_n(z)}{\xi_n(z)} \tag{33}$$

2.3.1.3 Expressions for the phase functions and extinction efficiencies

For spherical particles the expressions for the scattered field (subscript *s*) can be expressed as functions of the amplitude of the incident field (subscript *i*), for the two polarizations (parallel || and perpendicular ⊥ to the scattering plane) and the two amplitude functions S_1 and S_2:

$$\begin{pmatrix} E_{s\|} \\ E_{s\perp} \end{pmatrix} = \frac{e^{ik(r-z)}}{-ikr}\begin{pmatrix} S_2 & 0 \\ 0 & S_1 \end{pmatrix}\begin{pmatrix} E_{i\|} \\ E_{i\perp} \end{pmatrix} \tag{34}$$

with

$$\begin{aligned} S_1 &= \sum_{n=1}^{\infty}\frac{(2n+1)}{n(n+1)}\left(a_n\pi_n+b_n\tau_n\right) \\ S_2 &= \sum_{n=1}^{\infty}\frac{(2n+1)}{n(n+1)}\left(a_n\tau_n+b_n\pi_n\right) \end{aligned} \tag{35}$$

$$\pi_n=\frac{P_n^1}{\sin\theta}, \quad \tau_n=\frac{dP_n^1}{\sin\theta} \tag{36}$$

In the far-field we have for the electrical scattered field:

$$\begin{cases} E_{s\theta} \sim E_0\dfrac{e^{ikr}}{-ikr}\cos\phi S_2(\cos\theta) \\ E_{s\phi} \sim E_0\dfrac{e^{ikr}}{-ikr}\sin\phi S_1(\cos\theta) \end{cases} \quad \begin{cases} E_{s\theta} \sim E_0\dfrac{e^{ikr}}{-ikr}\cos\phi S_2(\cos\theta) \\ E_{s\phi} \sim E_0\dfrac{e^{ikr}}{-ikr}\sin\phi S_1(\cos\theta) \end{cases} \tag{37}$$

from the previous equation and using the Poynting vector it is easy to derive the relations for the scattering intensities $i_{\parallel} \sim |S_2|^2$ and $i_{\perp} \sim |S_1|^2$.

For the extinction cross section we get also (the subscripts abs, ext and sca stand respectively for absorption, extinction and scattering)

$$\begin{aligned} C_{sca} &= \frac{2\pi}{k^2}\sum_{n=1}^{\infty}(2n+1)\left(|a_n|^2+|b_n|^2\right) \\ C_{ext} &= \frac{2\pi}{k^2}\sum_{n=1}^{\infty}(2n+1)\,\mathrm{Re}\{a_n+b_n\} \\ C_{abs} &= C_{ext}-C_{sca} \end{aligned} \tag{38}$$

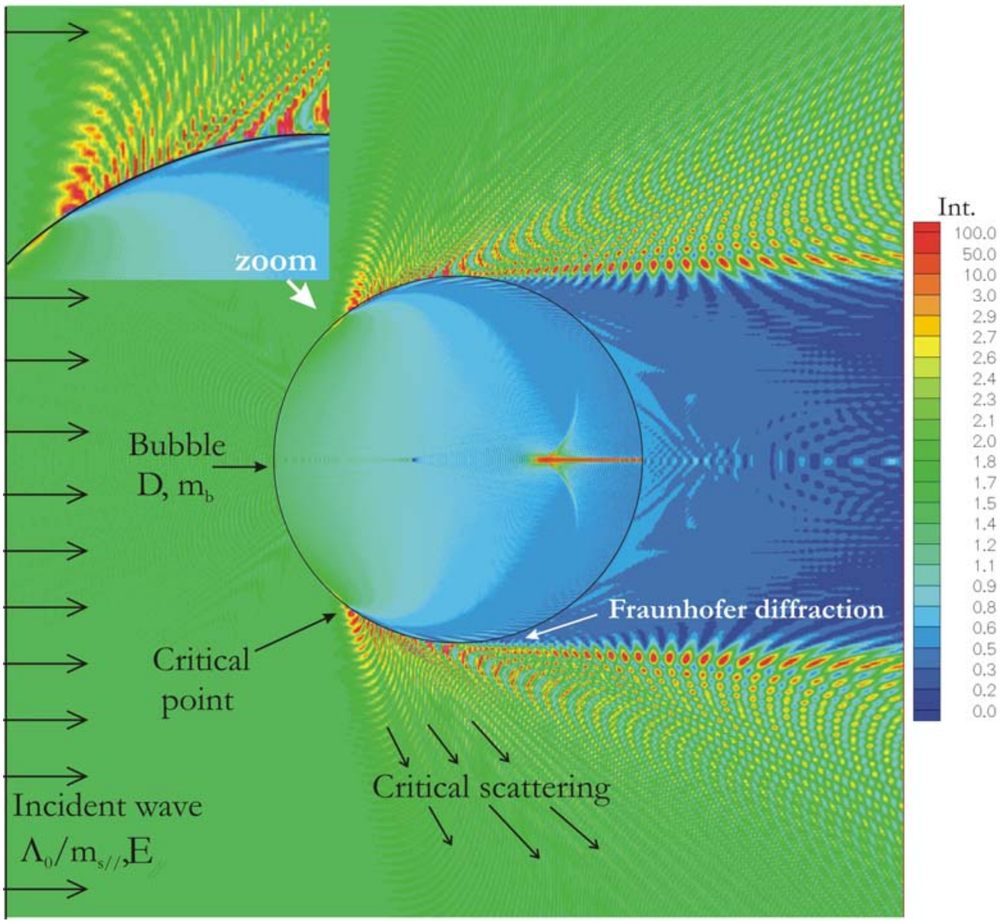

Figure 2.5 Intensity of the electromagnetic field inside and around an air bubble in water (D=100µm, m_b=1.0, m_s=1.333) calculated with LMT for a parallel polarized plane wave (λ_0=0.532µm).

Several important remarks:

- Numerically these infinite expansions series are truncated for $n_{stop} = x + 4x^{1/3} + 2$.

- According to the localization principle (van de Hulst, 1957), the expansion term n may be interpreted as rays that impinge onto the particle surface at distance R_n from the particle axis :

$$R_n = \left(n+\frac{1}{2}\right)\frac{\lambda}{2\pi} \tag{39}$$

- During the last twenty years this theory has been generalized to the case where the incident wave is a Gaussian beam (Gouesbet et al. 1988, Barton et al. 1988) or a laser sheet (Ren et al. 1994). In the same way it has been extended to spherical particles with internal refractive index gradients (Onofri et al. 1995), cylindrical particles (Ren et al. 1997), etc.

- This theory allows also computing quantities like the intensity of the electromagnetic field inside and at the vicinity of the external surface of a particle (Barber et Hill, 1989). As example, we have computed the intensity of the electromagnetic field inside and outside an air bubble in water illuminated by a plane wave with parallel polarization, see Figure 2.5 . Despite the huge dynamic range and the complexity of the intensity map, the critical scattering phenomena appears clearly as a sharp transition from a low to high scattering region and then, by what may be called "fringes". Note that in the right part of the zoomed subfigure, the electromagnetic intensity reaches its first maxima inside the bubble and just before the first critical scattering "fringe". This small region may be reasonably associated to input region of the tunneling effects depicted by Lötsch, 1971.

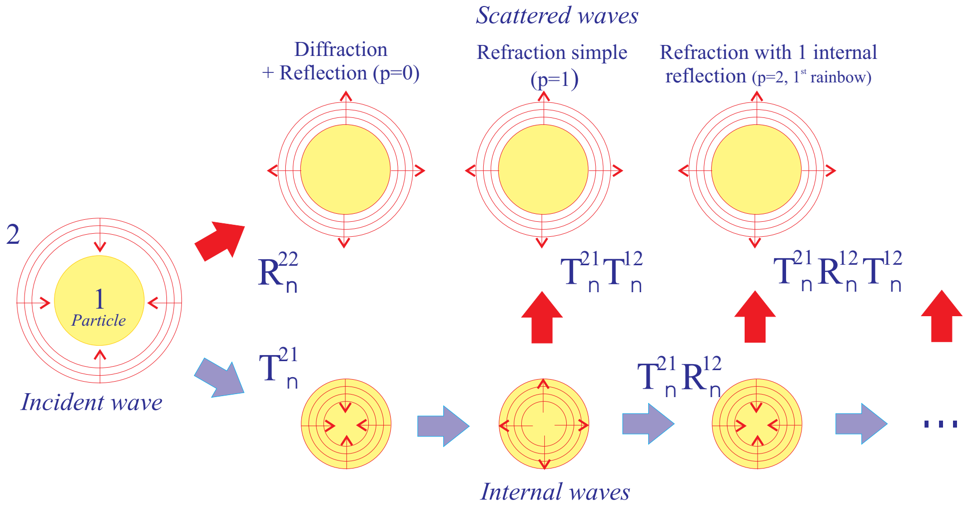

Figure 2.6 Debye decomposition: the incident, internal and scattered fields are decomposed into partial waves which have experienced reflections with the particle/environment interface.

2.3.2 Debye's theory

It follows from the work of Debye that we can reorganize the terms of LMT's expansion series in contributions corresponding to waves that are partially reflected and partially transmitted by the particle. These partial waves are spherical and propagate out or within the particle. This leads to the introduction, like with geometrical optics (see §2.4.1), of reflection and transmission coefficients for these partial waves. Figure 2.6 presents a schematic of Debye's decomposition method, as reformulated by Hovenac and Lock (1992). The particle is associated with the medium 1 $(\equiv b)$ and the external environment to the medium 2 $(\equiv s)$, with:

- $R_n^{(22)}$: Coefficient of reflection of the incident wave which is partially reflected (specular reflection and diffraction) to the external environment,

- $T_n^{(21)}$: Coefficient of transmission of external partial waves into the particle, so that a part of the incident wave is transmitted inside the particle (see Figure 2.5),
- $R_n^{(11)}$: Coefficient of reflection of the internal waves onto the inner surface of the particle,
- $T_n^{(12)}$: Coefficient of transmission of internal partial waves to the external environment.

For the partial wave *p* and the order *n* expansion, the Debye coefficients read as:

$$\left.\begin{matrix} a_n(p) \\ b_n(p) \end{matrix}\right\} = \frac{1}{2}\left\{\begin{matrix} 1-R_n^{(22)} \\ -T_n^{(21)}\left(R_n^{(11)}\right)^{p-1}T_n^{(12)} \end{matrix}\right. \quad \text{pour} \quad \left\{\begin{matrix} \text{p=0} \\ \text{p} \geq 1 \end{matrix}\right. \tag{40}$$

$p=0$ corresponds to the diffraction and specular reflection, $p=1$ to single refraction, $p=2$ to the partial wave which has undergone an internal reflection, $p=3$ with two internal reflections, etc.

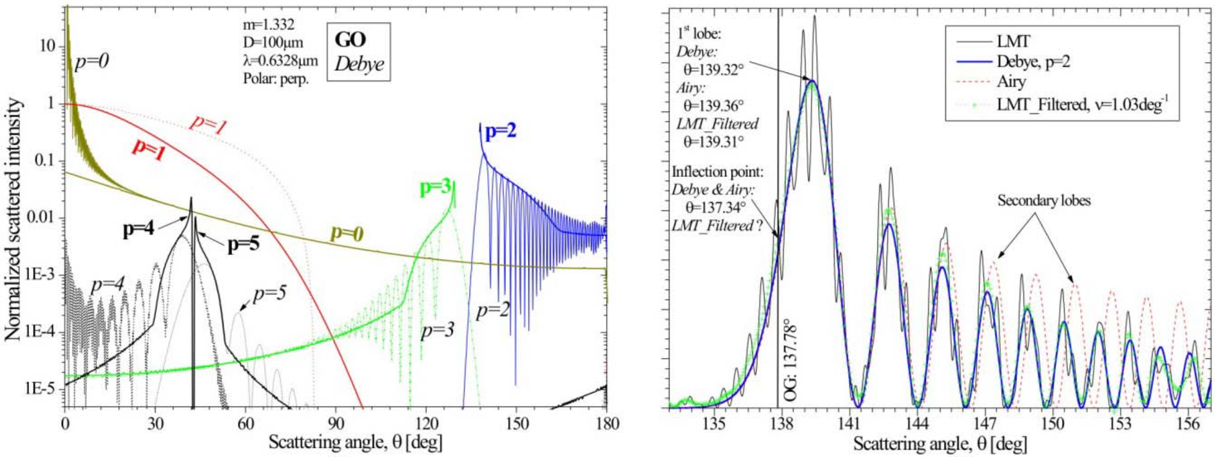

Figure 2.7 a) Comparison of the predictions of Geometrical optics, Lorenz-Mie and Debye theories for the scattering diagrams of a D=100µm water droplet: a) full diagrams and b) first rainbow region only, with λ=0.6328µm and ⊥ polarisation.

It is important to note that there is a strict equivalence between the external scattering coefficients of the theory of Lorenz-Mie and the theory of Debye (provided that the order of decomposition $p \to \infty$, although in practice $p \geq 100$ is usually large enough):

$$\left\{\begin{matrix} a_n \\ b_n \end{matrix}\right\}_{LMT} = \frac{1}{2}\left[1-R_n^{(22)}-\sum_{p=1}^{\infty}T_n^{(21)}\left(R_n^{(11)}\right)^{p-1}T_n^{(12)}\right] \text{pour } \alpha = \left\{\begin{matrix} m \\ 1 \end{matrix}\right. \text{ et } \beta = \left\{\begin{matrix} 1 \\ m \end{matrix}\right. \text{ et p} \to \infty \tag{41}$$

The direct numerical calculation of these series is relatively stable. In fact, Debye's series require complex summation of more functions than LMT. The calculation of these series is therefore more sensitive to the development of numerical noise.

Figure 2.7 illustrates the interest of the Debye theory by comparing the scattering diagrams of a water droplet calculated with geometrical optics, LMT and Airy. Indeed, the predictions of the Debye theory are significantly more accurate than those of any geometrical or physical optics theories and, at the same time, this theory provides more physical insight than the Lorenz-Mie theory.

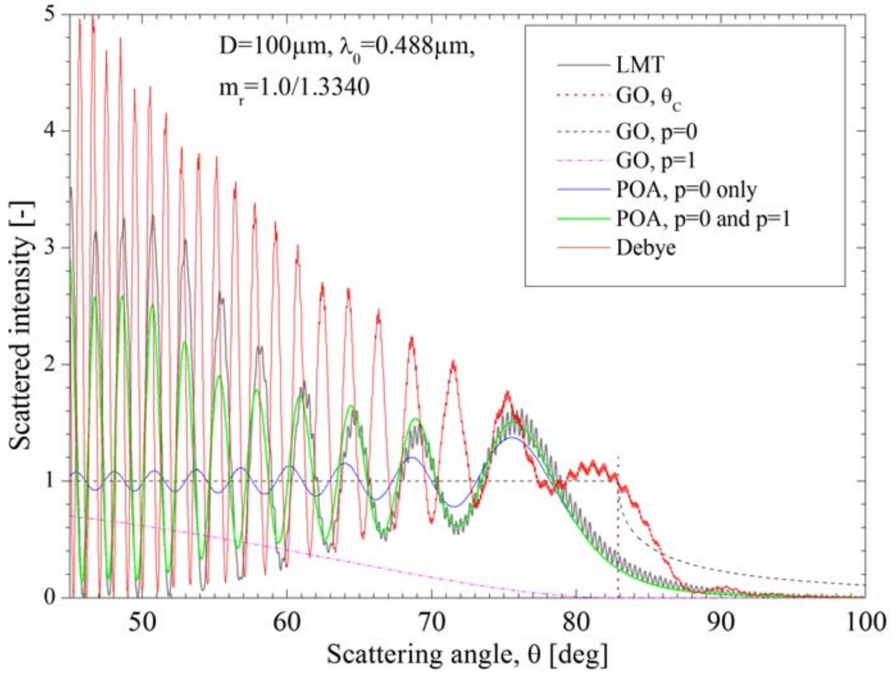

Figure 2.8 Comparison of scattering diagrams in the near-critical-scattering region according to various models and theories.

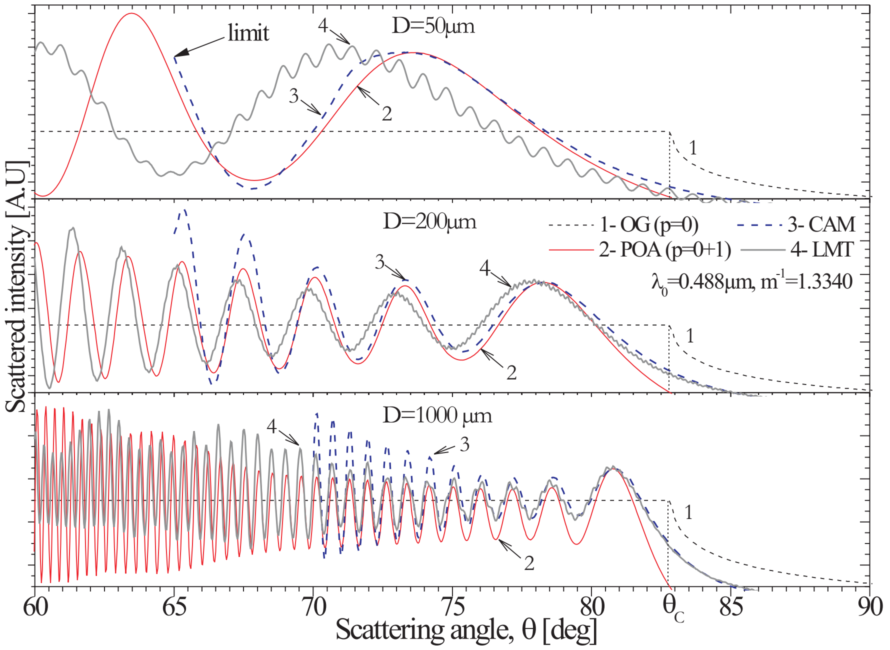

Figure 2.9 CSP of a single air bubble in water according to LMT, CAM, POA (p=0 and 1) and GO, for three different bubble sizes.

We did also calculations with the Debye theory around the critical scattering angle, see for instance Figure 2.8. But, surprisingly, these results are not in agreement with the Lorenz-Mie theory, even for $p \to \infty$. From the theoretical point of view we have no explanation for this discrepancy. So we have repeated these calculations with codes developed by other groups, without more success. This problem is then still open and will be the subject of future works.

2.4 Complex Angular momentum theory

Fiedler-Ferrari et al. (1991) have developed a zero order approximation of the near-critical-angle scattering from a curved interface. It is based on the Complex Angular Moment theory (CAM, e.g. Nussenzweig 1992). The description of the CAM theory is clearly beyond the scope of this Ph.D. work. Our objective, here, was only to evaluate the potentialities of this theory in order to predict the CSP. Let say nevertheless that the CAM theory is based on two theoretical concepts: (i) the scattering particle can be described by a Debye electromagnetic potential (Fiedler-Ferrari et al. 1991); (ii) the localization principle, allows establishing a relation between the expansion order of the electromagnetic fields and the impact parameter of rays onto the particle (van de Hulst 1957).

As an illustration of the accuracy of this CAM approximation, we compare in Figure 2.9 the CSP predicted by different methods: LMT, POA for p=0 and p=*1*, GO for p=0 and CAM only for the rays $p \leq 2$. It should be noted that our CAM code is based on the Fortran code available on the Wiscombe's ftp site (Wiscombe, 2006). The only modification we have made in Wiscombe's code was to replace the subroutine used to calculate the Airy function for large and complex arguments (this subroutine was not properly working in the initial code).

We find from Figure 2.9 that the CAM approximation provides only a good description of the CSP's coarse structure for very large bubbles (typically *D*> 1000 μm). This last result was already noticed by Fiedler-Ferrari et al. (1991). But, to our opinion, as such large bubbles are usually not spherical; the interest of the CAM theory appears to be more theoretical than practical.

2.5 Additional numerical results for a single bubble

In this section we use the LMT and the POA to point out the behavior of the critical scattering regarding to various parameters: the size of the bubbles, their refractive index, the laser wavelength and polarization, a low coherence illumination.

Figure 2.10 shows the evolution of the CSP for air bubbles in water regarding to their size, and for the parallel polarization. From these figures it appears clearly that the CSP intensity and fringes number (or frequency) increases rapidly with the size of the bubbles. The CSP shifts toward larger scattering angles as far as the size of the bubbles increases. Indeed, CSP tend to be closer and closer to the critical scattering angle predicted by geometrical optics ($\approx 82.9°$ for these parameters). POA for p=0 and p=1 shows the same tendencies as LMT, except for the CSP-intensity dependence with the size of the bubbles which is strongly underestimated with this approach.

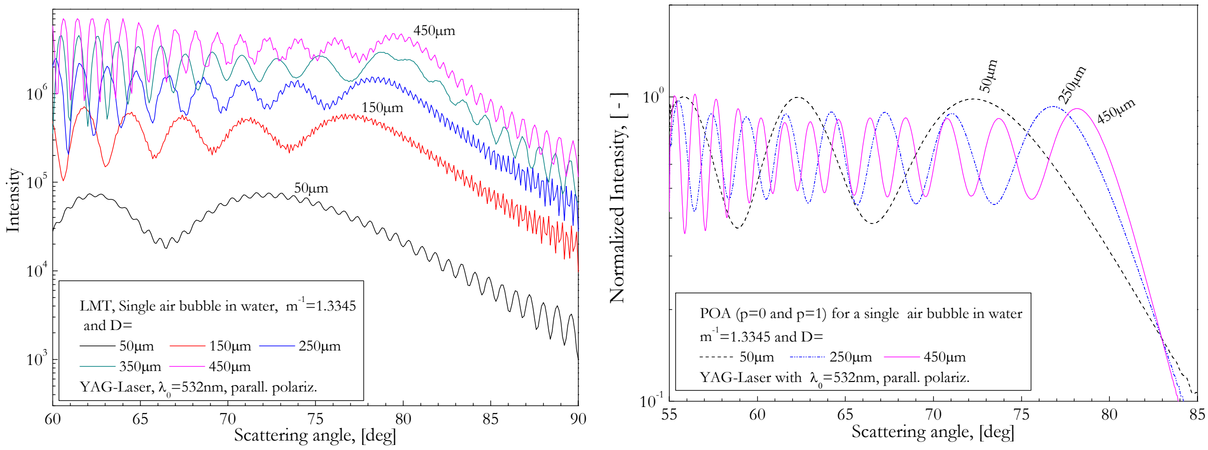

Figure 2.10 LMT and POA (p=0 & p=1) predictions of the CSP intensity profiles CSP of air bubbles in water with different sizes.

Figure 2.11 puts on view, for two totally different bubble sizes, the evolution of the CSP for the parallel and the perpendicular polarizations. For both cases, with the parallel polarization, the low frequency structure of the CSP is more contrasted: higher amplitude range and more cleary harmonic nature of the fringe pattern. This can be explained by the fact that for the parallel polarization the Fresnel coefficients associated to the reflected rays (p=0) are stronger than for the other polarization (see § 2.2 and §5). For the same reason, the CSP obtained with the perpendicular polarization exhibits a much powerful high frequency structure (due to $p \geq 1$). From an experimental point of view, it is easier to detect and process high contrast fringes. This is why in all the following, we consider only the parallel polarization.

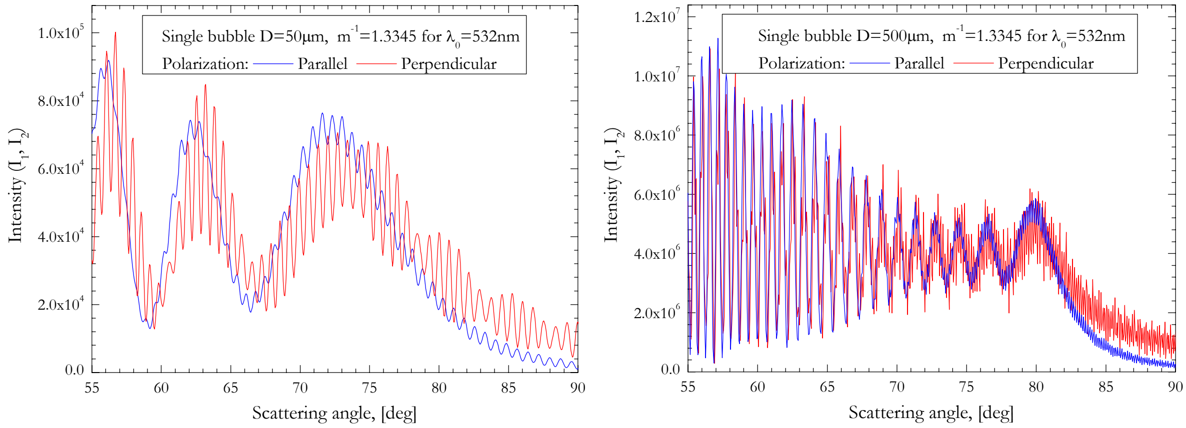

Figure 2.11 Effect of the polarization state of the incident beam onto the contrast of the CSP, for a small and a large bubble (i.e. D=50 and 500µm).

Figure 2.12 (with LMT) and Figure 2.13 (with POA) present for the two previous bubbles sizes the evolution of their CSP for three different relative index, $m^{-1} = 1.3305, 1.3405$ and

1.3505. Despite a slight increase of the CSP intensity with refractive index, the main effect of this parameter is to shift towards larger scattering angles the whole diagram. This is in agreement with geometrical optics predictions (see §2.1). This displacement (or rotation) is done without significant modification in the shape of the CSP. The latter feature will be used in §3.2.2.

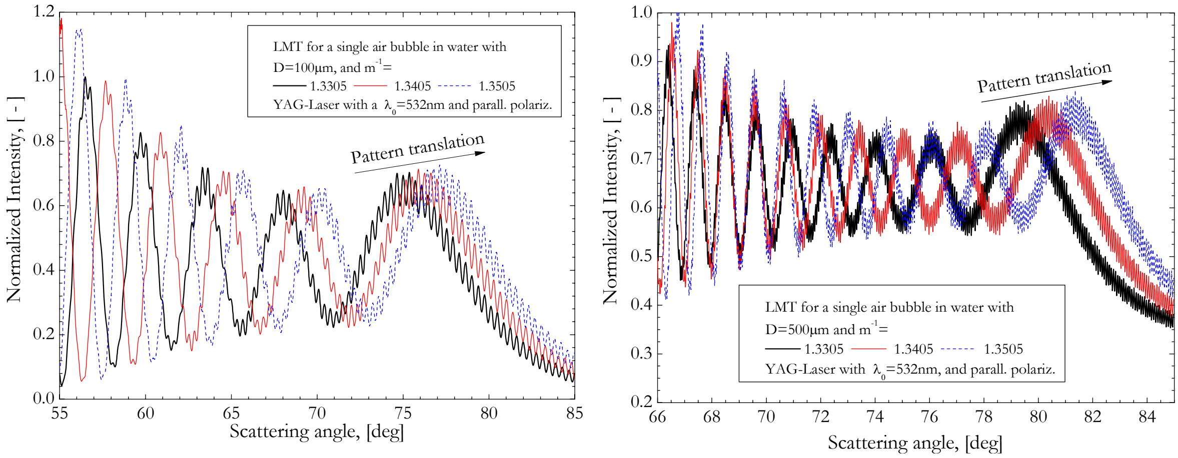

Figure 2.12 CSP calculated with LMT for a) D=100µm and b) D=500µm, and various bubbles' compositions $m^{-1}=1.3305 \sim 1.3505$

In real flows, particles, droplets or bubbles are not necessarily composed of the same pure product. There can be some dispersion in their refractive index. Figure 2.14 shows the evolution of these CSP for a population of $D=200\mu m$ bubbles with mean refractive index $m^{-1}\approx 1.3345$, and an increasing refractive index dispersion: $\Delta m^{-1}=0.0015, 0.0030$ and 0.0045. Noticeably, the major effect of the refractive index dispersion (bubble composition) is to smooth the CSP, to decrease their visibility (like a band pass filter would make).

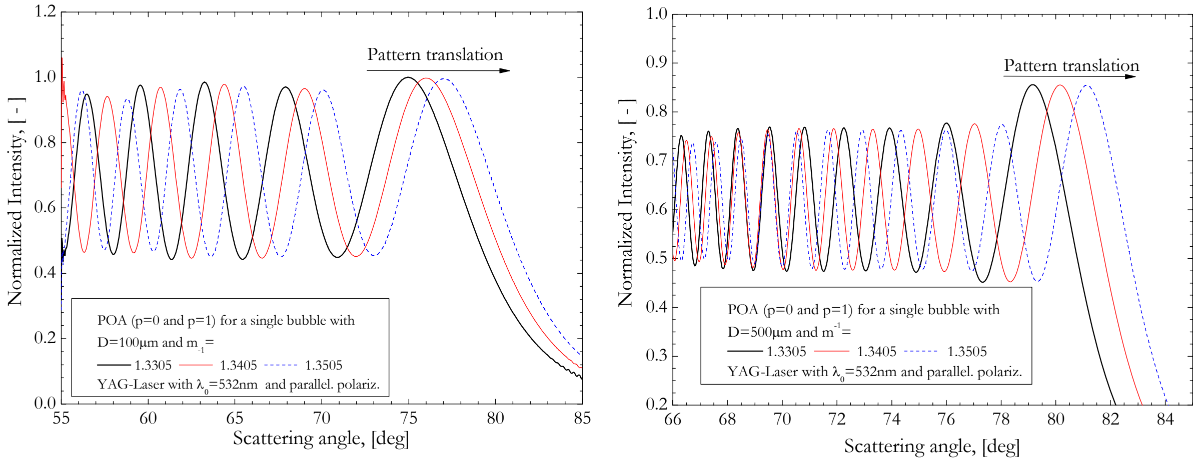

Figure 2.13 CSP calculated with POA (p=0 and p=1) for a) D=100µm and b) D=500µm, and various bubbles' compositions $m^{-1}=1.3305 \sim 1.3505$

Figure 2.15 illustrates the influence of the laser wavelength on CSP patterns of air bubbles in water. Note that for these calculations, performed with LMT, we took into account the dispersion of the refractive index of water with the wavelength. Indeed, the main effect of the wavelength is rather similar to the one obtained when we change the bubble size.

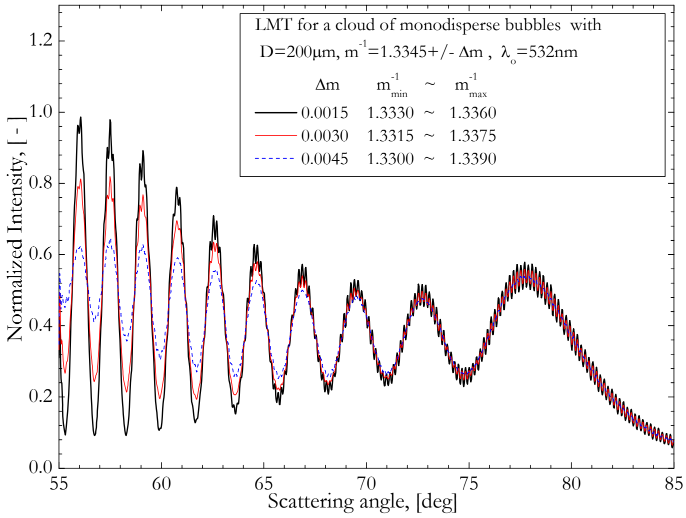

Figure 2.14 Effect of bubble refractive index dispersion of the CSP, LMT and D=200µm.

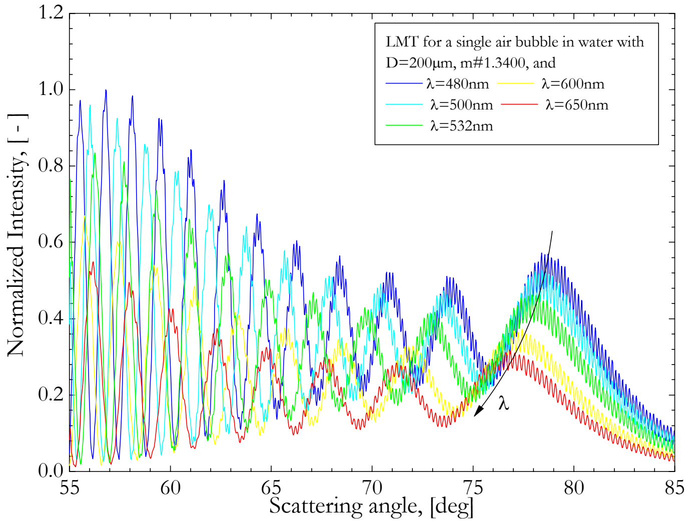

Figure 2.15 LMT predictions a D=200µm air bubble in water, different wavelengths λ=480~650nm.

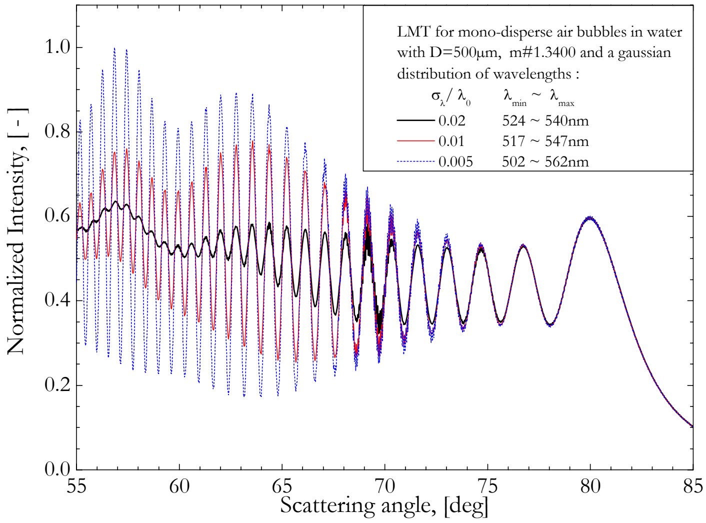

Figure 2.16 CSP obtained with LMT for a D=200µm air bubble in water illuminated with three different low coherence light beams (i.e. three wavelength dispersions).

This is not surprising as the bubble size parameters $x = \pi D / \left(\lambda_0 / m_s \left(\lambda_0 \right) \right)$ is much more sensitive to the bubble diameter D than to the dependence $m_s \left(\lambda_0 \right)$. In LMT formalism $m_s \left(\lambda_0 \right)$ appears also in the expressions of the scattered fields but, once again, the variation of $m_s \left(\lambda_0 \right)$ are really small in comparison to those of x.

Figure 2.16 shows the influence on the CSP of the spectral coherence on the incident beam. For that purpose we have averaged the CSP of the same bubble over 20 wavelengths. The mean wavelength is kept constant but we consider three different widths for the wavelength distribution (Gaussian probability function). Indeed, this kind of simulation may be thought as a first step to model the CSP produce by a bubble illuminated by a low coherence laser or a collimated light emitting diode. Clearly, with the broadening of the incident spectrum, we get almost the same behavior as when we have simulated the influence of dispersion in the bubble refractive index (see Figure 2.14). The contrast of the CSP decreases with the incident light source spectral width. Effects of the bubble absorption is discussed in §5.2.3, see for instance Figure 5.34.

2.6 CARS technique for bubble clouds characterization

2.6.1 Scattering of a cloud of bubbles under single scattering assumption

When the bubbles are randomly distributed in an optical probe volume and the multiple scattering is negligible (e.g. Onofri et al. 1999b), the scattering of a cloud of bubbles can be considered as the result of the incoherent summation of the contributions of all bubbles. Once the intensity scattered by a single bubble $I\left(\theta,D,m,\lambda_0\right)$ is calculated by the LMT, the POA or the CAM, the total intensity scattered by the cloud is obtained by

$$I_t\left(\theta,m,\lambda_0\right)=N\int_{D_{\min}}^{D_{\max}} I\left(\theta,D,m,\lambda_0\right)f\left(D\right)dD \tag{42}$$

where N is the bubble number concentration, $f\left(D\right)$ is the normalized Bubble Size Distribution (BSD) in number such that:

$$\int_{D_{\min}}^{D_{\max}} f(D)dD=1 \tag{43}$$

In principle, from the measured collective scattering intensity pattern $I_t\left(\theta,m,\lambda_0\right)$, we can deduce the size distribution $f(D)$ and the mean refractive index m (see § 5.2.1).

Regarding to the concentration limit, the validity of Eq. (42) can be *estimated* like it is done for laser diffractometry, with the photon mean free path concept. In a bubbly flow the mean free path of a photon between two scattering events is given by $\Lambda=\left(NC_{ext}\right)^{-1}$. C_{ext} is the mean efficiency cross section of the bubbles (Bohren et Huffman, 1983). Let L be the path length of the beam through the cloud of bubbles (Onofri et al. 2008a-b, 2009a). It is usually admitted that multiple scattering effects can be neglected if $\Lambda<L$ which leads to $N<\left(LC_{ext}\right)^{-1}$.

For numerical calculation, the integral limits $D_{\min}$ and $D_{\max}$ are set equal to the roots of the equation $f(D)/\max\left\{f(D)\right\}=1/1000$. Given $f\left(D\right)$ the mean diameter $\bar{D}$ and the standard deviation σ_D can be deduced:

$$\begin{gathered}\bar{D}=\int_{D_{min}}^{D_{\max}} f\left(D\right)DdD\\ \sigma_D^2=\int_{D_{\min}}^{D_{\max}} f\left(D\right)D^2dD-\left(\int_{D_{\min}}^{D_{\max}} f\left(D\right)DdD\right)^2\end{gathered} \tag{44}$$

The size distribution of a large variety of particle systems can be reasonably approximated by analytical particle size distribution laws such as log-normal, power, Gamma-distribution, etc. In our study the log-normal distribution with two free parameters μ,s is exclusively used:

$$f(D)=\frac{1}{Ds\sqrt{2\pi}}\exp\left[\frac{-1}{2}\left(\frac{\ln D-\mu}{s}\right)^{2}\right] \tag{45}$$

The parameters μ , s , the mean diameter $\bar{D}$ and the standard deviation σ_D are related by

$$s=\sqrt{\ln\left(\sigma_D{}^2/\bar{D}^2\right)+1} \qquad \mu=\ln\bar{D}-s^2/2 \tag{46}$$

$$\bar{D}=\exp\left[\mu+s^2/2\right] \qquad \sigma_D^2=\bar{D}^2\left[\exp\left(s^2\right)-1\right] \tag{47}$$

Figure 2.17 illustrates the behavior of the CSP regarding to the bubble clouds characteristics, with $\lambda_0=0.532\mu m$ like for all calculations presented in this section. This figure shows the intensity profiles simulated by using Eq. (42) and the LMT, for various log-normal BSD and the following cases:

a) clouds of air bubbles in water $m^{-1}=1.3334$ with different mean diameters $\bar{D}=12.5\sim 800\mu m$ keeping the relative width of the size distribution constant $\sigma_D/\bar{D}=0.05$;

b) clouds of air bubbles in water with different BSD widths $\sigma_D/\bar{D}=0.025\sim 0.5$ keeping the mean size diameter constant $\bar{D}=100\mu m$;

c) clouds with different bubble compositions $m^{-1}=1.33\sim 1.52$ and with the same BSD, with parameters $\bar{D}=100\mu m$ and $\sigma_D/\bar{D}=0.25$.

In addition to classical effects (like the strong dependence of the scattered intensity on the bubble size), Figure 2.17 shows clearly that $\bar{D}$, $\sigma_D/\bar{D}$ and m^{-1} have a particular and determinant influence on the three main characteristics of the CSP (Onofri et al. 2006 a-b):

a) the mean diameter controls the angular spreading of CSP (i.e. the latter parameter is somewhat connected to the local radius of curvature of the bubble surface),

b) the size distribution width acts mainly on the fringes visibility (i.e. adding CSP patterns with different angular frequencies damps the overall signal intensity modulation),

c) the main influence of refractive index is on the global angular position of the CSP (in agreement with GO predictions, see Davis 1955).

These remarks will be the basis for the development of the 3-points inverse method (see §3.2.2).

Figure 2.18 illustrates the evolution of the main characteristics of CSP produced by various air-water bubble clouds, according to LMT, CAM and POA. For this purpose, we have plotted respectively the evolution of the position of the first fringe $\bar{\theta}_1$, the angular distance between the two first fringes $\Delta\bar{\theta}_{12}=\bar{\theta}_1-\bar{\theta}_2$ and the visibility of the CSP defined here as $\bar{V}_{12,13}=\left(\bar{I}_1-\bar{I}_3\right)/\left(\bar{I}_1-\bar{I}_2\right)$ (see § 3.2.2.2 and Onofri et al. 2008a).

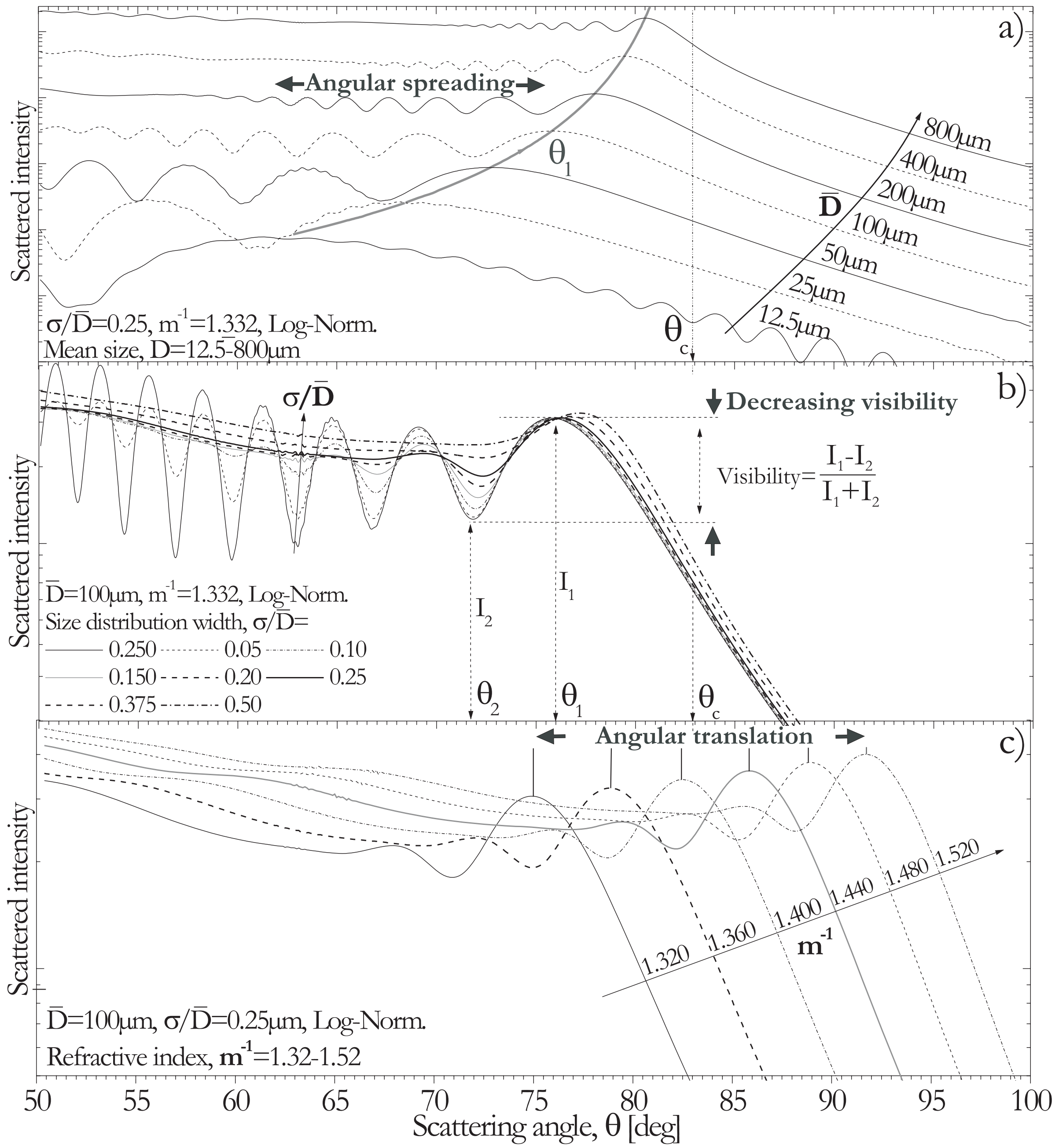

Figure 2.17 CSP calculated by LMT for a log-normal BSD showing the influence of a) the mean size, b) the size distribution width and c) the composition of the bubble cloud onto the CSP main characteristics: angular spreading, visibility (contrast) and absolute angular position.

Conclusion

To conclude on the modeling of CSP produced by cloud of bubbles, we found that only the results obtained by the LMT can be considered as reliable. The POA provides analytical expressions and allows fast calculations but it gives only a rough estimation of parameters like the fringes visibility. From a metrological point of view, the interest of the CAM approximation is found quite limited. In fact, CAM appears to be not really computational efficient and its predictions are only correct for large bubbles that usually are not spherical (see later one).

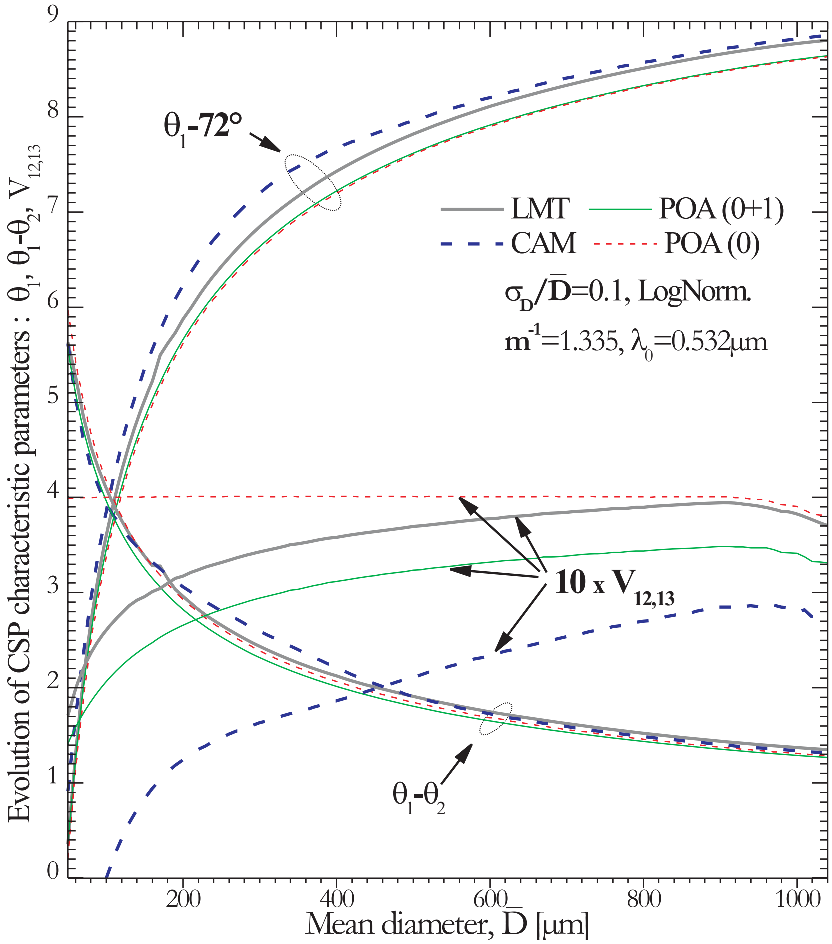

Figure 2.18 Comparison of the evolution of the angular position, the angular spreading and the visibility of CSP versus with the bubble cloud mean size, according to LMT, CAM and POA.

Chapter 3

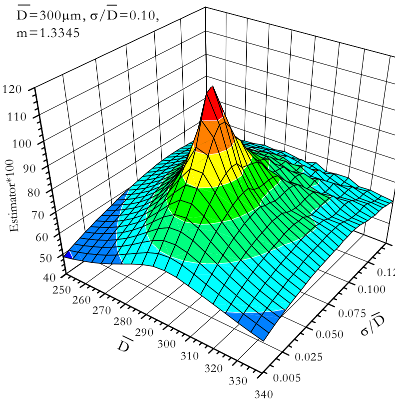

INVERSION PROCEDURES

The intensity profile of the critical scattering pattern generated by a cloud of bubbles is described by the integral equation Eq. (42), known to be an inhomogeneous Fredholm equation of the first kind. Our problem is to find $f(D)$ from the measurement of $I_t(\theta, m, \lambda_0)$ by using the calculated kernel $I(\theta, D, m, \lambda_0)$. This problem requires a specific inverse procedure. In what follows, different approaches to solve this problem are compared.

3.1 Solving the linear algebra problem (NNLSQ method)

3.1.1 Principle and mathematical formalism

The right hand term of Eq. (42) can be discretized as follows

$$\int_{D_{\min}}^{D_{\max}} I(\theta, D, m, \lambda_0) f(D)\, dD = \sum_{j=1}^{M} S_{i,j} F_j \tag{48}$$

where F_j, $j = 1, 2 \cdots M$, is the discretized form of $f(D)$ and $S_{i,j}$ represents the intensity scattered at angle θ_i, $i = 1, 2 \cdots N$, by a bubble of diameter D_j. Further on, $\mathbf{F}(F_j)$ is considered as the unknown vector to be determined and $\mathbf{S}(S_{i,j})$ is a $N \times M$ scattering matrix defined by

$$S_{i,j} = \int_{D_j}^{D_{j+1}} I(\theta_i, D, m, \lambda_0) dD \tag{49}$$

where $I(\theta_i, D, m, \lambda_0)$ can be calculated by the LMT as well as the POA. A measured CSP can be represented as a vector $\mathbf{I}_t$ whose element I_i represents the intensity scattered at angle θ_i by bubbles cloud of size distribution $\mathbf{F}$. The latter is the solution of the linear algebraic equation:

$$\mathbf{I}_t = \mathbf{S} \cdot \mathbf{F} \tag{50}$$

One of the possible solutions can be expressed as:

$$\mathbf{F} = \left(\mathbf{S}^{\mathbf{T}}\mathbf{S}\right)^{-1}\mathbf{S}^{\mathbf{T}}\mathbf{I}_t \tag{51}$$

In fact, Eq.(51) is known as ill conditioned and numerically unstable. Thus, the solving strategy we use here is to minimize iteratively the square of the difference $\mathbf{S}\cdot\mathbf{F}-\mathbf{I}_t$, taking into account the fact that the BSD is always positive $\left(F_i > 0\right)$. This can be done by minimizing the residuals with a Non Negative Least-SQuare scheme (NNLSQ, Twomey 1979) :

$$r_F^2 = \underset{F>0}{Min}\left\|\mathbf{S}\cdot\mathbf{F}-\bar{\mathbf{I}}\right\|^2 \tag{52}$$

This minimization process can be performed by using orthogonal numerical algorithms (Lawson and Hanson, 1974) which are available in the literature or in Matlab environment.

The mean refractive index of the bubble cloud can be determined by minimizing the overall residual:

$$m = \left\{m_n \middle| Min\left(r_F^2\right)\right\} \tag{53}$$

3.1.2 Implementation

Practically, the inversion procedure runs as follows:

- A scattering matrix $\mathbf{S}$ is calculated for a given wavelength and a specific refractive index. For all calculations presented below the nominal matrix size is $N\times M = 565\times 550$, with $\theta_i = 71.1, 71.12\cdots 82.4°$ and $D_j = 100, 102\cdots 1200\mu m$. On an up-to-date computer desktop, this step takes several hours with the LMT and several ten seconds with the full POA. If the bubble relative refractive index is not known in advance, scattering matrices are calculated for all expected refractive indices (for Figure 3.1 or the results presented in Table 5.2 and Table 5.5, we have computed 50 scattering matrices with $m^{-1} = 1.3305,\ 1.3310\cdots 1.3550$).

- Each vector $\left(S_{i,j}, j = 1, 2\cdots M\right)$ of a matrix $\mathbf{S}$ is normalized by the maximal intensity of the corresponding first fringe.

- The experimental CSP profiles are automatically band-pass filtered, calibrated, rescaled and normalized by the intensity of the first fringe (see §3.2.2).

- The NNLSQ algorithm is applied to minimize the residual Eq.(52) and to get $\mathbf{F}$. Obviously the length of the unknown vector can be reduced (i.e. the bins width is increased) according to the expected BSD. With a matrix $N\times M = 565\times 100$ the computational time is limited to few seconds.

- When the refractive index is to be determined, both Eq. (52) and Eq. (53) must be used to determine $\mathbf{F}$ and m. To further improve the refractive index measurement, the corresponding residuals are fitted with a 4th degree polynomial. Figure 3.1 shows typical results obtained with this method when processing experimental CSP.

- **F** is directly used to obtain the bubble mean size and standard deviation by Eq. (44) (NNLSQ-raw method).

- To damp the noise generated by the inverse procedure, i.e. to reject the "ghost" bubbles (see for instance Figure 5.2), **F** can be low pass filtered prior to calculate the statistical moments (NNLSQ-filt. method). Filtering matrices can also be used (e.g. Xu 2007, Onofri et al. 2009b).

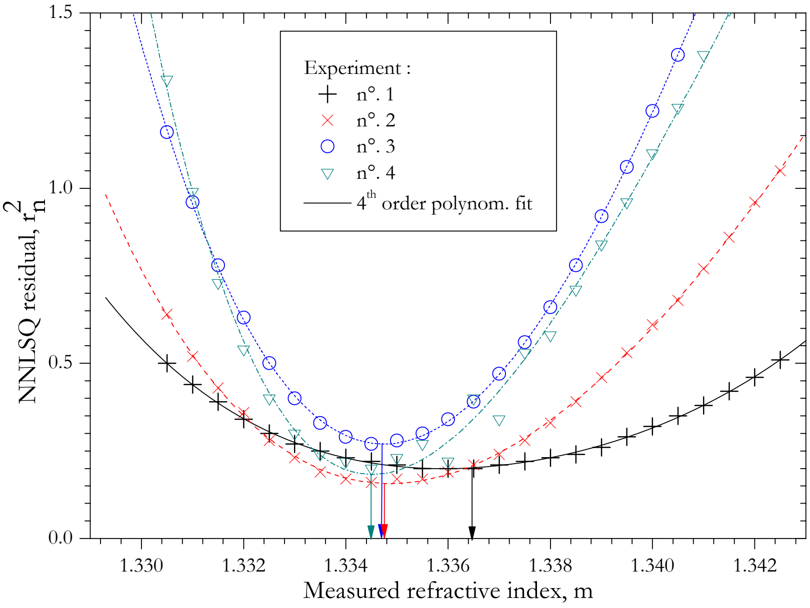

Figure 3.1 Evolution of the residual of the NNLSQ method versus the estimated bubble cloud mean refractive index: cases 1 to 4 corresponds to experiments performed on different iar-xater bubbly flows, respectively presented in Figure 5.2, Figure 5.3, Figure 5.4 and Figure 5.5.

3.1.3 Exemplifying numerical results

From Figure 5.2, Figure 5.4, Figure 5.5 and Figure 5.3 we can have a good idea of the efficiency of the NNLSQ method to inverse experimental CSP. This technique gives good results but, with experimental data it is extremely difficult to fully evaluate the capability of this technique. In fact, with experimental CSP we are limited by the capacities of the bubble generators and the accuracy of the so-called "reference" techniques. So, the objective of the present section is not to be exhaustive but simply to give some overview about the minimum size width that can be determinated with this method or the minimum distance between two distributions that can be separated (bimodal distribution).

For this purpose we have simulated a bimodal bubble size distribution composed of two log-normal samples with the same width and different weights for the modes. For all cases the first mode is centered on $\overline{D} = 400\mu m$ as it corresponds to a stable regime of the piezo-jet (see §4.2.1).

The second mode starts at $\overline{D} = 400\,\mu m$ and it is moved successively to $\overline{D} = 420, 450, 500$, 700, and $1000\,\mu m$. We consider finally four different cases:

- Figure 3.2 shows the results obtained for $\sigma_D = 4\,\mu m$; and modes weights 50% and 50%.
- Figure 3.3 shows the results obtained for $\sigma_D = 20\,\mu m$ and mode weights 50% and 50%.
- Figure 3.4 shows the results obtained for $\sigma_D = 10\,\mu m$ and mode weights 75% and 25%.
- Figure 3.5 shows the results obtained for $\sigma_D = 10\,\mu m$ and mode weights 25% and 75%.

For all these figures we present on the right the corresponding CSP, as it could be observed experimentally. The Bubble size distributions are plotted on the left: the simulated one is represented as a histogram with bars while the reconstructed one takes the form of a histogram with a continuous red line.

Looking at these figures, we may first say that the NNLSQ inverse method works pretty well. All modes are detected and correctly localized. Their relative weights are also correctly estimated. For relatively large distribution widths this parameter is well estimated for the two modes, see Figure 3.3. However, the NNLSQ method overestimates the width of the narrower distributions (see for instance Figure 3.2). This effect may be explain by that fact that the size resolution of the scattering matrix used as a kernel of the Fredholm integral (Eq. (48) and §3.1.2) is necessarily limited. One additional reason is probably that high frequency oscillations of the CSP (due to $p \geq 1$) are not dumped by narrow BSD. These oscillations may be considered, in some extend, as a source of noise for the NNLSQ method. By the way, it may be noticed that for the narrowest modes (see Figure 3.2) some noise appears (what we call “ghost” bubbles in the experimental part, see for instance Figure 5.2).

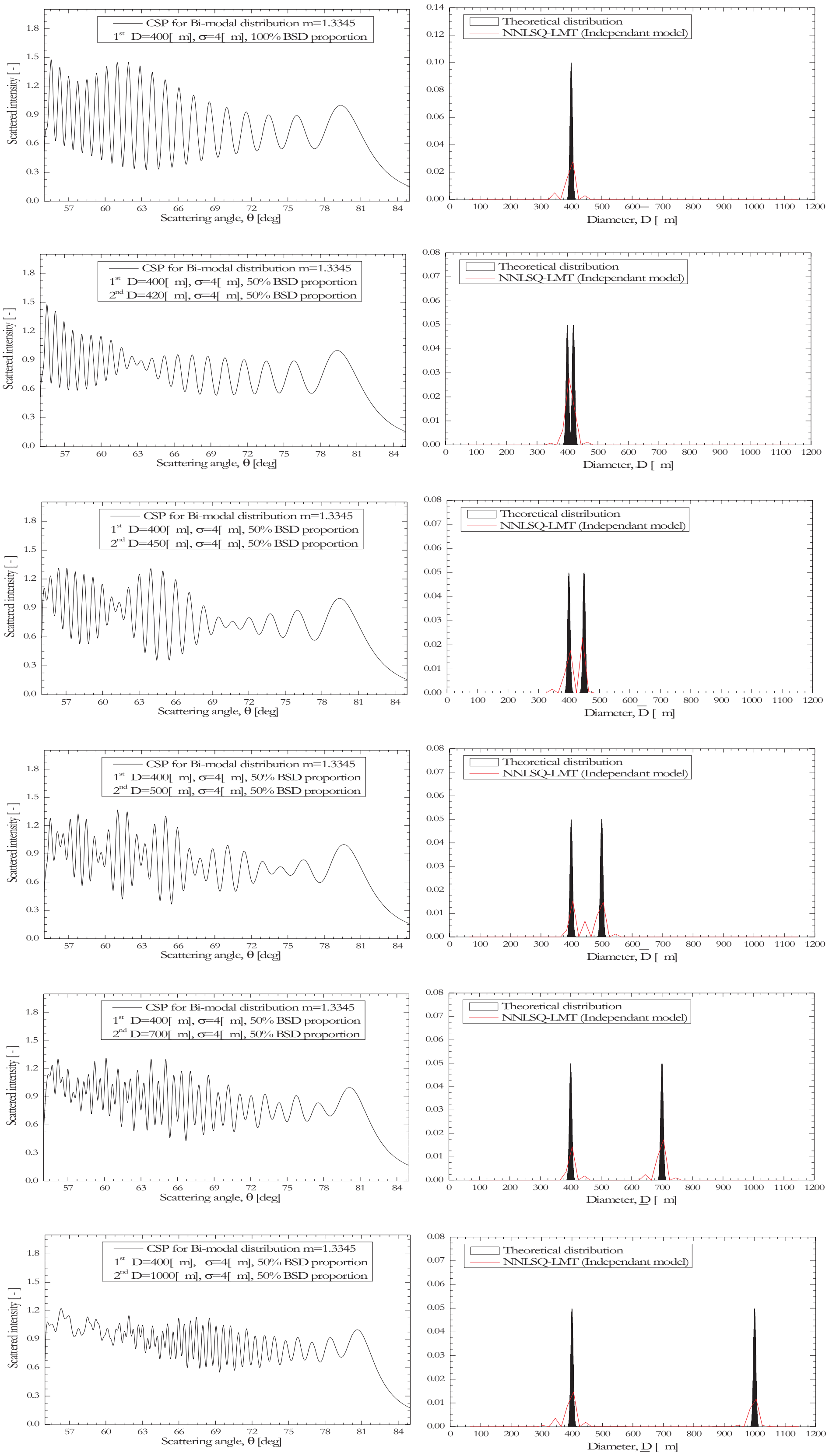

Figure 3.2 Bimodal bubble size distributions composed of two log-normal distributions with equal widths $\sigma_D = 4\,\mu m$ and mode weights 50% and 50%.

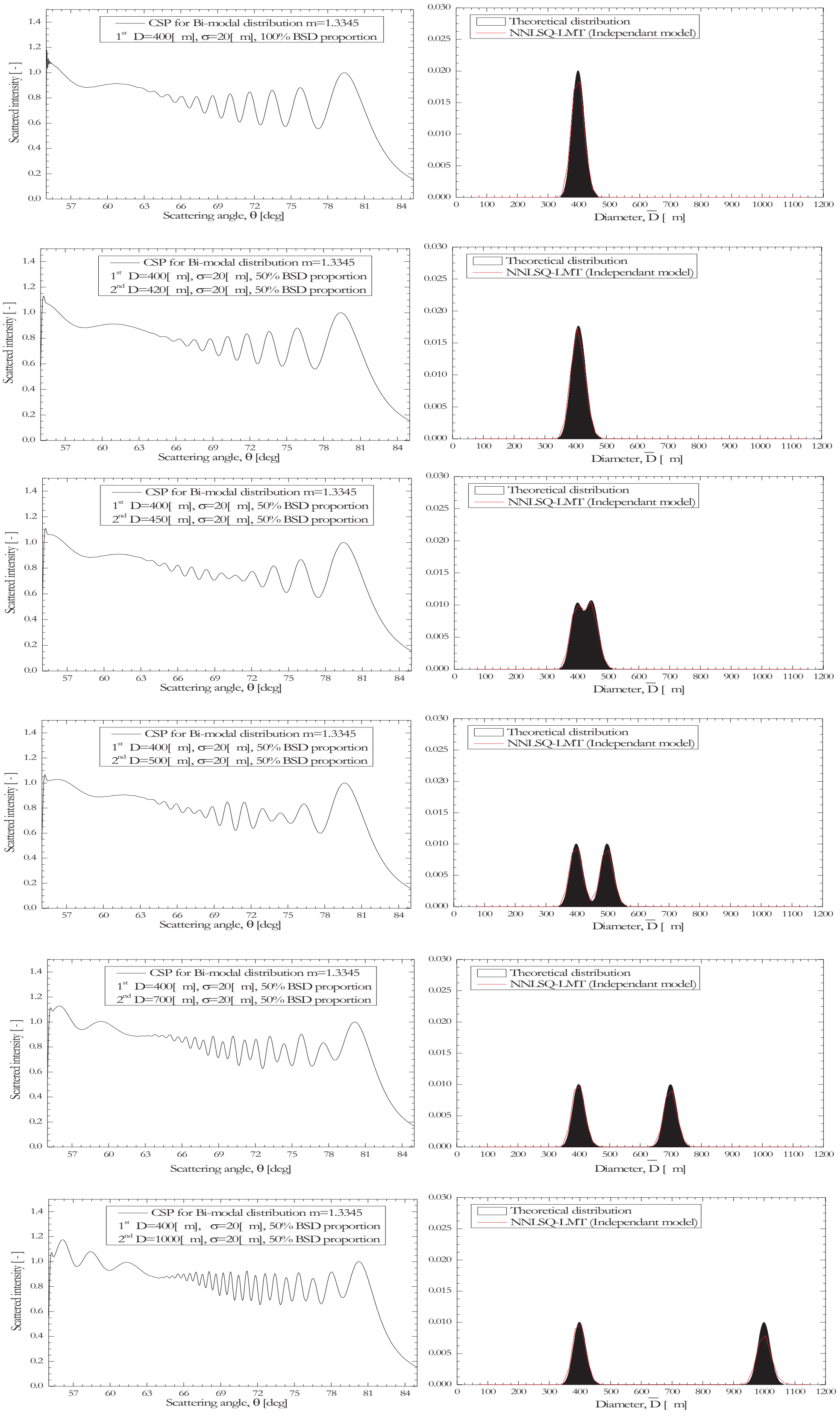

Figure 3.3 Bimodal bubble size distributions composed of two log-normal distributions with equal widths $\sigma_D = 20\,\mu m$ and modes weights 50% and 50% .

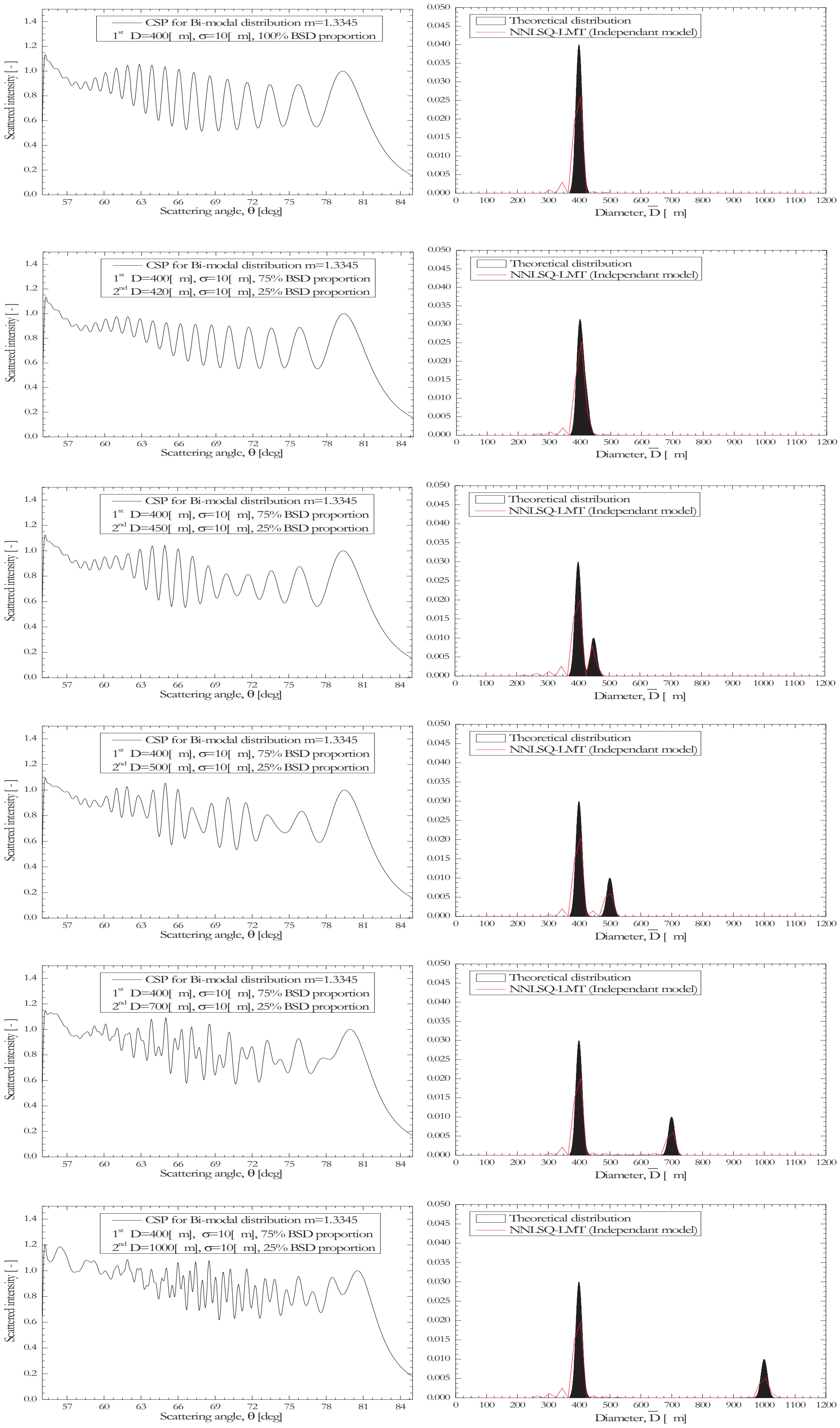

Figure 3.4 Bimodal bubble size distributions composed of two log-normal distributions with equal widths $\sigma_D = 10\,\mu m$ and modes weights 75% and 25%.

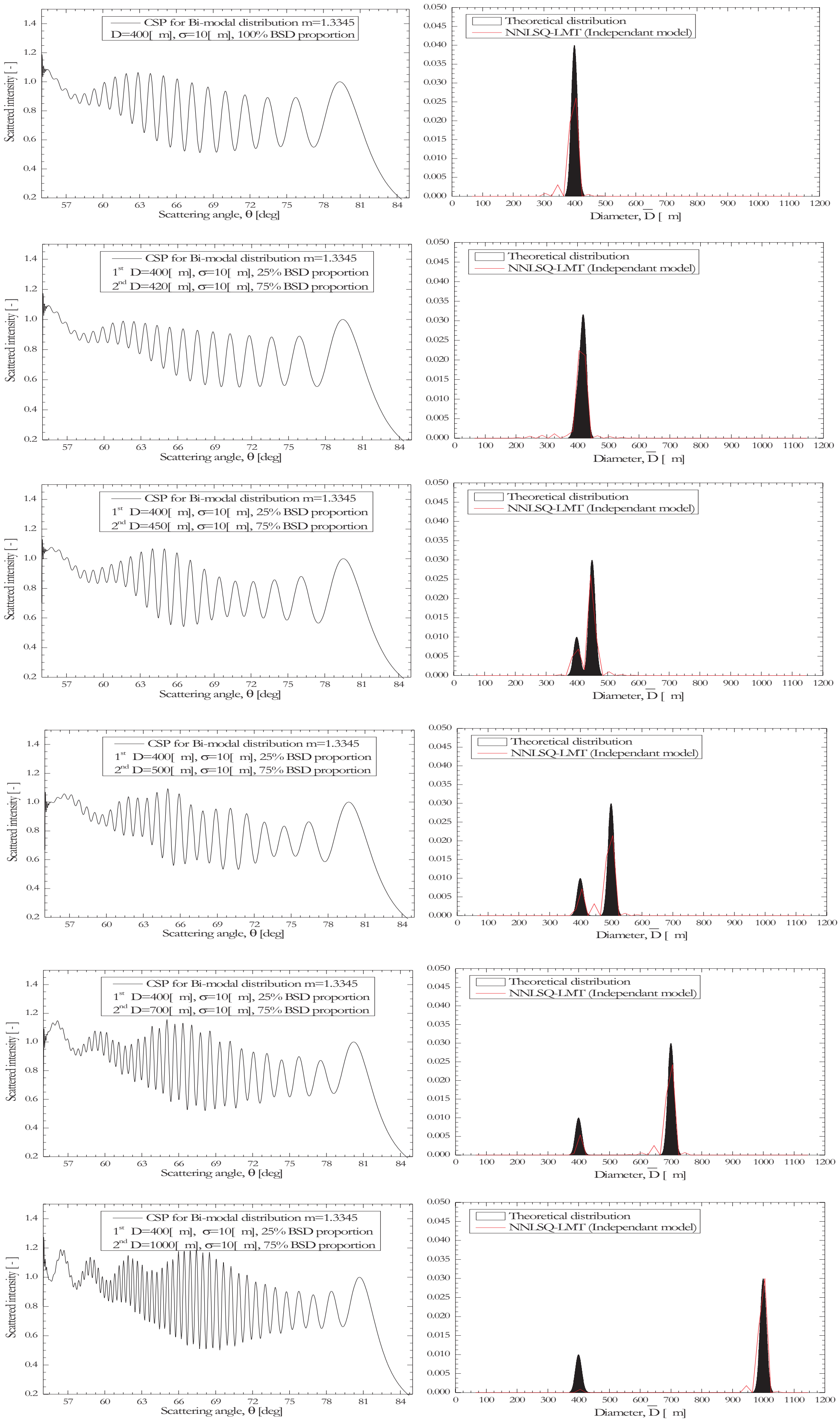

Figure 3.5 Bimodal bubble size distributions composed of two log-normal distributions with equal widths $\sigma_D = 10\,\mu m$ and modes weights 25% and 75%.

3.2 Dependent models

3.2.1 Full correlation estimator (LSQ-LMT-LogNorm. method)

3.2.1.1 Principle

We have mentioned earlier that the assumption of a particular size distribution is a quite common procedure to inverse experimental data (e.g. Xu, 2007). In what follows, and for what will be called further on the "LSQ method", we assume a log-normal BSD and try to minimize the following residual:

$$r^2_{\bar{D},\sigma_D,m} = \sum_{j=1}^{M} \left| S_{i,j} F_{Log-Norm.}\left(\bar{D},\sigma_D\right)_j - I_i \right|^2 \tag{54}$$

where $F_{Log-Norm.}\left(\bar{D},\sigma_D\right)_j$ is the BSD of a Log-Normal type with only two unknown parameters $\bar{D}$ and σ_D. The inverse problem is here strongly constraint. This allows canceling out the inversion noise, but can lead to totally misleading results if the BSD is not correctly chosen (like in case of multimode distributions).

3.2.1.2 Numerical results

To test the accuracy of this method we basically did the same as for the 3-points methods (see next section). To resume, the idea is simply to produce noisy signals from LMT-CSP and to analyze them as they were experimental signals, see Figure 3.6 to Figure 3.9. For all figures we use Eq. (54) and a least-square method, with as an input: the scattering models, i.e. LMT in Figure 3.6 and Figure 3.7, and POA (p=0+p=1) in Figure 3.8 and Figure 3.9

For all these figures the results obtained with the 3-points method are presented on the left, and the ones with the LSQ method, on the right. According to our terminology we are presenting here numerical results from the 3pts-LMT-LogNorm, the LSQ-LMT-LogNorm and the LSQ-POA-LogNorm. inverse methods.

From these figures it appears that the overall error with the LSQ-LMT-LogNorm is about 1.5% for $\bar{D}$, 1.3% for $\sigma/\bar{D}$, and 0.15% for relative refractive index. The resolution of the 3-points method is lower. In the same way, LMT allows more accurate predictions than POA. Figure 3.9 clearly shows that with inverse techniques the resolution of the measurements does not only depends on the quality of the inversion scheme, it also strongly dependents from the quality of the approach used to model the response of the system (i.e. light scattering theories).

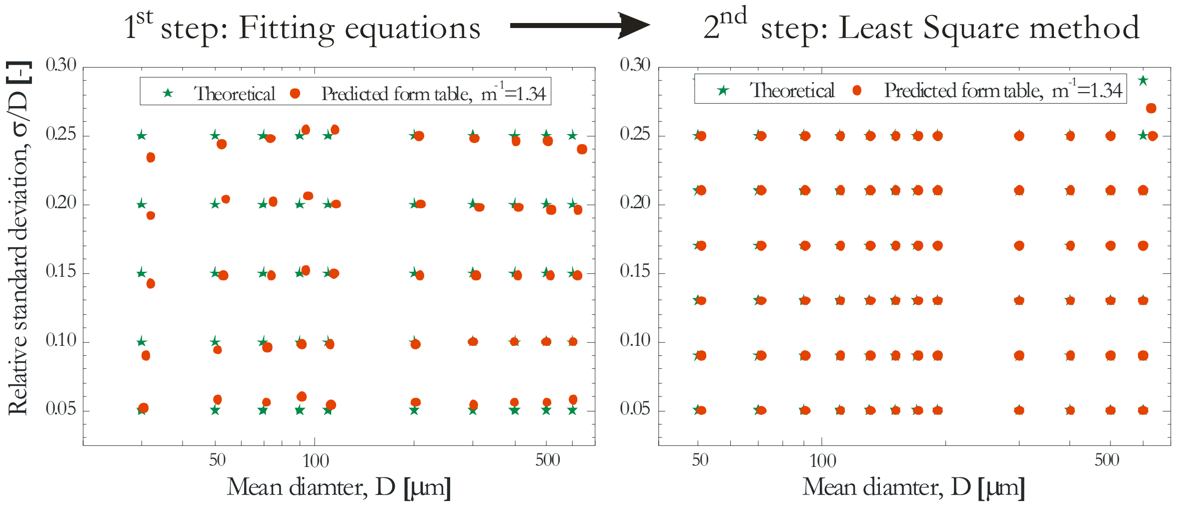

Figure 3.6 Predictions of the 3-points (left) and the LSQ (right) inverse methods for the mean diameter and the relative size distribution width. For both cases we use a Log-Normal BSD and the data tabulated from LMT calculations (green stars).

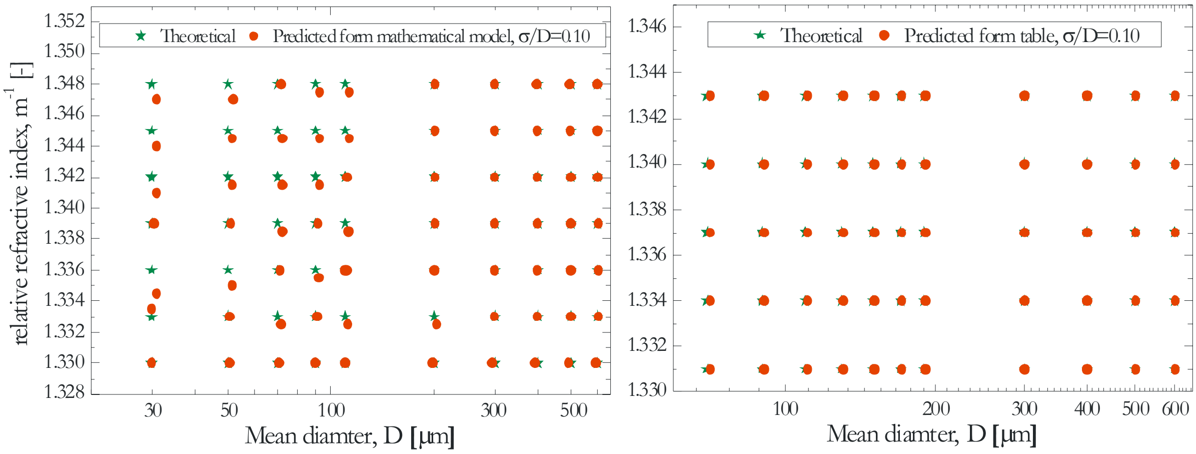

Figure 3.7 Same parameters as in the previous figure but in the mean diameter-refractive index plane.

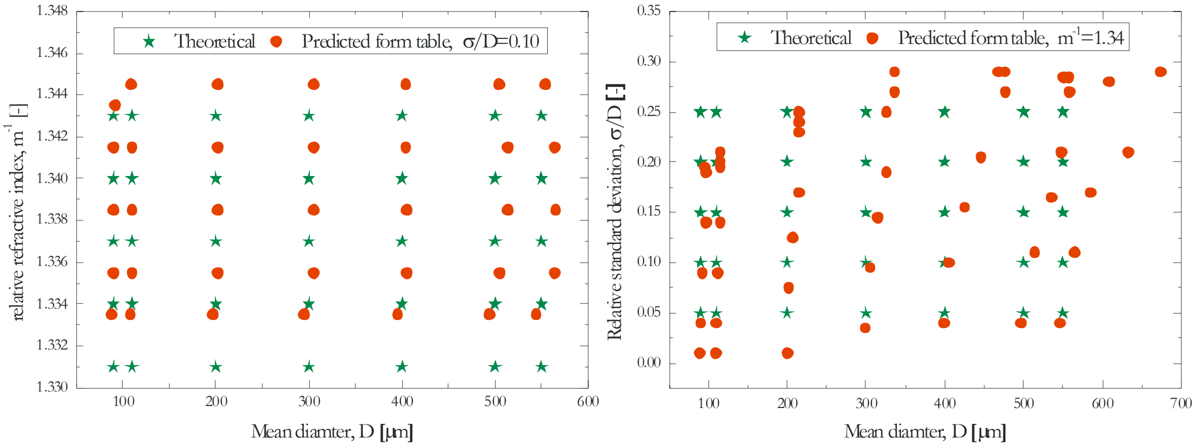

Figure 3.8 Same parameters as in Figure 3.6 but for POA (p=0 & p=1) as the scattering theory.

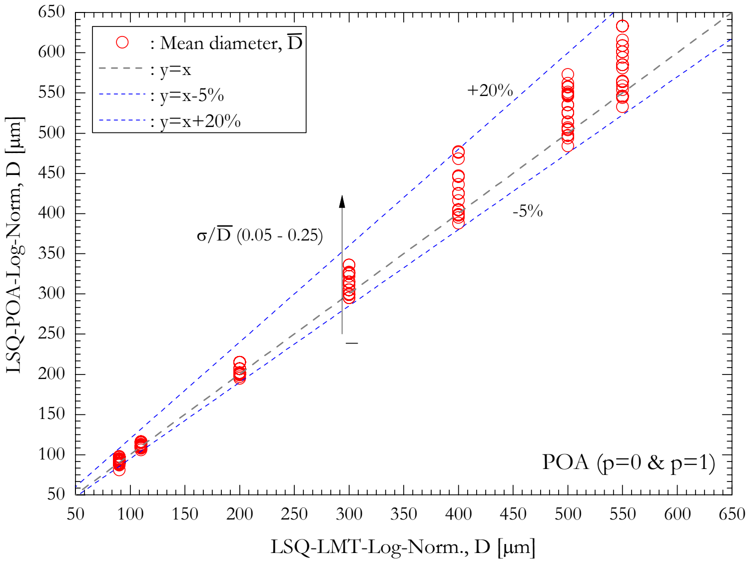

Figure 3.9 Comparision of the results obtained with the LSQ method for a Log-Normal bubble size distribution, with LMT or POA (p=0 & p=1) as scattering theories.

3.2.2 Partial correlation estimator (3points-LMT-LogNorm. method)

3.2.2.1 Principle

The two previous inverse methods require rather large computational resources as, basically, they compare the simulated and the measured CSP over all measured angular range. A simple approach to speed up the inversion procedure consists in only comparing the three main characteristics of experimental and theoretical CSP, namely the angular position, the angular spreading, and the visibility. So the idea here is to look for the values $\bar{D},\sigma_D,m$ that minimize the following correlation estimator:

$$\Gamma^2 = \alpha\left[\bar{\theta}_1^{Th}\left(\bar{D},\sigma_D,m\right)-\bar{\theta}_1^{Exp}\right]^2+\beta\left[\Delta\bar{\theta}_{12}^{Th}\left(\bar{D},\sigma_D,m\right)-\Delta\bar{\theta}_{12}^{Exp}\right]^2+\gamma\left[\bar{V}_{12,13}^{Th}\left(\bar{D},\sigma_D,m\right)-\bar{V}_{12,13}^{Exp}\right]^2 \quad (55)$$

where α, β and γ are normalization and weighting parameters, while superscripts Th and Exp stand for calculated and experimental quantities respectively. This method requires creation of a look-up table containing all possible expected values for $\bar{\theta}_1^{Th}$, $\Delta\bar{\theta}_{12}^{Th}$ and $\bar{V}_{12,13}^{Th}$. This is done by using the matrix $\mathbf{S}$ and by iterating along the parameters $\bar{D},\sigma_D$ and m with a log-normal BSP assumption. With this method the inversion procedure is almost "instantaneous" (Onofri et al. 2006 a-b). Note that rather similar method was introduced by Onofri et al. (2004) to inverse with a lot of success forward diffraction patterns. We call this inverse method the "3-points" method which can be either based on LMT or POA predictions.

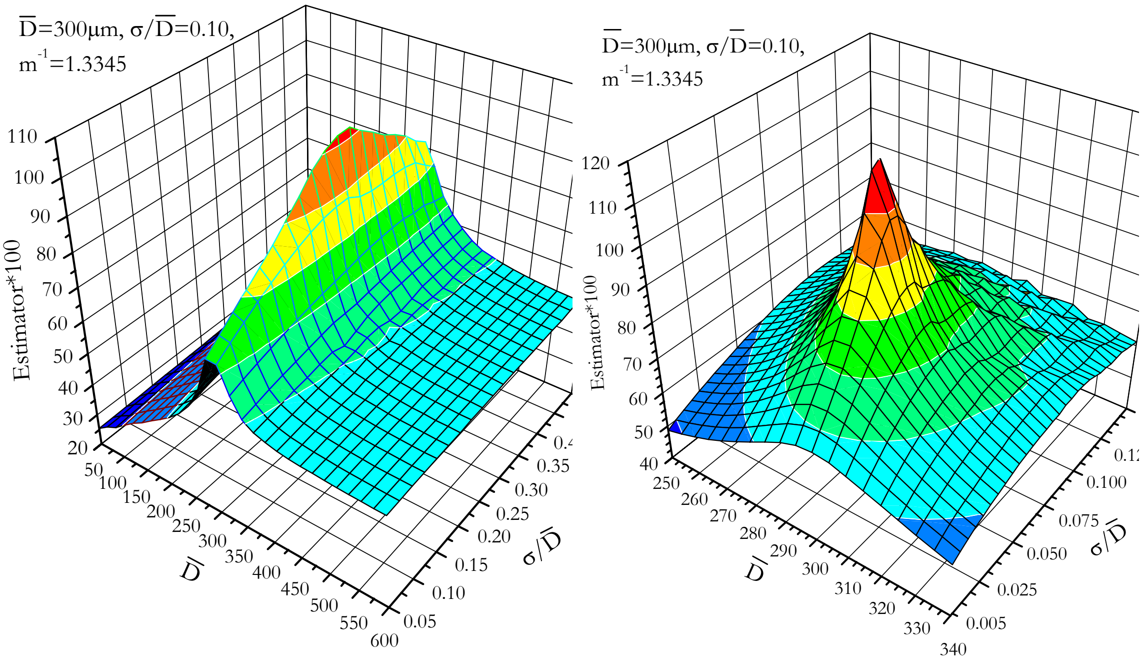

Figure 3.10 Evolution of the full correlation estimator for two size distributions ranges in size and width.

3.2.2.2 Implementation

To implement the “3-points” inverse method the first step is to extract the three basic aforementioned quantities.

In a CSP the main or easily remarkable point is the maxima of the first bright fringe I_1 and its angular localization θ_1, then it is the first dark fringe or “valley” with I_2 and θ_2, then the second bright fringe with I_3 and θ_3, see Figure 3.11. From the measurement of these quantities we can defined a contrast or “Visibility” criteria for this pattern:

$$V = \frac{I_1 - I_2}{I_3 - I_2} \tag{56}$$

The CARS technique use a Fourier setup which gives us absolute angle measurements but not, absolute intensity measurements. Let assume that the response of the optical system is linear (i.e. the response of the CCD chip). The measured intensity $I(\theta)$ is then equal to $I(\theta) = aI'(\theta) + b + n$, where $I'(\theta)$ is the “true” scattered intensity; a a scaling factor which depends on the camera gain, laser power, etc.; b is an offset due to the CCD chip, the background noise (supposed constant); n is some white noise. So for the instantaneous CSP visibility we get:

$$V = \frac{(aI_1^{'} + b + n_1) - (aI_2^{'} + b + n_2)}{(aI_3^{'} + b + n_3) - (aI_2^{'} + b + n_2)} = \frac{a\left(I_1^{'} - I_2^{'}\right) + n_1 - n_2}{a\left(I_3^{'} - I_2^{'}\right) + n_3 - n_2} \tag{57}$$

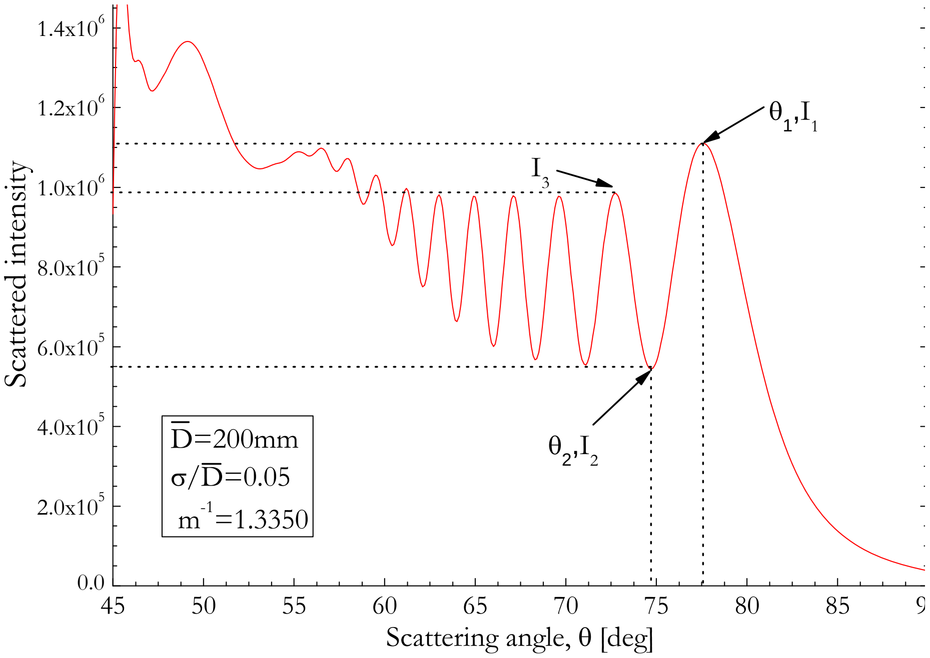

Figure 3.11 Three main characteristics of the critical scattering pattern for the “3-points” inverse method.

As we need to integrate CSP over a certain time (i.e. camera time exposure), statistically the time-averaged CSP is:

$$\langle V \rangle_t = \frac{I_1^{'} - I_2^{'} + \langle n \rangle - \langle n \rangle}{I_3^{'} - I_2^{'} + \langle n \rangle - \langle n \rangle} = \frac{I_1^{'} - I_2^{'}}{I_3^{'} - I_2^{'}} \text{ as } \langle n_i \rangle_t = 0 \tag{58}$$

Regarding to our hypothesizes, Eq. (58) gives us a measured visibility that can be directly compared to the theory.

Based on the above considerations we have built with LMT a database containing these three characteristic points θ_1, θ_2, V for many Log-Normal BSD mean size $\bar{D}$, size distribution width σ_D, and relative reflective index m. With this database, we can use Eq. (55) to inverse experimental CSP.

To accelerate the inversion procedure, an another solution is to find some analytical relations between (θ_1, θ_2, V) and $\left(\bar{D}, \sigma_D, m\right)$. For reasons already mentioned above, it is better to find relations between (θ_1, θ_2, V) and $\left(\bar{D}, \sigma_D / \bar{D}, m\right)$. To do so, two different software were used : Origin (OriginLab 2003) for two dimensional fitting and DataFit (Okdale – Engineering 2006) for multidimensional fitting. We begin this work by finding equations that can describe correctly the sensitivity of θ_1 with $\bar{D}$. From POA equations (see also Figure 3.12) we start with

$$\theta_1(D) = \frac{a_1 - b_1}{1 - \bar{D}^{c_1}} + b_1 \tag{59}$$

where a_1, b_1 and c_1 are coefficients to be determined numerically. Then, to add some dependency to the refractive index, we use a linear angular translation (see §2.5):

$$\theta_1(\overline{D},m)=\frac{a_1-b_1}{1-\overline{D}^{c_1}}+b_1+d_1\cdot m+e_1 \tag{60}$$

where d_1 and e_1 are two additional unknown coefficients. To take into account the stretching of CSP diagrams with the BSD relative width we transform the previous equation in :

$$\theta_1(\overline{D},m,\sigma_D)=\left(\frac{a_1-b_1}{1-\overline{D}^{c_1}}+b_1\right)\cdot\left(f_1\cdot s+g_1\right)+d_1\cdot m+e_1+h_1\cdot\left(\sigma_D/\overline{D}\right)+i_1 \tag{61}$$

where f_1, g_1, h_1 and i_1 are four more coefficients to be determined.

We can do basically the same for the two other functions so that we get finally, a system of three equations with 3 unknown variables and 29 unknown coefficients (see Table 3.1):

$$\theta_1(\overline{D},m,\sigma_D)=\left(\frac{a_1-b_1}{1-\overline{D}^{c_1}}+b_1\right)\left(f_1\sigma_D/\overline{D}+g_1\right)+d_1m+e_1+h_1\sigma/\overline{D}+i_1 \tag{62}$$

$$\theta_2(\overline{D},m,\sigma_D)=\left(\frac{a_2-b_2}{1-\overline{D}^{c_2}}+b_2\right)\left(f_2\sigma_D/\overline{D}+g_2\right)+d_2m+e_2+h_2\sigma/\overline{D}+i_2 \tag{63}$$

$$V(\overline{D},m,\sigma_D)=\left(\frac{a_3-b_3}{1-\overline{D}^{c_3}}+b_3\right)\left(f_3\sigma/\overline{D}+g_3\right)+d_3m+e_3+\frac{h_3}{1+\left(\frac{\overline{D}}{i_3}\right)^{j_3}}+k_3 \tag{64}$$

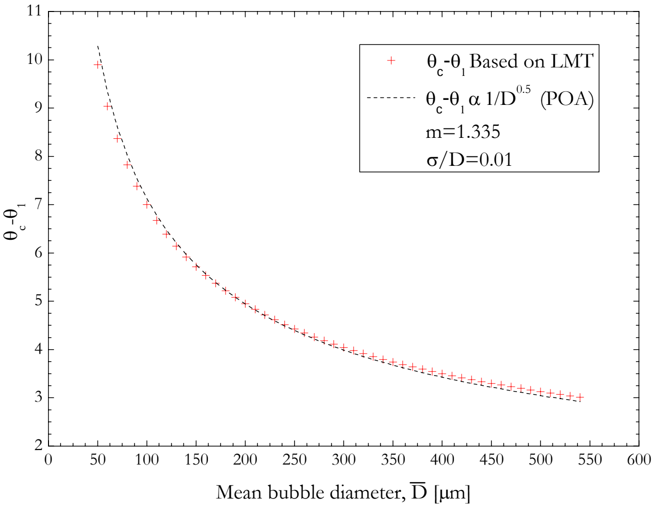

Figure 3.12 Change of $\theta_c-\theta_1$ dependant on mean size diameter of bubble $\overline{D}$, comparizon beetwen LMT and prediction based on (Onofri, 1999).

3.2.2.3 Numerical results

Table 3.1 shows the parameters obtained numerically with the multidimensional fitting software "DataFit". The next figures, from Figure 3.13 to Figure 3.18, show some comparisons between LMT predictions and the ones obtained with Eqs.(62)-(64) and the parameters of Table 3.1. The agreement is very good. So that, with this method, by measuring θ_1, θ_2, V and solving the system of three equations, we can get directly the three main parameters of the BSD: $\bar{D}, m, \sigma_D$.

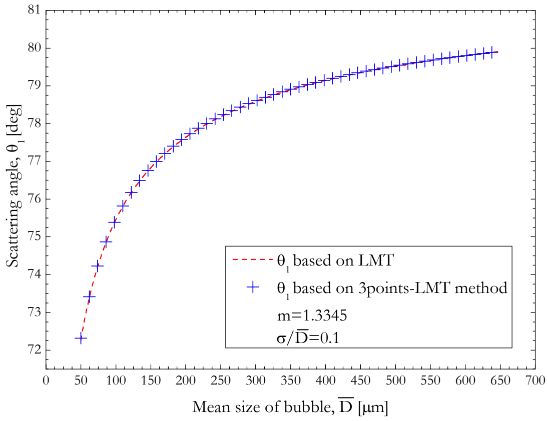

Figure 3.13 Comparison beetween the predictions of LMT and Eq. (62) for $\theta_1\left(\bar{D}\right)$

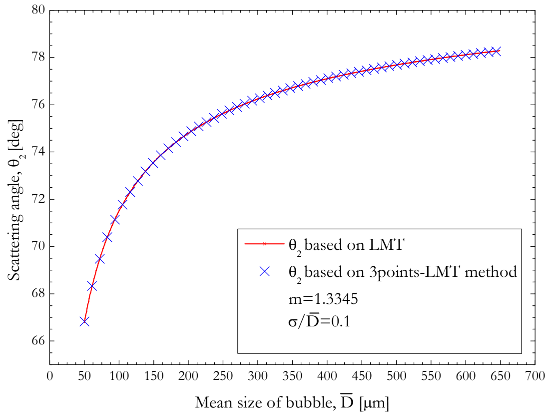

Figure 3.14 Comparison beetween the predictions of LMT and Eq. (63) for $\theta_2\left(\bar{D}\right)$

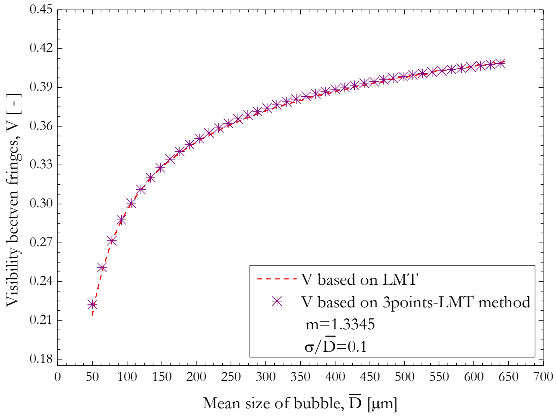

Figure 3.15 Comparison beetween the predictions of LMT and Eq. (64) for $V\left(\bar{D}\right)$

Coeff.	$\theta_1(\bar{D},m,\sigma_D)$	$\theta_2(\bar{D},m,\sigma_D)$	$V(\bar{D},m,\sigma_D)$
a	-31,11588	-79,78361	-2,68715
b	82,23532	82,10626	0,36734
c	0,59423	0,5748	0,5225
d	98,5244532101951	100,466938928936	0,474595356975684
e	-131,072124932896	-133,708211236054	-0,631365816542236
f	-0,362546228715568	-0,225230854193662	-2,15292145129313
g	1,01767560948619	1,00668330332316	0,983936238257257
h	29,738510659132	18,1800845686661	1,23018295907996
i	-1,41489744758847	-0,497482181874814	0,253798543061762
j			-1,95509526223828
k			0,00900972843721926

Table 3.1 Coefficients obtained with LMT for the “3-points” method

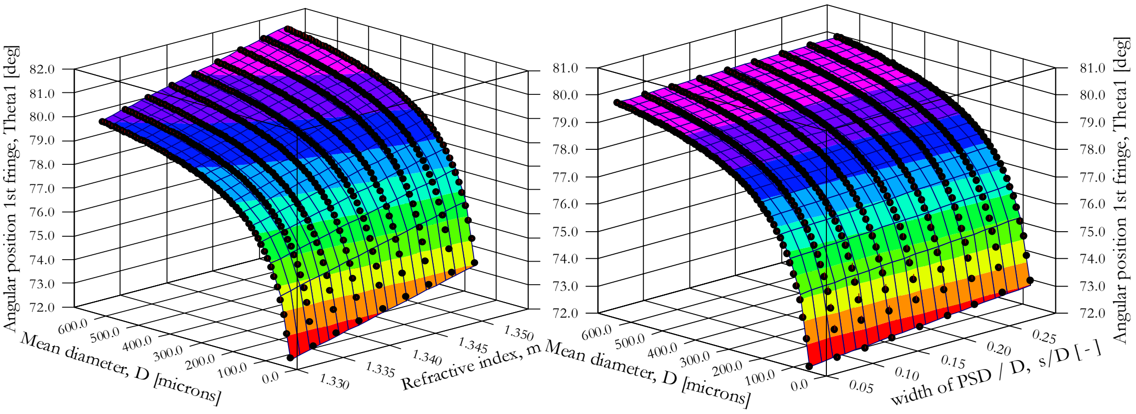

Figure 3.16 Prediction of $\theta_1 = f(\bar{D},\sigma_D,m)$: left for fixed size distributions relative widths : $\sigma/\bar{D}=0.10$; right: for a fix refractive index $m^{-1}=1.3400$. Results of Eq. (62) correspond to the colored and continuous surface and those of LMT to the black circles (●).

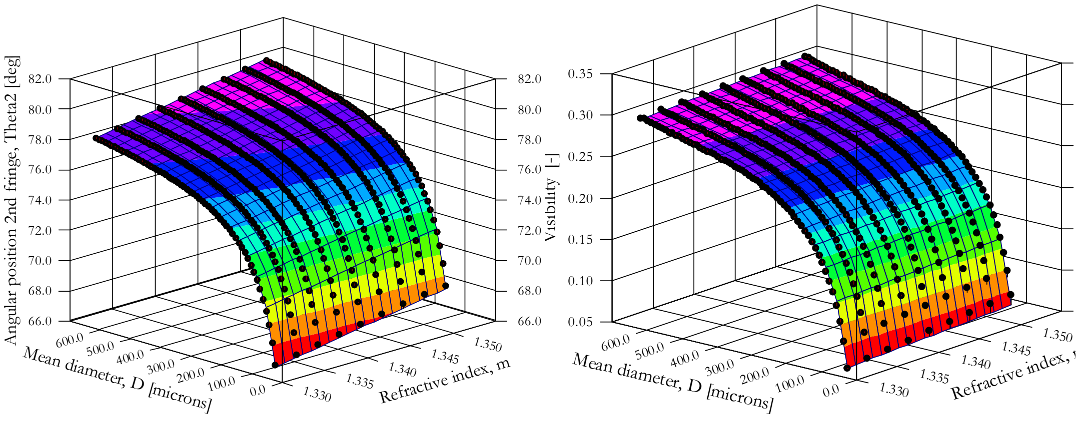

Figure 3.17 For $\sigma/\bar{D}=0.10$, left : predictions of $\theta_2 = f(\bar{D},\sigma_D,m)$ with Eq. (63) and LMT ; right: predictions of $V = f(\bar{D},\sigma_D,m)$ with Eq. (64) and LMT. The analytical results correspond to the colored and continuous surfaces and those of LMT, to the black circles (●).

To evaluate the accuracy of this inverse method in terms of BSD parameters we have prepared a large database of LMT-CSP, that were scaled and shifted randomly with some additional white noise (7%). So that these CSP can be considered as realistic "experimental" signals. Figure 3.18 and Table 3.2 compare the results obtained with the 3-points method: Figure 3.18 when we use the tabulated results, i.e. Eq. (55) and a data base; and Table 3.2 with the fitting equations, i.e. Eq.(62)-(64).The accuracy of both methods is found to be about $\delta\overline{D}=5\%$, $\delta\left(\sigma/\overline{D}\right)=15\%$ and for $\Delta m=\pm0.0001$. The fitting method is nevertheless faster. Note that these estimated resolutions do not take into account misalignment of the optics, bubbles non sphericity, etc.

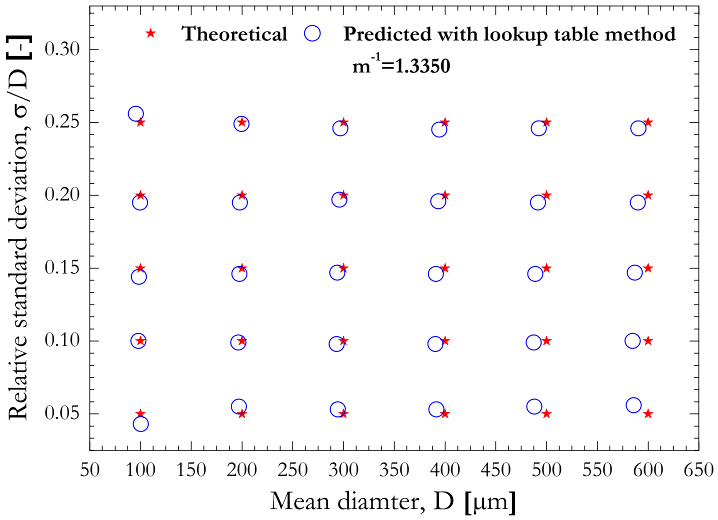

Figure 3.18 Prediction of 3points-LMT method for relative refractive index m=1.3350

		Mean size of bubble D [μm]					
		100	200	300	400	500	600
Size distribution widths, σ/D [-]	0,05	100 0,043	197 0,055	294,5 0,053	391,5 0,053	488 0,055	586 0,056
	0,10	98 0,1	196,5 0,099	293,5 0,098	390,5 0,098	487,5 0,099	585 0,1
	0,15	98,5 0,144	197,5 0,146	294 0,147	391 0,146	489 0,146	587 0,147
	0,20	99,5 0,195	198 0,195	296 0,197	393,5 0,196	491,5 0,195	590 0,195
	0,25	95,5 0,256	199,5 0,249	297 0,246	394,5 0,245	492,5 0,246	590,5 0,246

Table 3.2 Table of predictions of the 3points-LMT on numerical CSP: mean size and size distribution width.

3.2.3 Conclusion

The biggest interest of the NNLSQ inverse method is that it does not require any strong physical assumption on the shape of the bubble size distribution (BSD). So, we are not limited to size distributions that are described by an analytical shape, a mono mode BSD. Indeed we were rather surprised by the quality and the stability of the NNLSQ inverse method (see also chapter 5). The results are not always perfect as the method can generate some ghost bubbles, but regarding to other inverse methods or other optical sizing methods, the results are already very satisfactory. The resolution between two modes seems to be about $\sim 50\mu m$. It is hard to be more precise as it depends on the width and relative weight of the modes, the size range, the noise…. In its current state, it overestimates the width of mono-disperse size distributions. However, without any doubt, the performance of the NNLSQ could be improved by pre-processing the CSP (i.e. pass band angular filtering).

The 3-points method is the fastest inverse methods and it does not require large computation resources when compared to the NNLSQ or the LSQ methods. Although its accuracy is quite limited, it could be enough for some applications. The 3-points method could be used to inverse data from an integrated sensor using the principle of the CARS technique to characterize on-line bubbly flows. The LSQ method, with LMT as a scattering theory is limited by the bubble size distribution assumption and it is not really faster than the NNLSQ method, so its practical interest appears to be quite limited.

Chapter 4

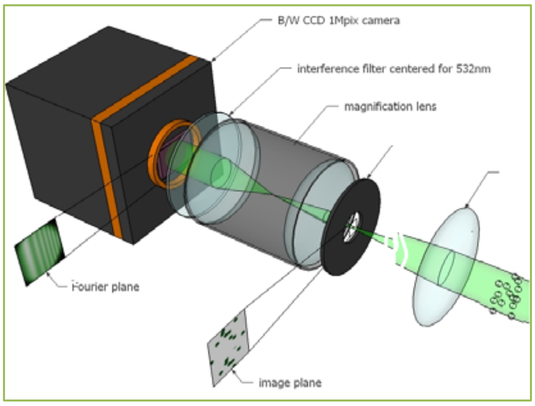

EXPERIMENTAL SETUPS AND PROCEDURES

In this chapter we present the different setups and procedures we have developed to generate controlled bubbly flows, the optical setup and calibration procedures for the recording of experimental critical scattering patterns, and the principles and setups of two techniques used to validate our experimental results.

4.1 Hydrodynamic considerations

To validate the principle of the CARS technique it is necessary to produce bubbly flows with different mean size, polydispersions and compositions. At the same time, it is interesting to recall and point out some basic characteristics of bubbles and bubbly flows regarding to hydrodynamics conditions.

4.1.1 Bubbles' shapes according to Grace's stability diagram

The shape and the aspect ratio of a bubble depend on its velocity, its size, as well as the properties of the two fluids (surrounding and internal). Bubbles and drops in free motion are described already by (Clift et al. 1978) considering free rising or falling bubbles and drops in semi infinite media. From observations it appears that the shape of the bubbles (and drops) can be classified in three main categories:

Spherical shape, generally speaking, bubbles and drops are closely approximated by spheres if the interfacial tension and/or viscous forces are much more important than inertia forces. For our purposes, fluid particles will be termed "spherical" if the minor to major axis ratio lies within 10% of unity. Spherical fluid particles in free rise or fall are discussed in Chapters 3 and 5.

Ellipsoidal shape, generally this shape is used to refer to bubbles and drops which are oblate with a convex interface (viewed from inside) around the entire surface.

Spherical-cap or ellipsoidal-cap shapes, large bubbles and drops tend to adopt flat or indented bases and to lack any semblance of fore-and-aft symmetry (see Figure 4.1). Such fluid particles may look very similar to segments cut from spheres or from oblate spheroids of low eccentricity.

For free rising bubbles and free falling droplets, in a semi infinite media, it is possible to prepare a generalized graphical correlation of the aforementioned shapes in terms of the Eotvos number (Eo), Morton number (Mo), Reynolds number (Re) and Weber number (We).

$$Re = \frac{\rho_l V_T D}{\mu_l} \tag{65}$$

$$Eo = \frac{g d^2 \left(\rho_l - \rho_g\right)}{\sigma} \tag{66}$$

$$Mo = \frac{\left(\rho_l - \rho_g\right) g \mu_l^4}{\sigma^3 \rho_l^2} \tag{67}$$

$$We = \frac{\rho_l V_T^2 D}{\sigma} \tag{68}$$

where ρ_l , μ_l are respectively the surrounding liquid density and dynamic viscosity, σ the surface tension; D, V_T and ρ_g the diameter, the terminal velocity and the density of the bubble; g the gravitational constant. The resulting diagram took from Grace 1976, is shown in Figure 4.1. From this diagram we can estimate terminal velocities as well as the particle shape (i.e. bubble or drop), although more accurate and predictive correlations are usually available in the literature (see later on). It is noticable that dynamic viscosity does not play an important role in determining terminal velocities and shape regimes since it does not appear in any of the three groups used to construct the diagram. The role of dynamic viscosity may be significant, however, for very pure (surfactant-free) systems or for large fluid particles in high Morton number liquids. While the boundaries between the principal shape regimes are somewhat arbitrary, it is clear that bubbles and drops are ellipsoidal at relatively high *Re* number and intermediate *Eo* number, while the spherical- or ellipsoidal-cap regime correspond to relatively large *Eo* and *Re* numbers. Note that we have reported on this diagram some of our experimental data points (triangular symbols) to gives an overview of the regimes and bubbles shapes investigated with our different bubble generators, i.e. from almost perfectly spherical to highly ellipsoidal shapes.

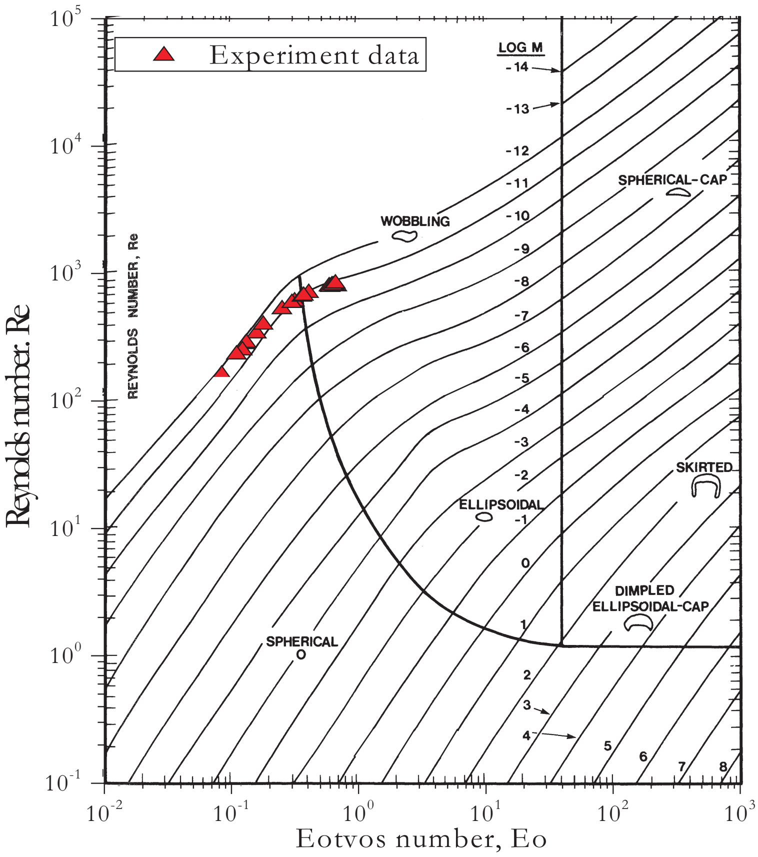

Figure 4.1. Grace's diagram showing shape regimes for bubbles and drops, Grace (1976).

As already mentioned bubbly flows occur in a wide range of natural systems and industrial processes, and sophisticated computational fluid dynamics codes are already available to simulate bubbly flows (see Chapter 1). In parallel to these models that require high computational resources, some authors try to develop and validate simplified models based on correlations. For instance, Celata et al. (2007) have developed a dedicated experiment to compare the prediction of these correlation models for immiscible fluids (mostly gas in liquid) and for adiabatic conditions. Most of the models tested in this study assume that the shape of the bubbles is ruled by the balance of buoyancy and drag forces, and describe it in terms of three dimensionless groups, generally the Reynolds, Eotvos and Morton numbers (see next paragraph). To conclude on that part, it must be pointed out that, from our literature review on bubbly flow studies several phenomena of interest were noticed, like:

- the bubbles' terminal velocity is influenced by the degree of fluid contamination (i.e. mainly by surfactants), which affects the dynamics of their interface;

- the bubbles' velocity fluctuate in connection to the oscillations of the bubbles shapes;

- the wakes produced by the preceding bubbles in a train may influence the terminal velocity when the bubbles are closely spaced;

- the bubbles trajectories may be either rectilinear, planar zigzagging or spiraling and may also shift from one mode to another one with increasing distance from the injection, etc.

4.1.2 Correlation models for bubbles' aspect ratios

Several attempts have been made in literature to correlate the aspect ratio ξ as a function of a single dimensionless parameter which could group all experimental data. The aspect ratio ξ (sometimes written *E*) is defined as $\xi = a/b$, where a is the minor axis (vertical) and b the major axis (horizontal) of the bubble.

Some authors have accomplished this task using the Eotvos number, others have adopted the Weber number, while Tadaki and Maeda (Tadaki & Maeda 1961) have proposed an original dimensionless group named nowadays the Tadaki number:

$$Ta = \mathrm{Re}\, Mo^{0.23} \tag{69}$$

As noted by Fan and Tsuchiya (1990), if in the above equation the exponent of *Mo* was equal to 0.25, the dynamic viscosity would be cancelled out in the product (complete independence of dynamic viscosity). This is equivalent to say that the bubble shape (for low-Mo liquids) is only determined by the balance among surface tension, inertial and gravity forces, and that the viscous forces are negligible. In the contrary, by adopting an exponent 0.23, a weak dependence on dynamic viscosity is retained (Tomiyama et al. 2001). When measuring the rising velocity of air bubbles in stagnant water it is observed that the aspect ratio, which depends on the magnitude of initial shape oscillation, is strongly correlated to the Weber number. For all the liquids they have tested ($Mo < 2.5 \cdot 10^{-4}$), except surfactant solutions, they have found the following correlations:

$$\xi^{1/3} = \begin{cases} 1 & Ta < 2 \\ 1.14 Ta^{-0.176} & 2 < Ta < 6 \\ 1.36 Ta^{-0.28} , \text{ when} & 6 < Ta < 16.5 \\ 0.62 & 16.5 < Ta \end{cases} \tag{70}$$

Later, Vakhrushev and Efremov (1970) have proposed to modify the above correlation as follows:

$$\xi = \begin{cases} 1 & Ta < Ta_1 \\ \{c_1 + c_2 \tanh[c_3(c_4 - \log_{10} Ta)]\}^2 , \text{when} & Ta_1 < Ta < Ta_2 \\ c_5 & Ta_2 < Ta \end{cases} \tag{71}$$

Eq. (71) contains nine empirical parameters, but only five among them are independent. Here is the set of coefficients suggested by Fan and Tsuchiya (Fan et al. 1990) for pure water:

$$\xi = \begin{cases} 1 & Ta < 0.3 \\ \{0.77 + 0.24\tanh[1.9(0.40 - \log_{10} Ta)]\}^2, \text{when} & 0.3 < Ta < 20 \\ 0.30 & 20 < Ta \end{cases} \tag{72}$$

For example, Figure 6.2 compares the evolution of the aspect ratio of air bubbles in water versus the Tadaki number, according to Eq. (72) and experimental results we have obtained with the micro-video imaging system (see also Figure 6.3). Table 6.2 resumes the parameters used for the calculations. The results are really in good agreements. It is one of the reasons why, in Chapter 6 we have tried to use Eq. (72) to better estimate the volume of non spherical bubbles.

4.2 Bubbles and bubbly flows generators

To investigate the response of the CARS technique to different bubble size ranges and compositions, we have developed five different systems to generate bubbles.

4.2.1 Solenoid valve (piezo-jet)

The best and most used system is a drop on demand generator based on a piezo-jet, see Figure 4.2. The VHS-LT solenoid valves from Lee Co. (2009) are designed for applications requiring high speed and precision dispensing of fluids. The valves can dispense small, consistent, undisturbed fluid droplets that can travel relatively long distances. This is attributed to a patented integral valve feature designed to absorb valve actuation induced fluidic disturbances. The closed coil design minimizes coil exposure to incidental splashing and corrosion and depending on the application. The VHS-LT valves feature low power consumption and the ability to consistently dispense a wide range of fluids despite low percentages of entrained air. Tested chemicals include many alcohols, organic solvents, and aqueous solutions. For us the basic properties of the piezo-jet are: integral nozzle for precise operation, response time as low as 0.25ms, high speed operation (up to 1000Hz).

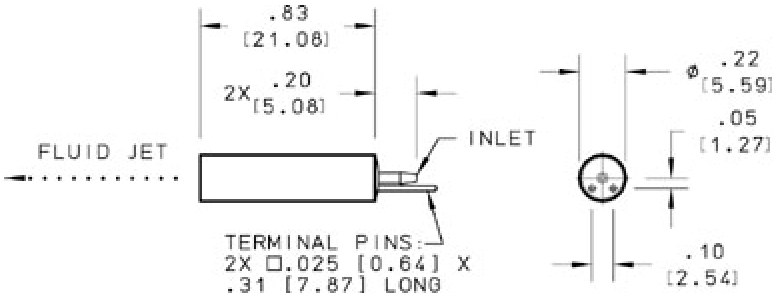

Figure 4.2 Lee Co piezo-jet VHS-LT (from Lee Co., 2009)

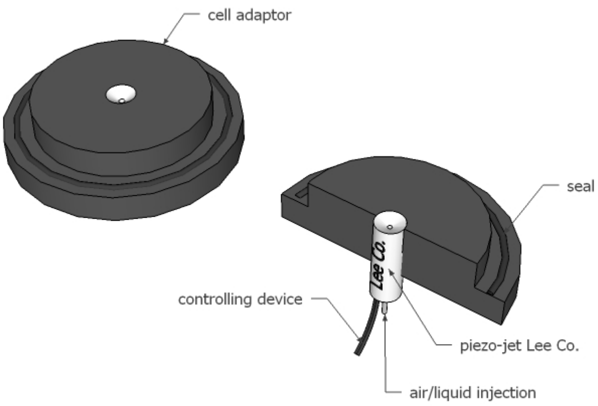

Figure 4.3 Piezo-jet connection system to our experimental tank.

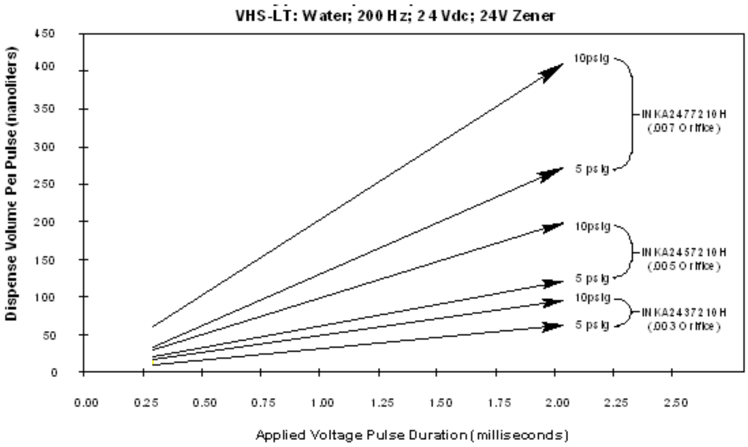

Figure 4.4 Typical water droplet dispense volumes (from Lee Co., 2009)

For water at ambient temperature, Figure 4.4 shows the typical volume of the droplets that can be dispensed on demand versus the opening time of the valve and for various diameters of the nozzle exit (172µm, 123µm, 74µm) and the water input pressure. This graph is only supplied for reference information. Results vary with fluids viscosity, density, surface tension and temperature.

Figure 4.5 High Speed VHS Valve Driver (IUSTI, S. Martinez)

In our study we have mainly used the piezo-jet, with the smaller nozzle exit, to generate air bubbles on demand, the air supply being ensured by a small electrical pomp as well as a high pressure tank. The piezo-jet was also used to generate air bubbles in ethanol or water droplets in silicon oil. To power up and control the generator we have developed a dedicated electronics, see

Figure 4.5, which is it self controlled via a PC through the RS232 COM port. The parameters of the whole injection system are selected via a software, see Figure 4.6, allowing to select the bubble rate (0-1kHz) and size (spherical and stable bubbles only for the range $400-700\mu m$), the synchronization with other systems (flash lamp, CARS system…).

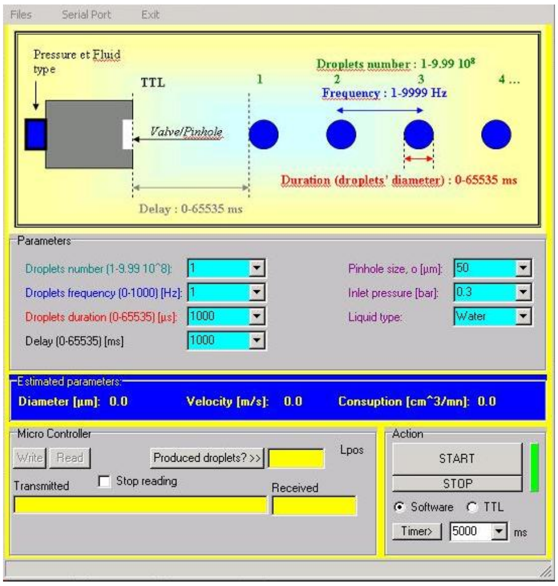

Parameters

Droplets number (1-9.99 10^8): 1
Droplets frequency (0-1000) [Hz]: 1
Droplets duration (0-65535) [µs]: 1000
Delay (0-65535) [ms]: 1000
Pinhole size, o [µm]: 50
Inlet pressure [bar]: 0.3
Liquid type: Water

Estimated parameters:
Diameter [µm]: 0.0
Velocity [m/s]: 0.0
Consuption [cm^3/mn]: 0.0

Micro Controller
Lpos
☐ Stop reading
Transmitted
Received

Action
● Software ○ TTL
5000 ms

Figure 4.6 Main screen of the software developped to control the Piezo-jet (IUSTI)

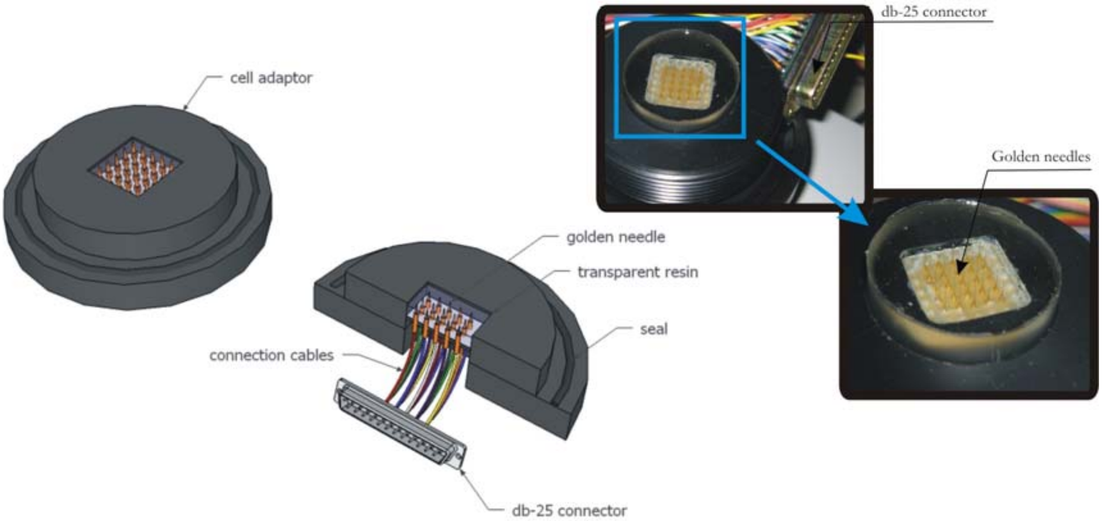

Figure 4.7 Schematics and images of the electrolytic bubble generator plugging and connection systems.

4.2.2 Electrolytic bubble generators

Electrolysis is a process that permits to induce a chemical change through the use of electrical energy. The most familiar example of electrolysis is the decomposition of water into small hydrogen and oxygen bubbles. Thus we have to develop a multidimensional electrolytic bubble generator able to produce clouds of very small bubble from the electrolyze of the surrounding fluid, see Figure 4.7.

Basic phenomena

In any sample of water, some small fraction of molecules exists in the form of ions, or charged particles. Ions are formed in water when water molecules break apart to form positively charged hydrogen ions and negatively charged hydroxide ions (Vanýsek 2007). Chemists describe that process with the following chemical equation: $H_2O \rightarrow H^+ + OH^-$. Seawater can be electrolyzed, because it contains many positively charged sodium ions $\left(Na^+\right)$and negatively charged chloride ions $\left(Cl^-\right)$. Normally, only one water molecule out of two billion ionizes. In contrast, sodium chloride breaks apart completely when dissolved in water. In our study, to work under controlled conditions and to avoid the development of bacteria, we have used bi-distilled and demineralised water. Electrolyze was then impossible without adding some substance to increase the liquid electrical conductivity. We did not want to use sodium chloride as it changes significantly the liquid refractive index. A bibliography review indicates that the best additive is a dilute solution of sulfuric acid $\left(H_2SO_4\right)$. The latter is a strong electrolyte which is fully dissociated in aqueous solution $H_2SO_4 \rightarrow 2H^+ + SO_4^{\;2-}$. Bringing electrons to the system with a power unit and two electrodes: one anode and one cathode, we get hydrogen bubbles on the cathode $4H^+ + 4OH^- + 4e^- \rightarrow 2\vec{H}_2 + 2OH^-$. Water reacts also on anode, loosing electrons, to produce oxygen bubbles $2H_2O \rightarrow \vec{O}_2 + 4H^+ + 4e^-$ producing oxygen in this reaction. The general equation may written as

$$6H_2O \rightarrow 2\vec{H}_2(cathode) + \vec{O}_2(anode) + 4H^+ + 4OH^- \tag{73}$$

Electrolytic bubble generator

To produce the bubbles to be analyzed, we develop an multi electrode head composed of 25 golden needles arrange in grid 5x5 on area 2x2cm. This grid was connected through special connectors allowing controlling the powered needles. In this way, the electrolytic bubble generator is able to produce bubbly flow plus or less dense and with different patterns : single stream, a curtain, square patterns, etc. The second electrode, with a golden coating, was simply put at the top of the tank in order to avoid any disturbance of the critical scattering patterns. The differential voltage between the two electrodes was adjusted with a stabilized power unit. Indeed, we found that this voltage has an influence of the bubbles rate and size. The size dependence is quite surprising, but probably due to some coalescence effects. For oxygen, the bubble size range obtained is within the range $50-100\,\mu m$ (see Table 4.1).

Differential voltage [V]	6.4	7.4	8.4	9.4	10.4
Mean size $\overline{D}$ [μm] (by Micro-Video system)	90.0	98.0	111.0	127.0	137.0

Table 4.1 Size of bubbles – voltage dependency.

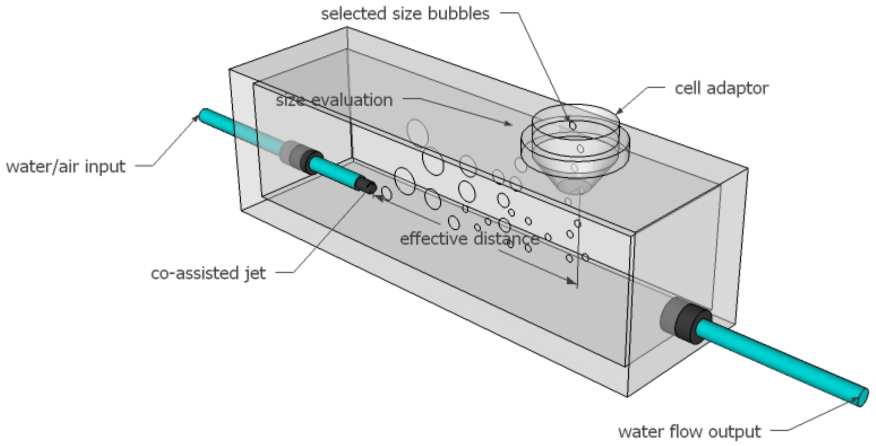

Figure 4.8 co-assisted air/water jet.

4.2.3 Capillary jet (natural and assisted)

The simplest idea to produce bubbles is to inject air in a needle with a small internal diameter. By changing the pressure of the air inlet one can expect to cover a large size range. Indeed, this simple injection technique leads to the formation of large bubbles, bigger than $200\,\mu m$. According to Oguz and Prosperetti (1993) model, two parameters influence the diameter of air bubbles in water when they are detaching from the needle output. The critical air flow rate through the needle Q_{cr} and the equilibrium bubble radius R_F. The latter can be determined from the balance between buoyancy forces and the surface tension forces during detachment

$$R_F = \frac{3\gamma a}{2\rho_l g} \tag{74}$$

where γ is the surface tension, a is the inner radius of the needle, ρ_l is the density of the surrounding liquid and g is the gravity constant. On other part, there is a limiting value Q_{cr} for the air flow through the needle

$$Q_{cr} = \pi\left(\frac{16}{3g^2}\right)^{1/6}\left(\frac{\gamma a}{\rho_l}\right)^{5/6} \tag{75}$$

So that all the bubbles generated will detach from the needle with the same equilibrium size, given by equation (74). However, if the airflow rate is larger than this critical value, the volume of the bubbles will be proportional to Q_{cr}. Disadvantage of this technique is that the bubble size is a pressure dependant parameter. Pressure also imposes the number of bubbles produced in time. It can be a quite limiting aspect if we want to adjust in parallel the flow rate.

In water, and with the previous system, the air bubbles obtained with reasonably small needle (not less than 100µm in diameter) are usually too large to be in the spherical regime. To solve this problem we have developed empirically a so-called "assisted jet". Basically the idea is to increase the slip velocity between the air stream and water, by using a co-axial double injection system, see Figure 4.8 This is why we use an additional pump to suck the water from the experimental tank toward the assisted jet water inlet, as a close loop. This system is hard to control and it produces largely polydisperse bubbles. One possible solution to limit the size distribution width is to place the injector horizontally and to select the bubble size range by adjusting its position in respect to the water tank inlet, see Figure 4.8. With this reverse "sedimentation technique" it was also possible to vary the mean size range.

It was impossible with these systems to produce reasonably small (less than 1 mm) bubbles of water in silicon oil, due to surface tension and viscosity differences. So, the solution found was to generate water droplets above the silicon free surface and to let them to drop down into the silicon oil. Note that the needle output distance from the silicon surface was about the size of the diameter of the water drop we want to generate, se Figure 4.9.

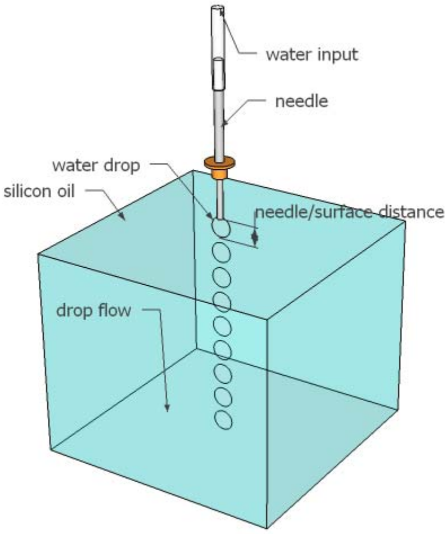

Figure 4.9 Jet surface breaking system to produce falling water drops in silicone oil.

4.2.4 Porous plate

We did several experiments by injecting air through a porous plate (we have tested several of them: paper, ceramics, polymer). At low flow rate, the porous plates produce few columns of rising bubbles that are rather mono-disperse. Unfortunately, from one experiment to another one, it is impossible to predict where the bubbling sites will appear onto the porous plate. When we increase the flow rate the bubbling rate rapidly increases. But, due to coalescence effects between bubbles produced by short distance bubbling sites, we get very large bubbles (above 1 mm). So this system was found to be not very convenient to carry out well controlled experiments. Nevertheless porous plates were used to test the limit of the CARS technique regarding to the high bubbly flow density and non spherical bubbles.

4.3 CARS system to record and analyze critical scattering patterns

We detail here the different optical, mechanical, electrical and numerical components we have developed to record experimental critical scattering patterns (CSP). Results and their analyses are presented in the next chapters.

4.3.1 Experimental setup

We have built a full setup allowing absolute angle measurements of the far-field CSP generated by all bubbles present in a optical probe volume of about 1 cm^3, see Figure 4.10 to Figure 4.13. The cell (or "tank") in which the scattering take place is basically a 300x100x100mm rectangular glass-walled aquarium in PVC with four glass walls (glass thickness: 3 mm). It is alternatively filled with bi-distilled and dematerialized water; water-ethanol and water-glycerin solutions, silicon oil. The bubble generators (see § 4.2) are usually placed at the bottom, sometimes at the top. The incident beam from a (2) 50mW YAG laser is (3) coupled to a mono-mode optical fiber with polarization conservation and finally (4) expanded (x10) to obtain a parallel polarized and collimated beam, with diameter 12 mm and wavelength $\lambda_0 = 0.532$ µm. The laser beam divergence is negligible ($\leq 0.001°$). Note that in this setup, the beam polarization can be rotated continuously with a (5) $\lambda/2$ plate, whatever we use mostly the parallel polarization. The main purpose of the mono-mode fiber is to adjust finely the laser beam intensity by controlling the coupling efficiency. The later point is important to calibrate the experiments since the beam must be sent onto the CCD chip (see later on). For some experiments the beam expander magnification was reduced from a factor x5, and even totally removed.

The rising bubbles (17) are produced at the bottom of the tank by different bubble generators (see §4.2): piezo-jet, assisted air jet, porous plate and electrolytic bubble generator.

Gaussian beam effects can be neglected as the diameter of the bubbles is always much smaller than the diameter of the incident laser beam (ratio $\approx 1:70$ to $\approx 1:10$, see also §7.1).

To minimize the depth-of-fields effects, the scattering of all bubbles located in the probe volume is collected by an optical system working in a Fourier configuration, see Figure 4.12. The collection optics is first composed of a (7) high Numerical Aperture camera lens (Nikon AF NIKKOR 50mm, N.A.=1.4). This lens collects the scattered light to form an image of the bubbly flow within the optical probe volume onto a (8) circular iris diaphragm with adjustable size aperture. This later component plays the role of a spatial filter and allows to control the lateral dimension of the optical probe volume (see §7.2). A pair of (9) achromatic doublets is used to obtain the Fourier Transform of the bubbly flow image onto a (11) CCD chip, see Figure 4.12.

Note that an (10) interference filter centered on the laser line λ_0 is used to minimize the surrounding optical noise.

The far field CSP are recorded by a (11) 12 bits and 1024×1024 digital camera, transferred and analyzed onto a (18) PC. For that purpose we have developed software that fully control via the RS 232 COM port the camera frame rate, exposure time, binning, digitizing depth, external and internal synchronization, etc. Figure 4.14 shows a screen copy of this acquisition and processing software (that work for rainbow technique too). Note that all components of the CARS system are fixed on a single optical bench $(\approx 400x400mm)$. This allows getting a rather compact and stable system. With this setup and a water solution, the typical angular range and resolution of this system are $\theta = 70.3 \sim 82.8°$ and $\Delta\theta \approx 0.02°$ respectively. This angular range can be adjusted by moving with respect to the collection lens, the Fourier lens and the camera.

Whatever they are not truly part of the CARS setup, Figure 4.10 and Figure 4.11 show additional systems used during our experiments. In (14) we see the camera of the Interferometric Laser Imaging for Droplet-Sizing system (ILIDS, see §4.5). The optical axis of this camera makes an angle of 37° with the laser beam of the CARS system (which is used to generate also the ILIDS images). These figures also show the (12) flash lamp and the (13) long distance micro-video imaging-system used to obtain shadowgraphy images of the bubbly flows (see § 4.4). The CARS and micro-video systems are synchronized via TTL signals. Note that it was necessary to develop an additional (15) optical triggering system to visualize and study large non spherical bubbles. This system (a lens, a spatial filter, a silicon diode and its electronics) detects the presence of each bubble presents in the probe volume. The latter system is helpful to trig and synchronize the two other systems.

4.3.2 Acquisition and pre-processing software

As mentioned in the previous paragraph the Critical Scattering Patterns (CSP) are recorded by a 12 bits and 1024×1024 digital camera from DALSA. The digital signal (LDVS) is processed by a PC embedding a NI PCI 5112 digital video board. A MS-Windows based software has been developed under DELPHI-Borland to control the video board and the camera. Figure 4.14 shows a copy of the main window of this software. The latter allows via the RS232 COM port and the LDVS digital link to fully control the camera configuration and operating mode: camera frame rate (up to 30Hz), exposure time (from 1µs to 1s), binning (1x, 2x, 8x), digitizing depth (8 and 12 bits), external and internal synchronization (TTL and software), etc. CSPs are directly saved on the PC hard disk or they can be time-averaged before to be analyzed and saved.

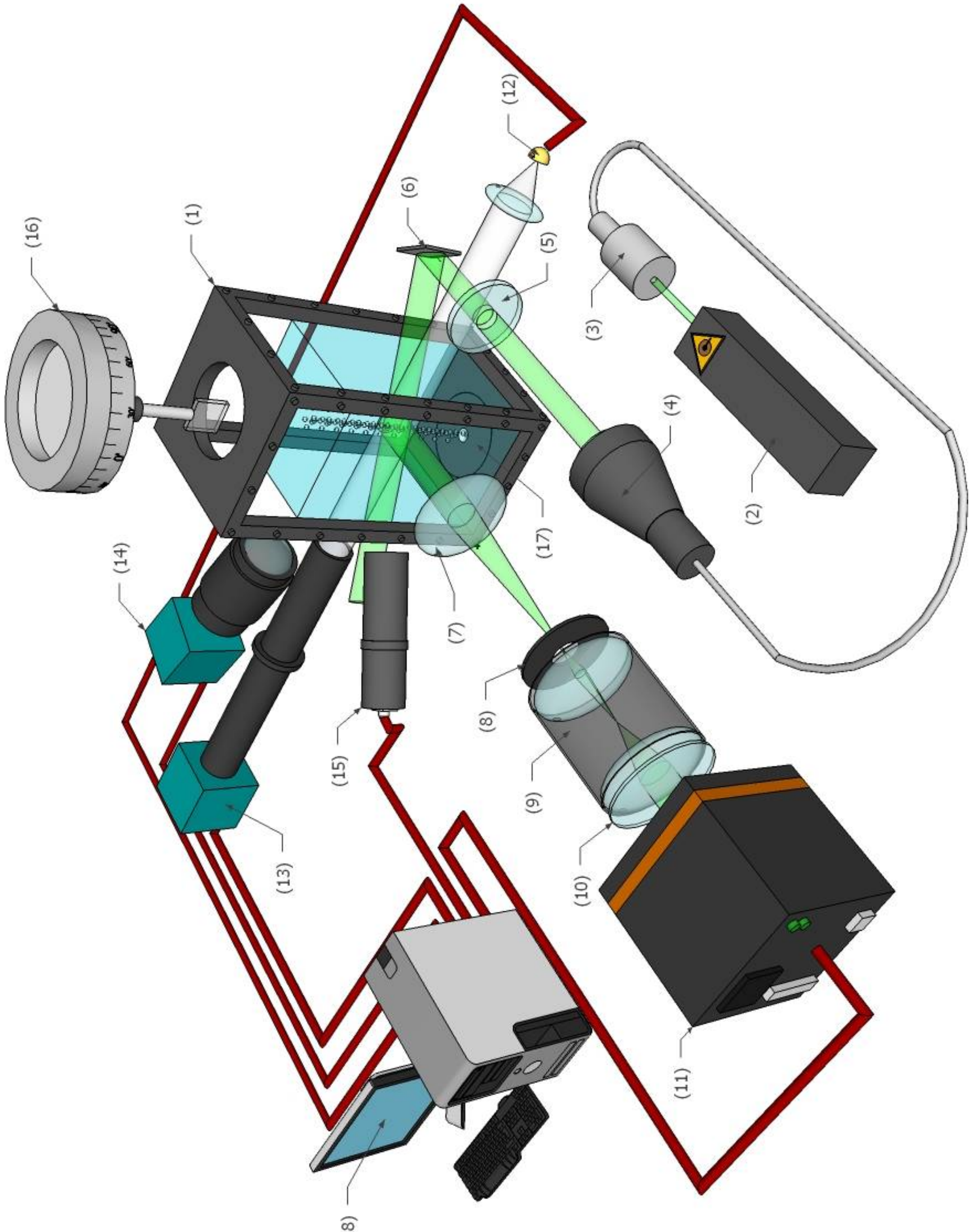

Figure 4.10 Experimental setup: (1) experimental tank; (2) YAG-Laser 50mW-532nm; (3) optical fiber; (4) beam expander; (5) λ/2 wave plate; (6) mirror; (7) Nikon AF NIKKOR lens 50mm 1:1.4D; (8) diaphragm; (9) Fourier/magnification lenses; (10) interference filter centered on for YAG line; (11) 1Mpix-12bits-B/W digital CCD camera; (12) flash lamp; (13) micro-video system; (14) ILIDS system: 1Mpix-8bits-B/W digital CCD camera with Nikon AF NIKKOR 35-80mm 1:4-5.6D lens; (15) bubble detector: lens, spatial filter and APD; (16) step-motor goniometer; (17) bubble generator, (18) PC.

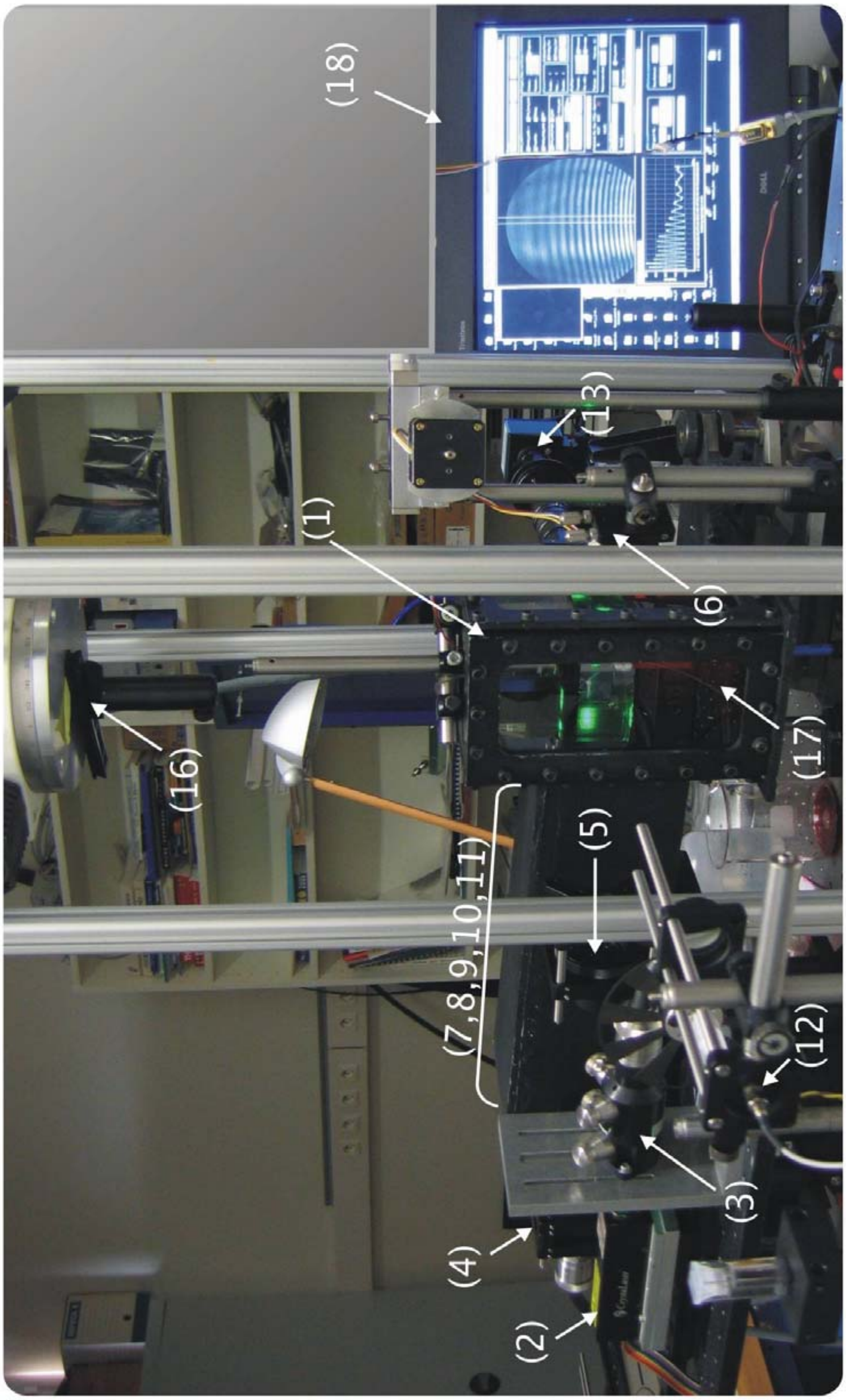

Figure 4.11 Picture of the experimental setup: (1) experimental tank; (2) YAG-Laser 50mW-532nm; (3) optical fiber; (4) beam expander; (5) λ/2 wave plate; (6) mirror; (7) Nikon AF NIKKOR lens 50mm 1:1.4D; (8) diaphragm; (9) Fourier/magnification lenses; (10) interference filter centered on for YAG line; (11) 1Mpix-12bits-B/W digital CCD camera; (12) flash lamp; (13) micro-video system; (14) ILIDS system: 1Mpix-8bits-B/W digital CCD camera with Nikon AF NIKKOR 35-80mm 1:4-5.6D lens; (15) bubble detector: lens, spatial filter and APD; (16) step-motor goniometer; (17) bubble generator, (18) PC.

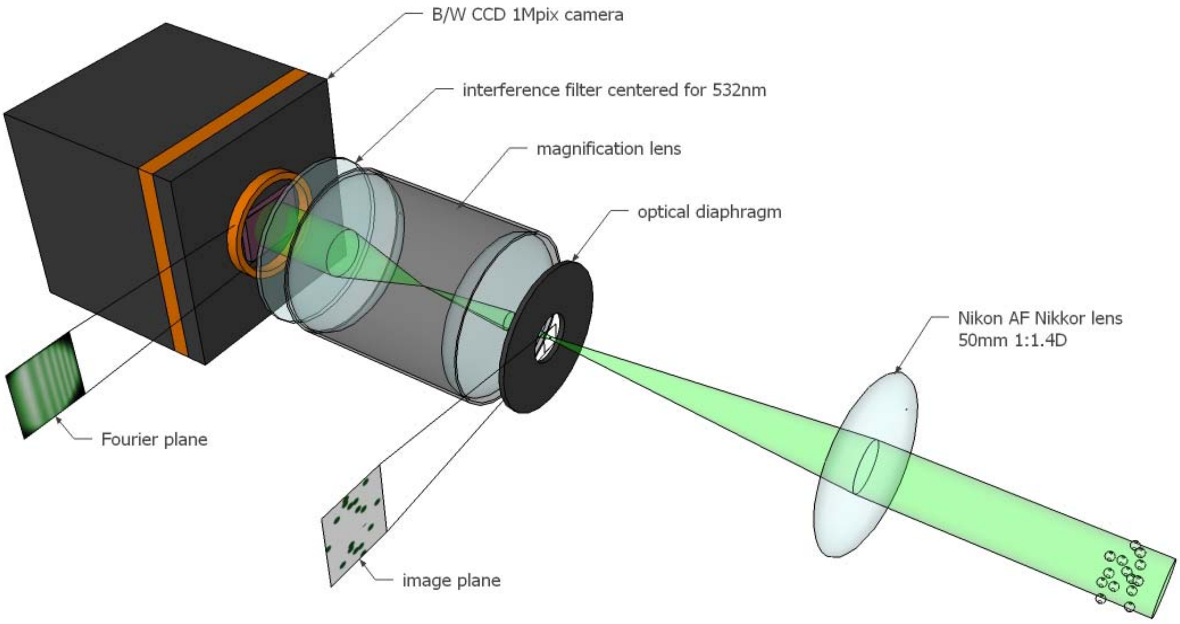

Figure 4.12 Details of the CARS collection optics

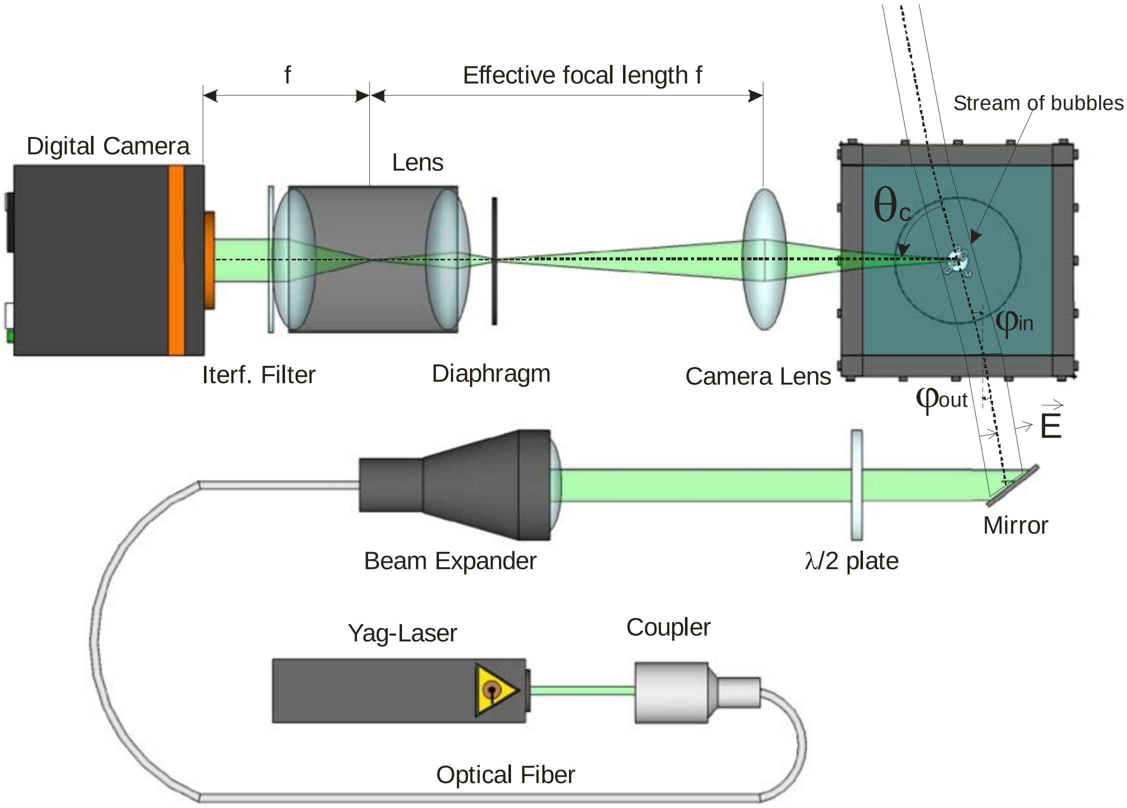

Figure 4.13 Schematic top view of the CARS setup

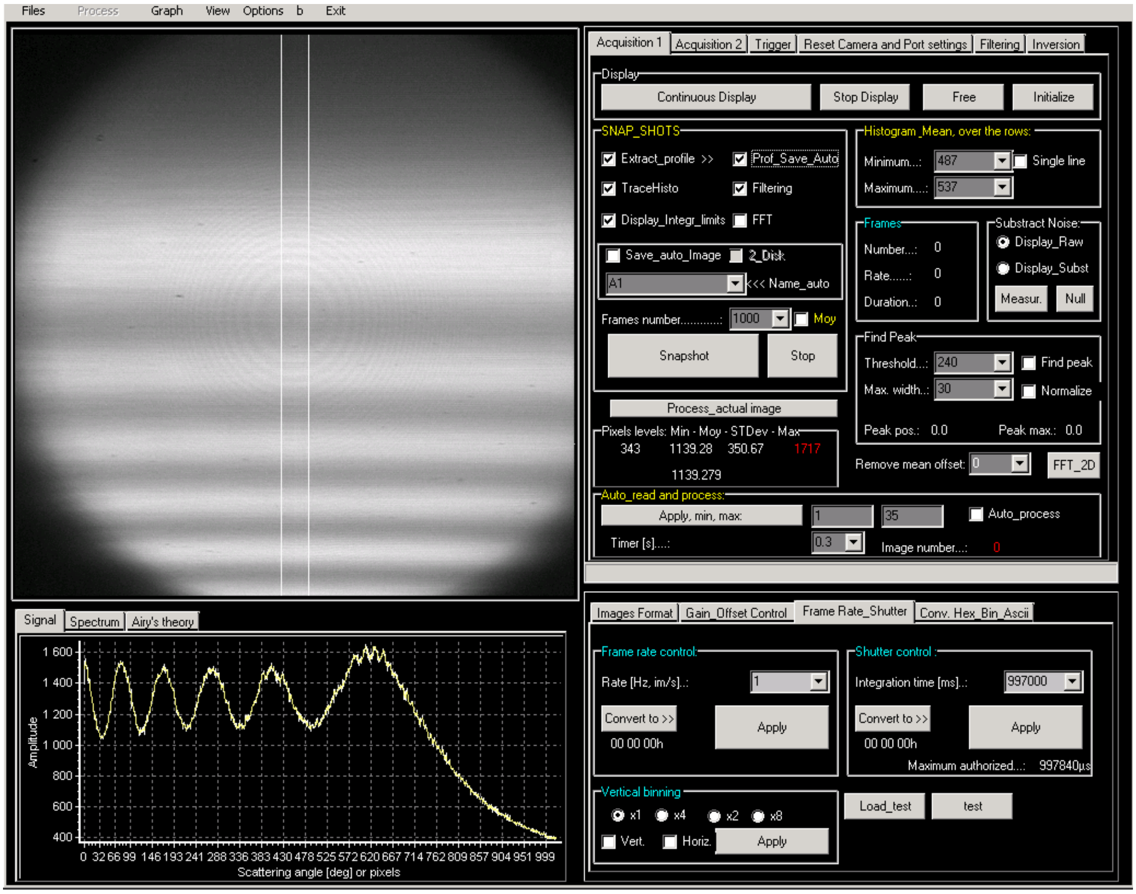

☑ Extract_profile >> ☑ Prof_Save_Auto
☑ TraceHisto ☑ Filtering
☑ Display_Integr_limits ☐ FFT
☐ Save_auto_Image ☐ 2_Disk
A1 <<< Name_auto
Frames number............: 1000 ☐ Moy
Minimum...: 487 ☐ Single line
Maximum....: 537
Number...: 0
Rate......: 0
Duration..: 0
● Display_Raw
○ Display_Subst
Threshold...: 240 ☐ Find peak
Max. width..: 30 ☐ Normalize
Peak pos.: 0.0 Peak max.: 0.0
Pixels levels: Min - Moy - STDev - Max
343 1139.28 350.67 1717
1139.279
Remove mean offset: 0
1 35 ☐ Auto_process
Timer [s]....: 0.3 Image number...: 0
Rate [Hz, im/s]..: 1
00 00 00h
Integration time [ms]..: 997000
00 00 00h
Maximum authorized...: 997840µs
● x1 ○ x4 ○ x2 ○ x8
☐ Vert. ☐ Horiz.

Figure 4.14 CARS acquisition and pre-processing software

For each image the intensity profiles can be extracted and averaged automatically within a given angular range (defined by the two white lines in Figure 4.14). Prior to be exported, the intensity profiles can be normalized and low pass filtered (Fourier, Butterworth...), etc. Different estimators (pixel saturation, maximum and minimum intensity, peak angular position, etc.) are also provided to facilitate the alignment procedure.

4.3.3 Analyzing and inversion software

Since acquisition software give raw images, raw CSPs intensity profiles and, if necessary, angularly and time averaged CSP, different processing software were developed to inverse CSP and to get the bubbly flows characteristics.

The main processing software is also developed under Borland-DELPHI. This software basically refines the filtering of the experimental signals (see Figure 4.15), normalizes them so they can be compared directly to the theory, and extracts automatically the positions of all fringes (brights and darks). For direct inversion, it uses three different methods: the so-called 3-points method, the LSQ-LMT and the Hybrid ones (see §3.2). This is reason why it allows performing iterative

Lorenz-Mie, CAM and POA calculations, as well as to process them in order to create look-up tables (see §3.2). A least-square correlation scheme is used to minimize the differences between experimental and theoretical CSPs (see Figure 4.15) and in fine, to deduce the bubbly flow parameters.

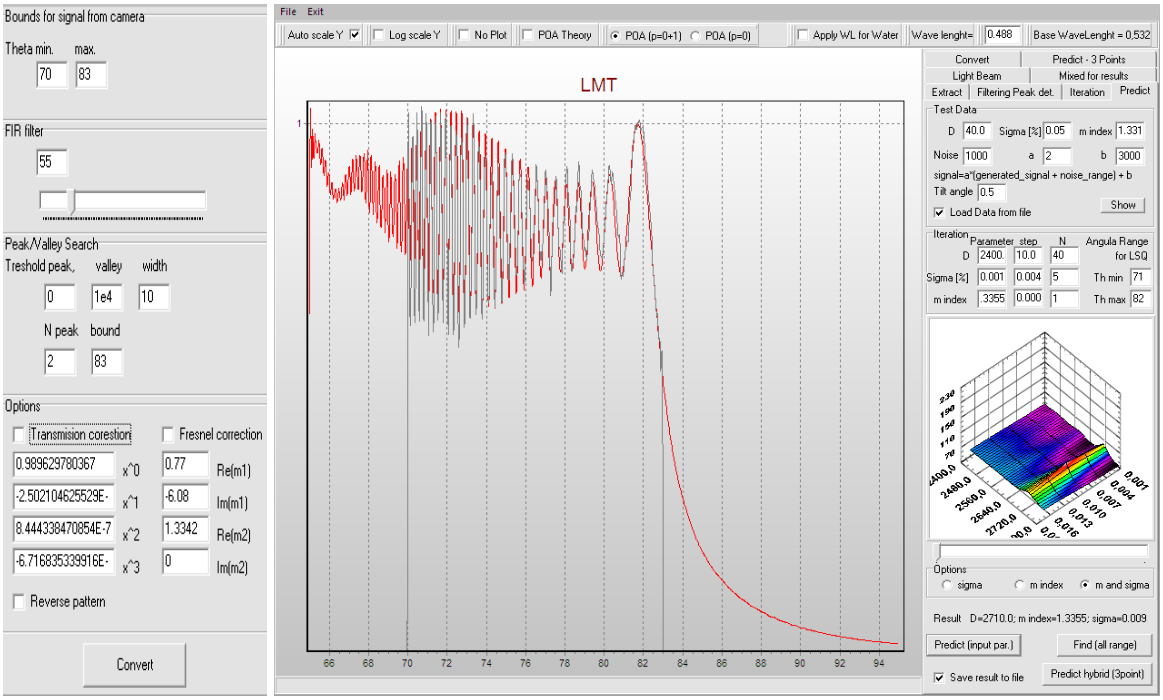
Bounds for signal from camera
Theta min. 70 max. 83
FIR filter 55
Peak/Valley Search
Treshold peak, 0 valley 1e4 width 10
N peak 2 bound 83
Options
☐ Transmision corestion ☐ Fresnel correction
0.989629780367 x^0 0.77 Re(m1)
-2.502104625529E- x^1 -6.08 Im(m1)
8.444338470854E-7 x^2 1.3342 Re(m2)
-6.716835339916E- x^3 0 Im(m2)
☐ Reverse pattern

Auto scale Y ☑ ☐ Log scale Y ☐ No Plot ☐ POA Theory ● POA (p=0+1) ○ POA (p=0) ☐ Apply WL for Water
Wave lenght= 0.488 Base WaveLenght = 0,532

Test Data
D 40.0 Sigma [%] 0.05 m index 1.331
Noise 1000 a 2 b 3000
signal=a*(generated_signal + noise_range) + b
Tilt angle 0.5
☑ Load Data from file

Iteration
	Parameter	step	N
D	2400.	10.0	40
Sigma [%]	0.001	0.004	5
m index	.3355	0.000	1

Angula Range for LSQ
Th min 71
Th max 82

Options ○ sigma ○ m index ● m and sigma
Result D=2710.0; m index=1.3355; sigma=0.009
☑ Save result to file

Figure 4.15 Main processing software: left, windows to control the CSP filtering and normalization step; right, window to control CSP inversion with the 3-points and the LSQ-LMT methods.

A second processing software was developed under Matlab environment. It allows to get with the so-called NNLSQ method (see § 3.1) the bubble size distributions from the inversion of experimental CSP are pre-processed with the software depicted in Figure 4.15.

4.3.4 Calibration and alignment procedures

The CARS technique is based on a Fourier optics system. In theory, this configuration allows absolute angular measurements wherever the bubbles are located within the probe volume. In practice this is not totally true as the measured intensity is not bubbles position independent. Indeed, the collected intensity is sensitive to the bubbles distance from the collecting lens and, in addition, it is weighted by the laser beam Gaussian intensity profile.

We have developed a specific calibration procedure to align the system and to get a pixel-angle relation. The first step is to align all components of the emission unit, optical fiber, half-plate and the beam expander, as well as the beam expander magnification. This last point is realized by controlling the beam collimation at a distance of 5 meters. The second step is to proper select the beam polarization. This is simply done by carefully adjusting the optical axis of the half-plate with respect to the transmission of the beam with a polarizer. The third step is to set the collection optics axis perpendicular to the output windows so that, in a image, the CSP are equally distorted (from left to right) by refraction effects at the windows-air interface. Fourth step, all optical components are aligned with a classical auto collimation procedure: reflection on the camera chip, onto the Fourier lens and then, on the collection lens. Newton's rings are helpful for this task (look for instance the center of the CSP image of Figure 4.14). Note that for mechanical reasons it was not possible to set the chip of the DALSA camera exactly at the center of the optical bench, but this is not required by the CARS technique.

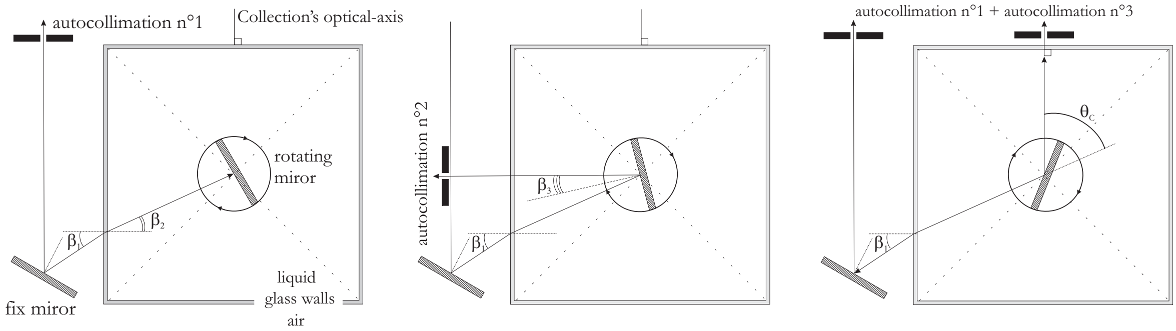

Figure 4.16 Schematic of the angular calibration procedure

Fifth step of the alignment procedure, the angular magnification of the system is chosen by moving the Fourier lens and the camera with respect to the collection lens. To do so, the best is to observe simultaneously rising bubbles and to scan with a goniometer the collection lens. The smallest possible spot onto the CCD chip corresponds to a Fourier configuration. To do so and to prevent any damage of the CCD we reduce the coupling efficiency of the laser beam into the mono-mode fiber (component 13 in Figure 4.10). Sixth step, it is necessary to angularly calibrate the system. For this purpose a high precision goniometer is used (component 16 in Figure 4.10). A mirror is fixed onto this goniometer (the mirror surface contains the goniometer rotation axis) and immersed in the cell.

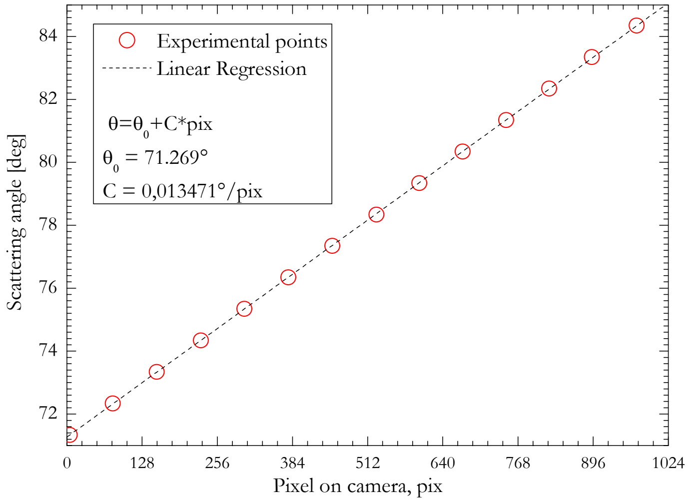

Figure 4.17 A typical pixel-angle calibration curve of the CARS system

This angular calibration is performed in three steps, see Figure 4.16. We first auto-collimate the laser beam with itself, to get a reference point. If we want to deduce the liquid refractive index from Snell-Descartes refraction law, we can turn the mirror so that we have a second auto collimation condition when the transmitted beam is perpendicular to the first glass wall (i.e. refraction angle β_3 in Figure 4.16). Finally we turn up to the desired angle θ_C so that the laser beam is perpendicular to the second glass-wall and superimposed to the optical axis of the collection optics. By rotating the mirror around this angle we obtain a calibration curve like the one presented in Figure 4.17. The same procedure can be used to calibrate in intensity the system (see also §7.2).

4.4 Micro-video imaging system (shadowgraphy)

We review and discuss now the working principle and setup requirements of the long distance micro-video imaging technique. Figure 4.18 sketches the formation of the image of a circular disk onto a CCD chip, when this object is in focus and out-focus.

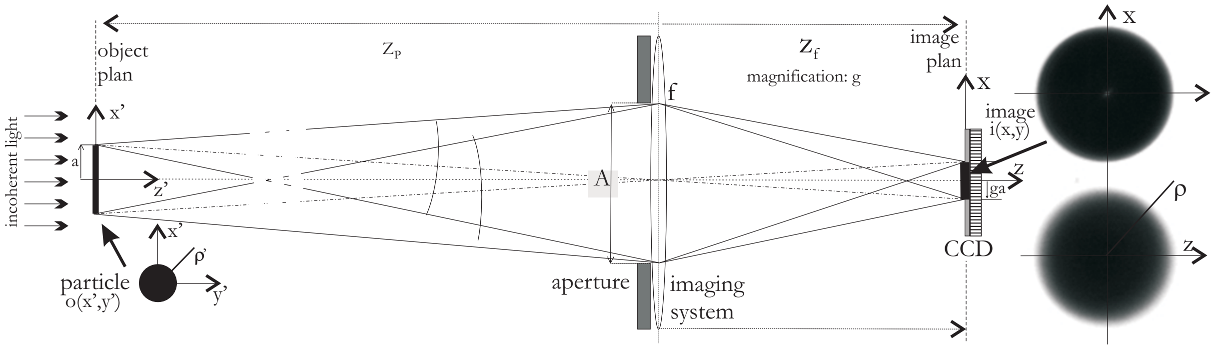

Figure 4.18 Schematic of the formation of an image

4.4.1 Simple model for the formation of images

The full calculation of the image of a particle lighted by a laser requires complex calculations. Nevertheless, for a particle lighted by an incoherent light source, this image can be reasonably modeled as the convolution product of its luminance profile and the point spread function (PSF) of the optical system (e.g. Goodman 1996; Fdida, 2008):

$$i(x,y) = o(x,y) \otimes s(x,y) \tag{76}$$

where $o(x,y)$ is profile of luminance of the particle, i.e. how it transmits/blocks light, $s(x,y)$ is the impulse response of the optical system, considered as linear. These two functions are defined in the image plane on digital sensor of the optical system.

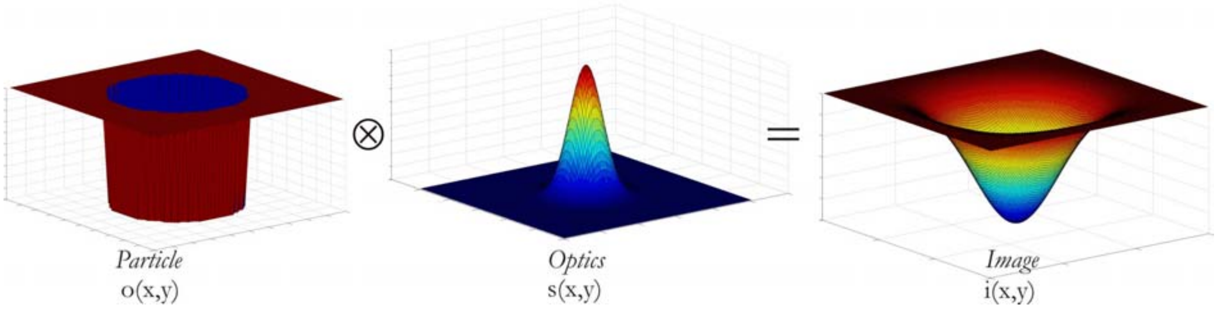

Figure 4.19 Illustration of the convolution product

If τ is the rate of transmission of light through the particle, the luminance function of the latter can be approximate by

$$o(x,y)=1-(1-\tau)circ\left(\frac{\sqrt{x^2+y^2}}{\gamma a}\right)$$
$$circ(r)=\begin{cases}1 & for \quad r<1\\ 0 & \text{otherwise}\end{cases} \tag{77}$$

For the PSF of a classical optical system, Pentland (1987) recommends to use a Gaussian function,

$$s(r)=\frac{2}{\pi\chi^2}\exp\left(-\frac{2r^2}{\chi^2}\right) \tag{78}$$

where $r^2=x^2+y^2$ is the radial coordinate, χ the half-width of the impulse response at e^{-2}, γ the image magnification. Note that the predictions of this simple model have been compared successfully with more rigorous models using the GLMT (see Ren et al., 1996). In practice both χ and γ depend of the optical system size aperture, the wavelength, the particle distance to the object plane (out-of-focus effects).

The analytical result of the convolution product Eq. (76) is given by

$$i(r)=1-\frac{4(1-\tau)}{\chi^2}\int_0^d \exp\left(-2\frac{r^2\gamma a}{\chi^2}\right)I_0\left(\frac{4\rho r}{\chi^2}\right)d\rho \tag{79}$$

The resulting image intensity profile depends on the real radius a of the particle, the radial coordinate r in the object plane, the half-width χ of the impulse response, the optics magnification factor g, a variable ρ of integration in the image plane. Let's introduce the following three non dimensional quantities:

$$\tilde{a}=\frac{\sqrt{2}a}{\chi},\tilde{r}=\frac{\sqrt{2}r}{\chi},\tilde{\rho}=\frac{\rho}{a} \tag{80}$$

From equations (79) and (80) we obtain the expression of the transmitted light intensity in the plane of the camera (image plane), in cylindrical coordinates:

$$i(\tilde{r})=1-2(1-\tau)\exp\left(-\tilde{r}^2\right)\int_0^{\tilde{a}}\rho\exp\left(-\rho^2\right)I_0\left(2\tilde{r}\rho\right)d\rho \tag{81}$$

where $\tilde{r}$ is the polar radius and $\tilde{a}$ the reduced radius of the objetc. The distribution of light intensity $i(\tilde{r})$ being a function of radius $\tilde{r}$, it depends of two parameters:

- the rate τ of transmission of light corresponding to the minimum level of gray in the image. This parameter is related to the contrast.

- the reduced particle radius $\tilde{a}$.

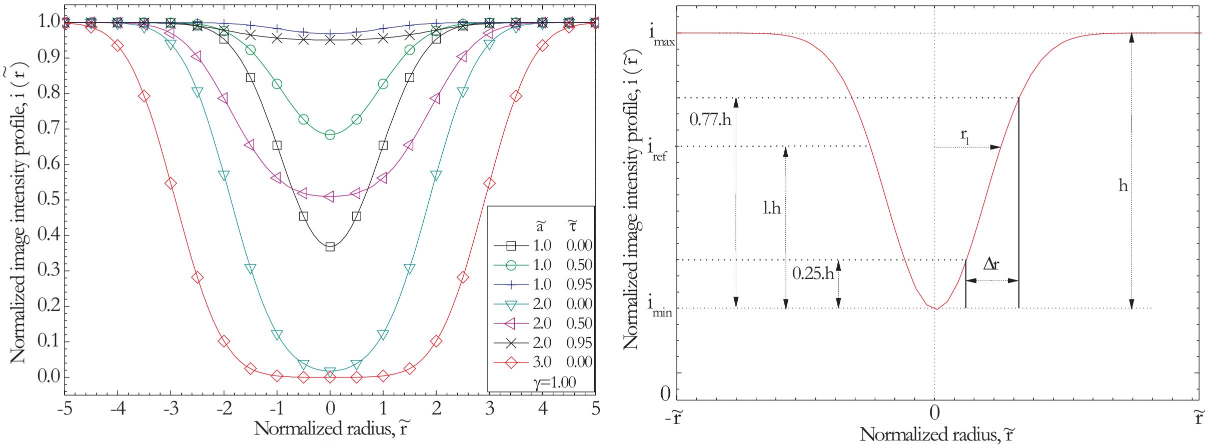

(a) (b)

Figure 4.20 a) Intensity profiles obtained for different reduced radius and light intensity transmissions, with $\gamma=1$; b) Schematic of the influence of the thresold onto the measured diameter.

The influence of these two parameters onto the intensity profile of an image is shown in Figure 4.20 (a). It appears clearly that the light transmission parameter τ plays only a role in the global contrast of the image (mean gray level). The reduced radius $\tilde{a}$, which is proportional to a and inversely proportional to χ, influences what may be called “the sharpness” of the image border (i.e. slope of the intensity curve in the border region).

The profile height of the image is equal to the height of the object if the latter is large enough. For low values of $\tilde{a}$, i.e. when the object is small in the impulse response, the minimum level of intensity is greater than τ, which implies a high profile level. Looking at Figure 4.20 (a) it appears difficult to get a single particle radius from a given profile. To do so, the idea is to first consider the height $h=i_{\max}-i_{\min}$ (see Figure 4.20 b) and to define an intensity threshold level $i_{ref}=i_{\min}+lh$ (Fdida, 2008). To each value of l corresponds an image half-width $\tilde{r}_l$. As can be seen in Figure 4.20 (a) the true particle radius corresponds to a value of h which is close to 50%. According to the literature the best optimization and compromise seems to be for $l\approx 0.61$. Note that for large particles (mostly our case except for electrolytic bubbles) and low impulse response (we use a long distance microscope), the particle image profile is rather sharp.

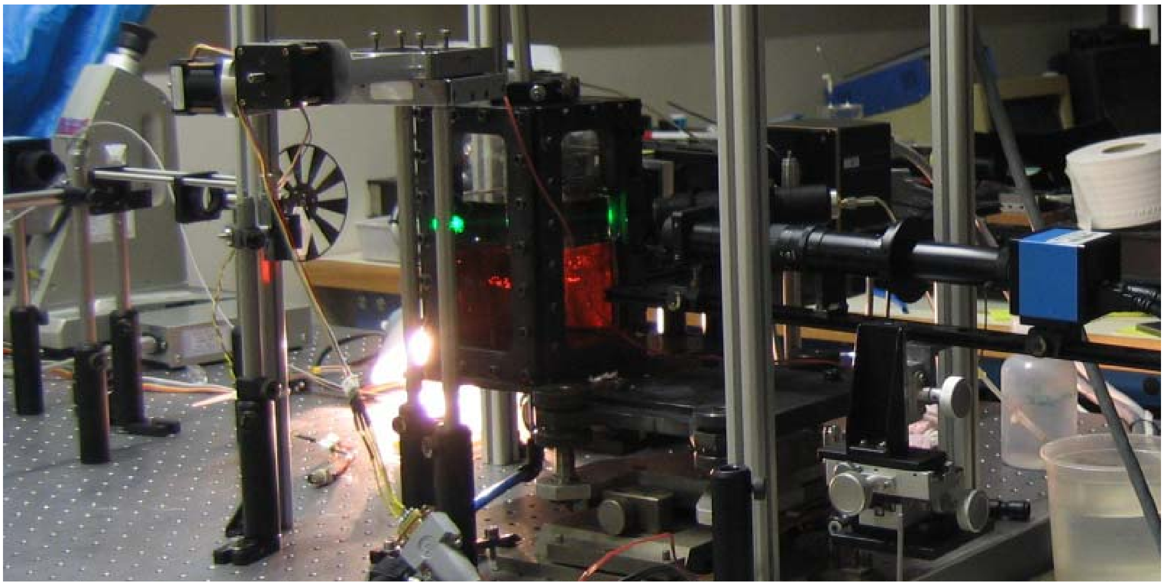

Figure 4.21 View of the experimental setup from the micro-video imaging system side.

4.4.2 Experimental setup

Figure 4.21 shows a picture of the micro video imaging setup that we have developed. The corresponding schematics are shown in Figure 4.22, as well as in Figure 4.11. The system basically uses a broadband light source which generates short time (few microseconds) and low coherence pulses of light (it covers the visible spectrum). The output of this flash lamp is focused onto the aperture of a polymer fiber (1 mm core) before to be collimated and directed to the experimental cell. The camera is located on the other side of the cell, so that the CCD chip surface is perpendicular to the low coherence light beam. In front of the camera it was necessary to use a band pass filter to block the light from the laser beam (CARS system). The camera lens is a long distance microscope objective, which allows high magnification and high field depth. This objective has a fix working distance of 90 mm. The camera, from “Imaging Source” (ImagingSource, 2007) is a digital USB camera with 8 bits depth and 1024x1024 pixels. The camera was fully controlled (exposure time, frame rate, data storage, compression…) with a software provided by the “Imaging Source”.

We have also built a complete synchronization system. The imaging measurements can be independent; meaning that only the camera and the flash lamp are synchronized together or the measurements can be conditioned by an external event, the CARS system or the “bubble detector”. The latter system was very helpful to detect bubbles passing through the probe volume, randomly (i.e. large non spherical bubbles have complex trajectories), and to trig simultaneously the CARS and the imaging systems.

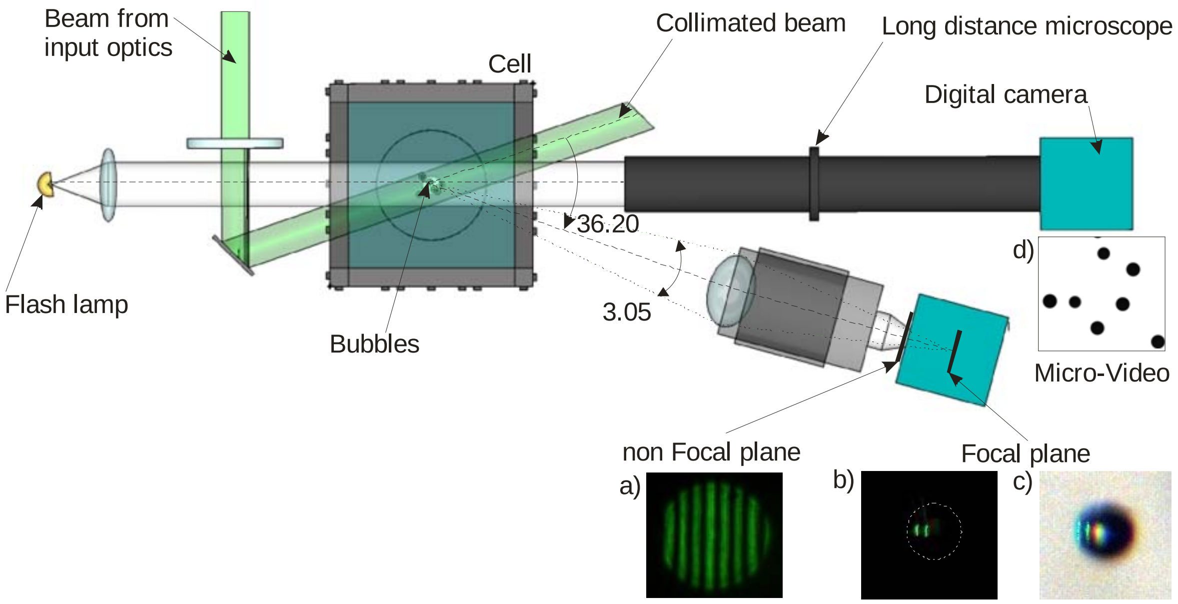

Figure 4.22 ILIDS and Shadowgraphy setups: a) ILIDS fringes pattern obtained for the out-focused image of a bubble, b) ILIDS image of "glare points" when the image is in-focus, c) like image (b) but when the bubble is also illumitated by a white light beam too.

4.4.3 Signal processing and statistics

To analyze automatically the recorded image we have used a classical blob analysis. For that purpose we have developed scripts using the image analysis software called "Matrox Inspector 2.1" (see Matrox Electronics Systems, 1997). For the blob analyze, two different intensity thresholds are defined so that for each detected particle within an image, we get two diameters. If the two measured diameter deviates from more than few percent, the corresponding particle was rejected from the analysis. In fact, this procedure may be thought as a rejection criteria based on the image sharpness (see §4.4.1). Additional criteria are used in this analysis like: the minimum and maximum particle size, the maximum roughness of the image (i.e. signature of an out-focused image), the particle maximum non sphericity (based on the measurements of the two Ferets's diameters), the particle center location, etc. Figure 4.23 shows a screen copy of the Matrox Inspector application with a typical image to be processed, a part of the script and some of the raw results of the analysis. The particles detected by the blob analysis are indicated by a blue circle and an identification number ("label"). Note that particles with truncated images are rejected. The blob analysis output is a text file containing several thousands to several tens thousands of lines corresponding each to a particle which has been detected, with its label and all measured parameters. For the post-processing of these data, mainly to apply the different filters (sharpness, sphericity, aspect ratio, orientation angle…) and to perform statistics, we have developed a windows application under Borland Delphi environment, see Figure 4.24.

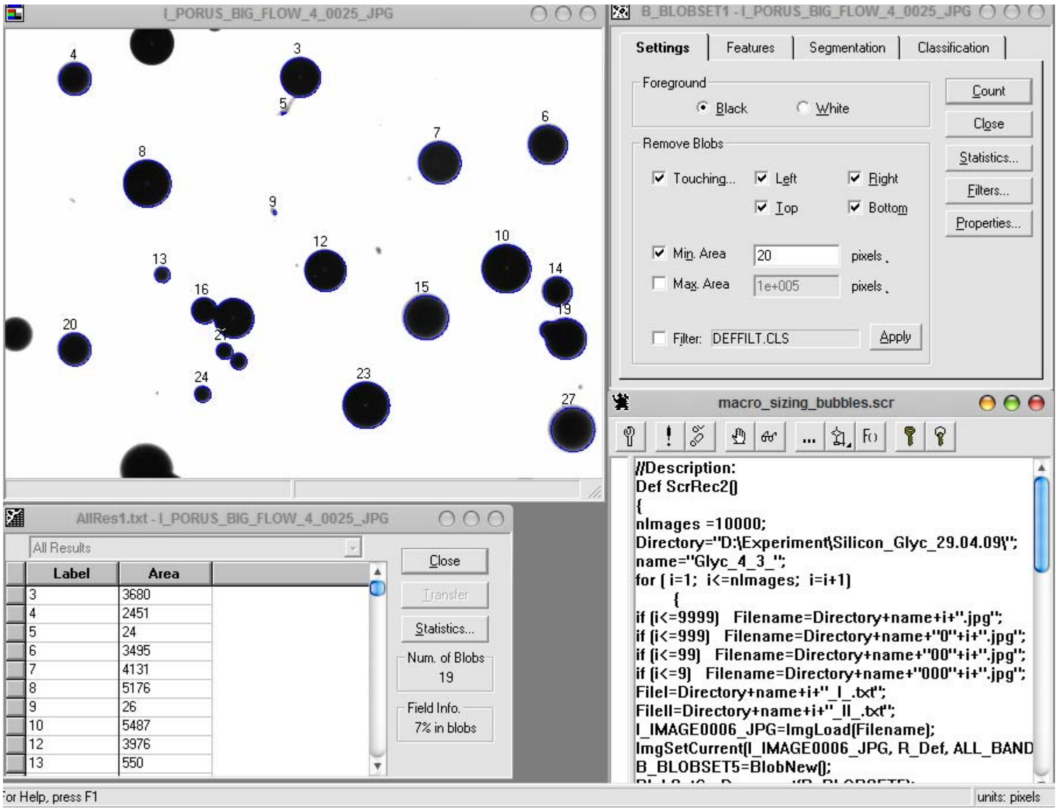

Foreground: ● Black ○ White

Remove Blobs

☑ Touching... ☑ Left ☑ Right

☑ Top ☑ Bottom

☑ Min. Area 20 pixels.

☐ Max. Area 1e+005 pixels.

☐ Filter: DEFFILT.CLS

All Results

Label	Area
3	3680
4	2451
5	24
6	3495
7	4131
8	5176
9	26
10	5487
12	3976
13	550

Num. of Blobs: 19

Field Info.: 7% in blobs

macro_sizing_bubbles.scr

```
//Description:
Def ScrRec2()
{
nImages =10000;
Directory="D:\Experiment\Silicon_Glyc_29.04.09\";
name="Glyc_4_3_";
for ( i=1;  i<=nImages;  i=i+1)
      {
if (i<=9999)   Filename=Directory+name+i+".jpg";
if (i<=999)   Filename=Directory+name+"0"+i+".jpg";
if (i<=99)   Filename=Directory+name+"00"+i+".jpg";
if (i<=9)   Filename=Directory+name+"000"+i+".jpg";
FileI=Directory+name+i+"_I_.txt";
FileII=Directory+name+i+"_II_.txt";
I_IMAGE0006_JPG=ImgLoad(Filename);
ImgSetCurrent(I_IMAGE0006_JPG, R_Def, ALL_BAND
B_BLOBSET5=BlobNew();
```

Figure 4.23 The blob analysis (particle image detection and analyse) is performed with a script that we have developped under Matrox Inspector 2.1 software environment.

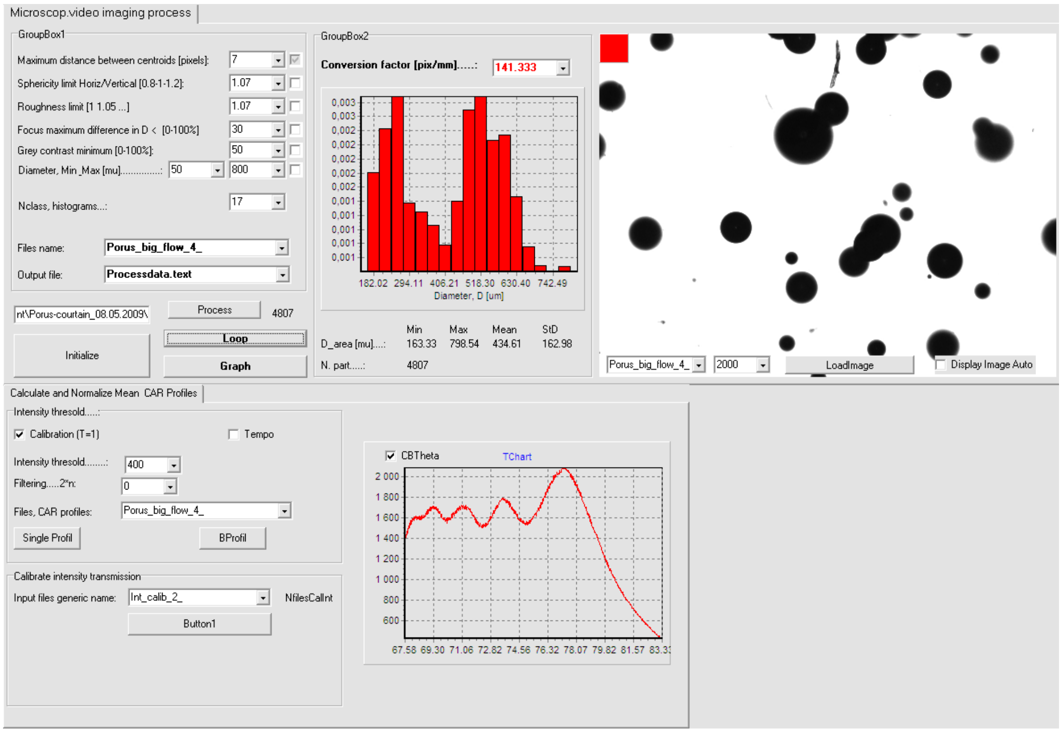

Maximum distance between centroids [pixels]: 7 ☑

Sphericity limit Horiz/Vertical [0.8-1-1.2]: 1.07 ☐

Roughness limit [1 1.05 ...]: 1.07 ☐

Focus maximum difference in D < [0-100%]: 30 ☐

Grey contrast minimum [0-100%]: 50 ☐

Diameter, Min_Max [mu]..............: 50 800 ☐

Nclass, histograms...: 17

Files name: Porus_big_flow_4_

Output file: Processdata.text

nt\Porus-courtain_08.05.2009\

4807

Conversion factor [pix/mm].....: 141.333

	Min	Max	Mean	StD
D_area [mu]....:	163.33	798.54	434.61	162.98
N. part.....:	4807			

Porus_big_flow_4_ 2000 ☐ Display Image Auto

Intensity thresold.....:

☑ Calibration (T=1) ☐ Tempo

Intensity thresold........: 400

Filtering.....2^n: 0

Files, CAR profiles: Porus_big_flow_4_

Calibrate intensity transmission

Input files generic name: Int_calib_2_ NfilesCalInt

☑ CBTheta

Figure 4.24 Copy of the main screen of the post-processing software of raw blob analysis output.

4.4.4 Remarks and conclusion

The imaging system and software that we have developed are rather efficient for the analysis of spherical bubbles and low density flows (see comparisons with CARS technique in Chapters 5 & 6).

The imaging method needs really a lot of computational resources to digitize, store and process (blob analysis and statistics) these images. In the present study, to get reliable statics, it was usually necessary to acquire about one thousands images, and to processes several tens thousands of particles images. This means really a lot of time and disk space when performing parametric studies. Nevertheless, the major limitations of this technique are in respect to the smaller particles and high density bubbly flows.

Small particles require a higher optical magnification. But in this case, as shown in §4.4.1, we get rapidly low contrast images that are difficult to analyze. This is particularly true when we have a broad band size distribution since, in this case, it is extremely difficult to adjust properly the detection thresholds for all size classes. For small particles, depth of focus effects may be really severe and the size distribution is surely biased by these effects. Large non spherical bubbles can be missed by the blob analysis if the parameters are not properly adjusted. High bubbly flow density means, partial or total overlapping of bubbles images, loss of contrast of all images. Partial overlapping cannot be managed by our system (but some do), so bubbles are simply rejected. Indeed, to threat the overlapping it is necessary to use much more efficient detection scheme and then, more computational resources. Total overlapping means that some particles have totally "disappeared" from the image. Once again this introduce a bias on the particle count number. In that case, the size distribution is bias towards the smaller particles which have a greater probability to be totally masked by a bigger one. So, although the imaging technique is very flexible and easy to use (or seems to), it suffers from several draw backs (e.g Dehaeck, 2007).

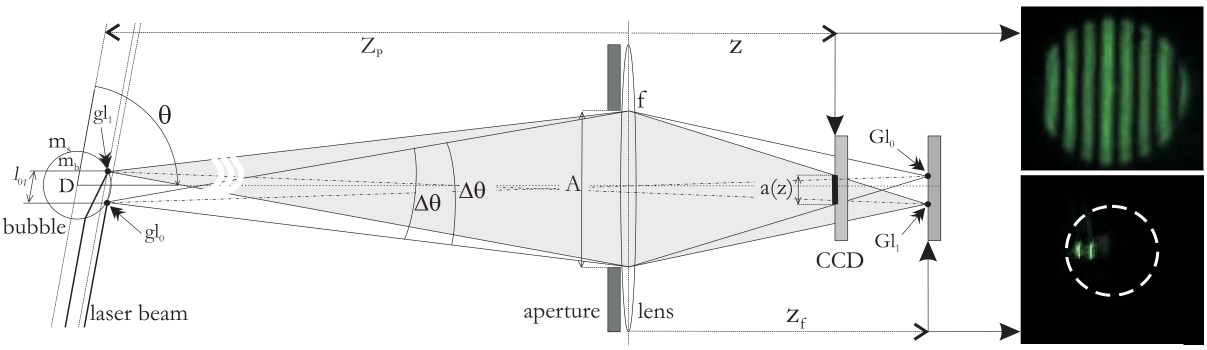

Figure 4.25 Basic setup of an interferometric laser imaging droplet sizing system. On the right two images of an air bubble in water are presented: out focus (top) and in focus (bottom).

4.5 Interferometric sizing of particle by out-of-focus imaging of the glare spots

4.5.1 Principle

This rather new technique was developed by several authors (Hess 1998, Pagot 1998, Maeda et al. 2000, Semidetnov 2004) even if, various aspects of this techniques were prior known (Koning et al. 1986, Glover et al. 1995). According to the authors this technique is called « *Interferometric Laser Imaging Droplet Sizing* technique (ILIDS) » or « *Interferometic Particle Imaging (IPI)* ». In our opinion a better name for this technique would have been something like "Interferometric particle sizing technique by out-of-focus imaging of the glare spots" but, for convenience, we will use further on the acronym ILIDS to designate this laser technique.

ILIDS allows getting the diameter and two velocity components of all particles lighted by a laser sheet, provided the particles are spherical, transparent and not too small, and if the particle number density is not too high. The optical setup is identical to the one of a PIV/PTV system (i.e. Raffel et al. 1998). Basically, it is composed of a double pulse YAG laser which generates two superimposed and time delayed laser sheets, and of a digital camera from a PIV-type (Figure 4.25). One significant particularity to notice here is that the camera is localized at an observation angle where the scattering pattern is dominated by only two scattering processes (for a water droplet in air and for the perpendicular polarization, reflected and refracted rays have the same intensity at $\theta \approx 67°$). Indeed, this technique has been mainly used to characterize droplets $(m > 1)$, and only few studies were devoted to the sizing of bubbles (i.e. Kawaguchi et al. 2002, Dehaeck 2007). Let us remember that for an air bubble in water and parallel polarization, refracted and reflected rays have the same intensity for $\theta \approx 45°$. For such particular angle, if the camera lens is perfectly focused onto the bubble surface, we do not really observe the contour of the bubble since its surface is a specular one. In fact we observe only two bright spots : the so-called "glare points" which correspond to the two exit points of the refracted and reflected rays which are scattered in the camera direction. These points are noted gl_0 et gl_1 in Figure 4.25. From the measurement of the distance (l_{01}) between the two glare spots one can deduce the diameter of a spherical particle, but the accuracy and dynamics will be quite limited. If now we slightly un-focus the camera lens, the particle image will take the form of a circular disk containing a fringe pattern (see Figure 4.25). The number N of fringes in each disk depends of the particle diameter D and refractive index m, the laser wavelength λ_0 and the camera optical aperture, A. The principle of ILIDS is then to determine the angular frequency of the fringe pattern in each disk present to infer the size of the corresponding particle, i.e. the particle size distribution. In the next paragraphs we present the work we have done to derive analytical expressions and build numerical tools to predict the response of ILIDS, with both geometrical optics and the Lorenz-Mie theory.

4.5.2 Modeling the fringe patterns

Geometrical Optics model

The glare spots are rather punctual sources. Their close distance makes them coherent each other and, like in the famous Young's interference experiment with two slits, they interfere at infinity.

When the camera lens is in focus, positioned in the forward scattering domain, the particle image onto the CCD chip is composed of two bright spots, noted GL_0 and GL_1 in Figure 4.25. If the camera lens is out of focus ($z < z_f$ or $z > z_f$, but the first condition gives less optical aberrations) the images of the glare spots superimpose each other and interfere onto the CCD chip, which explains the observed fringes. The diameter of the disk which contains the fringes can be deduced from simple geometrical considerations (see Albrecht et al. 2004):

$$a\left(z_P\right) = A\left|1 - z\left(f^{-1} - z_P^{-1}\right)\right| \tag{82}$$

where A, z, f et z_P correspond respectively to the lens aperture diameter, the distance between the aperture (diaphragm) and the CCD chip, the back focal of the camera lens and the distance between the particle and the camera lens. We notice that the diameter of the image of the disk changes with the distance $\left(z_P\right)$. This feature can be used to measure the particle distance from the camera lens and then, to get the 3D coordinates $\left(x, y, z\right)$ of the bubble. At this step it is important to note that, by some aspects, ILIDS technique is halfway between the shadowgraphy technique, which works in the space domain, and the CARS technique, which works in the Fourier Domain.

Lets now calculate, with geometrical optics, the properties of the interference pattern produced by the refracted and reflected rays, with respect to the scattering angle (observation) θ, the laser wavelength in vacuum λ_0, the refractive index of the surrounding medium m_s and the bubble properties (diameter D and refractive index m_b). To simplify, we define a reference plan $\left(\Sigma\right)$ for the incident wave and a reference plan $\left(\Sigma'\right)$ for the scattered rays. Figure 4.26 shows on the right the path of the aforementioned rays for a droplet $\left(m > 1\right)$ and, on the right, for a bubble $\left(m < 1\right)$. We also define a reference ray coming from and perpendicular to the reference plan $\left(\Sigma\right)$. Afterwards, this reference ray passes through the particle centre and stop onto the reference $\left(\Sigma'\right)$ being perpendicular to this plan. The corresponding optical path is equal to $\delta_{\mathbf{Ref}} = m_2 D$. The optical path difference between the optical path δ_0 and the reference ray scattered in the direction θ is

$$\delta_0 - \delta_{\mathbf{Ref}} = m_s\left(a_1 + a_2\right) - m_s D = -m_s D \sin\left(\theta / 2\right) \tag{83}$$

From the previous equation we can derive the related phase delay ϕ_0:

$$\phi_0 = \frac{2\pi}{\lambda_0 / m_s}\left(\delta_0 - \delta_{\mathbf{Ref}}\right) = -\frac{2\pi}{\lambda_0} m_s D \sin\left(\theta / 2\right) \tag{84}$$

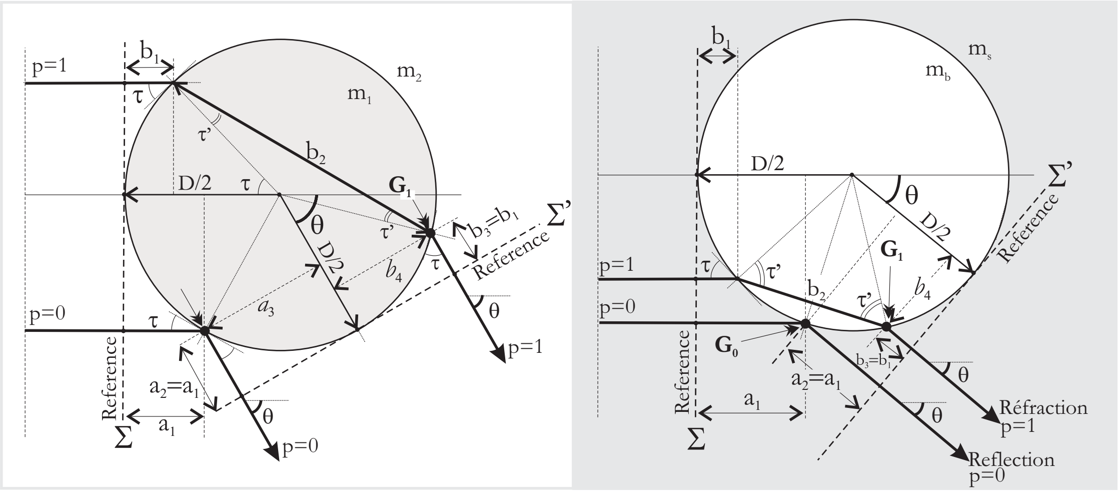

(a) (b)

Figure 4.26 Geometry of our ILIDS model: sketch of the refracted (p=1) and reflected (p=0) rays scattered by a droplet (left) and a bubble (right) in the scattering direction θ.

For a droplet as well as a bubble, in the scattering direction θ, the optical path difference of the refracted ray compared to the reference ray scattered is

$$\delta_1 - \delta_{\mathbf{Ref}} = \left(m_s b_1 + m_b b_2 + m_s b_3\right) - m_s D \tag{85}$$

with $b_3 = b_1 = R\left(1 - \sin\tau\right)$ and $b_2 = D\sin\tau'$, we obtain the phase delay of the refracted rays ϕ_1:

$$\phi_1 = \frac{2\pi}{\lambda_0 / m_s}\left(\delta_1 - \delta_{\mathbf{Ref}}\right) = \frac{2\pi}{\lambda_0} m_s D\left(m_b \sin\tau' - m_s \sin\tau\right) \tag{86}$$

It is better to reformulated Eq. (86) as a function of the scattering angle θ (Bultynck 1998). To do this the relative refractive index $m = m_b / m_s$ is introduced and the quantity $m_b \sin\tau' - m_s \sin\tau$ is transformed as follows:

$$\begin{aligned}
&\left(m_b \sin\tau' - m_s \sin\tau\right)^2 \\
&\qquad = m^2\left(\sin\tau'\right)^2 - 2m\sin\tau'\sin\tau + m^2\left(\sin\tau\right)^2 \\
&\qquad = m^2 - m^2\left(\cos\tau'\right)^2 + 1 - \left(\cos\tau\right)^2 - 2m\sin\tau'\sin\tau \\
&\qquad = m^2 + 1 - \left(\cos\tau - m\cos\tau'\right)^2 - 2m\cos\tau\cos\tau' - 2m\sin\tau'\sin\tau
\end{aligned} \tag{87}$$

We now introduce the Snell-Descartes relation $\cos\tau = m\cos\tau'$ (Van de Hulst 1957), to get

$$\left(m_b \sin\tau' - m_s \sin\tau\right)^2 = m^2 + 1 - 2m\cos\left(\tau - \tau'\right) \tag{88}$$

The first refracted ray is scattered in the direction $\theta = 2\tau - 2\tau'$ (Van de Hulst 1957), so that Eq. (88) simplifies to

$$\left(m_b \sin\tau' - m_s \sin\tau\right)^2 = m^2 + 1 - 2m\cos\left(\theta/2\right) \tag{89}$$

Finally, with the above expression, Eq. (86) becomes :

$$\phi_1 = \left(-1\right)^i \frac{2\pi}{\lambda_0} m_s D \sqrt{m^2 + 1 - 2m\cos\left(\theta/2\right)} \tag{90}$$

In Eq. (90) $i = 2$ for a droplet and $i = 1$ for a bubble. The latter condition has been introduce to take into account that $\delta_1 - \delta_{\mathbf{Ref}} \geq 0$ for a droplet (i.e. $m_b \sin\tau' - m_s \sin\tau \geq 0$ in Eq.(86), see Figure 4.26) and $\delta_1 - \delta_{\mathbf{Ref}} \leq 0$ for a bubble (i.e. $m_b \sin\tau' - m_s \sin\tau \leq 0$ in Eq.(86), see Figure 4.26). It comes up that for the scattering direction θ the phase delay between the reflected and the first refracted rays read as:

$$\Delta\phi_{01} = \phi_0 - \phi_1 = -\frac{2\pi D}{\lambda_0 / m_s}\left[\sin\left(\theta/2\right) + \left(-1\right)^i \sqrt{m^2 + 1 - 2m\cos\left(\theta/2\right)}\right] \tag{91}$$

Assuming an equal amplitude for these rays, noted $\sqrt{I}$, the interference scattering pattern produced by these rays is of the general form:

$$I\left(\theta, m, \lambda_0, D\right) = 2I_0\left[1 + \cos\left(\Delta\phi_{01}\right)\right] \tag{92}$$

We are looking for periodicity in θ of Eq. (92), i.e. when $I\left(\theta, m, \lambda_0, D\right) = I\left(\theta + d\theta, m, \lambda_0, D\right)$. It requires to determine the occurrence of the maxima of $\Delta\phi_{01}$. For an harmonic function it means that $d\left(\Delta\phi_{01}\right)/d\theta \equiv 2\pi N$, where N is a natural integer quantifying the number of indeterminate cycles or more simply the "fringe count". With Eq. (91) and derivating Eq. (91) we obtain that, in the vicinity of θ , over a small angle region $\left[\theta - \Delta\theta/2, \theta + \Delta\theta/2\right]$ with $\Delta\theta \approx 0°$, the particle diameter can be infer from the optical parameters of the setup and from the measurement of the number N of fringes present in one disk :

$$D \approx \frac{2\lambda_0}{m_s}\frac{N}{\Delta\theta}\left[\cos\left(\theta/2\right) + \frac{\left(-1\right)^i m\sin\left(\theta/2\right)}{\sqrt{m^2 + 1 - 2m\cos\left(\theta/2\right)}}\right]^{-1} \tag{93}$$

Physically $\Delta\theta$, in radians, represents the collection angle of the camera lens. For a low aperture camera lens the collection angle is about $\Delta\theta \approx A/f$. It can also be measured with a goniometer (as we did, see later on) or deduced both from the camera lens numerical aperture (N.A.) as well its aperture number (#F/D) :

$$\Delta\theta \approx 2N.A. \approx \left(F/D\right)^{-1} \quad [rad] \tag{94}$$

The quantity $F_a = N/\Delta\theta$ is an angular frequency averaged onto the angular range $\Delta\theta$. This frequency can be obtained with a Fourier analysis of the recorded image pattern, or by any other fringes counting technique.

To conclude, the basic equation to get the particle diameter read as :

$$D \approx \omega\left(m_b, m_s, \theta, \lambda_0\right) F_a \tag{95}$$

with

$$\omega \approx \left(2\lambda_0 / m_s\right)\left[\cos\left(\theta/2\right) + \left(-1\right)^i m \sin\left(\theta/2\right) / \sqrt{m^2 + 1 - 2m\cos\left(\theta/2\right)}\right]^{-1} \tag{96}$$

where ω is an optical constant which only depends on the particle relative refractive index and the angular position of the camera lens axis, with $i=1$ for bubbles ($m<1$), and $i=2$ for droplets and other spherical particles with ($m>1$). Eq. (96) relates directly the measured frequency to the diameter to be determined. As a example, for air bubble in water with $m^{-1}=1.334$, $\lambda_0 = 0.532\mu m$ and $\theta = 67°$ we get that $\omega \approx 8.59\mu m$. For the latter parameters, the angular frequency of the ILIDS fringes pattern of a $D=400\mu m$ bubble is of $F_a = D/\omega \approx 46.6\ rad^{-1}$, i.e. 0.26 fringes per degree, which is in rather good agreement with LMT predictions .

Basically, the main limitation of the model we derive above is in the assumption of the existence of two dominant scattering processes: reflection and first refraction with, in addition, similar intensities. For air bubbles in water for instance, this model is only valid for $30 \le \theta \le 60°$ as, outer of this region, other scattering processes may be not negligible and even more intense that rays $p=1$, see Figure 4.27.

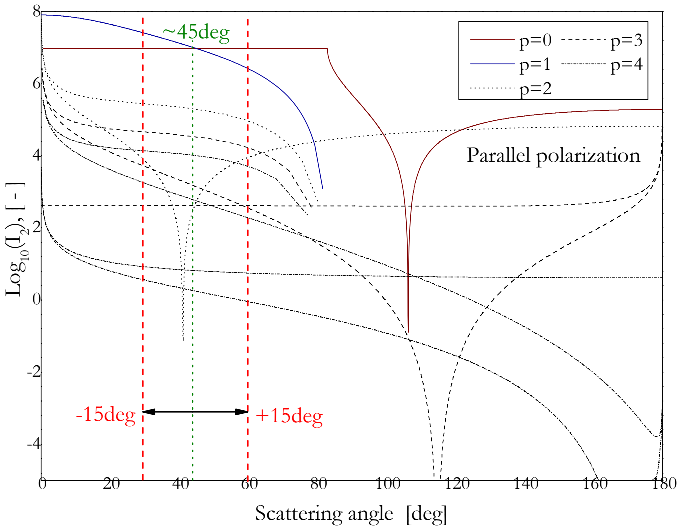

Figure 4.27 Intensity of p=1, 2, 3, 4 rays for air bulles in water (Fresnel coefficients only)

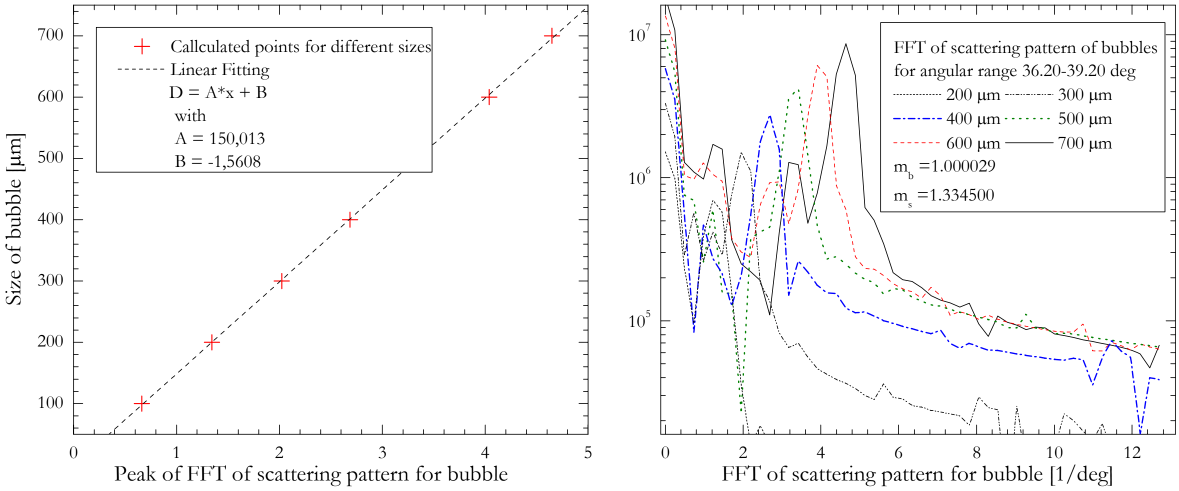

(a) (b)

Figure 4.28 a) LMT caculations of the ILIDS fringes main angular frequency versus the bubble size; b) raw Fourier spectra of the corresponding scattering diagrams.

Lorenz-Mie theory and numerical examples

According to the Lorenz-Mie theory the ILIDS fringes correspond only to the natural oscillations of the scattering diagrams, i.e. “Mie’s lobes”. Thus, it turns out that this technique is simply based on the counting of the periodical structures observed in any scattering diagram. Indeed, in the LMT framework, it is known from the beginning that the number of lobes is related to particle size parameter $\left(m\pi D / \lambda\right)$. To determine with LMT the relation between the number of fringes in an image and the particle diameter, it is just necessary to calculate the angular frequency of the scattering patterns over the angular range corresponding to the view angle of the camera. It is obvious that the scattering diagram must be calculated for the appropriate polarization, laser wavelength and refractive indices. Figure 4.28 shows the calibration curve calculated with the LMT and the parameter used in the experiment (see next section).

4.5.3 Experimental setup and exemplifying results

The ILIDS setup is rather simple. Basically we use the CARS laser beam to light the bubbles and a third digital CCD camera (similar to the one used for the shadowgraphy tectnique, but with a color sensor) located at $\theta = 37°$. This angle was imposed by the fact that it remains only a limited access around the experimental cell. The ILIDS camera was equipped with an out-focused photographic camera lens. For the camera control and the images recording we use the same software as the micro-video imaging system (see §4.4).

For the alignment we use the same procedure as the CARS technique. The idea is to scan the ILIDS camera lens with a strongly reduced laser power and a mirror fixed onto a motorized goniometer. Knowing the angular position of the mirror, we can deduce the relation between the number of pixels and the scattering angle. The big difference with CARS is the size of the beam onto the CCD chip, as ILIDS does not operate with a Fourier configuration. So, for the calibration of ILIDS it is necessary to reduce the laser beam size (with a diaphragm). Figure 4.29 shows the typical results obtained during the calibration of the ILIDS system. Figure 4.29 a) shows the intensity profile recorded when the laser beam was hitting the ILIDS camera under 7 different scattering angles. By extracting the position of the various maxima, the pixel-angle calibration curve of the system is obtained as visible on Figure 4.29 b).

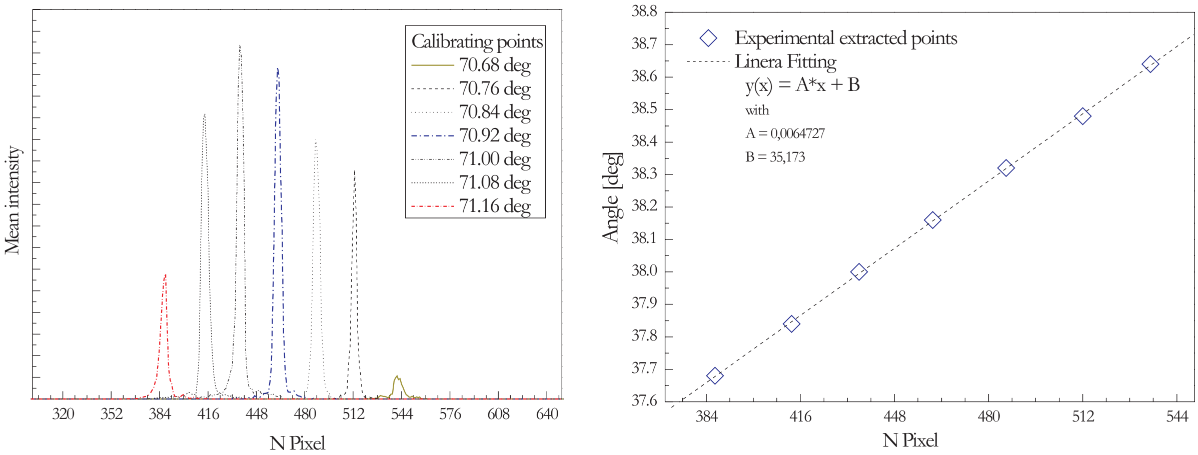

(a)

(b)

Figure 4.29 a) Calibration laser profiles for different positions; Linear regression for extracted calibration points

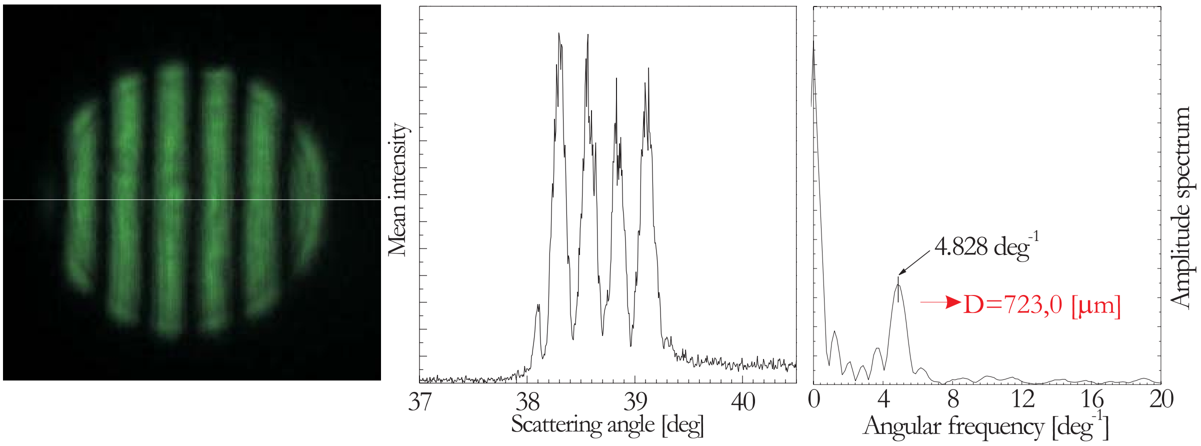

Figure 4.30 Calibration and signal processing steps for the ILIDS system.

Figure 4.30 shows images of air-bubbles in water recorded with the ILIDS system, after the alignment and the calibration steps. In this figure we have from left to right: the ILDS image of a single bubble, its intensity profile averaged over the fringes axis and the corresponding amplitude spectra. From the localization of the main peak in the Fourier spectrum we get the angular frequency of the fringe pattern and, with help of the previously derived equations, we get the bubble diameter.

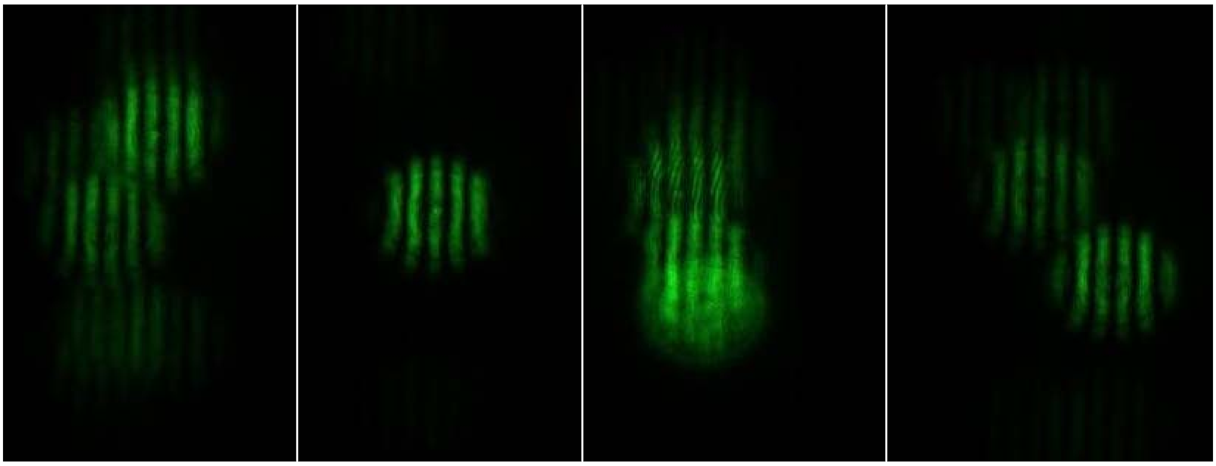

Figure 4.31 Different ILIDS images obtained when there is several bubbles within the probe volume.

If now we generate a denser bubbly flow, we get overlapping ILIDS images such as the four ones presented in Figure 4.31. From the image processing point of view, it seems extremely difficult to detect all bubbles and to perform a reliable frequency analysis for ILIDS images presented in Figure 4.31. This is a general drawback of this technique (see §4.5.1) and it is the reason why we only use ILIDS to characterize very dilute bubbly flows.

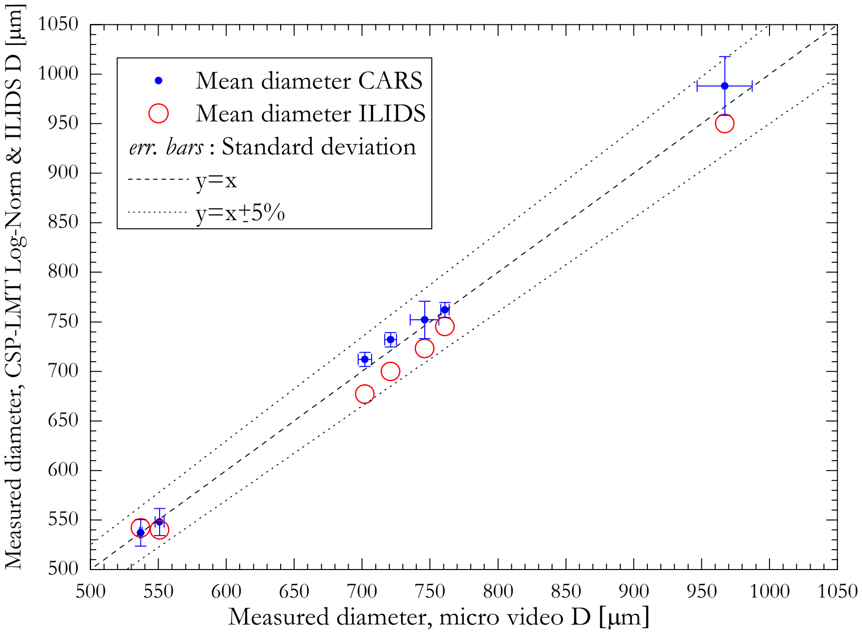

Figure 4.32 Comparison between three techniques: Shadowgraphy, CARS and ILIDS

As an example, Figure 4.32 compares bubble sizes measured with ILIDS, the micro-video imaging (shadowgraphy) and the CARS systems, see also Table 4.2. This comparison was done for air bubbles in water produced by the piezo-jet. The observed angular range was of $\sim 72.0-86.0°$ for the CARS and $\sim 36.2-39.2°$ for ILIDS systems. Note that there were too few measurements with the ILIDS system to put error bars. But, the agreement between the three methods is nevertheless already rather satisfactory (better than 5%).

Air bubble in water	Micro.Video			LSQ-LMT-log-norm.			ILIDS	
Experiment label	[um]	[um/um]	[-]	[um]	[um/um]	[-]	[um]	angular freq.
Piezo_ilids_10_	746	0,014	1,3345	752	0,025	1,3345	723	4,828
Piezo_ilids_11_	761	0,004	1,3345	762	0,010	1,3345	745,50	3,610
Piezo_ilids_13_	551	0,006	1,3345	548	0,025	1,3345	539,98	4,980
Piezo_ilids_14_	537	0,002	1,3345	537	0,025	1,3345	542	3,620
Piezo_ilids_15_	967	0,021	1,3345	988	0,030	1,3345	950	6,337
Piezo_ilids_16_	702	0,007	1,3345	712	0,010	1,3340	677	4,526
Piezo_ilids_17_	721	0,006	1,3345	732	0,010	1,3340	700	4,677
Piezo_ilids_18_	908	0,027	1,3345	908	0,030	1,3350	1085	7,243

Table 4.2 Comparison between three techniques: Shadowgraphy, CARS and ILIDS

4.5.4 Discussion and conclusion

The raw results of ILIDS are really aesthetic, but in its classical version this technique is limited to very dilute flows (to avoid images superimposition, see Figure 4.31). As remedy to this problem Kawaguchi et al. (2002) have proposed to compress the images along the fringes direction (Figure 4.33) by inserting cylindrical optics (lenses) between the collection lens and the CCD. This solution increases somewhat the number of particles per image that can be managed and then the size and bubble density number of the flow field. Some authors put a slit (thin aperture) in front of the camera lens instead using cylindrical lenses. Unfortunately, optically the slit method is not as good and it leads to a significant loss of energy.

Another important limitation of ILIDS is that it requires transparent particles of known refractive index. To overcome this constraint, Semidetnov and Tropea (2004) have proposed to light the particles with two laser beam crossing each other with a small angle. This setup, named “Global Phase Doppler System (GPDS)”, allows in addition to control the number of fringes in a particle image. In principle, the latter feature allows to measure small particles (one key limitation of classical ILIDS) but, in practice, the so-called Mie resonances limit its applicability. Due to the beam crossing, the GPDS configuration limits also strongly the field of view that can be observed.

The signal processing of ILIDS images is also a difficult point as it requires large computational resources and storage capacities. For the particle detection one interesting solution to simplify the problem is to use a PIV system working in parallel to the ILIDS system, but localized at $\theta = 90°$. In PIV images, with minimum distortion (90° angle view of the laser sheet), all particles are identified by spots of few pixels. These PIV spots can be used to make easier the localization of the centers of the disks in the ILIDS image. This setup is rather bulky, difficult to align and not so cost effective.

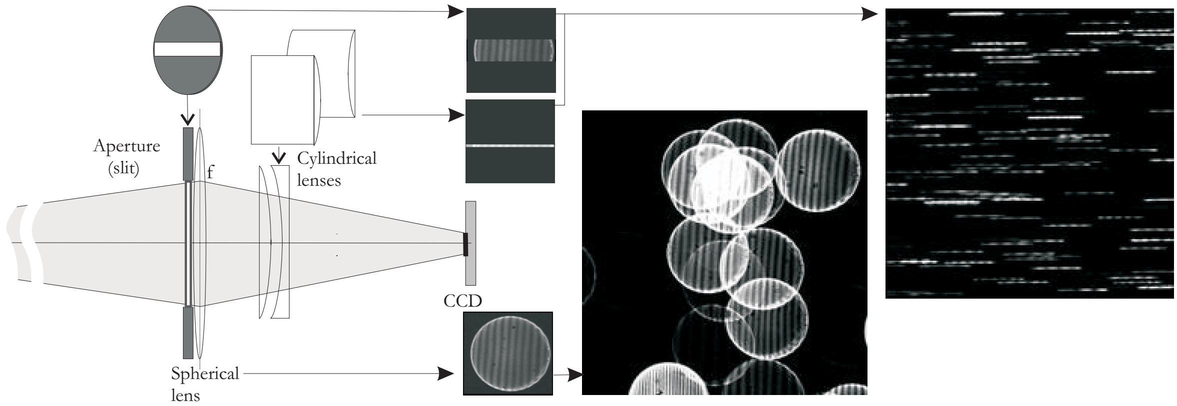

Figure 4.33 Two techniques to compress interferometric images along the fringes axis: slit based method and the cylindrical optics one. The real images presented on the right were obtained for water droplets by Kawaguchi et al. (2002).

To conclude on ILIDS, from our own experience and from the literature review, this technique suffers from severe drawbacks. However, it is still under development with good potentials (particle size and position in 2D/3D, two velocity components). In our opinion, the CARS technique is more simple to implement and much less costly. The CARS technique does not provide any information about the bubble velocity and position, but it gives information on the bubble composition and it is much less sensitive to bubbles non-sphericity. Another major difference between both techniques is that CARS is an integral technique which requires low computational resources to get bubble size distributions in contrary to the ILIDS technique, it can manage denser flows.

Chapter 5

EXPERIMENTAL RESULTS FOR CLOUDS OF SPHERICAL BUBBLES

In this chapter we present experimental results on the measurement of the size distribution and the relative refractive index, for bubbly flow conditions where the bubbles are reasonably spherical.

5.1 Bubble size distribution measurements

5.1.1 Natural & rather dilute bubbly flows

Figure 5.1 shows a small region the micro-video images for four different bubbly flows generated by (a) the assisted jet; the piezo-jet operating in (b) a stable mode, (c) a quasi-stable mode and (d) unstable mode. The bubble mean sizes are respectively of $\sim 275, 550, 550,$ and $960\mu m.$ These bubbly flows are dilute. However, they are denser than it is suggested by Figure 5.1. Indeed these images only show the bubbles that are in the effective depth-of-view of the micro-video system. From our own experience and for the considered cases and settings, the particle number in volume is estimated to be about 3 to 4 times larger than what we see in the micro-video images. Thus, we *estimate* that for results presented in this section the bubbles concentration is in the range 10 to 200 bubbles/cm^3, i.e. void fraction $\varepsilon \sim 0.001$–0.1%. In Figure 5.2 to Figure 5.5 we present the results obtained for the flow depicted by, respectively, Figure 5.1 (a) to (d). All of these figures contain subfigures showing:

(a) a typical CARS image;

(b) the corresponding pass band filtered and calibrated profile that is compared to the reconstructed one;

(c) the BSD obtained by the micro-video imaging-system;

(d) the BSD measured by the CARS system with the LSQ inverse method, using LMT as a scattering theory and the Log-Norm. BSD;

(e) the BSD measured by the CARS system with the NNLSQ method using LMT and without any low pass filtering (raw-method).

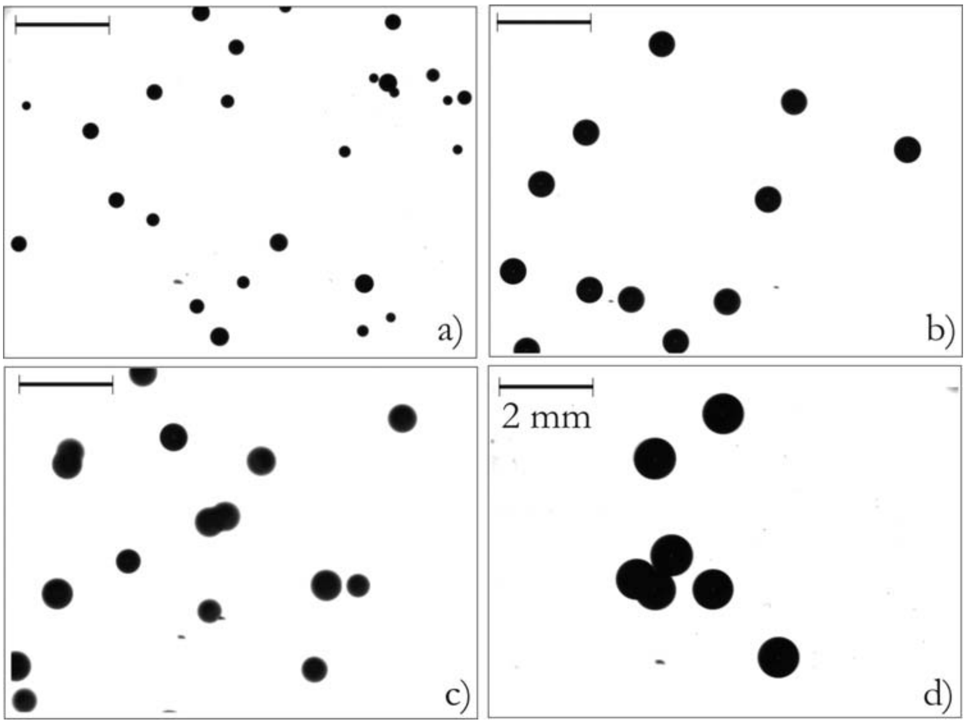

Figure 5.1 Partial micro-video images of four different bubbly flows.

The CSP in Figure 5.2 exhibits a low angular frequency modulation that is characteristic of rather small bubbles. The experimental and reconstructed CSP are similar whatever the latter overestimates the decay of the visibility for high order fringes. However, the BSD obtained by the micro-video system and by the CARS are in good agreement, they are of a log-normal type, with $\bar{D}$ centered between $274\mu m$ and $300\mu m$. All the corresponding statistics are summarized in Table 5.2. The NNLSQ method, with LMT as a scattering theory and a low pass filtering procedure, gives clearly the best results when compared to micro-video and Abbe refractomer measurements. The POA (p=0) gives here a very good estimation of the mean diameter, however from our experience, it is not always the case. The same holds for the refractive index. In fact the way we use here the POA is rather sensitive to CSP noise and distortion (due to the poor statistics).

In Figure 5.3, which corresponds to the case presented in Figure 5.1 (b), the experimental and reconstructed CSP are in perfect agreement except for the higher order fringes. The mean diameter for all measured BSD is centered between $269\mu m$ and $474\mu m$. Both the micro-video imaging-system and the NNLSQ-LMT method show that the BSD is bimodal, this is due to the fact that the piezo-jet was operating in an unstable regime.

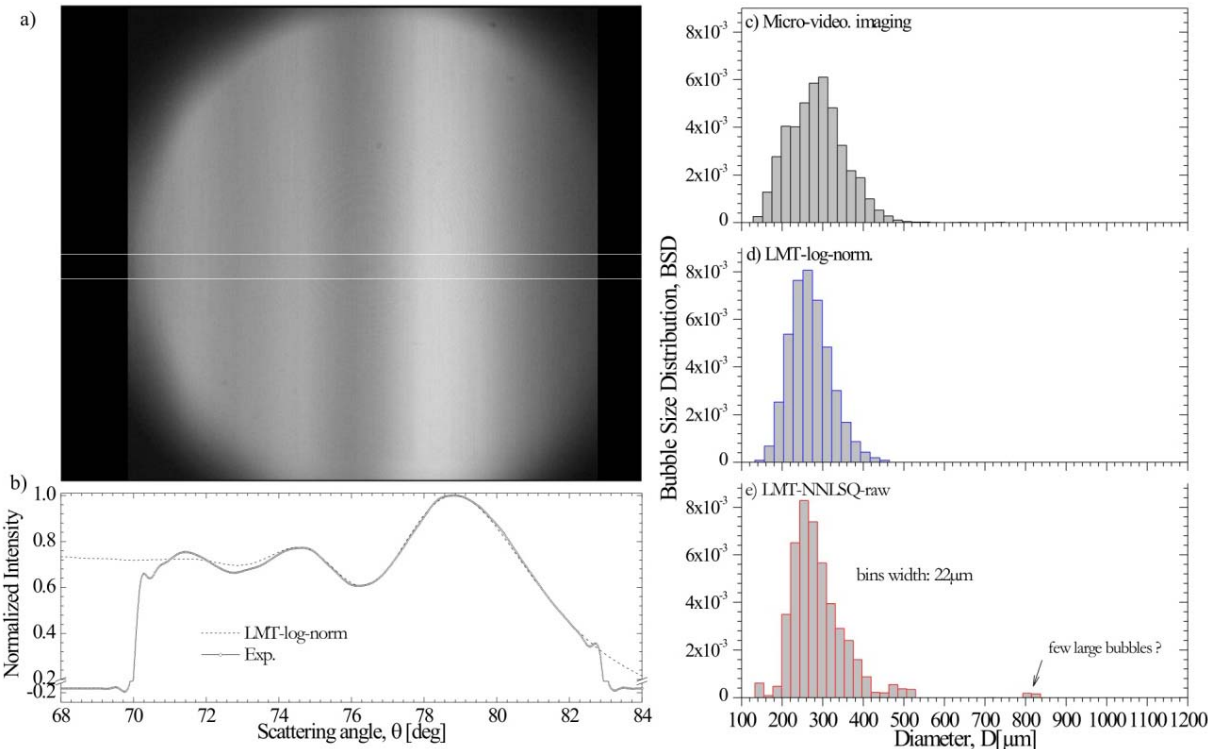

Figure 5.2 Experimental results for bubbly flows produced by a water assisted air injector: a) critical scattering pattern; b) experimental and reconstructed intensity profiles; BSD obtained with c) the micro-video imaging-system; (d-e) the CARS technique with d) the LSQ-LMT-log-norm and e) the NNLSQ-LMT as inverse methods.

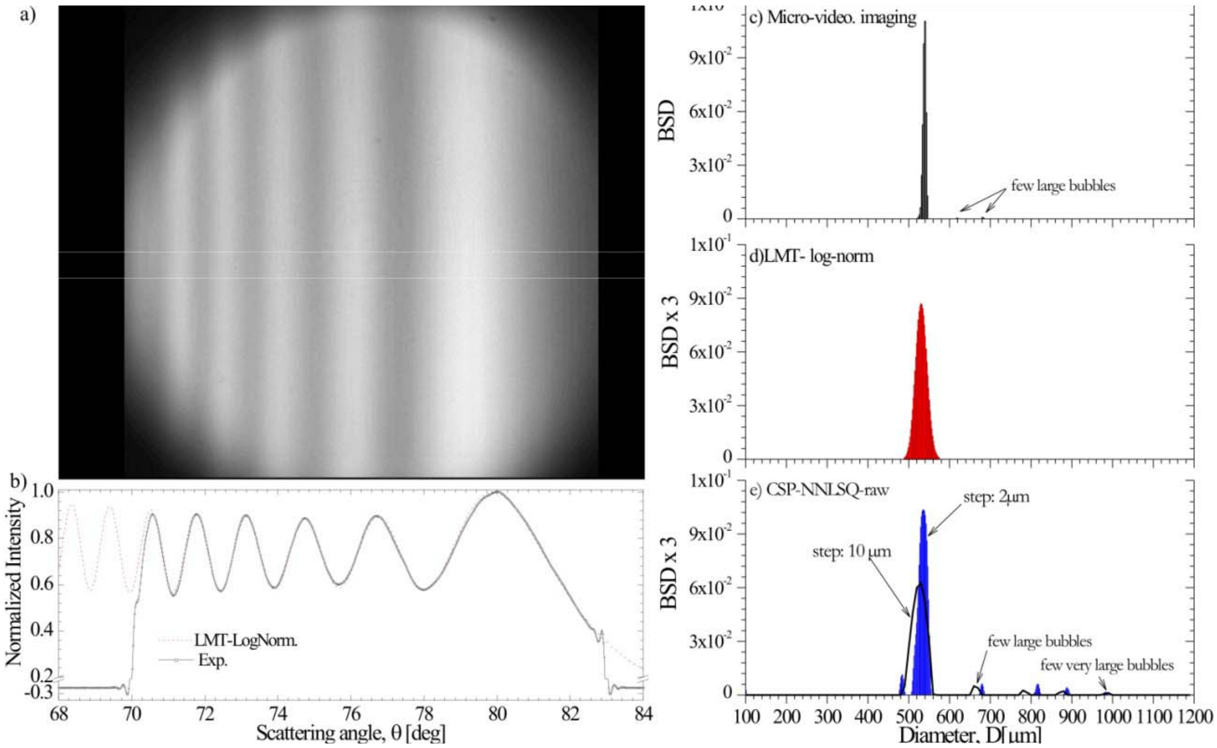

Figure 5.3 Same as Figure 5.2 but for larger bubbles, produced by the piezo-jet operating in a stable mode (for very narrow size distribution).

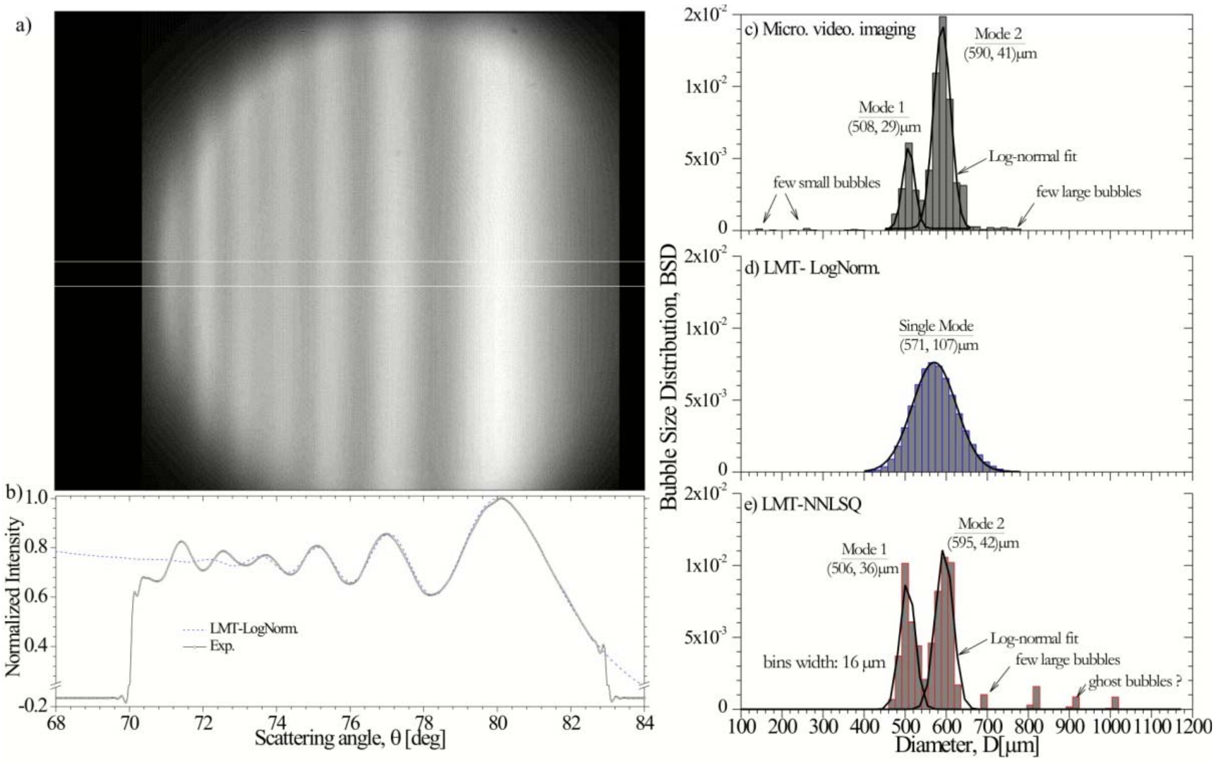

Figure 5.4 Same as Figure 5.2 but for larger bubbles produced the piezo-jet operating in a quasi-stable mode (bi-modal size distribution).

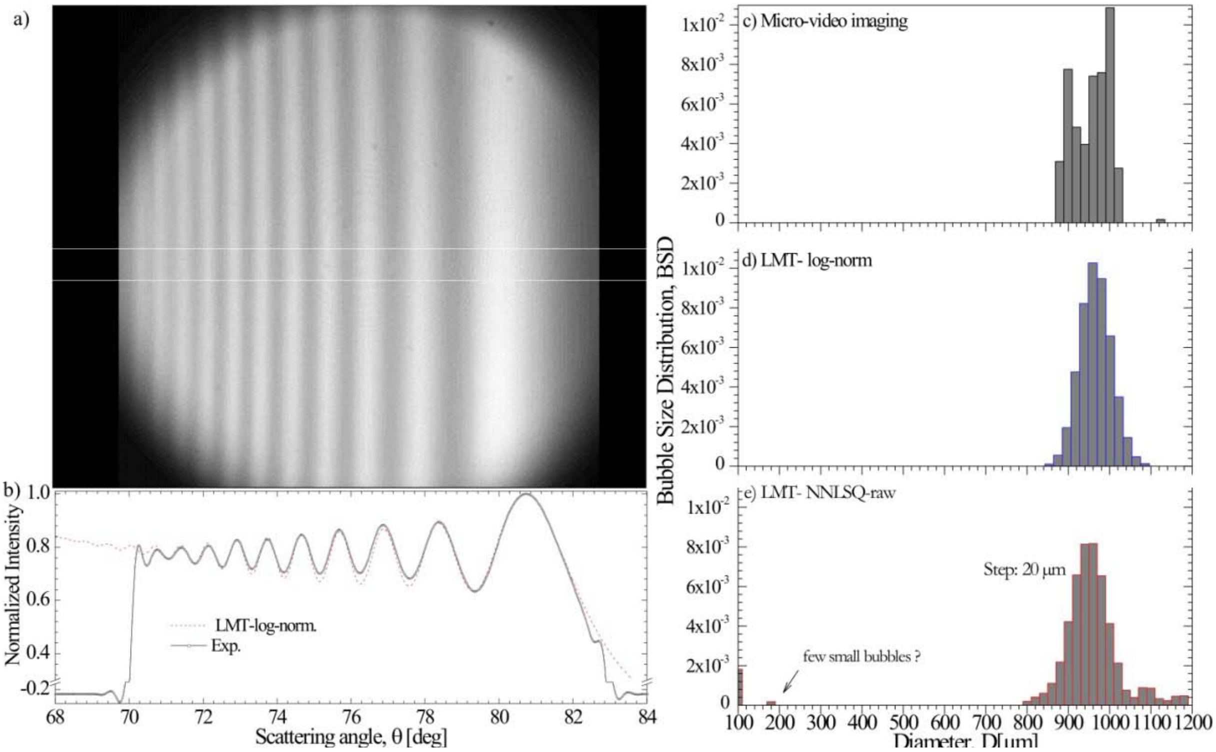

Figure 5.5 Same as Figure 5.2 but for larger bubbles produced by the piezo-jet running is an unstable mode (largest bubbles).

If positions of the two modes are in very good agreement, relative weights are not as good. On the other hand, it should be noted that the NNLSQ-LMT-raw method generates noise, or 'ghost bubbles", that induces a strong overestimation of the bubble size standard deviation (Table 5.1). The noise generated by the inversion is clearly a problem. Although it is not totally surprising as it is a general drawback when dealing with ill-posed inverse problems. This could be managed by improving the regularization scheme of the scattering matrix. For the moment, to get reliable statistics with the NNLSQ method, the BSD must be low pass filtered (NNLSQ-Filt.) prior calculating the standard deviation with Eq. (44). This filtering procedure can not correct the fact that the weight of the first mode is slightly overestimated, but it significantly improves the estimation of the standard deviation on the bubble size (see Table 5.1, Table 5.2). For this bi-modal distribution, the agreement between the CARS technique (with the NNLSQ-LMT-Filt. method) and the micro-video & Abbe refractomer measurements is better that 1 and 4% for the mean value of the diameter and standard deviation, and 0.03% for the relative refractive index. The results obtained with other inverse methods are less satisfactory. Compare to case presented in Figure 5.2 POA (0+1) gives much better estimation of the bubble cloud parameters. The latter remark explains why combined with its high computation efficiency POA is always interesting to get a first estimation of the parameters of the bubble clouds.

	$\bar{D}$ [µm]	σ_D [µm]	m [-]
Micro video / Abbe refract.	277	69	1.3345
POA (0)	275	-	1.3424
POA (0+1)	243	51	1.3432
LMT-3pts	256	49	1.3374
LMT-Log-norm.	256	49	1.3390
LMT- NNLSQ-filt.	283	55	1.3359
LMT-NNLSQ-raw	296	63	1.3359

Table 5.1 Statistics corresponding to Figure 5.2.

	$\bar{D}$ [µm]	σ_D [µm]	m [-]
Micro video / Abbe refract.	574	54	1.3345
POA (0)	491	-	1.3428
POA (0+1)	550	55	1.3393
LMT-3pts	495	50	1.3382
LMT-Log-norm.	575	55	1.3350
LMT-NNLSQ-filt.	569	56	1.3349
LMT-NNLSQ-raw	471	130	1.3349

Table 5.2 Statistics corresponding to Figure 5.4.

Figure 5.6 and Figure 5.7 compare statistics obtained simultaneously with the micro-video imaging systems and the CARS technique (mainly with the LSQ-LMT-Log. Norm inversion procedure) for $\bar{D}$ and $\sigma_D / \bar{D}$, and various air/water bubbly flows. The agreement is about 5% and ± 0.05 for these two parameters respectively. In these experiments, the bubble relative refractive index is determined also by the CARS technique. For the results presented in Figure 5.6 and Figure 5.7, the standard deviation on the measured refractive index, compared with Abbe refractometry measurements, is ±0.0015 with the LSQ-LMT-Log-Norm. inverse method and ±0.0005 with the NNLSQ- LMT-raw one.

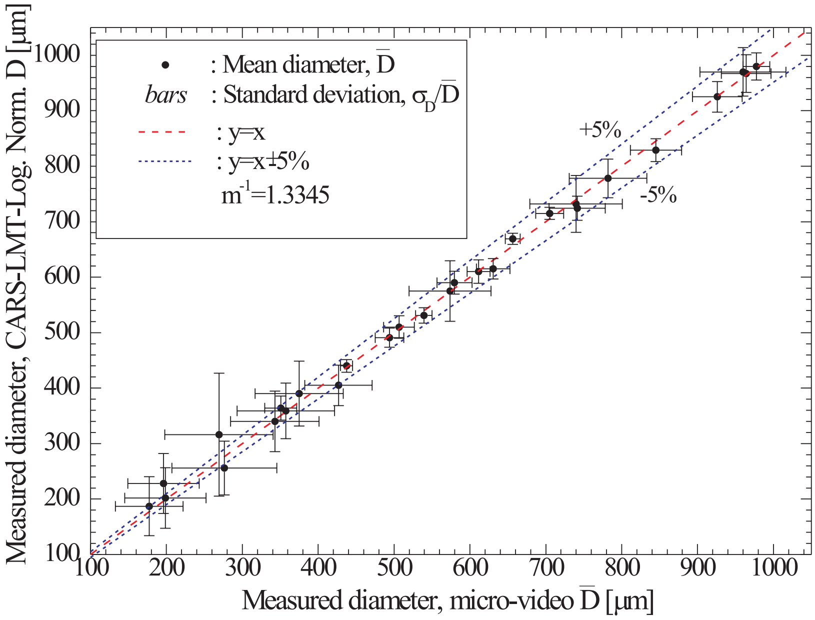

Figure 5.6 Comparison of the bubble mean diameter measured for air/water bubbly flows, with the micro-video system and the CARS (with the LSQ-LMT-Log-Norm. inverse method).

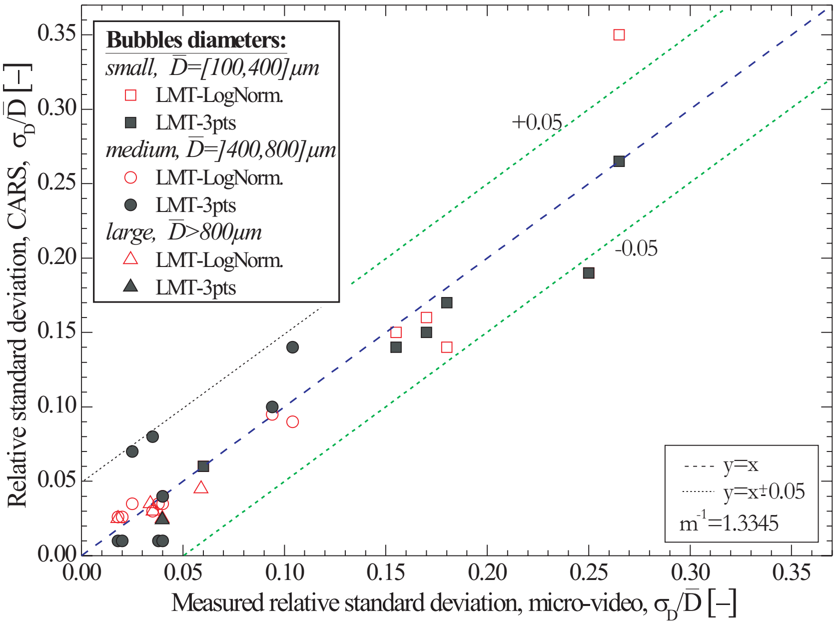

Figure 5.7 Same as Figure 5.6 but for the relative standard deviation of the bubble size, and for two different inverse methods.

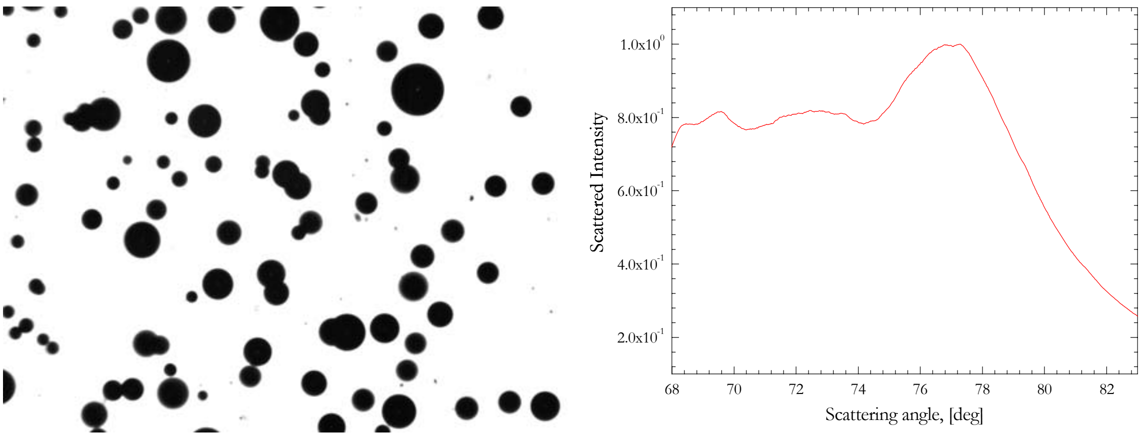

Figure 5.8 typical micro-video image and CSP for an air-water flow generated by a porous medium. (*Exp. Porus_big flow_1*).

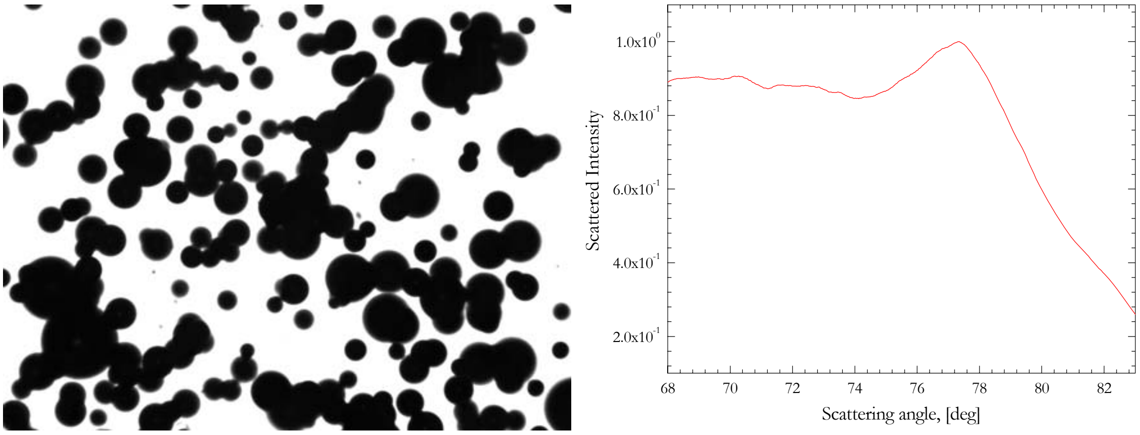

Figure 5.9 Typical micro-video image and CSP for a air-water flow generated by a porous medium (*Exp. Porus_big flow_2*).

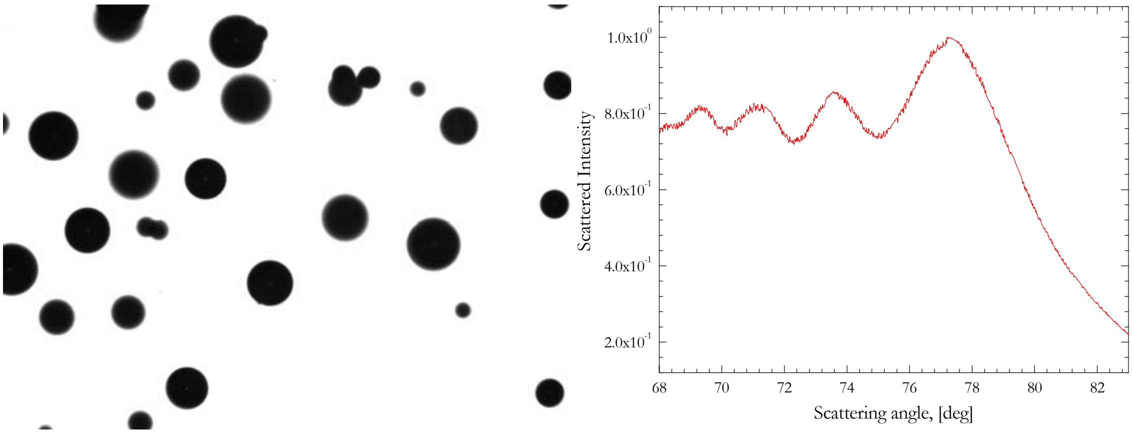

Figure 5.10 Typical micro-video image and CSP for a air-water flow generated by a porous medium *(Exp. Porus_big flow_4).*

Figure 5.8, Figure 5.9 and Figure 5.10 show typical micro-video images and the related CSP for denser air-water bubbly flows that were generated by a porous medium. The corresponding statistics are summerized in Table 5.3 (see last rows). Note that in Figure 5.9 the micro-video image contains a lot of particle images that strongly overlap. Indeed, the validation rate of our image processing method (see §4.4.3) was very low. The corresponding CSP is easily recognizable, but the visibility of higher order fringes is almost null. The latter remark is in agreement with numerical simulations (see §2.5): the contrast of CSP is dumped by the broadening of the bubble size distribution (and not with the particle number). The statistics obtain with both methods, and with the Abbe refractometer, are in rather good agreement. But it is difficult to say, except for refractive index, which method is more accurate than the other one.

Experiment	N of particles ecognized (Micro-Video)	Micro.Video /Abbe refract.			LSQ-LMT-log-norm.			LMT-3pts		
		D [um]	σ/D [-]	m [-]	D [um]	σ/D [-]	m [-]	D [um]	σ/D [-]	m [-]
Piezo_cur_alone_	185	565,0	0,010	1,3345	548,0	0,010	1,3340	507,0	0,040	1,3350
Piezo_cur_left_	55	559,0	0,010	1,3345	556,0	0,010	1,3330	576,0	0,010	1,3330
Piezo_cur_right_	11	574,0	0,015	1,3345	549,0	0,010	1,3340	542,0	0,040	1,3340
Piezo_curt_back_	117	560,0	0,010	1,3345	546,0	0,010	1,3340	518,0	0,040	1,3350
Piezo_curt_front_	219	562,0	0,010	1,3345	546,0	0,010	1,3340	576,0	0,010	1,3310
Porus_big_flow_1	37208	285,0	0,377	1,3350	280,0	0,450	1,3360	266,0	0,308	1,3390
Porus_big_flow_2	5508	308,0	0,339	1,3350	340,0	0,500	1,3320	208,0	0,290	1,3470
Porus_big_flow_4	-	411,0	0,360	1,3350	514,0	0,130	1,3320	426,0	0,114	1,3345

Table 5.3 Statistics for dense bubbly flows (centered porous medium) and the experiment with the curtain on bubbles (porous medium on the side ways of the CARS probe volume).

5.1.2 Bubbly flows with particular configurations

The CARS technique is based on the assumption that each bubble within the probe volume scatters a part of the incident beam independently from the presence of the other bubbles, see Eq. (42). This assumption means that interference effects and multiple scattering phenomena are negligible, as well as the disturbances induced by the surrounding bubbles on the incident laser beam and the scattered light. Note that this is a classical assumption made by most optical sizing methods. In this section we present results that give some physical insight about the above mentioned effects. For this purpose, bubbly flows with a special configurations were produced: twins bubbles, bubbles outside the probe volume and densely packed streams of bubbles.

5.1.2.1 Twins bubbles (interference between two close bubbles)

The CARS technique like, to our knowledge, all optical particle characterization, assumes that the scattering of all bubbles within the probe volume can be threaten as an incoherent process. This is a key underlying hypothesis used in the integral equation Eq. (42).

Under particular operating conditions, the piezo-jet injector can generates in silicon two twins water bubbles at the same time. So, there is way to study with this system the coherent interactions, multiple scattering effects, between the light scattered by both bubbles. The goal of this section is not to present a complete study but some insight about interaction effects.

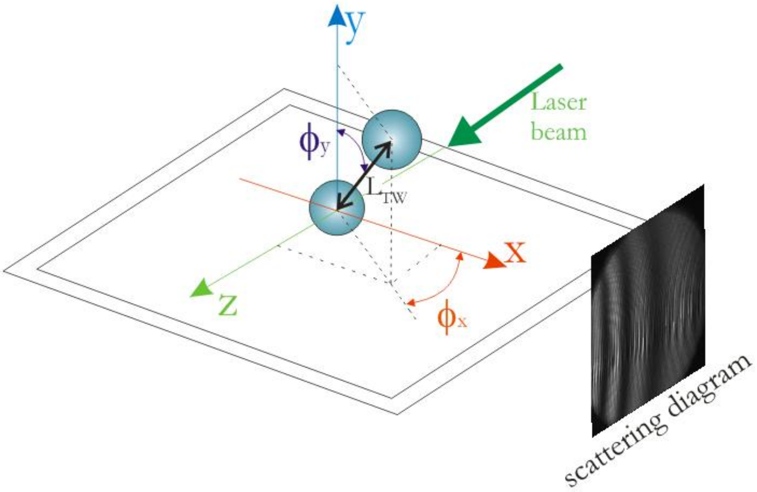

Figure 5.11 Coordinate system for the twins bubbles.

Due to hydrodynamics interactions between the two falling bubbles, they are not exactly located each other in the same way from one experiment to another one. However, by carrying many experiments and with the help of the micro-video imaging system, it is possible to trig the CARS system and record CSP patterns for specific twin bubble patterns. Figure 5.11 sketchs the twin's bubbles geometry. The micro-video imaging system gives an image of the twins bubbles in the *(yx)-plane* while the CARS system collection optics is parallel the *x-axis*. With the micro-video-imaging system we can estimate ϕ_y and L_{Tw} but not ϕ_x. So, the latter is just estimated visually. From Figure 5.12 to Figure 5.16 we present exemplifying results for different pairs of bubbles configurations with from left to right: the micro-video image, the recorded CSP and its corresponding intensity profiles, the reconstructed CSP. The size of the bubbles is about D=700 μm. The more severe interference effects are observed for the case presented in Figure 5.12: when the main axis of the twins bubbles is almost parallel to the CARS system collection optics. Indeed, in that case CSP exhibits an unusual high frequency fringes pattern which is superimposed to the low frequency (and usual) one. For the other cases, interferences effects change only the amplitude of the critical fringes. In Figure 5.15, where two bubbles with different size are very close from each other, we have a mix of both effects: high frequency fringes and reduced visibility. Figure 5.17 summarizes comparisons between the mean diameter measured with the micro-video and the CARS systems for different orientations of the twins bubbles. In most cases the CARS and micro-video system agree at better that 5%. For some cases, close to the one presented in Figure 5.12, the error is more significant. However, it must be kept in mind that even with the micro-video system errors come out when the twins bubbles are aligned along its optical collection axis (one bubble is in the shadow of the other one, so it is "non-visible") or partially aligned with it (the two images are superimposed and the imaging software fail to detect properly the two bubbles, or reject one or both of them, see next paragraph).

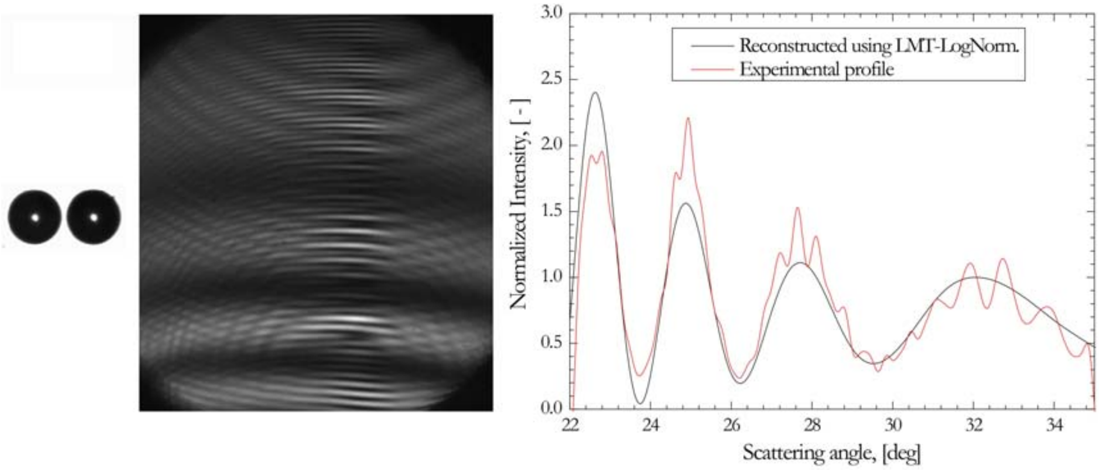

Figure 5.12 Twins water bubbles in silicon oil oriented along the CARS collection axis: $\phi_y \sim \phi_x \sim 0°$ and $L_{Tw} \approx 1.1D$ *(Exp: SiP1200_2Tw_2)*

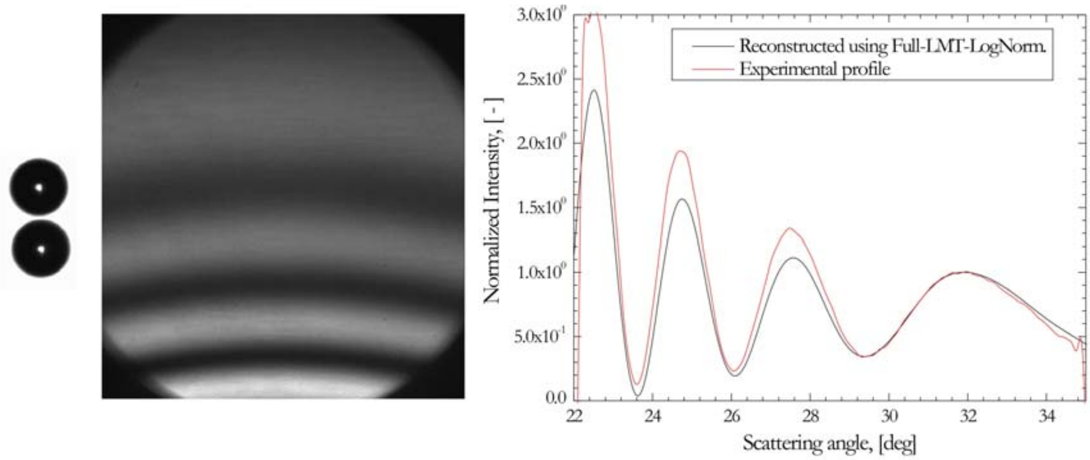

Figure 5.13 Twins water bubbles in silicon oil oriented close to the vertical axis (perpendicular to the CARS collection axis): $\phi_y \sim 5°; \phi_x \sim 0°$ and $L_{Tw} \approx 1.1D$ *(Exp. SiP1200_2Tw_6)*

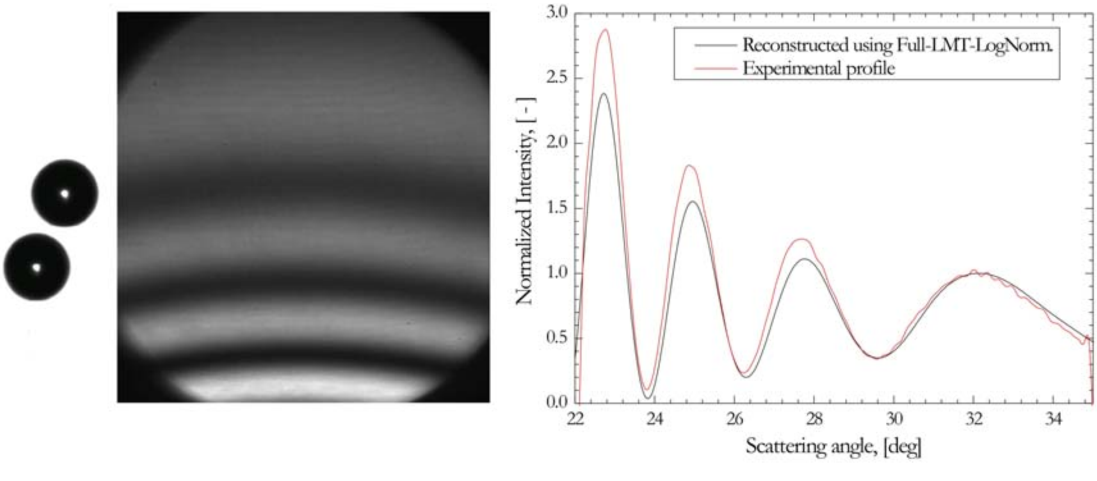

Figure 5.14 Twins water bubbles in silicon oil oriented like $\phi_y \sim 20°; \phi_x \sim -45°$ (the bubble at the top is behind the bottom one, with respect to z-axis) and $L_{Tw} \approx 1.3D$ *(Exp. SiP1200_2Tw_8)*

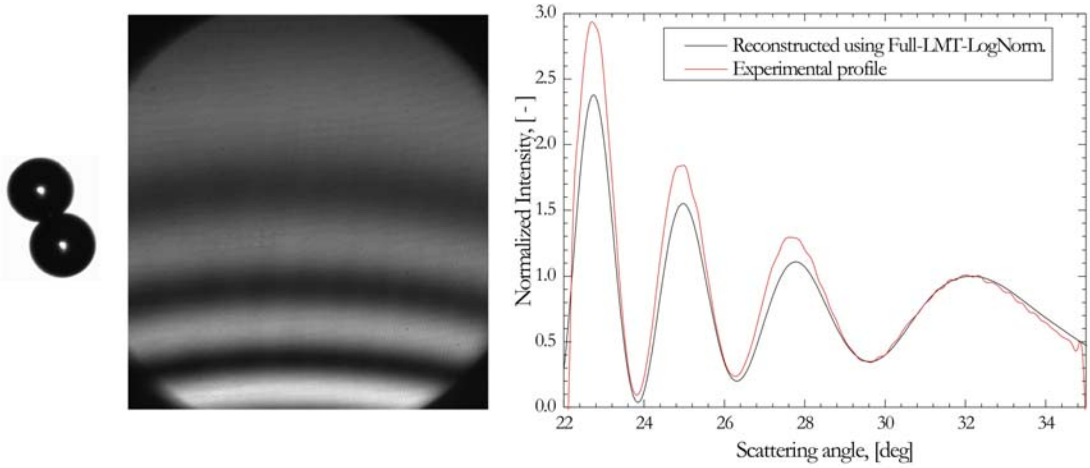

Figure 5.15 Twins water bubbles in silicon oil oriented like $\phi_y \sim -20°; \phi_x \sim 40°$ (the bubble at the top is in front of the bottom one, with respect to x-axis) and $L_{Tw} \approx 1.0D$ *(Exp. SiP1200_2Tw_9)*

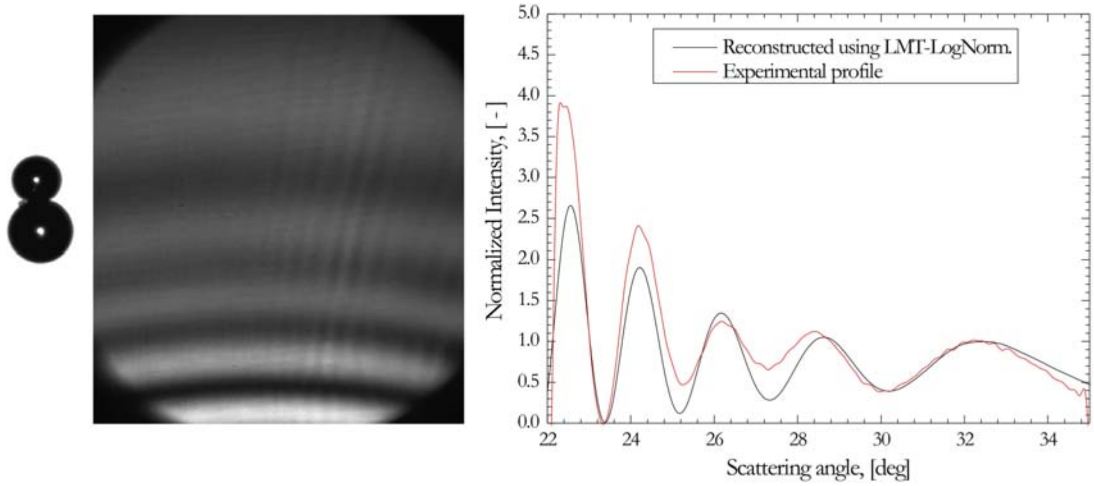

Figure 5.16 Twins water bubbles in silicon oil oriented like $\phi_y \sim -5°; \phi_x \sim 45°$ (the bubble at the top is in front of the bottom one, with respect to x-axis) and $L_{Tw} \approx 1.0(D_1 + D_2)/2$ *(Exp. SiP1200_2Tw_12)*

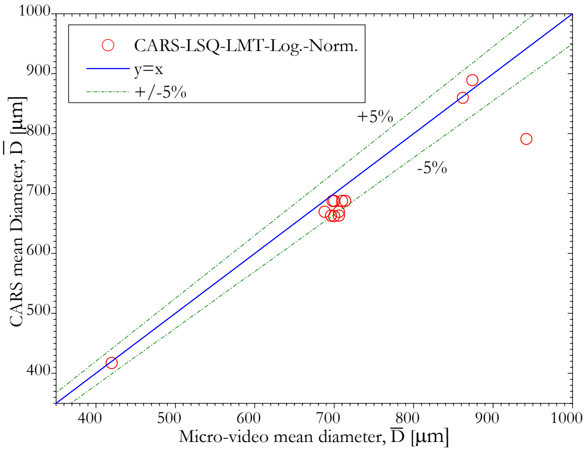

Figure 5.17 Comparison of the mean diameter measured with the micro-video and the CARS systems for different orientations of the twins water bubbles in silicon oil.

5.1.2.2 Bubbles out of the probe volume (influence of)

In the following experiment we have tried to get insight about the influence on CARS measurements of the bubbles that are outside the probe volume (i.e. surrounding bubbles). To do so, we use the piezo-jet to generate a stream of mono disperse bubbles within the probe volume. For producing surrounding bubbles we have used a long but narrow porous medium to generate a curtain of bubbles.

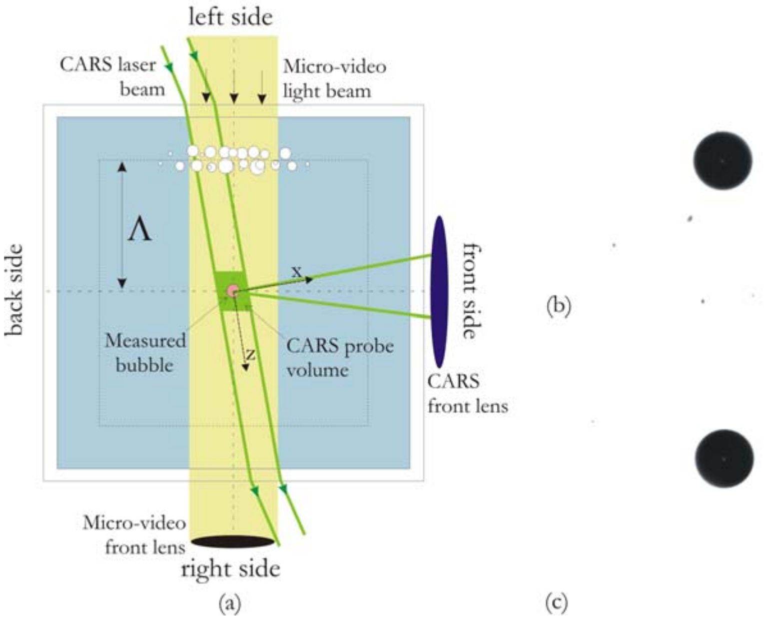

Figure 5.18 a) Schematic of the experimental setup to test the effect of bubbles outside the probe volume (i.e. in the present case it is on the “left side”); Micro-video images of monodisperse bubbles passing through CARS probe volume when the curtain of bubbles is b) on the front and c) back sides.

Four cases have been considered: the curtain of bubbles is in front of the CARS collection lens, behind the probe volume with respect to the CARS collection lens, on the left side and on the right sides, see Figure 5.18. The axis of the curtain of bubbles was kept parallel to the glass windows at a distance of about $\Lambda \sim 30-40mm$ from the probe volume center.

Figure 5.19 shows two typical images recorded with the micro-video systems when the curtain of bubbles was on the left side and, Figure 5.20, when the curtain of bubbles was on the right side. The bubble generated within the probe volume is pointed out with a red circle and an arrow. As the micro-video system was focused onto the bubble within the probe volume, the images of the surrounding bubbles are blurred (out-of-focus). Figure 5.21 shows the corresponding recorded CSP. Each subfigure corresponds to a particular position of the curtain of bubbles. Note that the CSP obtain for a single bubble, without curtain of bubbles, is supposed to be a reference. The corresponding statistical results are presented in the first five rows of Table 5.3.

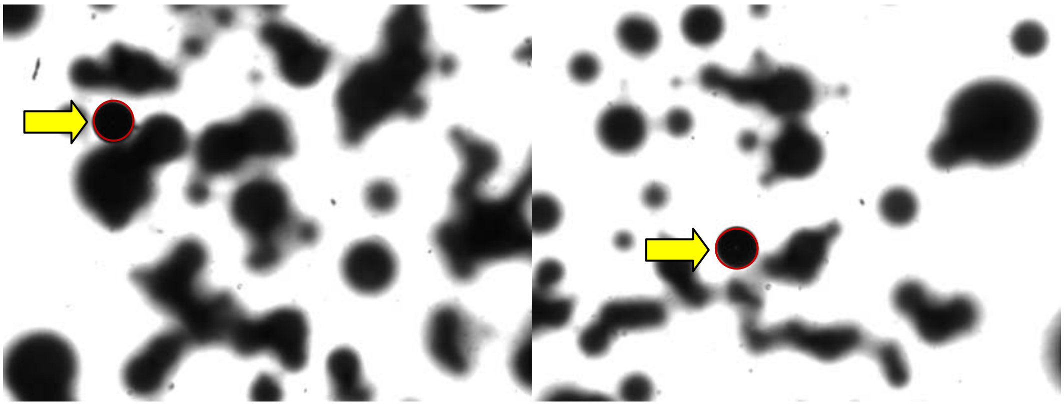

Figure 5.19 Typical micro-video images for a curtain of bubbles localized on the right side of the cell.

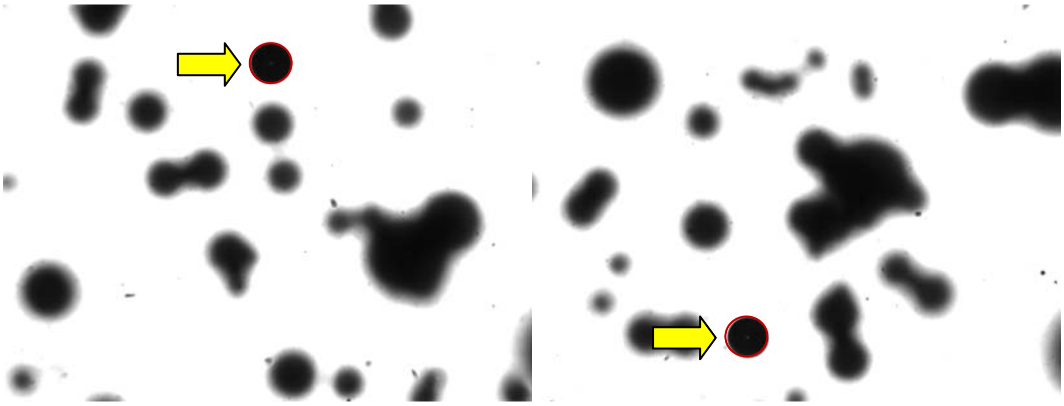

Figure 5.20 Typical micro-video images for a curtain of bubbles localized on the left side of the cell.

Looking at Figure 5.21 we may be first surprise by the weak influence of the bubble curtain on the recorder CSP. However, it can be noticed in Figure 5.21 that the right and the back side CSP are very similar and show almost the same deviation from the CSP obtained for single bubble. From this remark we can conclude that the single bubble case is probably not a true reference one. In fact we do not find any physical reason for the CSP to be sensitive to the surrounding bubbles when they are located in these two regions. The more convincing explanation is that the piezo-jet has slightly changed of operating regime during these experiments. They could be many reasons for that (noise, vibrations, temperature…), it could also be induced by the curtain of bubbles (which induces recirculation of the fluid within the experimental cell). So, we produce Figure 5.8 to compare only the most interesting cases: the left side (input beam blocked, wave front perturbed) and the front side case (scattered light attenuated, distorted), while the right side case being considered here as a reference one. Even with this simplified figure, the effects of surrounding bubbles onto the laser beam characteristics and the scattered light transmission towards the CARS system appears to be weak or, at least, difficult to detect visually. Table 5.3 which resumes the corresponding statistics tell us the same: the size and refractive index measurements obtained with the CARS technique are not really dependent on the surrounding bubbles. One additional interesting result in this table is that the micro-imaging validation count appears to be extremely sensitive to the location of the surrounding bubbles, this may be understood looking at Figure 5.19 (due to the curtain of bubbles, the image background appears to be noisy). Statistics with the micro-video system are then biased by this phenomenon too.

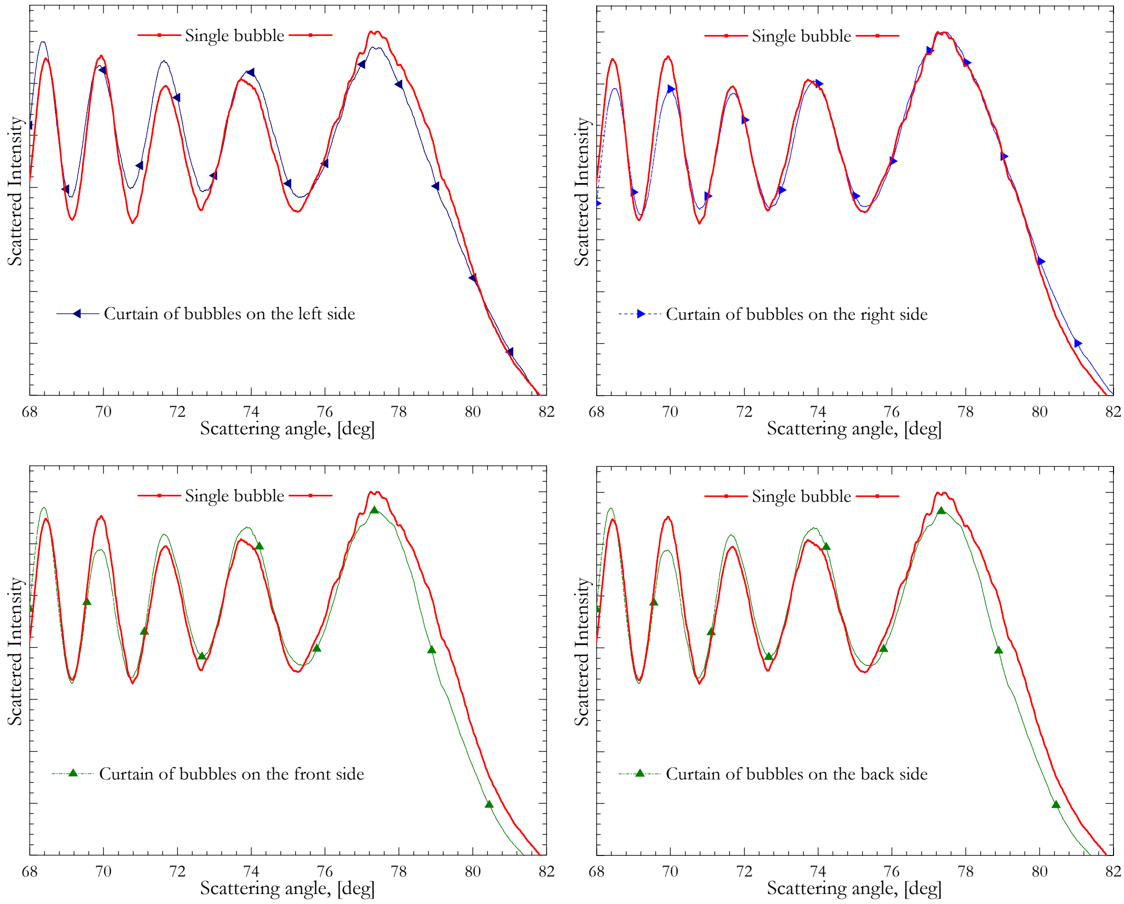

Figure 5.21 Comparison of CSP of a stream of monodisperse air-bubbles in water when a curtain of bubbles is blocking alternatively one of the four optical accesses of the experimental tank (see Figure 5.18).

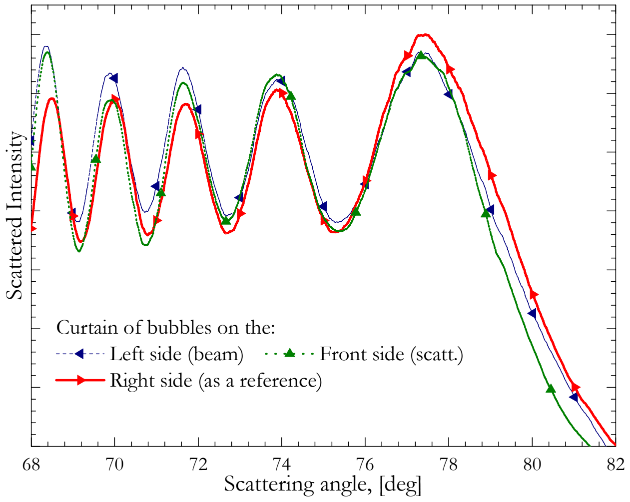

Figure 5.22 Comparison of CSP for a stream of single bubbles when a curtain of bubbles is blocking partly the incoming laser beam or the light scattered by bubbles towards the collection optics.

For a question of time, as well as technical reasons, it was not really possible to change the bubble curtain distance Λ with respect to the probe volume center. This could be an interesting study. In any case, and whatever this study has to be completed, we have shown that the CARS technique can manage complex flows and that it realizes a real local measurement.

5.1.2.3 Densely packed bubbles

Using the setup depicted in §5.1.2.1 and increasing the water flow rate it is possible to produce in silicon oil, streams of densely packet water bubbles. By doing so, we can test and illustrate the response of the CARS technique under such conditions whatever, we repeat ourselves: this technique is normally devoted to characterize dilute bubbly flows. Note that from refractive index measurements with the Abbe refractometer we have $m^{-1} \approx 1.0522$

Figure 5.23 shows a micro-video image of a stream of mono disperse bubbles that are not well aligned, the corresponding CSP (integrated over 1 second, i.e. hundred of the presented bubbles), the extracted intensity profile and the reconstructed one (with the LSQ-LMT-Log. Norm. inverse method). These results are rather similar to the one obtained for twins bubbles (see Figure 5.14 and Figure 5.15).

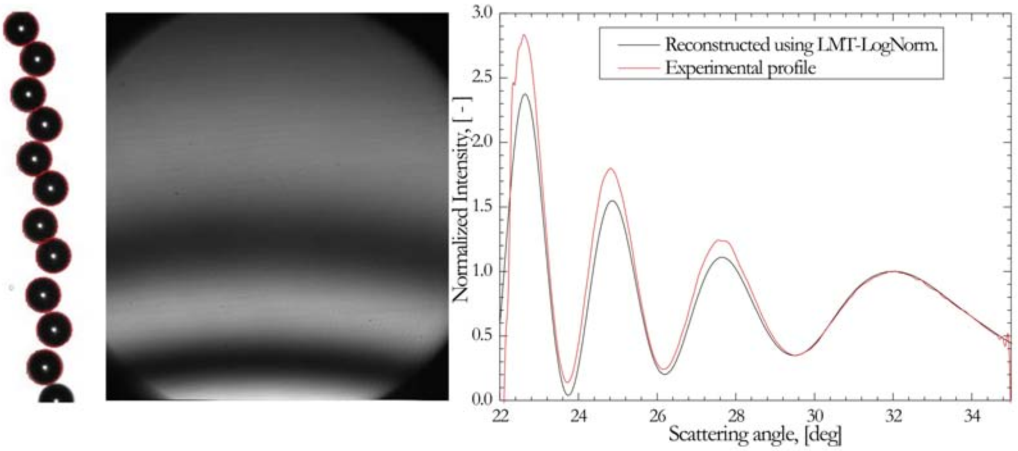

Figure 5.23 Stream of water droplets (i.e. optical bubbles) in silicon oil, cooresponding CSP with the reconstructed profile.

Figure 5.24 show different results and analyses for a stream of densely packed water bubbles in silicon. Visually, the stream seems to be composed of bubbles with a bi-modal size distribution: large bubbles and intermediate to small size bubbles. All bubbles within the micro-video image are not validated by the imaging system (i.e. their image is not surrounded by a red circle). The non validated bubbles are usually the one that seems to be behind the validated one. It is additional evidence that statistics obtained with the video imaging system are "not totally reliable. For the CARS system, it is not trivial to infer this particular bubbly flow arrangement from the observation of the corresponding CSP. The fact is that both the LSQ (with LMT and a single mode distribution) and the NNLSQ (with LMT) inverse methods fail to reconstruct a satisfactory CSP intensity profile.

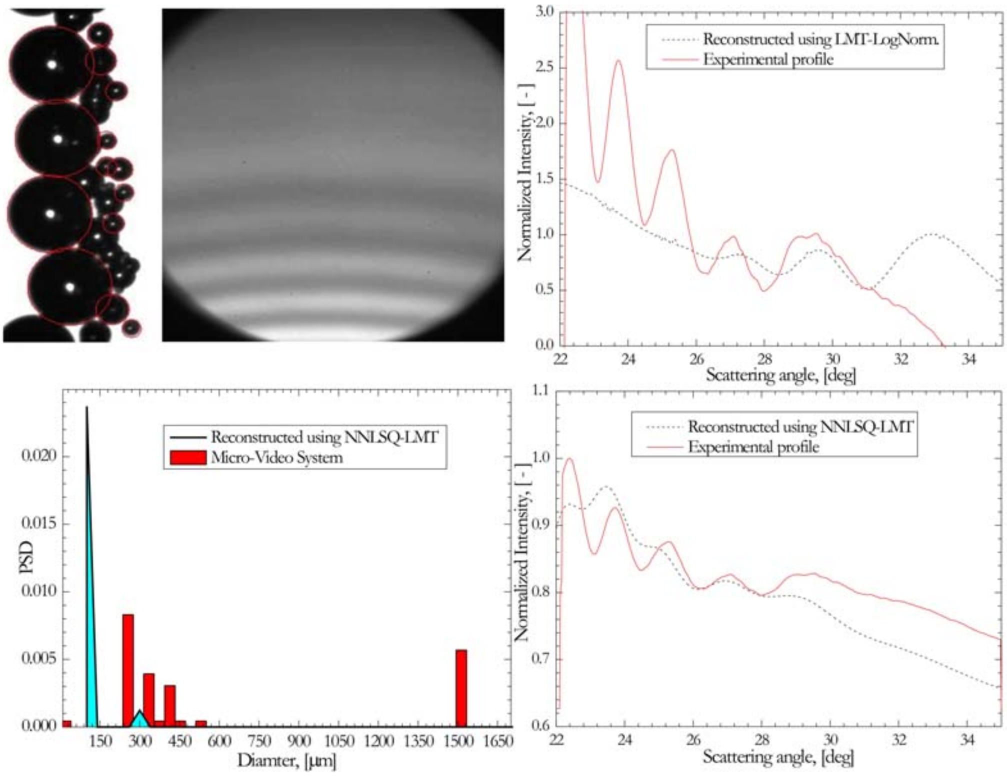

Figure 5.24 Stream of densely packed water droplets in silicon oil, corresponding CSP with the intensity profiles reconstructed with two inverse methods (NNLSQ-LMT and LSQ-LMT), the size distributions measured with NNLSQ-LMT and the micro-video system. *(Exp. SiWP_8_)*

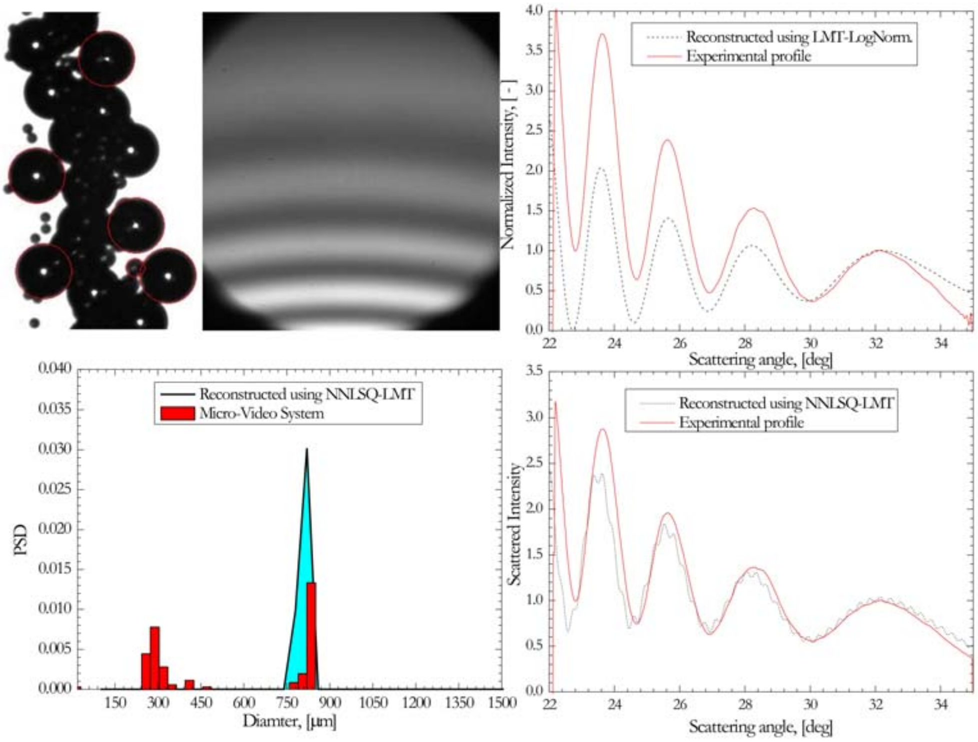

Figure 5.25 Same parameters as in Figure 5.24 but a denser flow *(Exp. SiWP_4_)*.

Indeed, looking at the bubble size histogram it is clear that the NNLSQ method predicts a two mode BSD but, unfortunately, the position of the two modes are not really correct in the sense that the larger bubbles $\left(D \approx 1.5mm\right)$ are not “detected”.

Dye water drop	Micro.Video			LMT-log-norm.		
	D [μm]	σ/D [-]	m^{-1} [-]	D [μm]	σ/D [-]	m^{-1} [-]
SiP1200_2Tw_13_ *Bi-modal distribution*	280.0 750.0	0.05 0.02	1,0525	715.0	0.001	1.0525
SiP1200_2Tw_14_ 3-mod distribution	280.0 580.0 720.0	0.002 0.002 0.002	1,0525	610.0	0.150	1.0520
SiP1200_2Tw_15_	430.0	0.180	1,0525	440.0	0.150	1.0510
SiP1200_2Tw_16_	470.0	0.160	1,0525	590.0	0.150	1.0505
SiWP_1_ Bi-modal distribution	220.0 720.0	0.03 0.02	1,0525	720.0	0.001	1.0515
SiWP_4_ Bi-modal distribution	320.0 820.0	0.15 0.01	1,0525	850.0	0.001	1.0520
SiWP_5_ Bi-modal distribution	420.0 1120.0	0.150 0.001	1,0525	1090.0	0.001	1.0520
SiWP_8_ Bi-modal distribution	320.0 1200.0	0.200 0.001	1,0525	1180.0	0.150	1.0520
SiWP_9_ Bi-modal distribution	370.0 1200.0	0.300 0.080	1,0525	1390.0	0.001	1,0525

Table 5.4 Tabuled data for experiments with densely packed water bubbles in silicon oil.

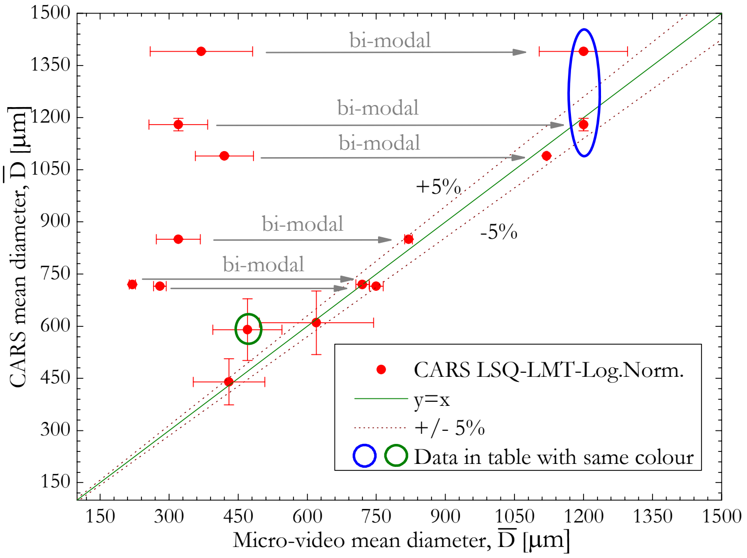

Figure 5.26 Results of LMT-Log. Norm. inverse method for densly packed bubbly flows. Results in color circles corresponds to the one with the same colour in Table 5.4

If we use the POA (p=0) with $\theta_1 \approx 29.31°$, $\theta_1 \approx 28.04°$, the CARS technique gives $m^{-1} \approx 1.0394$ and $\bar{D} = 0.385mm.$ This refractive index is in good agreement with the expected one. For the diameter, it corresponds to the main mode of the size distribution measured with the micro-video imaging system. In the case presented in Figure 5.25 the BSD obtain with the NNLSQ method fits better with the one given by the micro-video imaging analysis, at least for the larger mode. The presence of high frequency oscillations in CSP intensity profile indicates that the bubbly flow is rather mono-disperse or, that there is interference effects between the bubbles within the probe volume. Note that the mode corresponding to the smaller bubbles is not detected.

Table 5.4 and Figure 5.26 displays the results obtained with the LMT-Log.Norm. and micro-video imaging technique. The color coding of the data in the same in the table and the figure. We can see that for densely packed bubbles, with a multimodal distribution, the NNLSQ-LMT method gives usually the mode corresponding to the biggest diameter with accuracy about 5%. This can be understood in the sense that large particles (compared to the wavelength) scatter more light that the smaller one.

5.2 Relative refractive index and absorption measurements

With the CARS technique the measurement of the bubble clouds relative refractive index is possible. This is a quite unique feature when compared to other optical sizing methods. We are speaking about a relative refractive index, so that it means that CARS could be able to probe at the same time the particle composition and the surrounding medium one. Obviously, the measurement of the refractive index of particles is only interesting if they are not of a gaseous type as, in this case, changes in refractive index would be too small to be measured. For liquid bubbles (e.g. aqueous droplets in oil) the measurement of their refractive index could be a way to characterize their composition and to study coalescence effects for instance (e.g. pure water / water-ethanol droplets in oil). For the surrounding medium the change in refractive index could be a way to detect changes in composition, temperature or pressure. But, like the rainbow or the Fraunhofer diffraction, the CARS technique would not work if there is refractive index gradient within the surrounding medium. The reason for that is that the incident beam as well as the scattered waves usually not propagate straightly in such medium. In this section we will consider the two cases: changes of the bubble composition and afterwards, changes in the surrounding medium composition.

Let first recall some basic properties of refractive index. The refractive index is a complex number, $\tilde{m} = m + i\,k$. Its real part m quantify the light velocity in the medium with respect to its velocity in vacuum, $m = c_0 / c \geq 1$. Its imaginary part $k \geq 0$ quantify the medium absorption. It is usual to introduce the absorption constant $K = 4\pi km / \lambda_0$ as, according to the Beer-Lambert law, the absorption *1-T* of a light beam travelling over a distance L in an absorbing medium is just:

$$1 - T = I / I_0 = \exp(-KL) \tag{97}$$

where *T* if the beam transmission.

Indeed both the real and the imaginary part of refractive index are wavelength dependent with $\tilde{m}(\lambda_0)=m(\lambda_0)+ik(\lambda_0)$. $\tilde{m}(\lambda)$ is the dispersion equation of the medium. For some particular transparent medium, there exists empirical relationships between the real part of the refractive index and the wavelength. Sellmeier and Cauchy's have derived for instance a general expression for modeling dispersion:

$$m^2(\lambda)=1+\frac{B_1\lambda^2}{\lambda^2-C_1}+\frac{B_2\lambda^2}{\lambda^2-C_2}+\frac{B_3\lambda^2}{\lambda^2-C_3}\cdots\frac{B_n\lambda^2}{\lambda^2-C_n} \tag{98}$$

where B_n and C_n are constants which are characteristic from the material. Unfortunately, we cannot find in the literature values of these parameters for all materials. One of the reasons for that is that Eq. (98) works well for glasses, crystals… it does work too much for organic material, and liquids. Clearly, the determination of the refractive index of particles is a common problem for all optical sizing techniques. Fortunately in our case, we are working mainly with liquids. So in what follows the refractive index of all used liquids was controlled with an Abbe-Refractometer. It is interesting to recall here that both the CARS technique and the Abbe refractometry are based on the detection of the total reflection angle.

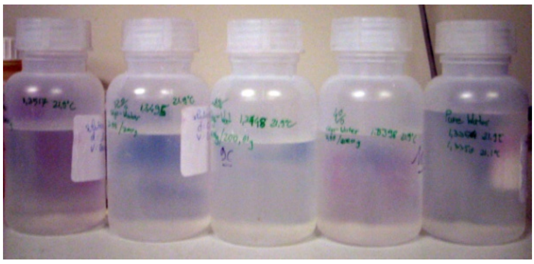

Figure 5.27 Image of prepared water/glycerin solutions

	Water – Glycerin mass mixture				
Mixture [%]	0.00	4.00	8.02	12.00	14.01
m^{-1} λ_0=532nm	1.3354	1.3398	1.3448	1.3495	1.3517
m^{-1} λ_0=589nm	1.33303	1.33762	1.34238	1.34729	1.34980

Table 5.5 Refractive index for different water-glyceryn mass fractions, with λ_0=532nm at T =21.9°C and for λ_0=589nm at T = 20.0°C

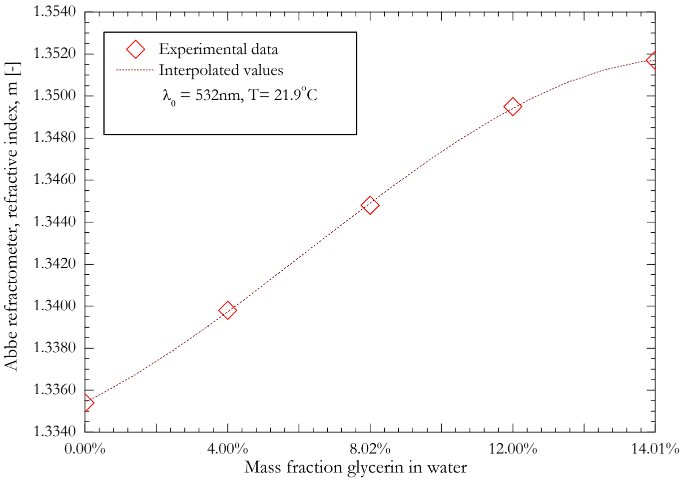

Figure 5.28 Refractive index of a water-glycerin solution versus the mass fraction of glycerin

5.2.1 Refractive index of bubbles

To test bubbles refractive index measurements with the CARS technique, bubbly flows of water-glycerin droplets in a silicon oil (from Clearco) were produced. The latter has a low refractive index $(m=1.4042 \text{ at } \lambda=532nm)$ and a low viscosity (20 cSt) at ambient temperature. Note that the density of these droplets (≈ 1.0) is larger than the one of the silicon oil (≈ 0.953). Indeed they are bubbles from the optical point of view but droplets from the mechanical one. To change bubbles refractive index we prepare water-glycerin solutions of different mass-fractions, see Figure 5.27, Figure 5.28 and Table 5.5. A mentioned above the refractive index of the different solutions was controlled with an Abbe refractometer. For this purpose we sample with an optical fiber a part of the light from the YAG-laser of the CARS system to light a liquid sample within the Abbe refractometer.

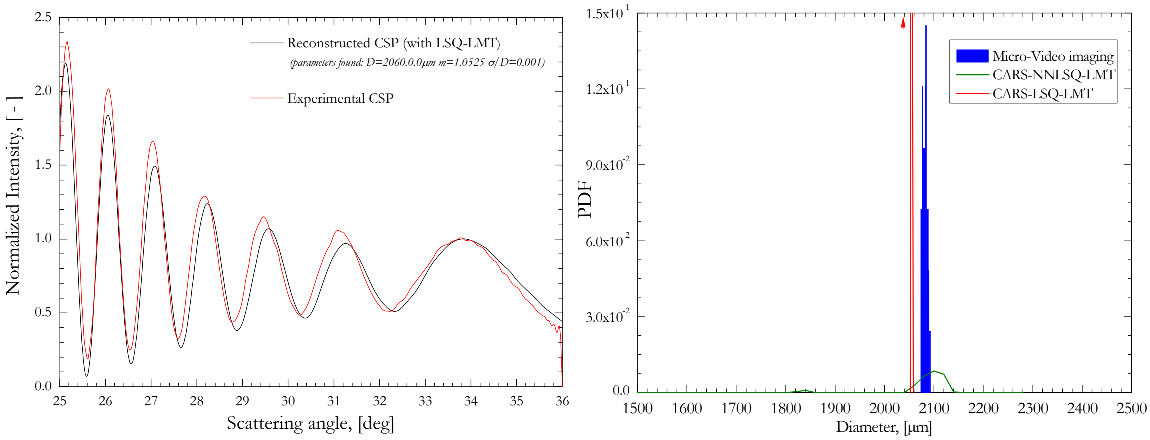

Figure 5.29 Typicall results for pure water bubbles with, of the left, the recorded CSP pattern and the reconstructed one and, on the right, bubble size distributions measured with the CARS and the micro-vido imaging systems.

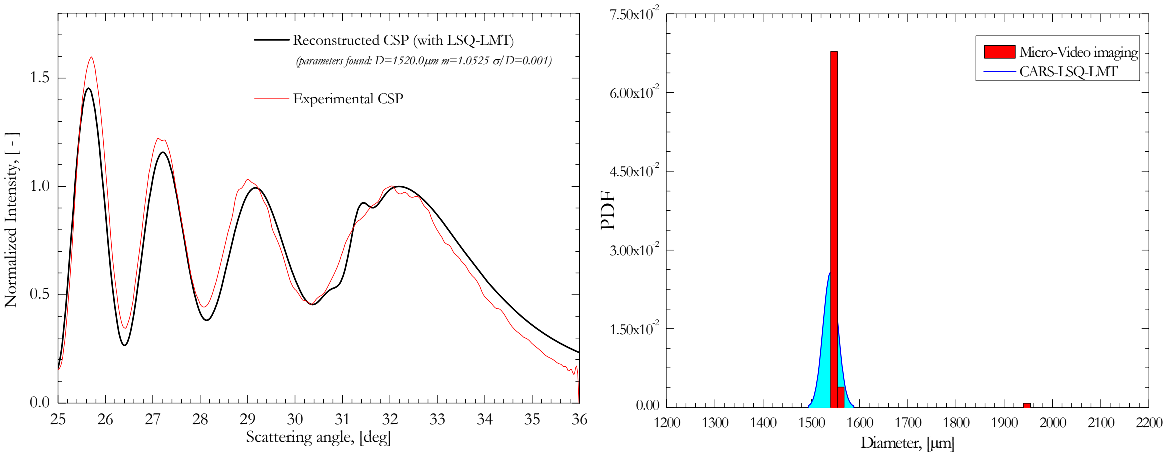

Figure 5.30 Like Figure 5.29 but for water-glycerin bubbles containing 4% of glycerin in mass.

To produce water-glycerin bubbly flows we use the piezo-jet in the reverse direction as the water-glycerin bubbles sink in silicon oil. Figure 5.29 and Figure 5.30 show for rather mono disperses bubbles, respectively: a typical experimental CSP pattern and the reconstructed one, the size distributions measured with the CARS and micro-video imaging techniques. With this silicon oil/water-glycerin experiment, we did not succeed to produce really polydisperse as well as small bubbles (by increasing the water-glycerin flow rate we were just able to produce larger and densely packed bubbles).

Figure 5.31 a) compares the mean diameter measured with the CARS and the micro-video imaging techniques for droplets containing different mass fractions of glycerin (0-12% in mass). Figure 5.31 b) compares refractive indices measured by the CARS (on sinking bubbles) and the Abbe refractometer techniques (on sample solutions). The next Table summarize all data obtain during the present test. As it can be easily remark, the measurements obtained with the CARS techniques, size and refractive index, are in very good to the "reference" techniques.

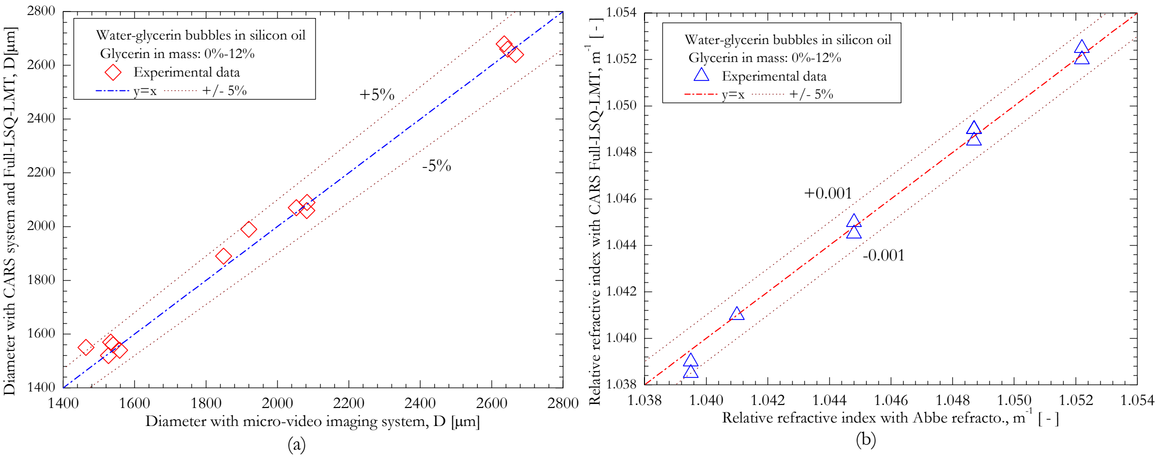

(a) (b)

Figure 5.31 Comparisons of the statistics obtained on water-glycerin droplets with the micro-video imaging system (mean diameter) and Abbe refractometry measurements (refractive index).

Solution	m^{-1} of glycerin Abbe Refract.	m^{-1} (m of silicon 1.4049)	Micro.Video			LMT-log-norm.		
[%]			D [µm]	σ/D [-]	m^{-1} [-]	D [µm]	σ/D[-]	m^{-1} [-]
0.00%	1.3354	1,0522	1527,0	0,001	1,0522	1520,0	0,001	1,0525
0.00%	1.3354	1,0522	2082,0	0,001	1,0522	2060,0	0,001	1,0525
0.00%	1.3354	1,0522	2635,0	0,001	1,0522	2680,0	0,001	1,0520
4.00%	1.3398	1,0487	1558,0	0,001	1,0487	1540,0	0,001	1,0490
4.00%	1.3398	1,0487	1849,0	0,001	1,0487	1890,0	0,030	1,0485
4.00%	1.3398	1,0487	2667,0	0,001	1,0487	2640,0	0,001	1,0490
8.02%	1.3448	1,0448	1540,0	0,001	1,0448	1560,0	0,001	1,0450
8.02%	1.3448	1,0448	1920,0	0,001	1,0448	1990,0	0,001	1,0445
8.02%	1.3448	1,0448	2645,0	0,001	1,0448	2660,0	0,001	1,0445
12.00%	1.3495	1,0410	1533,0	0,001	1,0410	1570,0	0,001	1,0410
12.00%	1.3495	1,0410	2053,0	0,001	1,0410	2070,0	0,010	1,0410
14.01%	1.3517	1,0395	1464,0	0,001	1,0395	1550,0	0,001	1,0385
14.01%	1.3517	1,0395	2083,0	0,001	1,0395	2090,0	0,001	1,0390

Table 5.6 Tabuled data for experiments with water-glycerin bubbles in silicon oil.

5.2.2 Refractive index of the surrounding medium

The CARS was not initially thought as a technique that can measure the refractive index of the surrounding medium. But, at least, it was thought to be necessary to study the effect of a change of this parameter on bubbles size and absolute refractive measurements. Indeed, each time the refractive index of the surrounding medium changes, it should be necessary to recalibrate the system (with the goniometer procedure). If true, this would be a severe drawback of this new optical sizing method.

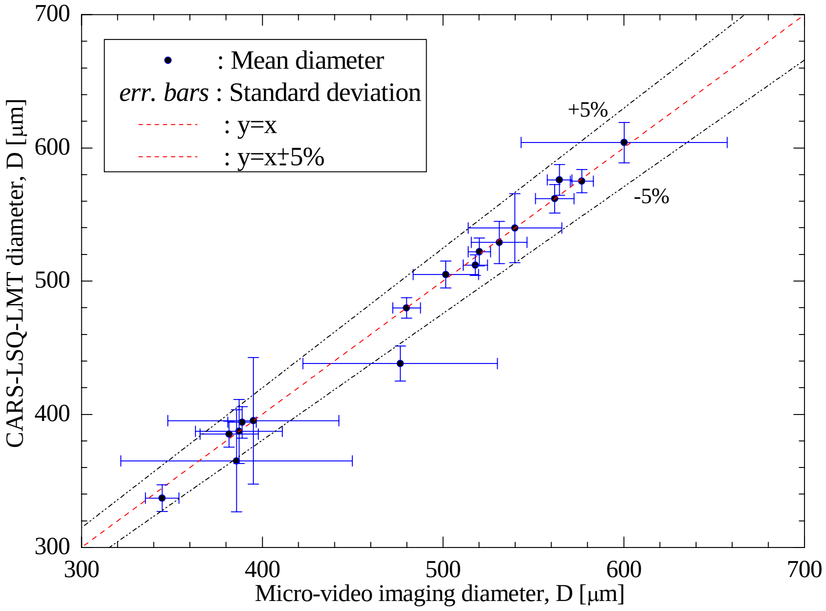

Figure 5.32 Comparison of the mean size measured with the micro video and the CARS (without reclalibration) systems, when the refractive index of the surrounding medium is changing from 1.335 to 1.355

Indeed, the recalibration is not strictly necessary. To demonstrate this, the piezo-jet is used to produce air bubbles in different water-ethanol solutions. Figure 5.32 and Table 5.6 shows statistics obtained for mass fractions in ethanol increasing from 0 up to 40%, giving a relative refractive index ranging from $m^{-1}=1.3345$ to $m^{-1}=1.3555$. Figure 5.32 compares the mean diameters measured with two inverse methods, while Figure 5.33 shows the relative refractive index measurements obtained with the NNLSQ-LMT method. Table 5.7 summarized all results. CARS and Abbe refractometry measurements are in good agreement. The size measurements seem almost non-sensitive to changes in the liquid composition. Refractive index measurements with CARS, on rising bubbles, are better than ± 0.002. In fact, the standard deviation between CARS and Abbe refractometry measurements is equal to ± 0.0002. So that CARS can estimate the water/ethanol concentration at better 4% (i.e. 0.4% when considering the global standard deviation). From these results it is clear that for most applications requiring bubbles size characterization, the recalibration of the CARS system would be not necessary for similar conditions.

Figure 5.33 shows the results obtained for the measurement of the refractive index of water-ethanol solutions: with CARS (from rising air bubbles' relative index, without recalibration of the system), and with the Abbe refractometer (onto a liquid sample). The results of the CARS technique fit rather well the measurements obtained with the Abbe refractometer whatever, CARS underestimates continuously the relative refractive index (i.e. the mass fraction in ethanol is overestimated of 4% around 25% in mass).

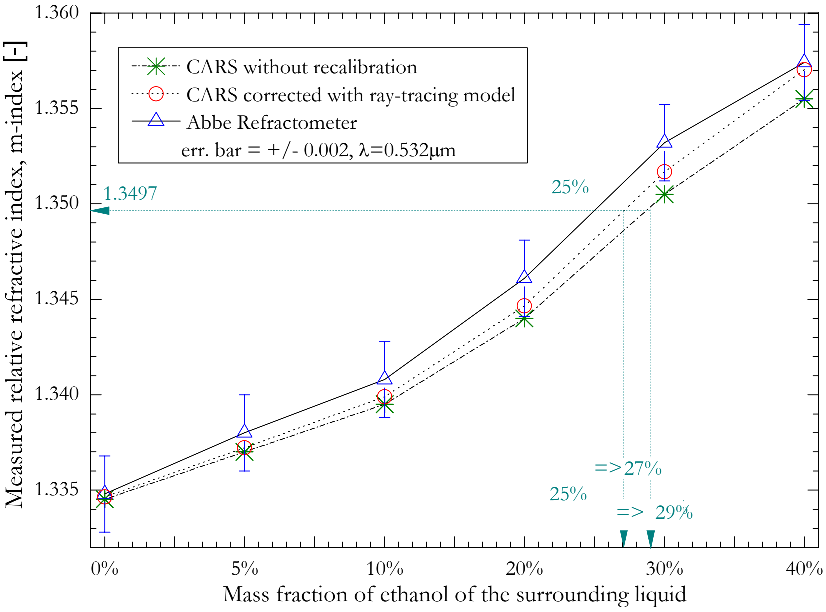

Figure 5.33 Comparison of the refractive index measured by the Abbe refractometer (on a liquid sample) and with the CARS (on rising bubbles and without reclalibration) systems, when the refractive index of the surrounding medium is changing from 1.335 to 1.355

Experiment	Micro.Video /Abbe refract.			LMT-log-norm.			LMT-3pts			POA (p=0)	
	D [μm]	σ [–]	m^{-1} [-]	D [μm]	σ [–]	m^{-1} [-]	D [μm]	σ [–]	m^{-1} [-]	D [μm]	m^{-1} [-]
Eta_0_v_200_10	344.65	0.027	1.33453	337	0.030	1.3350	351	0.010	1.3340	355.4	1.3381
Eta_0_v_210_10	476.38	0.113	1.33453	438	0.030	1.3360	390	0.070	1.3390	392.4	1.3433
Eta_0_v_220_10	517.86	0.013	1.33453	512	0.015	1.3350	545	0.040	1.3333	528.5	1.3372
Eta_5_v_200_10	388.81	0.020	1.3375	394	0.030	1.3375	373	0.020	1.3390	383.8	1.3421
Eta_5_v_210_10	520.11	0.012	1.3375	522	0.020	1.3370	545	0.030	1.3360	537.4	1.3398
Eta_5_v_220_10	564.47	0.012	1.3375	576	0.020	1.3360	579	0.060	1.3360	602.1	1.3387
Eta_10_v_200_10	381.73	0.042	1.3395	385	0.025	1.3395	377	0.010	1.3400	389.4	1.3433
Eta_10_v_210_10	501.52	0.036	1.3395	505	0.020	1.3390	521	0.040	1.3380	526.1	1.3417
Eta_10_v_220_10	576.79	0.011	1.3395	575	0.015	1.3395	558	0.050	1.3400	562.5	1.3433
Eta_20_v_200_10	385.81	0.166	1,3440	365	0.105	1.3455	400	0.120	1.3430	413.6	1.3469
Eta_20_v_210_10	531.11	0.029	1,3440	529	0.030	1.3445	564	0.060	1.3430	492.7	1.3497
Eta_20_v_220_10	600.20	0.095	1,3440	604	0.025	1.3445	579	0.130	1.3430	541	1.3503
Eta_30_v_200_10	395.09	0.120	1.3505	347	0.075	1.3500	342	0.128	1.3520	379.0	1.3573
Eta_30_v_210_10	539.83	0.048	1.3505	546	0.045	1.3505	440	0.092	1.3525	480.5	1.3573
Eta_40_v_200_10	387.12	0.062	1.3555	391	0.025	1.3550	366	0.084	1.3545	347.5	1.3638
Eta_40_v_210_10	479.87	0.016	1.3555	482	0.020	1.3550	440	0.078	1.3545	473.8	1.3596
Eta_40_v_220_10	561.89	0.019	1.3555	563	0.025	1.3550	518	0.080	1.3545	538.6	1.3601

Table 5.7 For different air bubbles/water-ethanol compositions, comparison between the measured mean sizes, standard deviations and refractive indices.

This effect is due to refraction effects at the wall that are not taken into account. In the Annex of this manuscript, we present briefly a simple model we have developed to take partly account the latter effects. CARS results corrected with this model are also shown in Figure 5.33. This model clearly contributes to decrease the small discrepancy between CARS and Abbe refractometer measurements (i.e. the mass fraction in ethanol is now only overestimated of 2% around 25% in mass). This correction is not perfect but however the resolution reached can be sufficient for some applications.

5.2.3 Effects of bubbles absorption (imaginary refractive index)

5.2.3.1 Background and setup

As the scattering of a bubble near the critical angle is dominated by a diffraction process of the "reflected" rays, we may assume that CSP should not be too sensitive to the bubble absorption. Indeed, as already suggested by Figure 2.5, the things are not so simple. The behavior of CSP regarding to bubble absorption may be somewhat understood from Figure 5.34. This figure presents simulations for absorbing bubbles (for water-ink droplets in silicon oil, with different imaginary part k). For this bubble size, there is no significant absorption effects when $k \le 10^{-4}$: the CSP are characterized by low and high frequency fringes. For k increasing from $\approx 10^{-4}$ to $\approx 5\ 10^{-2}$ the amplitude of the high frequency fringes is more and more dumped so that they rapidly disappear, the large fringes do the same but their dumping rate is much smaller. For huge absorptions, the scattering diagrams are totally flat in the near-critical scattering angle region.

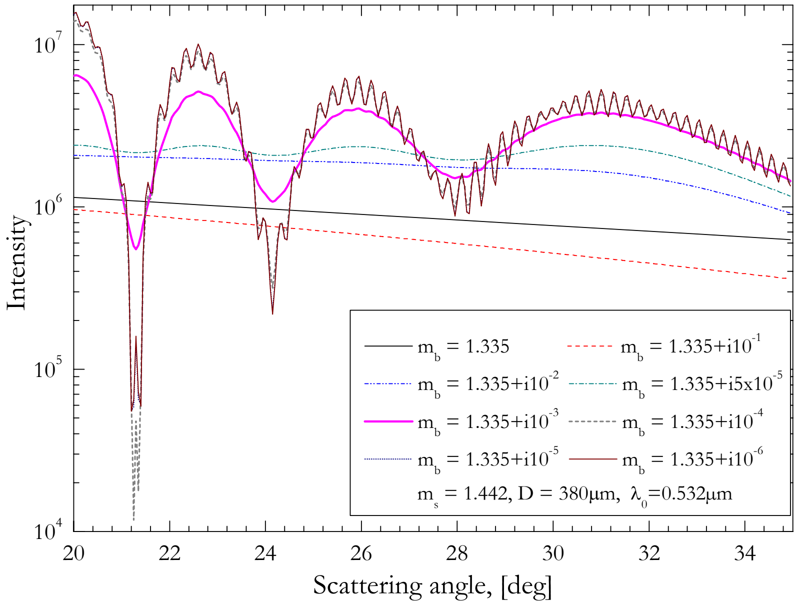

Figure 5.34 CSP calculated with LMT for water-dye bubbles in silicon oil with an increasing ink concentration (i.e. absorption), $m^{-1} \approx 0.926$.

To test experimentally bubbles absorption we have produced water-dye droplets in silicon oil, when the piezo-jet is impacting onto the silicon oil free surface. The dye was indeed an aqueous solution charged with "Red acid G" (from Colorey, see www.colorey.fr). The latter is a chemical dye commonly used in industry to color detergents, creams, paper, etc. It is non-toxic and miscible in water. We prepare different water-ink solutions with different absorptions, see Figure 5.35.

Figure 5.35 Image of water-ink (using "Rouge Acide G" dye) used in experiment.

To measure the absorption of these solutions we built a setup to measure the transmission of a collimated and chopped laser beam through a spectrophotometric cell (square cross section, width L) and filled with different water-dye solutions, see Figure 5.36. The Beer-Lambert law was used to deduce the samples absorption (i.e. their refractive index imaginary part). For that purpose we use the CCD camera of the ILIDS system as a photometric detector, and took advantage of its large dynamic range (adjustable integration time). Table 5.8 and Figure 5.37 show the results obtained for the imaginary part of the refractive index of the different water-dye solutions shown in Figure 5.35.

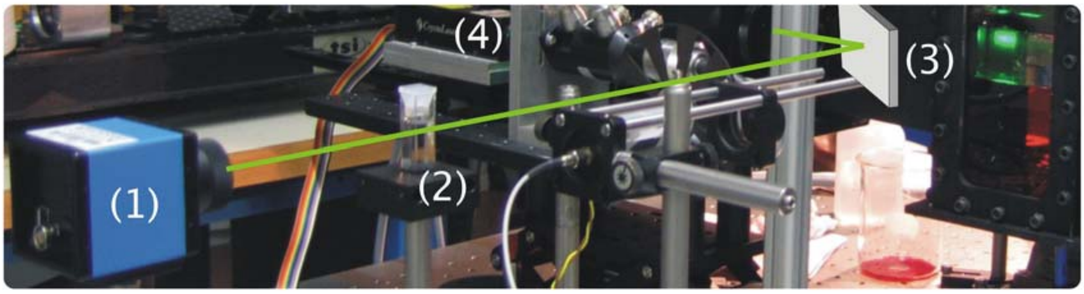

Figure 5.36 Experimental setup for absorption measurements. (1) Color digital camera, (2) spectrophotometric cell, (3) mirror, (4) YAG-Laser output beam

Exp.	Mass of Dye	Mass of water	Concentration	k
	[g]	[g]	[-]	[-]
sol1	1.00000	249.90	0.004	4.23796e-4
sol2	0.07887	250.30	3.15159e-4	3.36302e-5
sol4	0.03165	235.70	1.3426e-4	1.44841e-5
sol5	0.00511	250.30	2.04358e-5	2.43723e-6
sol6	0.00826	274.80	3.00471e-5	3.45447e-6
sol7	0.01943	262.40	7.40475e-5	8.11137e-6
sol8	0.02606	250.90	1.03874e-4	1.12682e-5
sol9	0.69000	2.25	0.30667	3.24572e-2
sol10	1.02000	11.00	0.09273	9.81434e-3
sol11	1.09000	21.90	0.04977	5.26801e-3
sol12	1.02000	86.28	0.01182	1.25149e-3

Table 5.8 Results for the imaginary part of water-dye refractive index

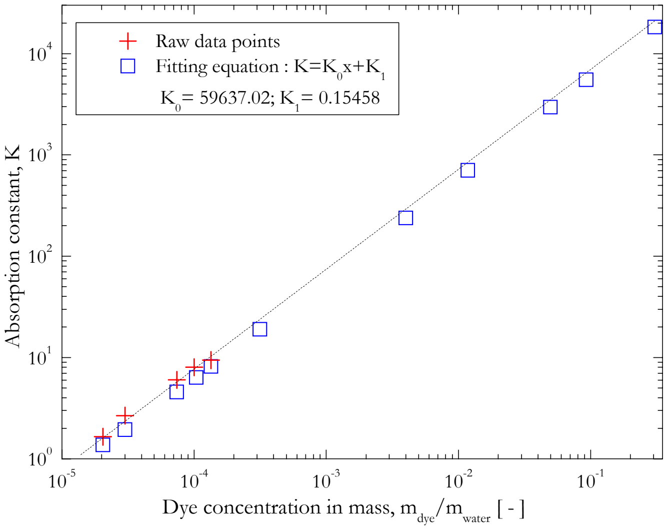

Figure 5.37 Experimental data for the laser beam transmission through the spectrophotometric cell, for different mass concentrations in Dye.

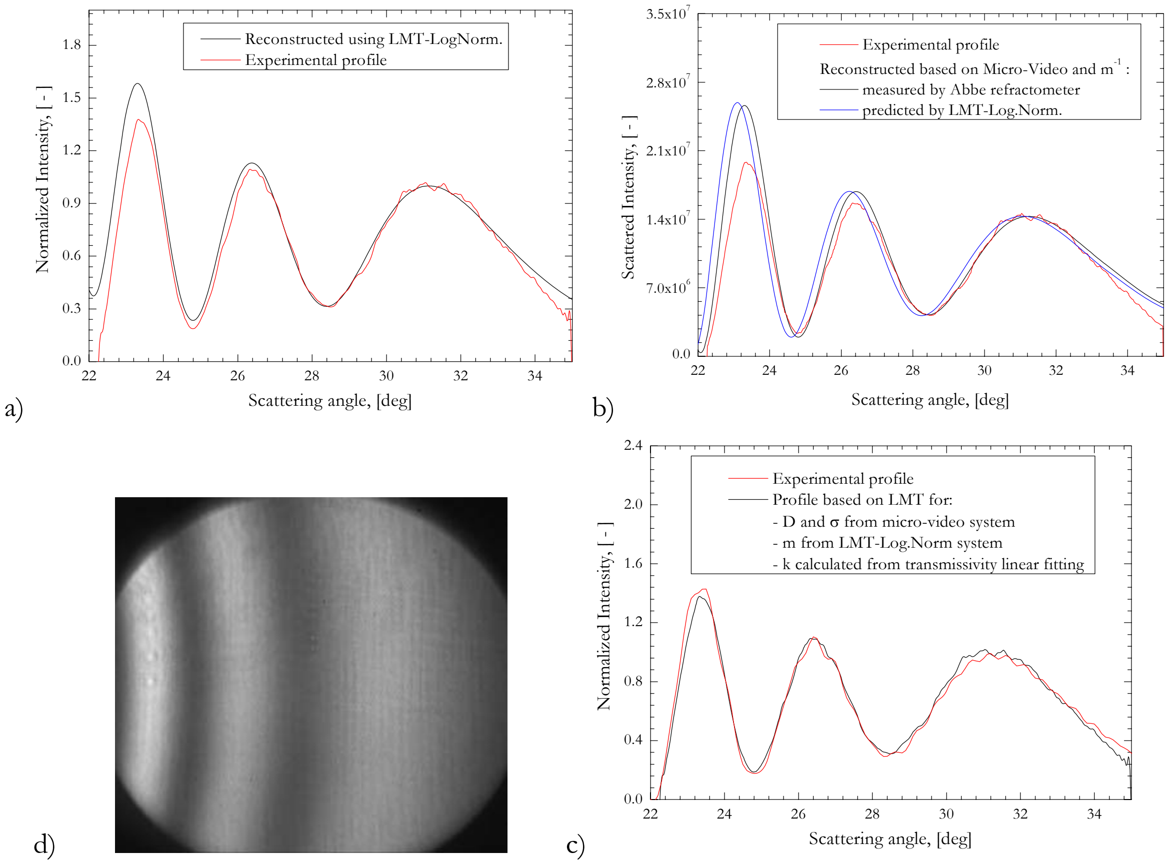

Figure 5.38 For dyed-water bubbles in silicon oil with D=565μm, σ=0.020, m^{-1}=1.052, k=4.2e-4 we have different comparions with the experimental profile: a) when the CARS technique infer all unkown properties; b) when D and m^{-1} are given by the micro-video system and the Abbe Refractometer; c) when D and σ are given by the micro-video system, m^{-1} is deduced by the CARS system with LSQ-LMT-Log.Norm. inverse method and k is calculated from beam transmission measurements; d) experimental CSP *(Exp. _Dye_TW_2_)*.

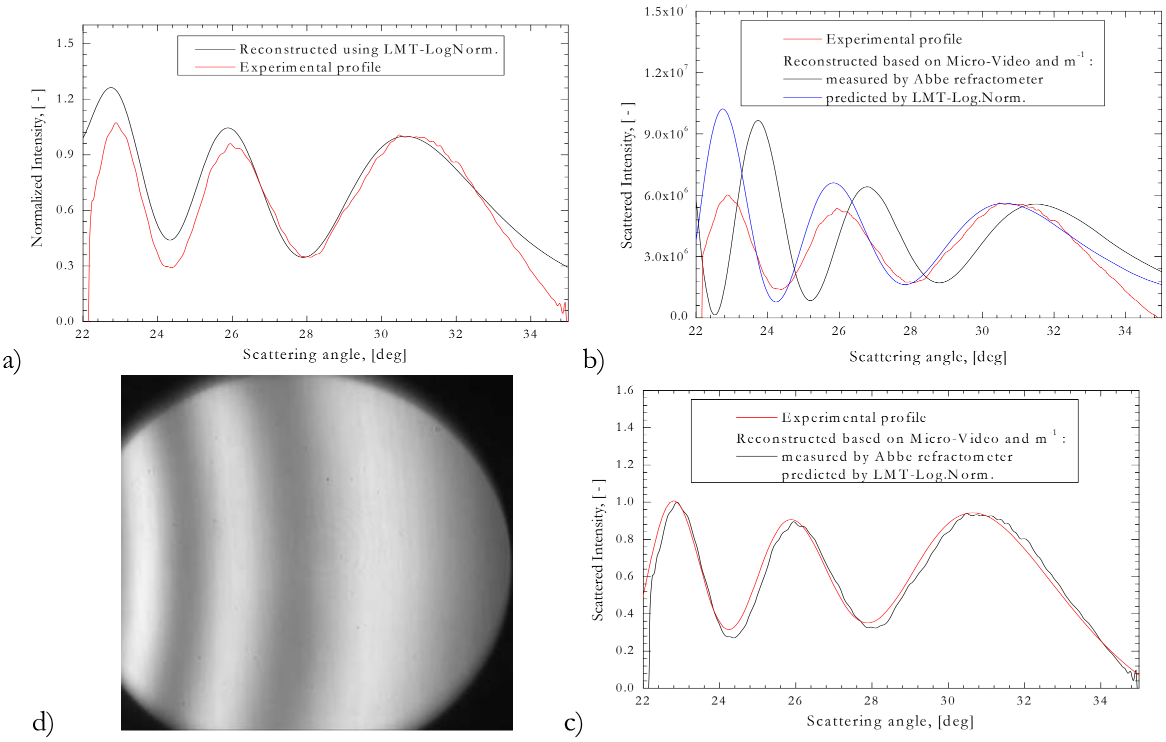

Figure 5.39 Same as Figure 5.38 but for D=585μm, σ=0.005, m^{-1}=1.050, k=1.24e-3 *(SiW_Dye_S12_1)*

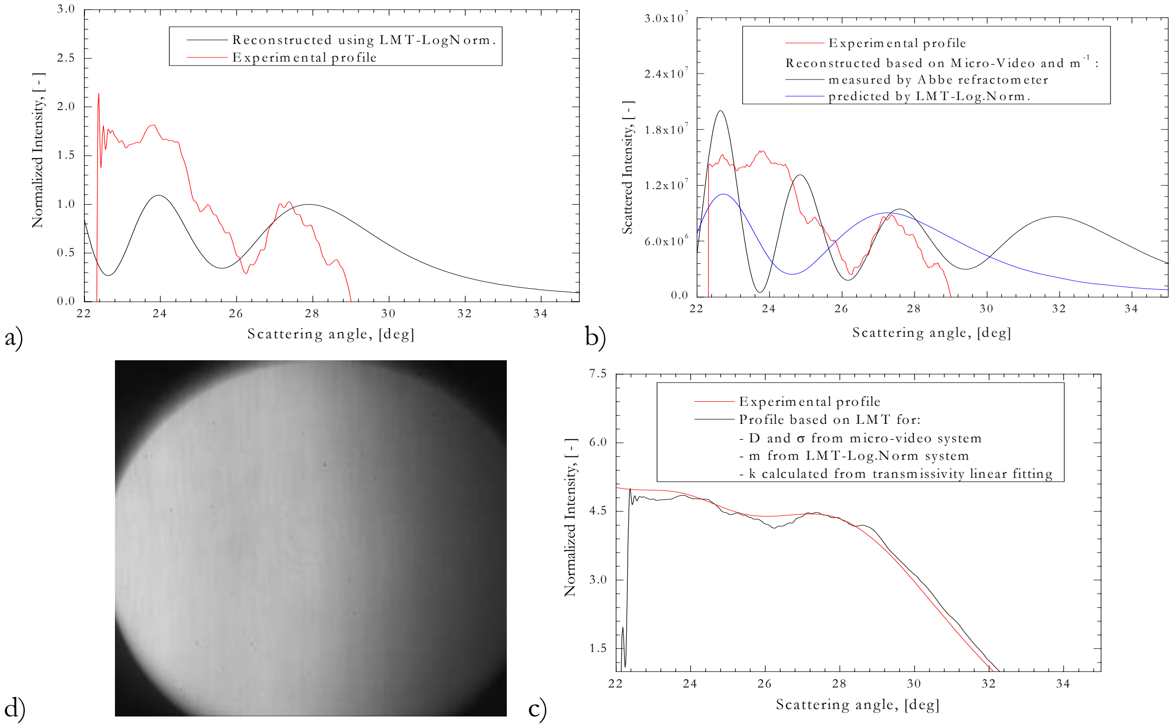

Figure 5.40 Same as Figure 5.38 but for D=732μm, σ=0.005, m^{-1}=1.042, k=5.2e-3 *(SiW_Dye_S11_1_)*

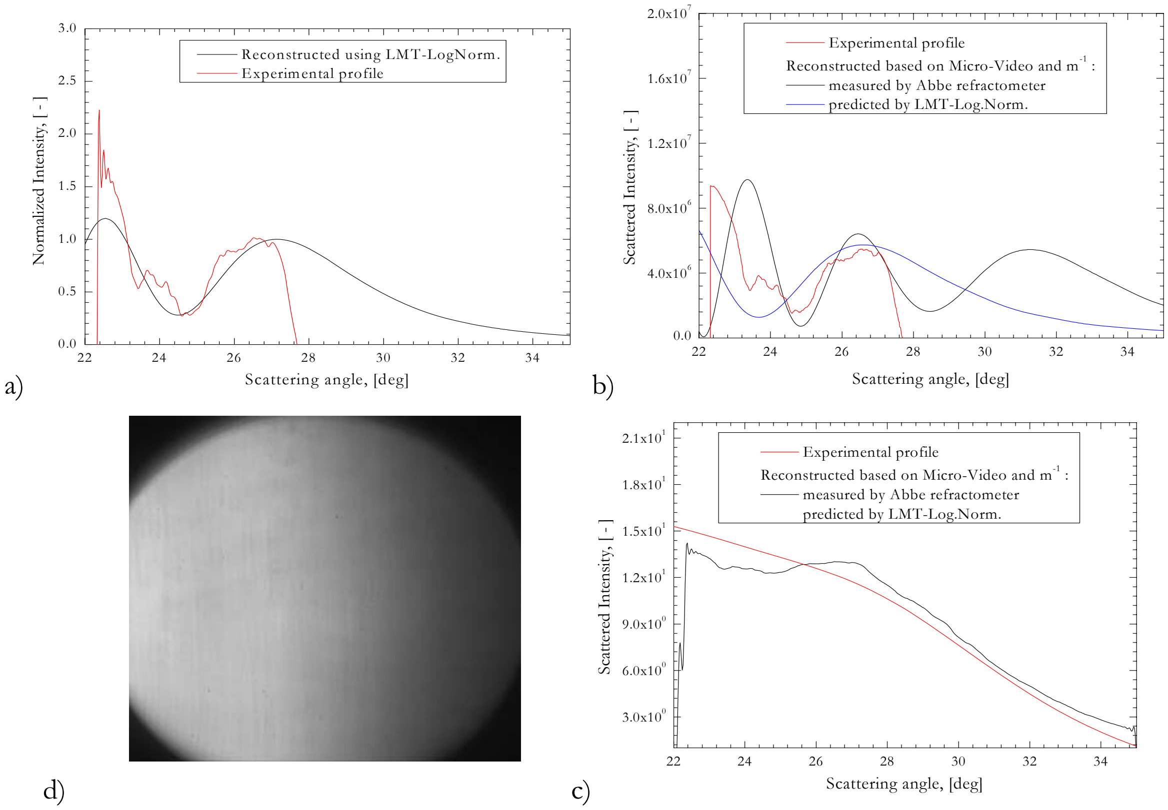

Figure 5.41 Same as Figure 5.38 but for D=570μm, σ=0.005, m^{-1}=1.0420,k=9.7e-3 *(SiW_Dye_S10_1_)*

5.2.3.2 Results on falling bubbles

From Figure 5.38 to Figure 5.41 are presented typical results for the CSP, and the intensity profiles (experimental and reconstructed) of dye-water droplets in silicon oil with increasing absorption and different size. All statistics are summarized in Table 5.9

Name / Solution	Micro-video system				LMT-Logn-Norm.		
	D [μm]	σ / D [μm/ μm]	m [-]	k [-]	D [μm]	σ / D [μm/ μm]	m [-]
SiW_Dye_in_line_1_/ Sol1	582.0	0.005	1.0520	4.2e-4	580.0	0.50	1.0520
SiW_Dye_in_line_2_/ Sol1	585.0	0.005	1.0520	4.2e-4	580.0	0.50	1.0520
SiW_Dye_dense_2_ / Sol1	596.0	0.050	1.0520	4.2e-4	590.0	0.50	1.0515
SiW_Dye_TW_1_ / Sol1	565.0	0.020	1.0520	4.2e-4	580.0	0.50	1.0515
SiW_Dye_TW_2_ / Sol1	565.0	0.020	1.0520	4.2e-4	580.0	0.50	1.0515
SiW_Dye_TW_3_ / Sol1	565.0	0.020	1.0520	4.2e-4	600.0	0.50	1.0510
SiW_Dye_S12_1_ /Sol12	585.0	0.005	1.0520	1.24e-3	580.0	0.100	1.0500
SiW_Dye_S11_1_ /Sol11	732.0	0.005	1.0520	5.2e-3	970.0	0.050	1.0420
SiW_Dye_S10_1_ /Sol10	570.0	0.005	1.0520	9.7e-3	700.0	0.50	1.0420

Table 5.9 For different dyed water drops in silicon, comparison of the measured mean sizes, standard deviations and refractive indices

Chapter 6

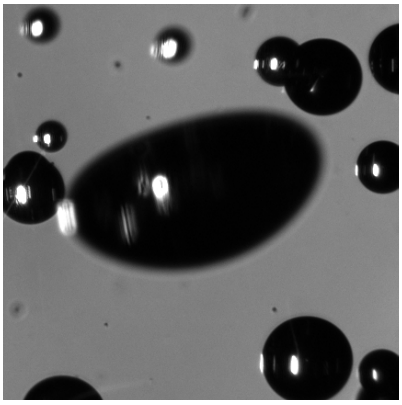

NON SPHERICAL BUBBLES

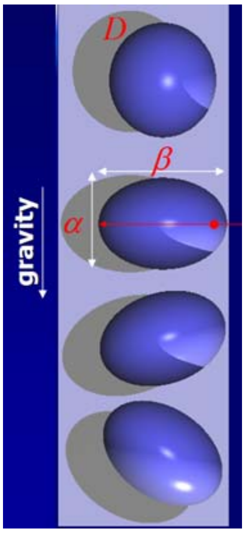

Figure 6.1
Schematic of ellipsoidal bubbles

The CARS technique is intended to characterize spherical bubbles. However, in many bubbly flows bubble shapes can deviate notably from the spherical one. According to the bubble-shape diagram of Grace et al. (1976), the ellipsoidal shape appears to be the most common when the bubbles begin to deviate from the sphericity (see §4.1). For this shape the interesting thing is that the response of the CARS technique could be interpreted, at least to a certain extent. Indeed, according to the POA, the CSP is mainly sensitive to the radius of curvature of the bubble in the scattering plane. For a bubble aspect ratio $\xi = a/b \equiv \alpha/\beta \le 1$, where $a \equiv \alpha$ is the small axis (gravity direction) and $b \equiv \beta$ is the major axis (horizontal/scattering plane) of the bubble; the diameter measured is expected to be $\bar{D}_{CARS} \sim b$. At the same time it is easy to show that the imaging technique gives us an equivalent surface diameter: $\bar{D}_{\mu-video} \sim \sqrt{\xi b}$. So from an experimental point of view, there is a possibility to study the effect on the CSP of ellipsoidal bubbles (Onofri 2006 a-b, Onofri 2007a).

In this chapter we first give some insight on the aspect ratio of the bubbles that can be generated with our experimental setup, we present exemplifying results and comparisons with micro-video imaging analyses, and we introduce the bases of a simple geometrical optics model to predict the change in curvature of the CSP fringes with respect to ξ .

6.1 Production of non spherical bubbles

To investigate the response of CARS system to non spherical bubbles it is important to generate appropriate bubbly flows. For free rising air bubbles in water, non-sphericity appears to be significant for equivalent diameter above $\approx 1.3mm$ (Clift et al. 1978). Indeed, it is the reason why in the previous chapter we limit the study to bubble sizes below $\approx 1mm$. Figure 6.2 summarizes the aspect-ratio covered in our experiments versus the Tadaki number calculated with Eq. (69) and the parameters of Table 6.2. The aspect ratio and the terminal velocity of the bubbles were measured with the micro-video imaging system. The evolution of ξ predicted by the correlation equation, Eq. (71), is also shown in this figure. Note the good agreement found between the Vakhrushev and Efremov (1970) model and our experimental results see also Table 6.1.

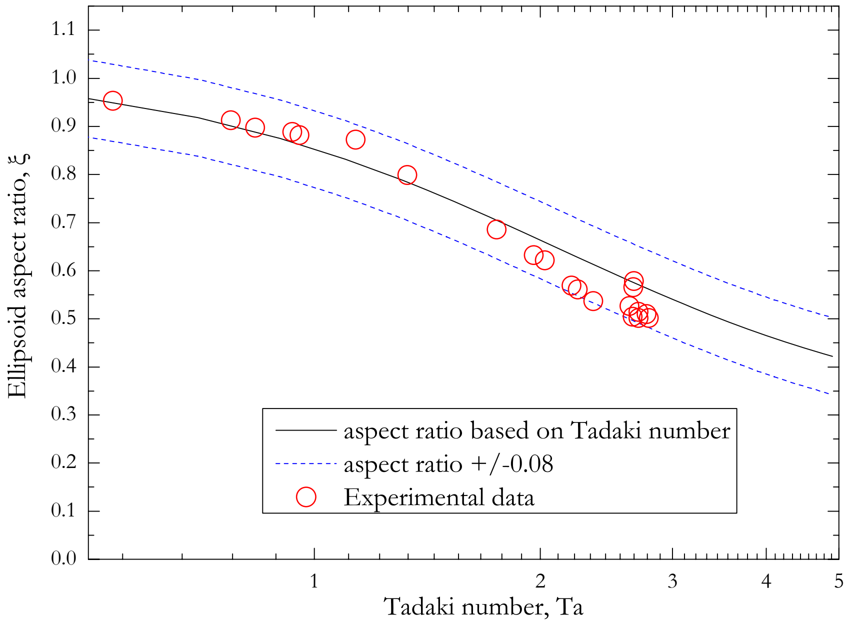

Figure 6.2 Aspect-ratio of bubbles: measured values and values predicted by Eq. (71).

Non dimensional numbers				Micro-video imaging system					Parameters based on Tadaki number		
Morton number	Reynolds number	Eotvos number	Tadaki number	b (=β) [um]	a(=α) [um]	velocity terminal [m/s]	R eq. sphere [um]	ξ aspect ratio [-]	ξ aspect ratio [-]	b [um]	a [um]
$1{,}7251\ 10^{-11}$	280,0	0,1277	0,935	1008,9	896,4	0,26	969,9	0,89	0,867	1017	882
$1{,}7251\ 10^{-11}$	339,5	0,1574	1,135	1127,1	982,9	0,28	1076,8	0,87	0,824	1148	947
$1{,}7251\ 10^{-11}$	397,6	0,1779	1,330	1233,8	985,9	0,31	1144,9	0,8	0,784	1242	974
$1{,}7251\ 10^{-11}$	606,2	0,3136	2,027	1781,4	1106,9	0,36	1520,1	0,62	0,659	1747	1151
$1{,}7251\ 10^{-11}$	703,6	0,4035	2,353	2121,6	1138,6	0,37	1724,1	0,54	0,612	2030	1244
$1{,}7251\ 10^{-11}$	808,0	0,6147	2,703	2678,5	1343,2	0,34	2128,0	0,5	0,57	2565	1464
$1{,}7251\ 10^{-11}$	828,3	0,6521	2,770	2744,2	1398	0,34	2191,6	0,51	0,563	2654	1495
$1{,}7251\ 10^{-11}$	794,0	0,5867	2,656	2611,6	1317,3	0,34	2078,8	0,5	0,576	2499	1439
$1{,}7251\ 10^{-11}$	795,5	0,6755	2,661	2697,8	1525,2	0,32	2230,7	0,57	0,575	2682	1543
$1{,}7251\ 10^{-11}$	786,0	0,5977	2,629	2598,3	1368,6	0,34	2098,3	0,53	0,579	2518	1458
$1{,}7251\ 10^{-11}$	285,4	0,1307	0,954	1023,3	902,2	0,26	981,2	0,88	0,863	1031	890
$1{,}7251\ 10^{-11}$	249,4	0,1220	0,834	982,9	882	0,24	948,1	0,9	0,889	986	877
$1{,}7251\ 10^{-11}$	797,0	0,6510	2,666	2628,6	1519,9	0,33	2189,9	0,58	0,574	2634	1514
$1{,}7251\ 10^{-11}$	808,0	0,6282	2,703	2684,5	1381,3	0,34	2151,2	0,51	0,57	2593	1480
$1{,}7251\ 10^{-11}$	231,5	0,1093	0,774	925,3	844,6	0,23	897,5	0,91	0,902	929	838
$1{,}7251\ 10^{-11}$	834,6	0,6555	2,792	2765,8	1387,1	0,34	2197,4	0,5	0,561	2664	1495
$1{,}7251\ 10^{-11}$	161,2	0,0838	0,539	798,4	761	0,18	785,7	0,95	0,95	799	760
$1{,}7251\ 10^{-11}$	523,1	0,2500	1,750	1539,3	1055	0,34	1357,1	0,69	0,704	1525	1075
$1{,}7251\ 10^{-11}$	586,1	0,2971	1,960	1723,7	1089,6	0,35	1479,3	0,63	0,669	1691	1132
$1{,}7251\ 10^{-11}$	658,1	0,3582	2,201	1960,1	1115,5	0,367	1624,4	0,57	0,633	1891	1198
$1{,}7251\ 10^{-11}$	671,0	0,3693	2,245	2000,5	1121,3	0,37	1649,4	0,56	0,627	1927	1209

Table 6.1 Data calculated for ellipsoidal air-bubbles in water

Property		Water
Dynamic Viscosity	μ_l [Pa s]	$0.9*10^{-3}$
Surface tension	σ_l [N/m]	0.072
Density	ρ_l [kg/m^3]	1.000
Other properties		Others
Density of gas	ρ_g [kg/m^3]	1.98
Gravitational acceleration	g [m/s^2]	9.80665

Table 6.2 Some thermophysical properties of water

To perform the present study, it was necessary to change the micro-video system. Instead of the Imaging Source camera we have utilized a fast digital camera from Photron. This camera has also a resolution of 1024x1024 pixels B/W but for a frame rate of 500Hz. This camera can also be operated at higher frame rate if its resolution is reduced (e.g. 2 kHz for 512x512pixels). Equipped with the long distance camera lens, the nominal resolution of the micro-video imaging was of 173.5 pixels/mm. To ensure as possible that the bubbles have reached their terminal velocity V_T, we have performed the analyses (CARS and micro-video) 100mm above the piezo-jet nozzle. With the high speed micro-video system and Matrox Inspector's scripts, it was possible to analysis precisely the bubble ellipticity and deformation along their trajectory. For this study the CARS system was trigged via the TTL-signal of the "bubble detector" (§4.3).

Figure 6.3 compares measurements of major and minor axes of elliptical bubbles, obtained with the micro-video system, with those deduced from the Tadaki number and bubble velocity measurements (bubble tracking with high speed camera).

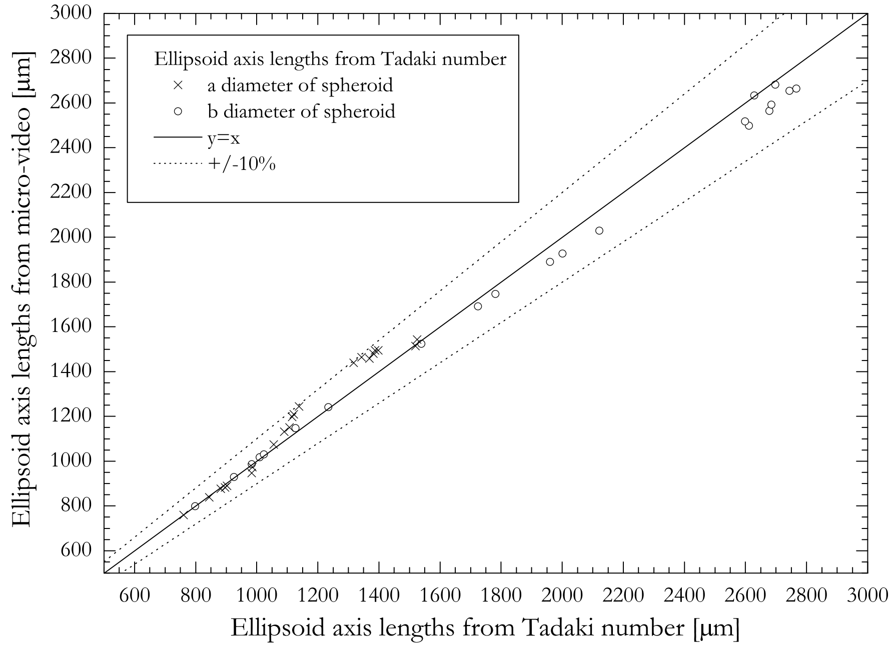

Figure 6.3 Ellipsoidal air bubbles in water: comparison between predictions based on Tadaki number and measurements obtained with the micro-video system.

6.2 Experimental results

6.2.1 Bubble axis parallel to the CARS optical axis (no tilt angle)

As a first step and to not mix several complex effects, we consider non spherical bubbles that are symmetric with respect to the gravity direction. They are referenced as bubbles with a tilt angle equal to zero $\delta = 0°$. To do so, the CARS system is only trigged on the corresponding bubbles. Increasing the piezo-jet input pressure and valve opening time generates different bubbles ellipticities, see Figure 6.4 to Figure 6.7. Each of these figures presents a recorded CSP image, its intensity profile and the profile reconstructed with the LSQ-LMT-LogNorm. inverse method.

These figures show that the experimental and the reconstructed profiles match almost perfectly. This is an important result, as it means that in the scattering plane the CSP of these elliptical bubbles are equivalent to the ones of spheres. CSP of ellipsoid bubbles are "understandable" (which is not necessarily the case for the rainbow scattering for instance). Table 6.3 presents the different parameters measured for these bubbles: the diameter and the refractive index measured with the CARS technique, the two axes of the ellipsoid and its equivalent spherical diameter measured with the imaging system; their refractive index, measured with the Abbe refractometer. Note that, for drawing considerations and because they were rather similar to case 1, we did not show figures for case 2.

Case/ N° Exp / FPS	Micro.Video/Abbe refract.		LMT-log-norm.			Micro-Video-Calculations				
	Equivalent Sphere [um]	Refract. index [-]	Size [um]	σ /D [-]	Refract. index [-]	Velocit [m/s]	b [um]	a [um]	Aspect ratio [-]	Tilt Angle [deg]
1/ 10 / 1000Hz	949,0	1,3345	1040,0	0,0001	1,3355	0,2599	1008,9	896,4	0,897	0,0
2/ 8 / 1000Hz	1048,9	1,3345	1140,0	0,0001	1,3355	0,2843	1127,1	982,9	0,872	0,0
3/ 29 / 1000Hz	1098,9	1,3345	1270,0	0,0001	1,3355	0,3132	1233,8	985,9	0,799	0,0
4/ 32 / 500Hz	1395,3	1,3345	1820,0	0,0001	1,3355	0,3596	1781,4	1106,9	0,621	0,0
5/ 35 / 500Hz	1544,9	1,3345	2180,0	0,0001	1,3355	0,3680	2121,6	1138,6	0,537	0,0

Table 6.3 Results corresponding to Figure 6.4 to Figure 6.7, plus one case.

Figure 6.8 compares the diameter measured with the CARS system and the two bubbles axis lengths measured with the high-speed micro-video imaging system. We found what we infer at the beginning of this chapter: the CARS measurement corresponds to the axis b of the ellipsoid. Indeed, the CARS technique measures the radius of curvature of the bubbles near the impact parameter corresponding to the critical angle and within the scattering plane. In fact, all CARS measurements in Figure 6.8 are almost aligned on the y=x axis. Good results are also obtained for the refractive index of these bubbles (see Table 6.3). However, by measuring the axis b as a diameter of the bubble instead of its equivalent spherical diameter CARS underestimates the volume of the bubbles (i.e. void fraction).

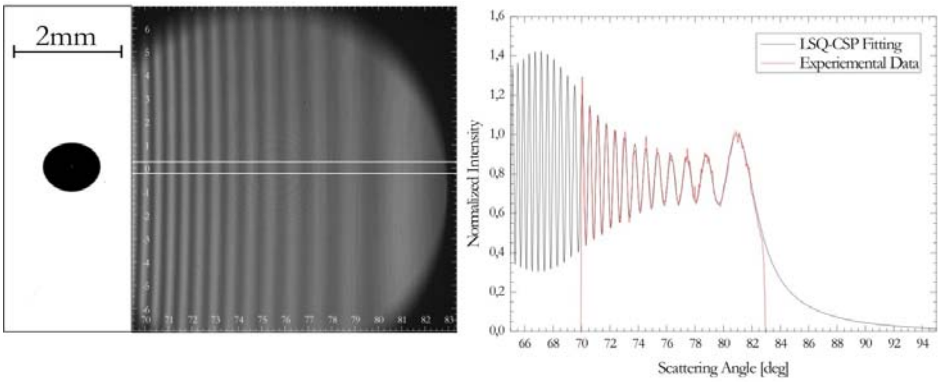

Figure 6.4 Micro-video image, CSP, experimental and reconstructed intensity profiles for a slightly elliptical air bubble in water *(Case 1, "Exp. FastCam_10")*

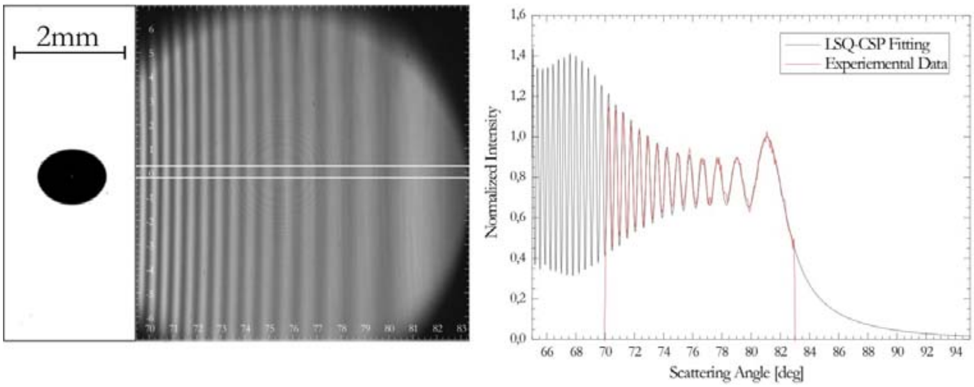

Figure 6.5 Like in Figure 6.4 but foe a larger aspect ratio *(Case 3, "Exp. FastCam_09")*

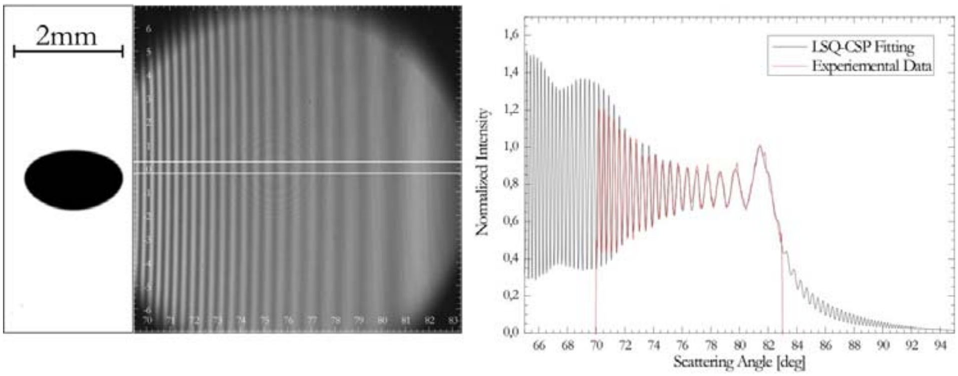

Figure 6.6 Like in Figure 6.5 but for a larger aspect ratio *(Case 4, "Exp. FastCam_32")*

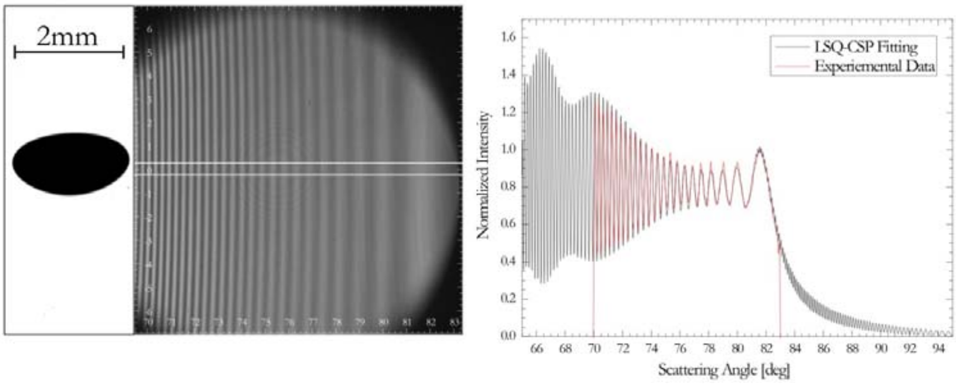

Figure 6.7 Like in Figure 6.6 but for a larger aspect ratio *(Case 5, "Exp. FastCam_35")*

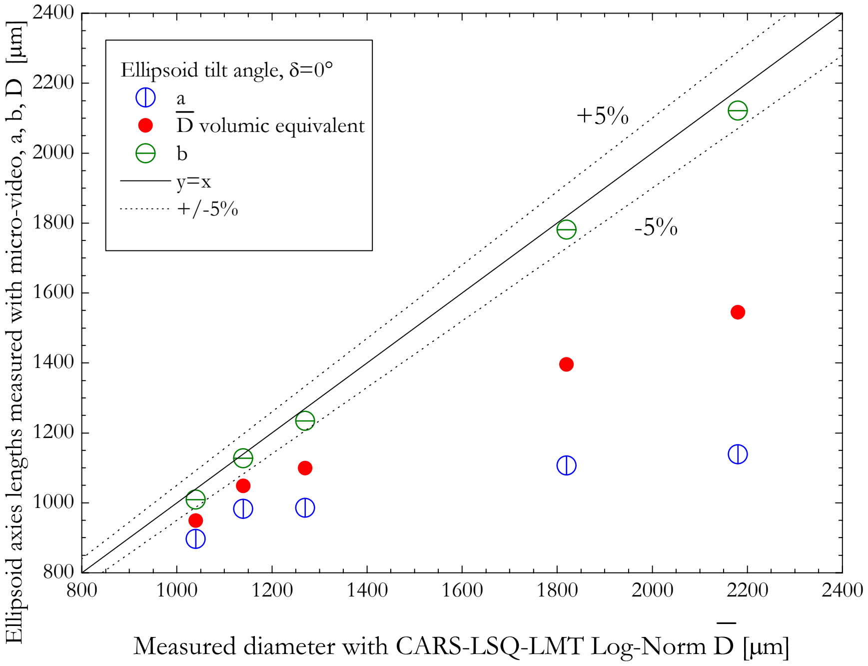

Figure 6.8 Comparison of the diameter measured with the CARS system with the two bubbles axis lengths measured with the high-speed micro-video imaging system.

Obviously, in natural bubbly flows, bubbles have random tilt angles so that this effect is expected to be less pronounced than for the results obtained when the tilt angle is null. To get an estimate of the spherical equivalent diameter with the CARS technique we need to access to the ellipsoid axis a. We have indentified two strategies to access to the ellipsoid axis a :

- This axis length could be deduced by analyzing more in details CSP characteristics (see §6.3).

- We could try to use hydrodynamics considerations to infer the bubble ellipticity ξ. For that purpose we have derived with the help of Maple (i.e. symbolic computational software), the dependence of the Tadaki number with the bubble aspect ratio:

$$Ta(\xi) = 10^{c_4} 10^{-\frac{1}{2c_3}\ln\left(-\frac{2c_2\sqrt{\xi}+\xi-c_1^2+c_2^2}{\xi-(c_1+c_2)^2}\right)} \tag{99}$$

Using the definition of the Tadaki number and remarking that the equivalent spherical diameter is $D = b\xi^{1/3}$, we get the following equation:

$$\frac{\rho_l V_T D}{\mu_l} Mo^{0.23} = 10^{c_4} 10^{-\frac{1}{2c_3}\ln\left(-\frac{2c_2 D^{3/2}/b^{/2}+D^3/b^3-c_1^2+c_2^2}{D^3/b^3-(c_1+c_2)^2}\right)} \tag{100}$$

Knowing the fluid properties and measuring b with the CARS technique one could expect to get the second axis length a. Unfortunately in Eq. (100) the terminal velocity is undetermined too. To our opinion there must be some way to cancel out V_T in the above expression but we did not have time to solve this problem. It will be the subject of a future work.

6.2.2 Ellipsoid bubble with a tilt angle

There is many publications in the literature that investigate tilt angle of free falling droplets (e.g. Pruppacher and Keltt, 1997). One main conclusion of these works is that, statistically, droplets tilt angle is null $\bar{\delta} = 0°$. For rain droplets, the standard deviation of the tilt angle is $\sigma_\delta \approx 3°$. We did not find such studies for bubbles. But, from analogy and symmetry considerations, we can infer that the mean tilt angle of bubbles should be also null. The underling idea is that, if positive and negative tilt angles produce CSP that statistically compensate each other, we could interpret CSP produced by non spherical bubbles with an equivalent spherical model.

Figure 6.9 present CSP and the correspond micro-video images for air-bubbles in water with aspect ratio $\xi \approx 0.5$ and a equivalent spherical diameter slightly below $\approx 2mm$. Five bubble tilt angles are considered (cases 1 to 5). First of all, it is interesting to notice that if the shape of the bubbles is close to the ellipsoidal one, it is not totally true as bubbles are slightly more flat on their front part than their back one (in respect to their trajectory). Second important remark: the fringe patterns are tilted with respect to the vertical axis and the fringes spacing is not constant, this is particularly visible for case 5. Without any surprise, case 3, which corresponds to a bubbles with a tilt angle close to zero, gives a CSP which is rather similar to the one of a large spherical bubble: the fringes visibility is important even for scattering angles far from the first critical fringe. On the opposite, the visibility of a tilted bubble is weaker and even, quite fluctuating along the whole pattern. The analyses of these CSP are shown in Figure 6.10 to Figure 6.14. To get the size distributions we have used the NNLSQ-LMT and the LSQ-LMT-LogNorm. inverse methods (spherical bubble model). It is easy to notice that, with both inverse methods, we obtain rather broadband size distributions where as we should get a monodisperse one (there is only one bubble in the probe volume at a given time !). The narrower size distribution is obtained for case 3 (tilt angle close to zero). Indeed, these distributions may be understood by the fact that CARS measures a local radius of curvature. At the same time, we must keep in mind that the CARS-camera needs a certain integration time to get images with a reasonable signal to noise ratio. So, the collected scattering pattern is the result of moving bubbles with various radius of curvature regarding to the scattering plane. This is our explanation for the broadening of the BSD that we observe for such bubbles.

For all cases 1-5 from extracted profile it was done measurements using CARS for LSQ-LMT and NNLSQ-LMT inverse method. Shadowgraphy system was used as reference technique.

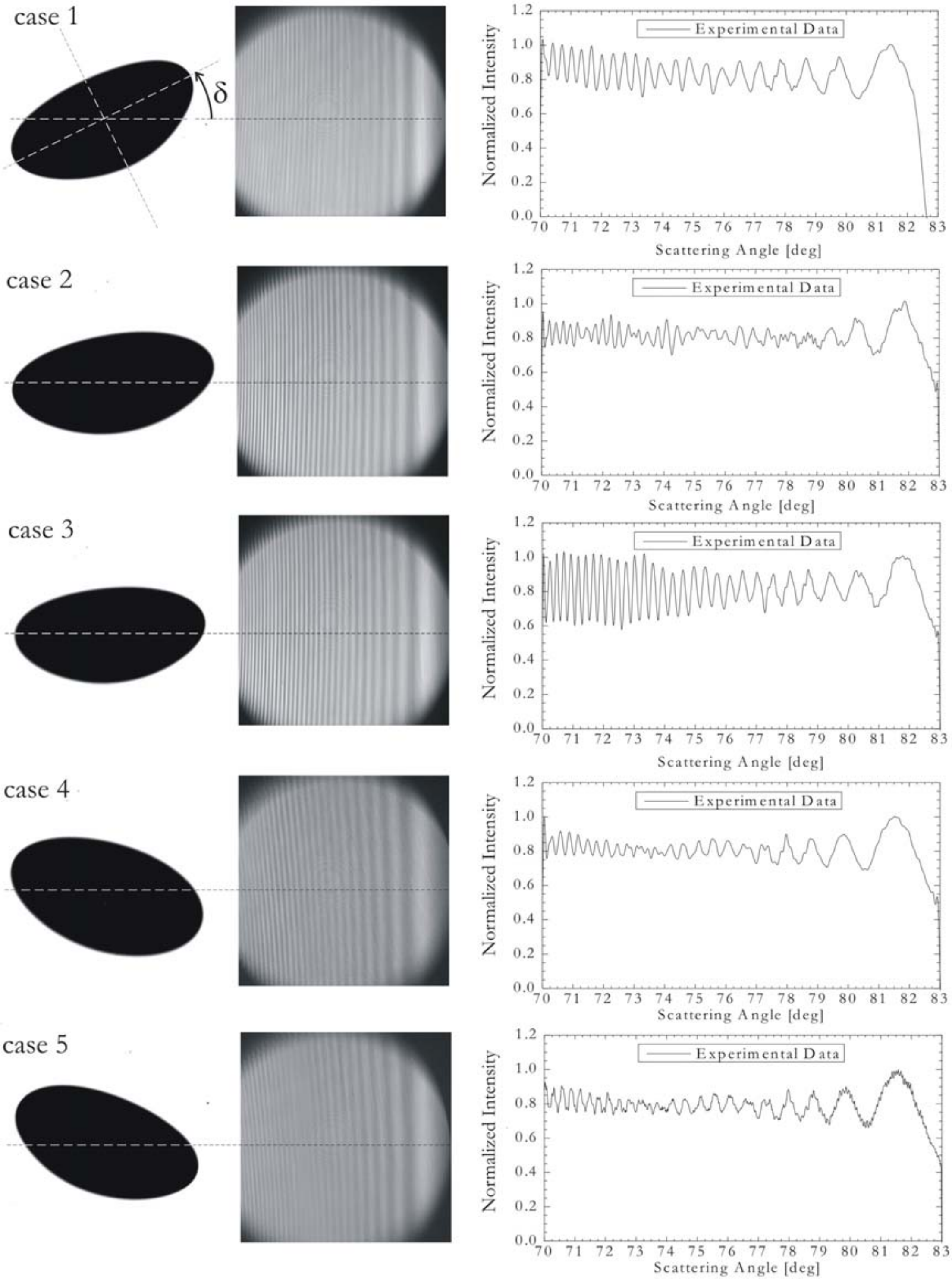

Figure 6.9 Micro-video image, CSP image and intensity profile of a single air bubble in water, with a large aspect ratio and a tilt angle with respect to the scattering plane.

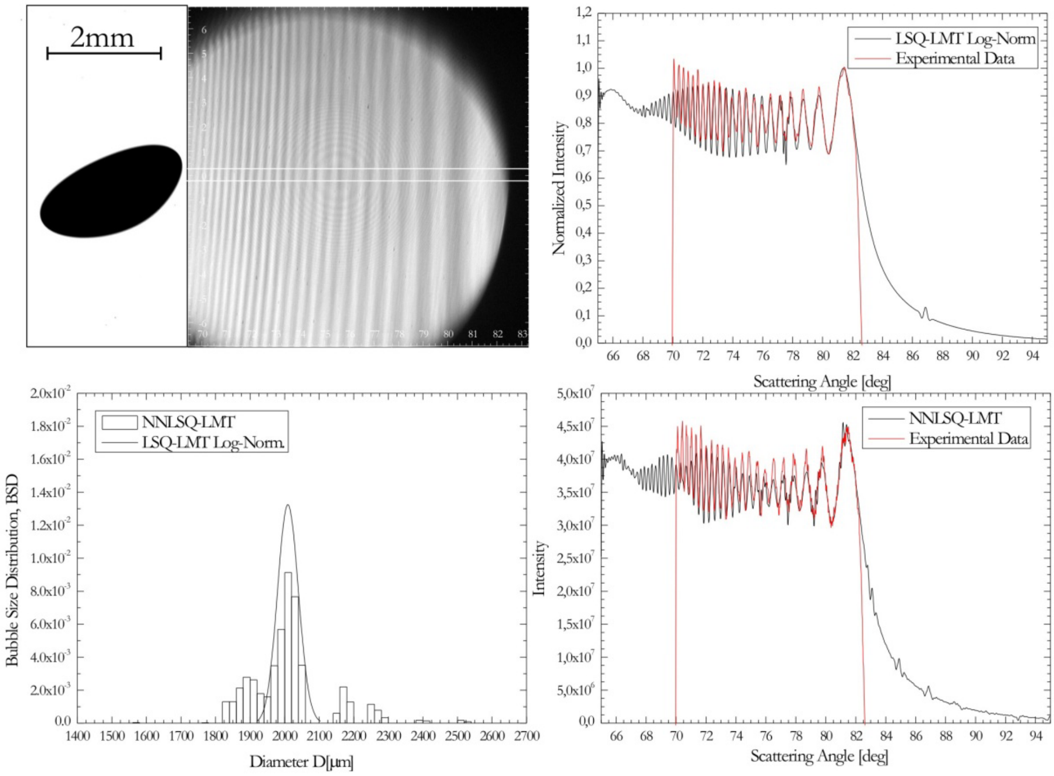

Figure 6.10 Analysis of the CSP of case 1 in Figure 6.9 *(Exp: Angle_FastCam_18)*

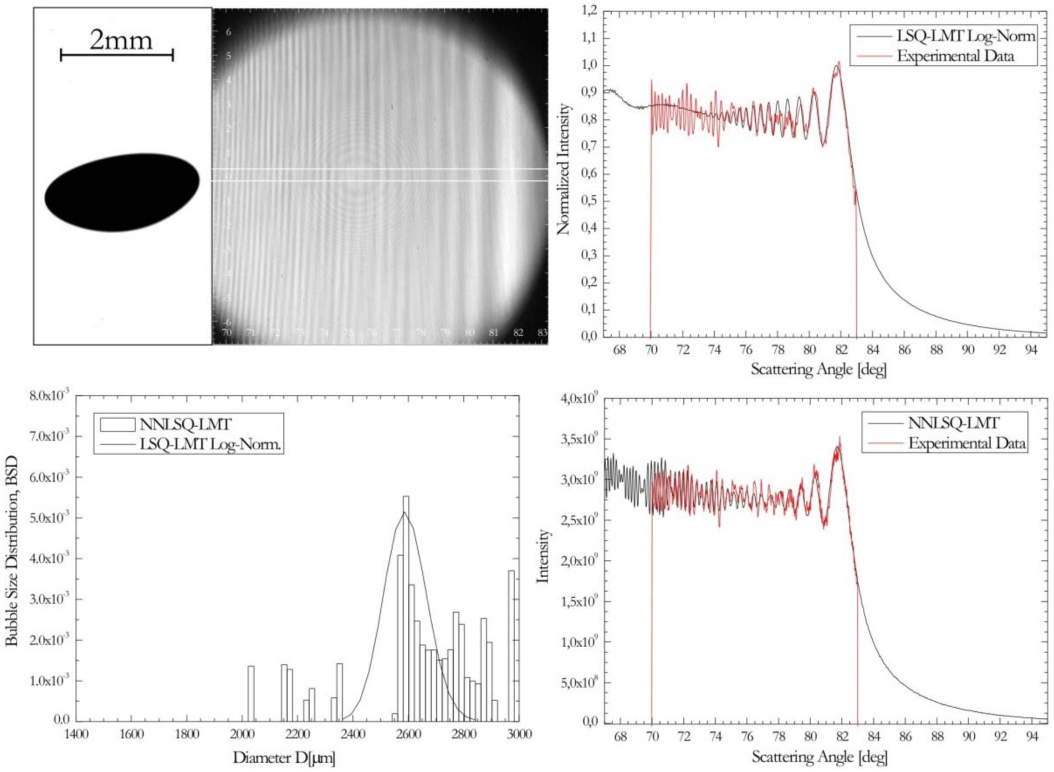

Figure 6.11 Analysis of the CSP of case 2 in Figure 6.9 *(files: Angle_FastCam_17)*

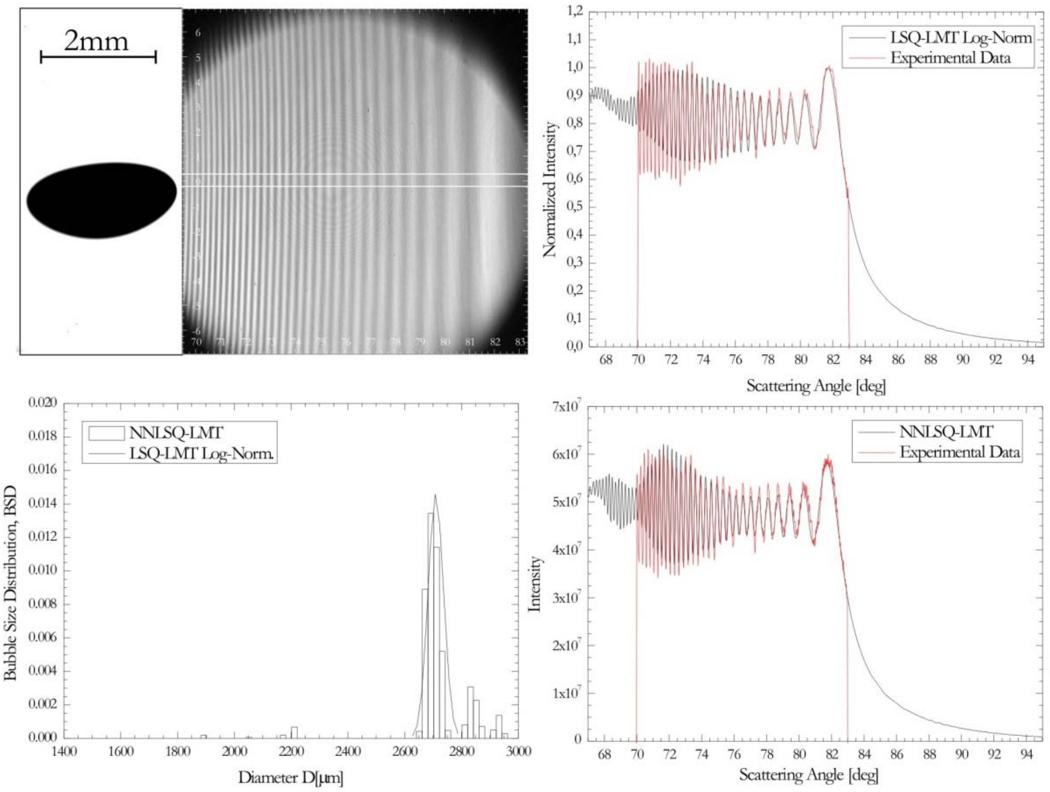

Figure 6.12 Analysis of the CSP of case 3 in Figure 6.9 *(Exp: FastCam_7)*

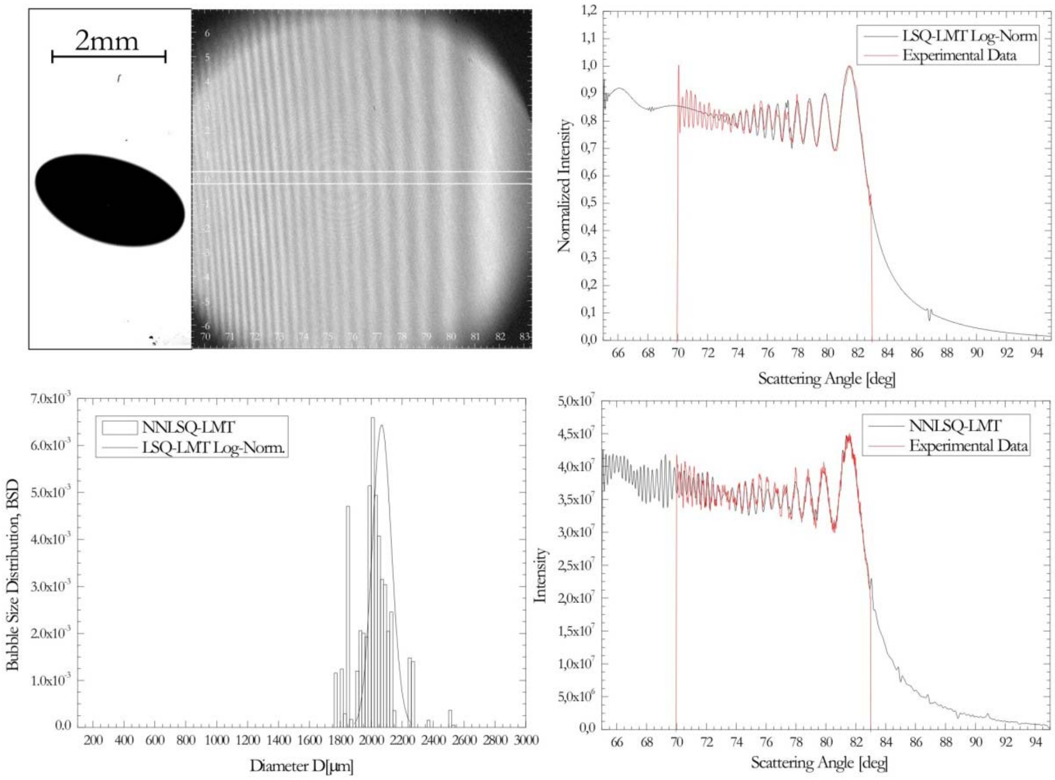

Figure 6.13 Analysis of the CSP of case 4 in Figure 6.9 *(Exp: FastCam_20)*

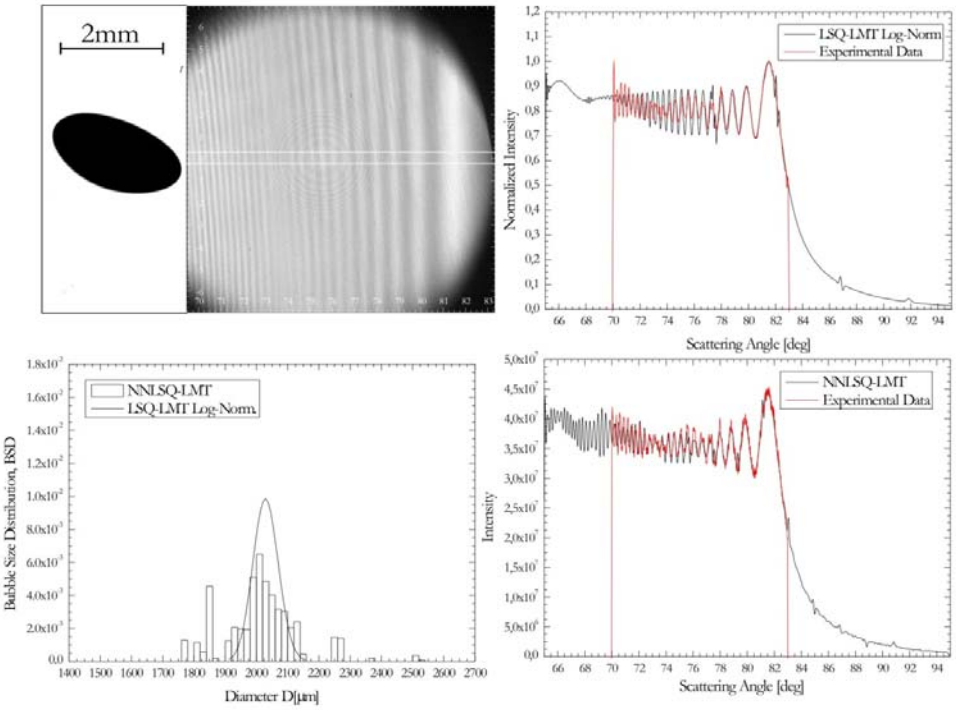

Figure 6.14 Analysis of the CSP of case 5 in Figure 6.9 *(Exp: FastCam_2)*

Case/ Nexp / FPS	Micro.Video		LMT-log-norm.			Micro-Video-Calculations				
	Equivalent Sphere [um]	Refract. index [-]	Size [um]	σ /D [-]	Refract. index [-]	Velocity [m/s]	b [um]	a [um]	Aspect ratio [-]	Angle [deg]
1/ 18 / 500Hz	1879	1,3345	2010	0,015	1,3345	0,3424	2677	1343	0,501	+24
2/ 17 / 500Hz	1927	1,3345	2580	0,010	1,3360	0,3408	2744	1398	0,509	9
3/ 7 / 500Hz	1838	1,3345	2680	0,020	1,3365	0,3444	2612	1317	0,504	+4
4/ 20 / 500Hz	2008	1,3345	2060	0,030	1,3350	0,3216	2698	1525	0,565	-21
5/ 2 / 500Hz	1869	1,3345	2030	0,030	1,3350	0,3378	2598	1369	0,527	-25

Table 6.4 Results for the five all tilt angles (Figure 6.9, Figure 6.10 to Figure 6.14)

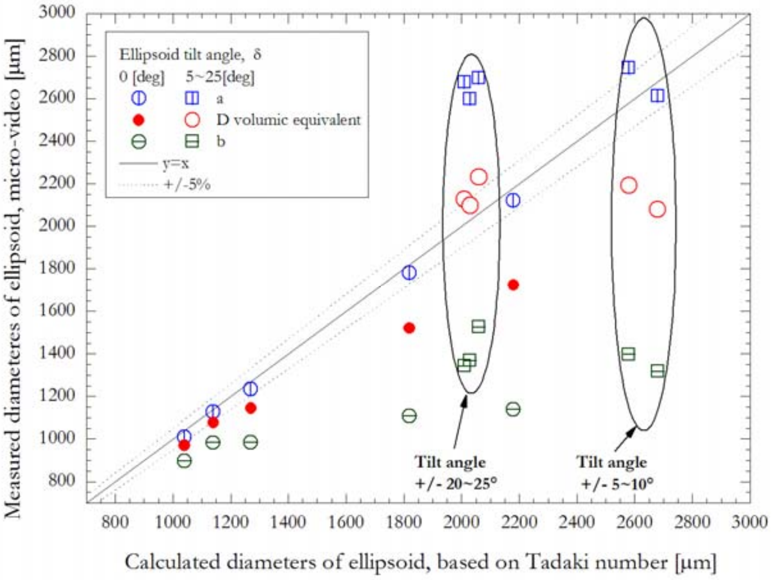

Figure 6.15 For tilted bubbles, comparison of the diameter measured with the CARS system (LMT-LogNorm. inverse method) with the two bubbles axis lengths measured with the micro-video system.

6.3 Geometrical model for the curvature of critical fringes

It was mentioned in the previous experimental part that the fringes of the CSP pattern of an ellipsoid bubble appears to be curved, tilted and with a variable fringe spacing, depending on the bubble aspect ratio and tilt angle. So, in this section, we introduce the formalism of a simple geometrical model to predict the above mentioned effects.

6.3.1 Model

As depicted in Figure 6.16, the bubble is modeled by a spheroid. In the Cartesian coordinate system $\Gamma(O,x,y,z)$, the spheroid is centered and it is defined by its explicit equation, see Eq (101). Its horizontal and transverse radius at the equator and, its vertical radius, are noted respectively: $b \equiv y$, $c \equiv z$ and $a \equiv x$. As the oblate case is the most interesting for rising bubbles, we will consider with more details the axisymmetrical case where $b = c,\ a/b = \xi$ with $\xi < 1$, where ξ is referred further on as the bubble ellipticity.

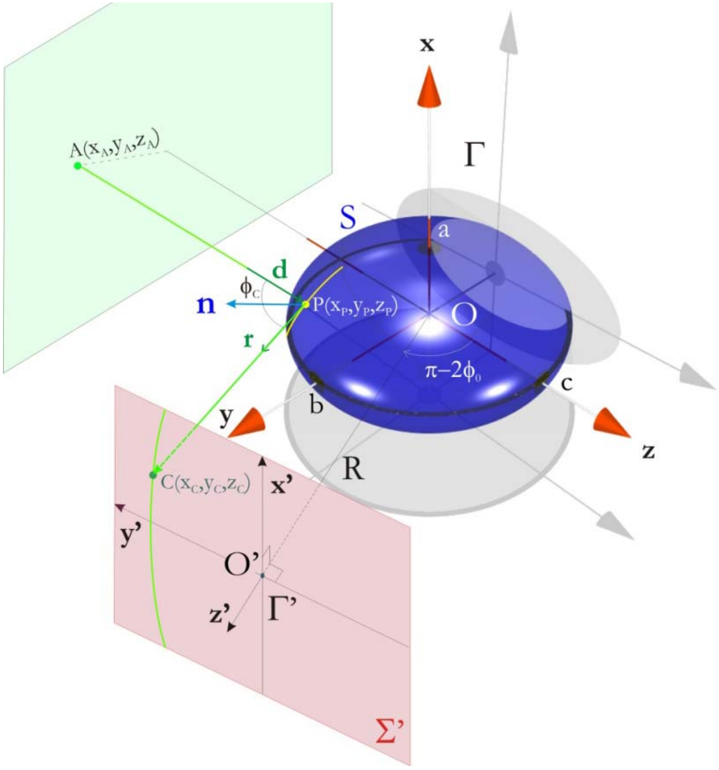

Figure 6.16 Coordinate systems, bubble surface and reflection process.

Incident rays are moving parallel to the z-axis, coming from a point source A localized in a plan perpendicular to the z-axis. Depending on the location of A, some of these rays hit the spheroid surface S, at point P, and are reflected in the critical scattering direction $\theta_c = \pi - 2\phi_c$. The latter is simply defined by the direction corresponding to a reflection angle equal to the critical incident angle. So, it is necessary to define for all point P the normal to the spheroid surface.

6.3.1.1 Ellipsoid equation and normal to the surface

The equation of the spheroid surface *S* is :

$$F(x,y,z)=\frac{x^2}{a^2}+\frac{y^2}{b^2}+\frac{z^2}{c^2}-1=0 \tag{101}$$

In a general way, the equation of the normal to a surface defined by an equation of the form $F(x,y,z)=0$, is given by

$$\mathbf{N}\equiv\nabla F(x,y,z)=\left(\frac{\partial F}{\partial x},\frac{\partial F}{\partial y},\frac{\partial F}{\partial z}\right) \tag{102}$$

The symbol ∇ stands for the gradient operator. For each point $P(x,y,z)\in S$ the unit normal (directed outward) is given by:

$$\mathbf{n}(x,y,z)=\frac{\nabla F}{|\nabla F|}\frac{\frac{\partial F}{\partial x}\mathbf{x}+\frac{\partial F}{\partial x}\mathbf{y}+\frac{\partial F}{\partial x}\mathbf{z}}{\sqrt{\left(\frac{\partial F}{\partial x}\right)^2+\left(\frac{\partial F}{\partial y}\right)^2+\left(\frac{\partial F}{\partial z}\right)^2}} \tag{103}$$

with $\partial F/\partial x=2x/a^2$, $\partial F/\partial y=2y/b^2$, $\partial F/\partial z=2z/c^2$, we get finally the equation of the normal

$$\mathbf{n}(x,y,z)=\frac{1}{\sqrt{\left(\frac{x}{a^2}\right)^2+\left(\frac{y}{b^2}\right)^2+\left(\frac{z}{c^2}\right)^2}}\begin{pmatrix}\frac{x}{a^2}\\ \frac{y}{b^2}\\ \frac{z}{c^2}\end{pmatrix}\equiv\begin{pmatrix}n_x\\ n_y\\ n_z\end{pmatrix} \tag{104}$$

6.3.1.2 Parametric equation of the incident ray or "photon"

In space, the trajectory of the initial ray is defined by a parametric equation depending on the localization of the point source A and its nominal ("launching" or "emission") direction **d**.

Starting from point $A(x_A,y_A,z_A)$, we want to determine the parametric coordinate of all points $M(x,y,z)$ of this line. The components of vector **AM** are

$$\mathbf{AM}=\begin{pmatrix}x-x_A\\ y-y_A\\ z-z_A\end{pmatrix} \tag{105}$$

The direction followed by the photon is described by a unit vector **d** directed toward the spheroid, so that we have:

$$\mathbf{AM}=t\mathbf{d},\ t\in\mathbb{R} \tag{106}$$

$$\mathbf{d}=\frac{1}{\sqrt{d_x^2+d_y^2+d_z^2}}\begin{pmatrix}d_x\\ d_y\\ d_z\end{pmatrix};\ \|\mathbf{d}\|=1 \tag{107}$$

The parametric trajectory of the ray or "photon" is then :

$$\begin{pmatrix}x\\ y\\ z\end{pmatrix}=\begin{pmatrix}td_x+x_A\\ td_y+y_A\\ td_z+z_A\end{pmatrix} \tag{108}$$

First intersection, point P

After leaving point A the photon intercepts the spheroid's surface if the following condition is fulfilled: $M\equiv P$, which means:

$$\frac{\left(td_x+x_A\right)^2}{a^2}+\frac{\left(td_y+y_A\right)^2}{b^2}+\frac{\left(td_z+z_A\right)^2}{c^2}-1=0 \tag{109}$$

$$b^2c^2\left(td_x+x_A\right)^2+a^2c^2\left(td_y+y_A\right)^2+a^2b^2\left(td_z+z_A\right)^2=a^2b^2c^2 \tag{110}$$

To get the parameter t we have to solve the following equation:

$$\kappa_1 t^2+2\kappa_2 t+\kappa_3=0 \tag{111}$$

with

$$\begin{cases}\kappa_1=b^2c^2d_x^2+a^2c^2d_y^2+a^2b^2d_z^2\\ \kappa_2=b^2c^2d_xx_A+a^2c^2d_yy_A+a^2b^2d_zz_A\\ \kappa_3=b^2c^2x_A^2+a^2c^2y_A^2+a^2b^2z_A^2-a^2b^2c^2\end{cases} \tag{112}$$

The general solutions is

$$t_\pm=\left(-\kappa_2\pm\sqrt{\Delta}\right)/\kappa_1 \tag{113}$$

with $\Delta=\kappa_2^2-\kappa_1\kappa_3$. There is no intersection when $\Delta<0$, we are at grazing incidence when $\Delta=0$ and there is two intersections when $\Delta>0$: the ray input $\left(z_P<0\right)$ and the ray ouput $\left(z>0\right)$. We are only interested in the input ray, corresponding to parameter $t_P\equiv t_-$. So the coordinate of the point P are

$$\begin{pmatrix}x_P\\ y_P\\ z_P\end{pmatrix}=\begin{pmatrix}t_Pd_x+x_A\\ t_Pd_y+y_A\\ t_Pd_z+z_A\end{pmatrix} \tag{114}$$

At point P, the normal to S is given by

$$\mathbf{n}(x_P, y_P, z_P) \tag{115}$$

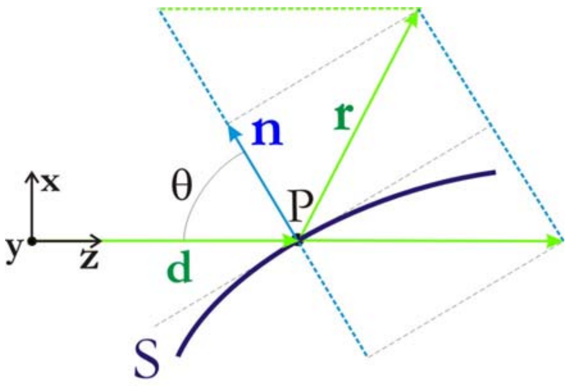

Figure 6.17 Reflected ray at point P

Reflected ray

For specula reflection on surface S, the vector equation of the reflected ray is:

$$\mathbf{r} = \frac{\mathbf{d} - 2(\mathbf{d}\bullet\mathbf{n})\mathbf{n}}{\left\|\mathbf{d} - 2(\mathbf{d}\bullet\mathbf{n})\mathbf{n}\right\|} \tag{116}$$

where $\mathbf{r}$ is the unit vector of the reflected ray, Figure 6.17. For normalized vectors we have:

$$\begin{pmatrix} r_x \\ r_y \\ r_z \end{pmatrix} = \frac{1}{\left\|\mathbf{d} - 2(\mathbf{d}\bullet\mathbf{n})\mathbf{n}\right\|} \begin{pmatrix} d_x - 2(\mathbf{d}\bullet\mathbf{n})n_x \\ d_y - 2(\mathbf{d}\bullet\mathbf{n})n_y \\ d_z - 2(\mathbf{d}\bullet\mathbf{n})n_z \end{pmatrix} \tag{117}$$

$$\begin{pmatrix} r_x \\ r_y \\ r_z \end{pmatrix} = \frac{1}{\sqrt{\left(d_x - 2(\mathbf{d}\bullet\mathbf{n})n_x\right)^2 + \left(d_y - 2(\mathbf{d}\bullet\mathbf{n})n_y\right)^2 + \left(d_z - 2(\mathbf{d}\bullet\mathbf{n})n_z\right)^2}} \begin{pmatrix} -2n_z n_x \\ -2n_z n_y \\ 1 - 2n_z n_z \end{pmatrix} \tag{118}$$

with $\mathbf{d} \equiv \mathbf{z}$ it comes that

$$\begin{pmatrix} r_x \\ r_y \\ r_z \end{pmatrix} = \frac{1}{\sqrt{\left(-2n_z n_x\right)^2 + \left(-2n_z n_y\right)^2 + \left(1 - 2n_z n_z\right)^2}} \begin{pmatrix} -2n_z n_x \\ -2n_z n_y \\ 1 - 2n_z n_z \end{pmatrix} \tag{119}$$

Note that for a sphere $a = b = c = 1$ and $\phi_C = \pi/4$, $x_P(0) \equiv +\sqrt{2}/2; y_P = 0; z_P(0) \equiv -\sqrt{2}/2$ we get $\begin{pmatrix} r_x & r_y & r_z \end{pmatrix}^t = \begin{pmatrix} 0 & 0 & 1 \end{pmatrix}^t$.

6.3.1.3 Critical curve

Critical scattering appears when the incident ray hits the bubble surface S with an angle ϕ above the critical incident angle ϕ_C:

$$\phi > \phi_C = \sin^{-1}(m) \tag{120}$$

where $m<1$ is the bubble relative refractive index. For a spherical bubble this critical curve (partly sketched in yellow in Figure 6.16) is a circle centered on z-axis (which explains the shape of critical bows).

We want here to determine the equation of this critical curve for a spheroid surface. To do so, we simply need to determine the ensemble of points P where the following condition is fulfilled:

$$\cos\phi_C = \mathbf{d.n} = n_z = \sqrt{1-m^2} \tag{121}$$

With previous results and conventions we get

$$\cos\phi_C = \left(\frac{\mathbf{d.n}}{\|\mathbf{d}\|.\|\mathbf{n}\|}\right) = \mathbf{d.n} = \frac{1}{\sqrt{\left(d_x^2+d_y^2+d_z^2\right)\left(n_x^2+n_y^2+n_z^2\right)}} \begin{pmatrix} 0 \\ 0 \\ 1 \end{pmatrix}^t . \begin{pmatrix} n_x \\ n_y \\ n_z \end{pmatrix} = \frac{n_z}{\sqrt{n_x^2+n_y^2+n_z^2}} \tag{122}$$

with

$$\cos\phi_C = \frac{\dfrac{z}{c^2}}{\sqrt{\left(\dfrac{x}{a^2}\right)^2+\left(\dfrac{y}{b^2}\right)^2+\left(\dfrac{z}{c^2}\right)^2}} \tag{123}$$

Finally all these points are at the intersection of the surface S and a cone with z-axis and with an elliptical cross-section:

$$\frac{1}{a^2}\left(\frac{x}{a}\right)^2+\frac{1}{b^2}\left(\frac{y}{b}\right)^2=\frac{1}{c^2}\left(\frac{z}{c}\right)^2\tan^2\phi_C \tag{124}$$

Note that for a spherical particle with $a=b=c=1$ and $\phi_C=\pi/4$, we get $x^2+y^2=z^2$ as the equation of the cone. By using Eq. (101) we obtain finally that the equation of the critical curve is $x^2+y^2=1/2$, i.e. a circle with radius $\sqrt{2}/2$.

From the equation of the spheroid we have

$$\frac{z^2}{c^2}=1-\frac{x^2}{a^2}-\frac{y^2}{b^2} \tag{125}$$

By putting Eq. (124) into Eq. (125) we obtain:

$$\frac{1}{a^2}\left(\frac{x}{a}\right)^2+\frac{1}{b^2}\left(\frac{y}{b}\right)^2=\frac{1}{c^2}\left(1-\frac{x^2}{a^2}-\frac{y^2}{b^2}\right)\tan^2\phi_C \tag{126}$$

which gives

$$x=\pm a\sqrt{\frac{a^2b^2\tan^2\phi_C-\left(\frac{y}{b}\right)^2a^2\left(c^2+b^2\tan^2\phi_C\right)}{b^2\left(c^2+a^2\tan^2\phi_C\right)}} \tag{127}$$

After some calculations we get the first equation of the critical line for the general case $a\neq b\neq c$ and $\phi=\phi_C$. This is the projection of the critical line on Oxy plane:

$$x_P\left(y\right)\equiv x=\pm a\sqrt{\frac{a^2b^2\tan^2\phi_C-\left(\frac{y}{b}\right)^2a^2\left(c^2+b^2\tan^2\phi_C\right)}{b^2\left(c^2+a^2\tan^2\phi_C\right)}}>0 \tag{128}$$

A second equation is necessary to define the critical line in space (i.e. the projection on the Oyz-plane). By injecting Eq.(128) into the spheroid equation (Eq. (125)):

$$z_P\left(y\right)\equiv z=\pm c\sqrt{1-\left(\frac{a^2b^2\tan^2\phi_C-\left(\frac{y}{b}\right)^2a^2\left(c^2+b^2\tan^2\phi_C\right)}{b^2\left(c^2+a^2\tan^2\phi_C\right)}\right)-\frac{y^2}{b^2}}<0 \tag{129}$$

It is interesting to derive expressions for the axis-symmetrical oblate spheroid case where:

$$b=c=cte;\xi=a/b\leq 1 \tag{130}$$

By replacing in Eq. (128) we get a more simple expression for the critical line in the $\left(x,y\right)$ cartesien plan:

$$x_P\left(y\right)\equiv x=\pm a\xi\sqrt{\frac{\tan^2\phi_C-\left(\frac{\xi y}{a}\right)^2\left(1+\tan^2\phi_C\right)}{1+\xi^2\tan^2\phi_C}}>0 \tag{131}$$

To get the critical line equation in the cartesien plan (z,y) we have to inject Eq. (131) into the spheroid equation Eq. (125), so that we get :

$$z_P(y) \equiv z = \pm \frac{a}{\xi}\sqrt{1-\xi^2\left(\frac{\tan^2\phi_C - \left(\frac{\xi y}{a}\right)^2\left(1+\tan^2\phi_C\right)}{1+\xi^2\tan^2\phi_C}\right) - \frac{\xi^2 y^2}{a^2}} < 0 \qquad (132)$$

To visualize the critical bows we restrict the domain to $\{0 \le x_P \le a,\ 0 \le y_P \le b,\ -c \le z_P \le 0\}$

Two limit cases of practical interest:

- for an oblate spheroid with $b = c = a/\xi$ we have

$$z_P(0) \equiv \pm\frac{a}{\xi}\sqrt{1-\xi^2\left(\frac{1}{1+\xi^2}\right)} < 0;\ x_P(0) \equiv \pm a\xi\sqrt{\frac{1}{1+\xi^2}} > 0 \qquad (133)$$

- for a sphere $a = b = c = 1$, $x_P(0) \equiv +\sqrt{2}/2 \approx -0.707; z_P(0) \equiv -\sqrt{2}/2 \approx -0.707$

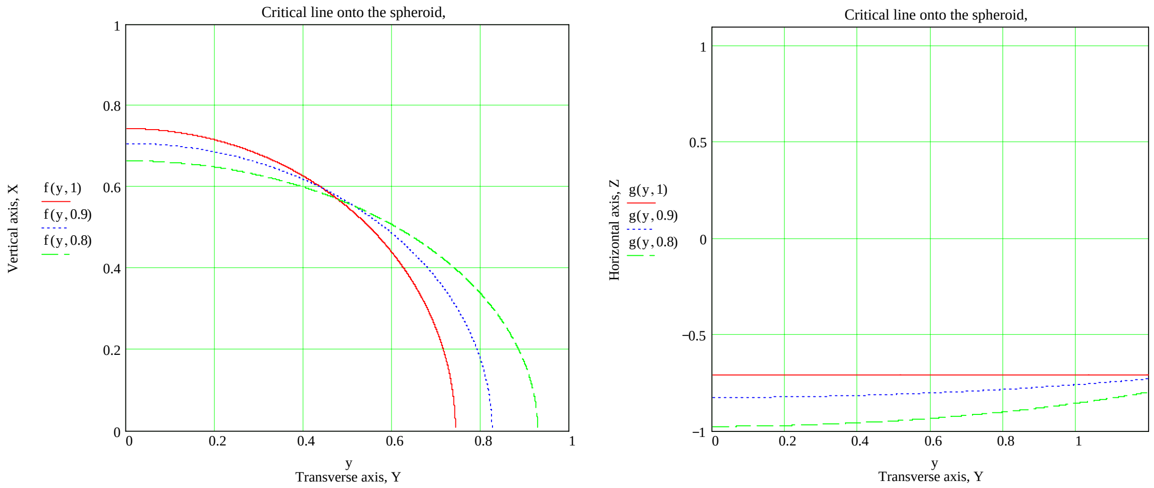

Figure 6.18 Evolution of the coordinates of point P, i.e. the critical curve, left: $x_P = f(y)$ and, right $z_P = g(y)$ for $y = 0:1$. The red curve corresponds to a sphere: x(y) describes a circle and z(y) is a constant.

Numerical example :

Figure 6.18 shows the critical curve onto the spheroid surface projected on the cartesien plans (x,y) and (z,y), for b=1, $\xi = 1, 0.9, 0.8$ and $\phi_C = \pi/4$. Note that, for instance, $f(y,1)$ stands for $x = f(y, \xi = 1) > 0$, and $g(z,1)$ stands for $z = g(y, \xi = 1) < 0$. The red curve corresponds to a spherical bubble.

6.3.2 Projection plane and critical bows

In the CARS set-up the scattering diagrams are observed at infinity by using a collecting lens operating in a Fourier configuration. To model this system, we simply consider a projection plane Σ' which satisfies the following criteria:

(i) Σ' is far from the bubble $R \gg Max\{a,b,c\}$,

(ii) Σ' is perpendicular to a direction defined by a scattering angle $\theta_0 = \pi - 2\phi_0$. Note that in experiments we have generally $\phi_0 \approx \phi_C$, but they are usually not equal. Σ' is parallel to the x-axis (like the CCD sensor)

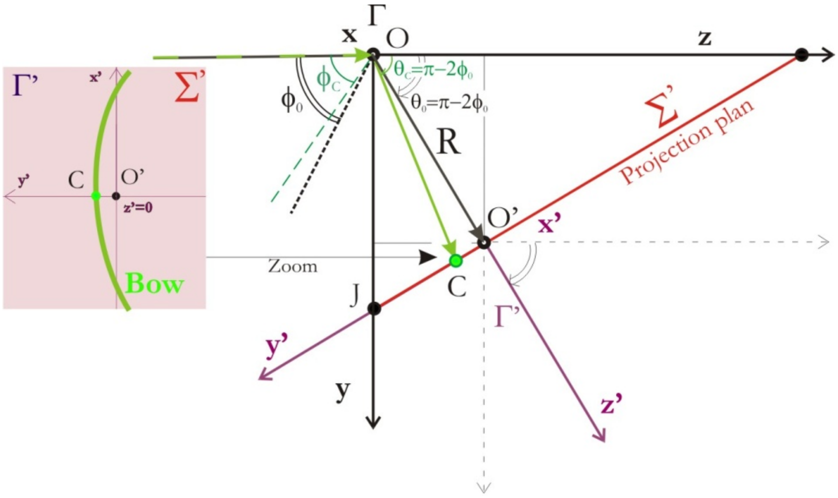

Figure 6.19 Link between the incident ray coordinate system and the coordinate system stick to the projection plan.

Looking at Figure 6.19, the projection plan Σ' crosses *y-axis* at point J

$$J\left(0,\frac{R}{\sin(2\phi_0)},0\right) \tag{134}$$

Σ' has a unit normal

$$\begin{pmatrix} 0 \\ \sin(2\phi_0) \\ -\cos(2\phi_0) \end{pmatrix} \tag{135}$$

The equation of Σ is obtained by posing that the scalar product of a vector **JM** and the normal of Σ' is null:

$$\begin{pmatrix} x-0 \\ y-\dfrac{R}{\sin(2\phi_0)} \\ z-0 \end{pmatrix} \bullet \begin{pmatrix} 0 \\ \sin(2\phi_0) \\ -\cos(2\phi_0) \end{pmatrix} = 0 \tag{136}$$

So the equation of projection Σ' is

$$y\sin(2\phi_0)-\cos(2\phi_0)z-R=0 \tag{137}$$

The parametric equation of the ray reflected, from point P toward direction $\mathbf{r}$ is

$$\begin{pmatrix} x \\ y \\ z \end{pmatrix}=\begin{pmatrix} t_q r_x + x_P \\ t_q r_y + y_P \\ t_q r_z + z_P \end{pmatrix} \tag{138}$$

This ray hits the projection plane Σ' if there is a value of t_q such as:

$$\begin{gathered}\left(t_q r_y + y_P\right)\sin(2\phi_0)-\cos(2\phi_0)\left(t_q r_z + z_P\right)-R=0 \\ t_q=\frac{R+z_P\cos(2\phi_0)-y_P\sin(2\phi_0)}{r_y\sin(2\phi_0)-r_z\cos(2\phi_0)}\end{gathered} \tag{139}$$

if $r_y\sin(2\phi_0)-r_z\cos(2\phi_0)\neq 0$

$$t_q=\frac{R+z_P-y_P\tan(2\phi_0)}{r_y\tan(2\phi_0)-r_z} \tag{140}$$

$$t_q=\frac{R-y_P}{r_y} \tag{141}$$

When $r_y\sin(2\phi_0)-r_z\cos(2\phi_0)\neq 0$ the crossing point is noted $C(x_C,y_C,z_C)$ with

$$\begin{pmatrix} x_C \\ y_C \\ z_C \end{pmatrix}=\begin{pmatrix} t_q r_x + x_P \\ t_q r_y + y_P \\ t_q r_z + z_P \end{pmatrix} \tag{142}$$

$$t_q=\frac{R-y_P}{r_y}$$

Bows equation in the projection plan

Eq. (142) describes the critical bows in a the 3D coordinate system $\Gamma(O,x,y,z)$. This representation is difficult to understand, except when $\phi_0=\pi/4$ as in this particular case Σ' is parallel to the (xOz) plan. In the general case, it is better to express this equation in a 2D coordinate system $\Gamma'(O',x'=x,y',z\equiv 0)$ simulating the plane of the CCD or a screen on which the critical bows are observed, see Figure 6.16. To move from $\Gamma(O,x,y,z)$ to $\Gamma'(O',x'=x,y',z')$ we need a translation and a rotation.

Translation from $O\rightarrow O'$:

$$\begin{pmatrix} x' \\ y' \\ z' \end{pmatrix} = \begin{pmatrix} x \\ y - R\sin\left(\pi - 2\phi_0\right) \\ z - R\cos\left(\pi - 2\phi_0\right) \end{pmatrix} = \begin{pmatrix} x \\ y - R\sin\left(2\phi_0\right) \\ z + R\cos\left(2\phi_0\right) \end{pmatrix} \tag{143}$$

Rotation from $\Gamma(O,x,y,z) \rightarrow \Gamma'(O,x'=x,y',z')$:

$$\begin{pmatrix} x' \\ y' \\ z' \end{pmatrix} = \begin{pmatrix} 1 & 0 & 0 \\ 0 & -\cos\left(2\phi_0\right) & -\sin\left(2\phi_0\right) \\ 0 & \sin\left(2\phi_0\right) & -\cos\left(2\phi_0\right) \end{pmatrix} \begin{pmatrix} x \\ y \\ z \end{pmatrix} \tag{144}$$

Composing the two transformations we get the equation of the bows in the 2D projection plane Γ' :

$$\begin{pmatrix} x_C'\left(y\right) \\ y_C'\left(y\right) \\ z_C'\left(y\right) \end{pmatrix} = \begin{pmatrix} 1 & 0 & 0 \\ 0 & -\cos\left(2\phi_0\right) & -\sin\left(2\phi_0\right) \\ 0 & \sin\left(2\phi_0\right) & -\cos\left(2\phi_0\right) \end{pmatrix} \begin{pmatrix} x_C\left(y\right) \\ y_C\left(y\right) - R\sin\left(2\phi_0\right) \\ z_C\left(y\right) + R\cos\left(2\phi_0\right) \end{pmatrix} \tag{145}$$

see Eq. (142) for the expressions of $x_C\left(y\right), y_C\left(y\right)$ and $z_C\left(y\right)$.

By plotting $x' = f\left(y'\right)$ we can visualize the bows as they are observed on a paper sheet or on the CCD for $R \gg Max\left\{a,b,c\right\}$. To get relative angular quantities, we have to plot something like $\tan^{-1}\left(x'/R\right) = f\left(\tan^{-1}\left(y'/R\right)\right)$.

Chapter 7

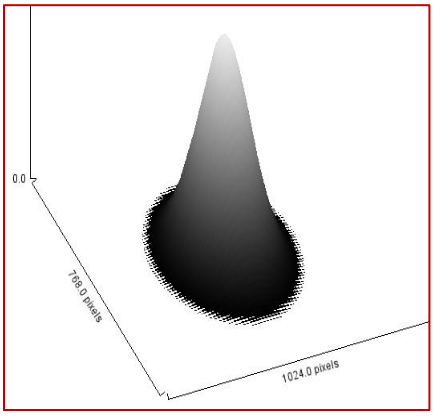

GAUSSIAN BEAM AND SPATIAL FILTER EFFECTS

As already mentioned earlier the CARS technique is mostly a angular based technique but, any angular technique is also partly intensity dependant. Two important intensity weighting effects contribute to the CSP: the laser beam intensity profile within the probe volume and the CARS collection optics spatial filtering. From chapters 5 and 6, it is clear that when the beam waist diameter and the spatial filter aperture are properly chosen, these two effects do not create any problem as we obtained reliable size distributions and refractive indices measurements. However, in this chapter we investigate these two effects to bring more physical understanding on CARS working principle, as well to clarify the limits of the CARS technique with respect to these two effects.

7.1 Gaussian beam effects

7.1.1 Exemplifying numerical results

To introduce the principle of the CARS technique, as well as for all numerical results presented earlier we did not take into account the intensity gradients within the probe volume (see §2.6). The reason for that is that we restrict ourselves to bubble sizes much smaller than the probe volume dimensions (see §4.3.1). Indeed, as a technique allowing instantaneous spatial statistics, there is no need to consider probe volumes smaller than the bubble size. However, for some applications, it can be necessary to study the bubbles one by one (low bubble concentrations), i.e. to use a small probe volume (huge bubble concentrations, correlation with other technique, time resolution, etc.). In fact it was the original operating mode of the CARS technique (see Onofri 1999a).

Most optical sizing techniques use lasers producing TM00 beams (Gaussian intensity profile). It is also the case of the CARS technique. For small bubble diameter/laser beam waist diameter ratios: $D/2\omega_0 \le 3$, it is necessary to consider the bubble position in respect to the laser beam waist center, see Figure 7.1.

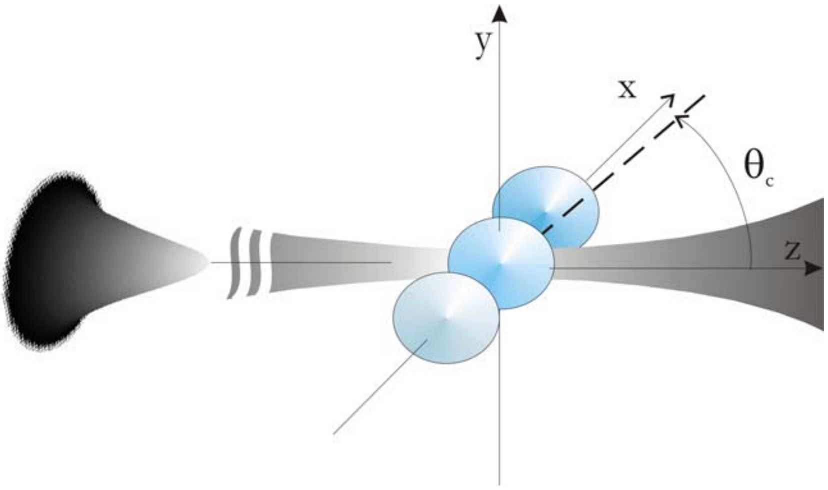

Figure 7.1 Positions (x,y=z=0) of the bubbles in respct to the laser beam-waist center (the CARS collection optical axis is close to the x-axis)

As an example Figure 7.2 shows the evolution of the scattering diagram of an air bubble in water lighted by a laser beam with beam-waist diameter $2\omega_0 = 1.5mm$, parallel polarization and $\lambda_0 = 0.532nm$, and for three positions of the bubble along the x-axis, with y=z=0. Note that the CARS optical axis is along the z-axis (see Figure 7.1). The calculations were performed with the generalized Lorenz-Mie theory (Gouesbet et al. 1988).

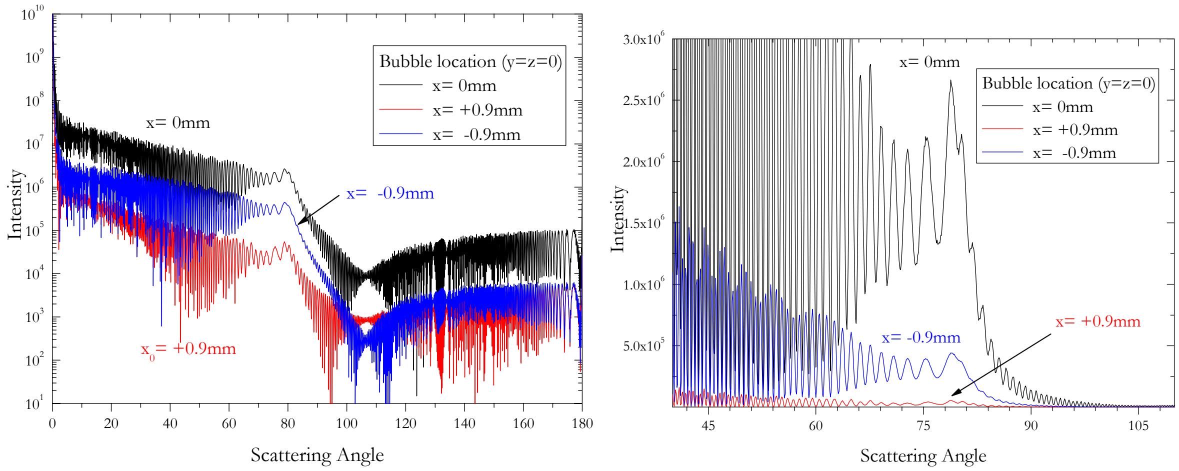

Figure 7.2 Scattering diagrams for three positions of a $D = 465\mu m$ air-bubble in water in a gaussian beam with diameter 1.5 mm, parallel polarisation, z=y=0. From left to right, scattered intensities are presented with logarithm and linear scales.

In the above two figures we remark that the scattered patterns are rather similar although with significant amplitude differences. Only for the case where $x = +0.9mm$ we see that the scattering diagram around the critical angle appears less contrasted. Indeed, this latter case corresponds to an impact parameter which is on the bubble surface side which is opposite to the side where the critical scattering takes place. Figure 7.3 shows a zoom of the previous scattering diagrams, in the critical scattering region and for more bubble positions. The bubble position for which the low frequency fringes (characteristic of the CSP, $p=0$) are maximum and the high frequency fringes are minimum (characteristic of $p \geq 2$) is $x \approx -0.3mm$. For that position, in the geometrical optics framework, we can say that the critical scattering pattern is enhanced by the laser beam intensity profile. Indeed, the impact parameters of the ray $p=0$ at θ_C corresponds to $x=-m^{-1}D/2$, i.e. $x \approx -174\mu m$ for an air-bubble in water. For optical sizing techniques like phase Doppler interferometry, this effect is called "particle trajectory effect" or "Gaussian beam effect"(see Naqwi et al. 1992).

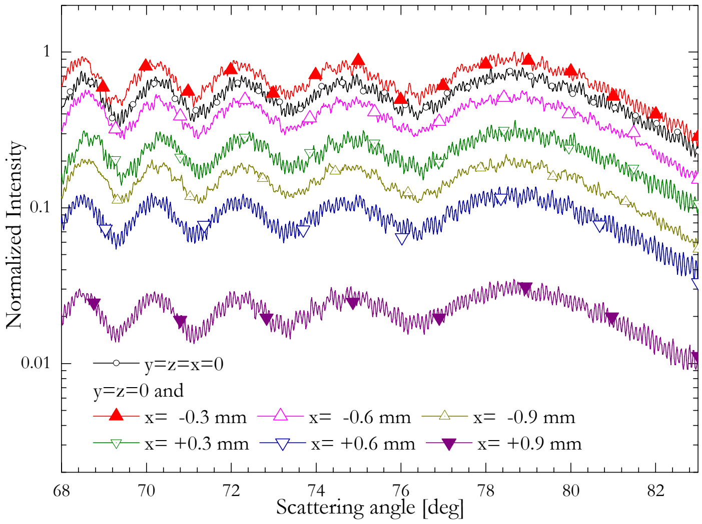

Figure 7.3 Scattering diagrams of an air bubble in water with $D=465\mu m$, for parallel polarisation with $\lambda_0 = 532nm$, and different location along the x-axis in a gaussian beam with $2\omega_0$=1.5mm..

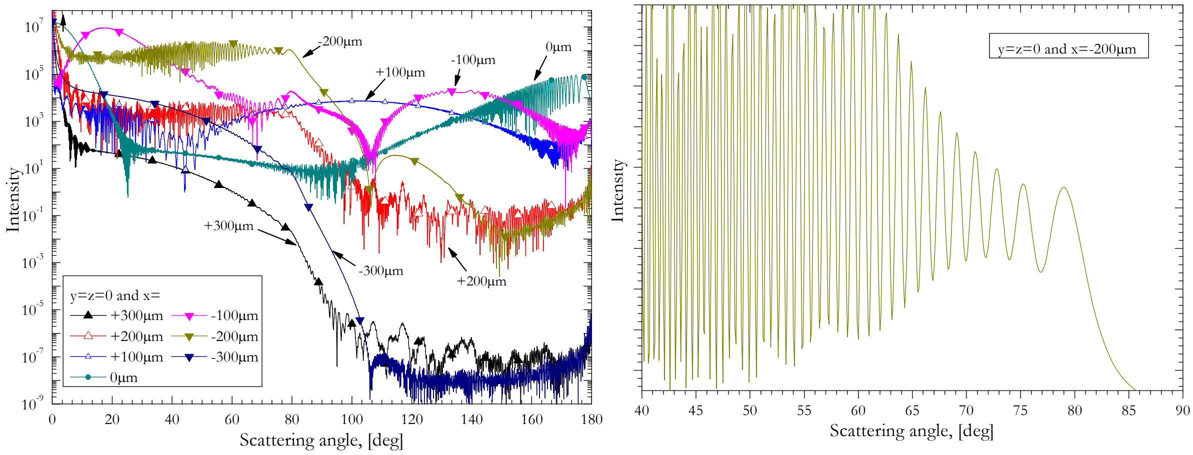

Figure 7.4 Scattering diagrams of a D=465µm air bubble in water, for parallel polarisation with $\lambda_0 = 532nm$, and different locations along the x-axis in a gaussian beam with $2\omega_0$=$75\mu m$ (from left to right, the scattered intensites are in logarithm and linear scales).

Figure 7.4 shows the full scattering pattern for a much smaller beam size, $2\omega_0 = 75\mu m$, of a $D = 465\mu m$ air-water bubble localized at different positions along the beam x-axis. Here the Gaussian beam effects are much more pronounced. It is obvious that the maximum amplification of the critical scattering is reached for $x \approx -200\mu m$: the CSP is only composed of law frequency fringes and there is no more signature of contribution from rays with $p \geq 2$. Eliminating the case $x \approx -100\mu m$ (which is rather similar to the previous case), the second CSP with maximum intensity appears for $x \approx +100\mu m$. The corresponding CSP is rather flat in the critical scattering region. Looking at Figure 2.1 this position seems to correspond to rays $p = 2'$.

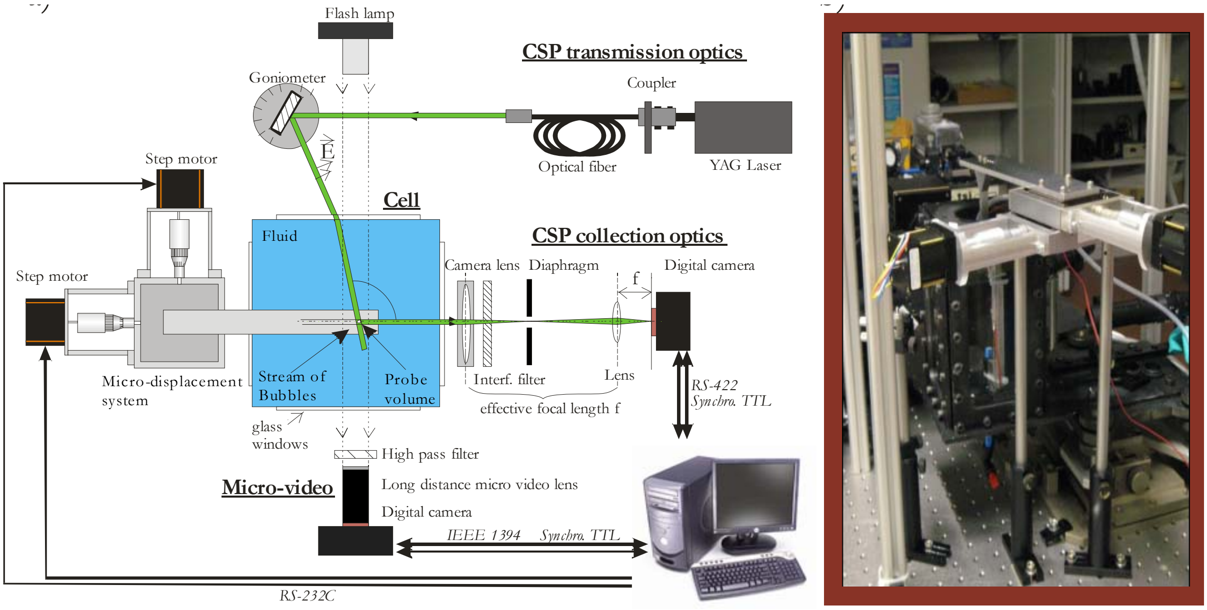

Figure 7.5 Sckematic and photography of the micro-displacement system developped to test Gaussian beam and spatial filter effects onto CARS measurements.

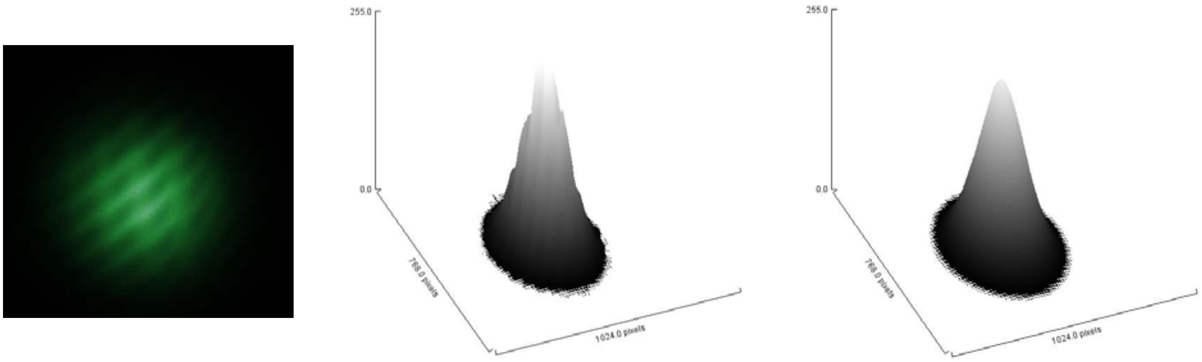

Figure 7.6 Image of the laser beam onto the CCD chip; and the related raw and low pass filtered 2D-profiles.

7.1.2 Setup and procedure

To study experimentally the influence of the diameter of the input beam as well the spatial filter aperture onto the response of the CARS technique we have developed a 2D-motorized bench controlled via a PC, see Figure 7.5. With this system it is possible to adjust precisely $(\pm 10\mu m)$, regarding to the CARS probe volume, the position of the piezo-jet (x,y). By removing the beam expander and using a focusing lens we can reduce the laser beam diameter from $2\omega_0 \approx 15mm$ down to $\approx 50 \sim 1500\mu m$. To analyze the intensity profile of the input beam we have used a CCD camera located at the same distance from the laser output than the true CARS probe volume (but not in water). Figure 7.6 shows that the laser beam profile exhibits a ripple structure that can reasonably be attributed to some back reflected light and interference effects.

From the low pass 2D-profile we get two 1D intensity profiles along the x- and y-axes, see Figure 7.7. Fitting these profiles with the normal distribution:

$$I(x,\bar{x},\omega_x) = \frac{1}{\omega_x\sqrt{\pi/2}} e^{-2\left(\frac{x-\bar{x}}{\omega_x}\right)^2} \qquad (146)$$

we have found for the laser beam-waist dimensions $2\omega_x \approx 2\omega_y \approx 1.5mm$.

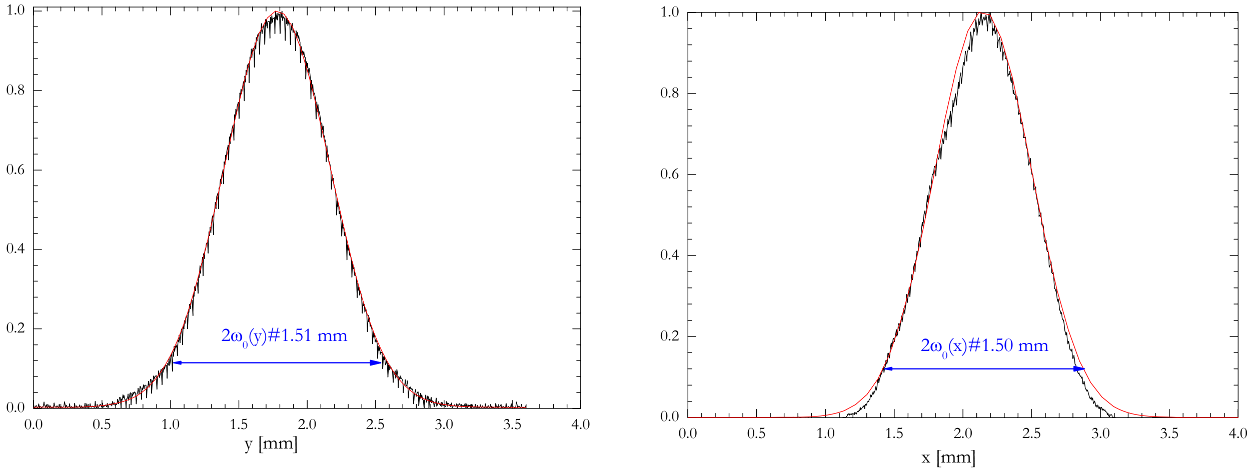

Figure 7.7 Measured laser beam intensity profiles within the probe volume, along y and x-axes.

To test Gaussian beam effect we produced with the piezo-jet injector streams of 400~500µm mono-disperse bubbles in interval of 4Hz (see §4.2.1). Statistics were performed over 100 bubbles, then the stream of bubbles (rising up along the y-axis for a given x and for z=0) was moved along the x-axis with the micro-displacement system (steps: -900, -800…900µm).

7.1.3 Experimental results and comparisons with the theory

The bubbles were analyzed with the micro-video system and with the CARS system (inverse method: LSQ-LMT-LogNorm.). Figure 7.8 show a typical micro-video image and the CSP of a bubble localized at $x,y,z \approx 0\mu m$. Figure 7.9 shows the results of the analysis of the previous CSP. Indeed, for all results presented in this section the bubble mean diameter is $\bar{D} \approx 465$µm and the size distribution is very narrow ($\sigma/\bar{D} \approx 0.05$, close to the resolution limit of both methods – see chapter 5). Figure 7.10 compares experimental results (averaged over 100 bubbles) and numerical results for the above parameters. The agreement is extremely good. Even the high frequency fringes are observed. Note that the dynamic of the experiment signals is a little bit smaller than for the numerical ones, but this may be attributed to the CCD electronic and scaling effects.

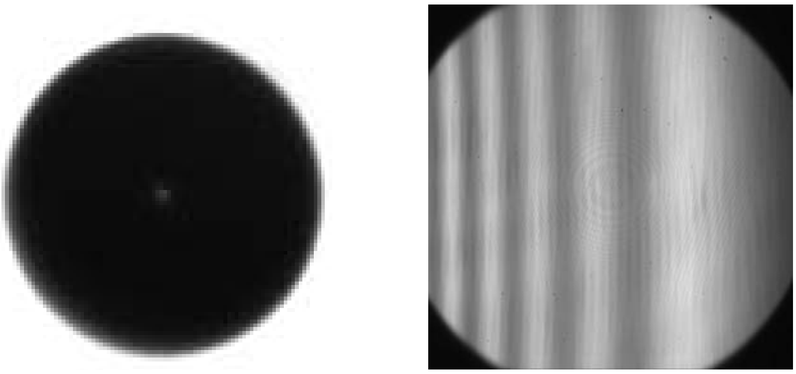

Figure 7.8 Typical micro-video and CSP images for mono-disperse bubbles at the center of the probe volume (x=y=z=0)

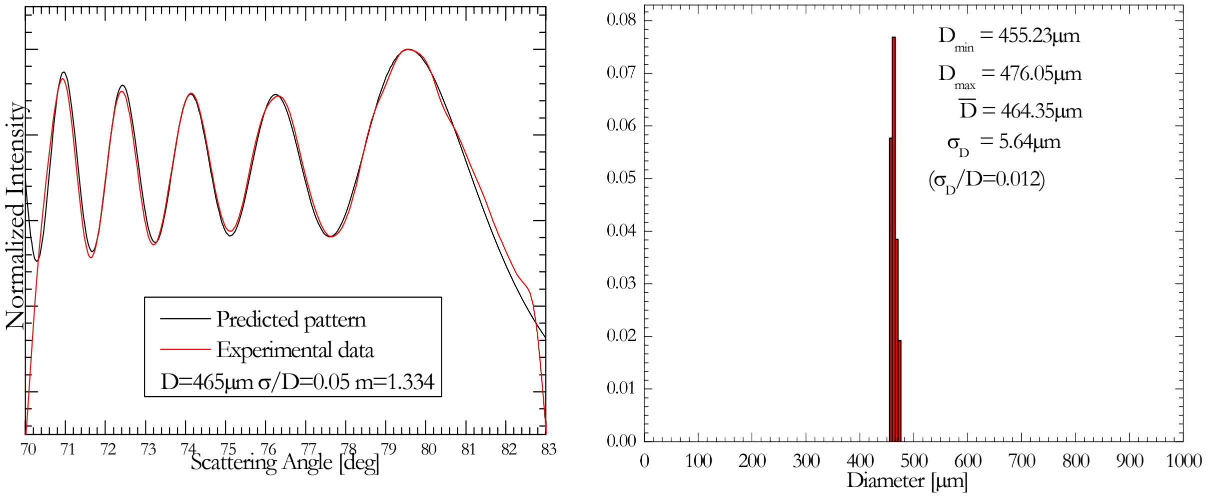

Figure 7.9 Experimental and reconstructed CSP profiles corresponding to Figure 7.9, and the size distribution obtained with the LSQ-LMT inverse method.

To go in this way we have reduced the probe volume size by focusing with a spherical lens the laser beam down to $2\omega \approx 75\mu m$. In that case the bubbles are almost six time bigger that the nominal probe volume diameter. Note that the trajectories of bubbles generated with the piezo-jet are close to a pure vertical line but, as there is some recirculation and wakes in the tank, there is some jitter in their trajectory. So that, with an injector at few centimeter from the probe volume, it was not possible to control the position of the bubble at better $\approx 100\mu m$ over x and z. Figure 7.12 shows six CSP intensity profiles selected randomly from a set of one hundred of them. Figure 7.13 displays the mean CSP obtained by adding one hundred CSP, the size distribution obtained with the micro-video system. Table 7.1 compares statistics obtained with both methods, there are in very good agreement provided that bubbles are really random trajectories in the probe volume.

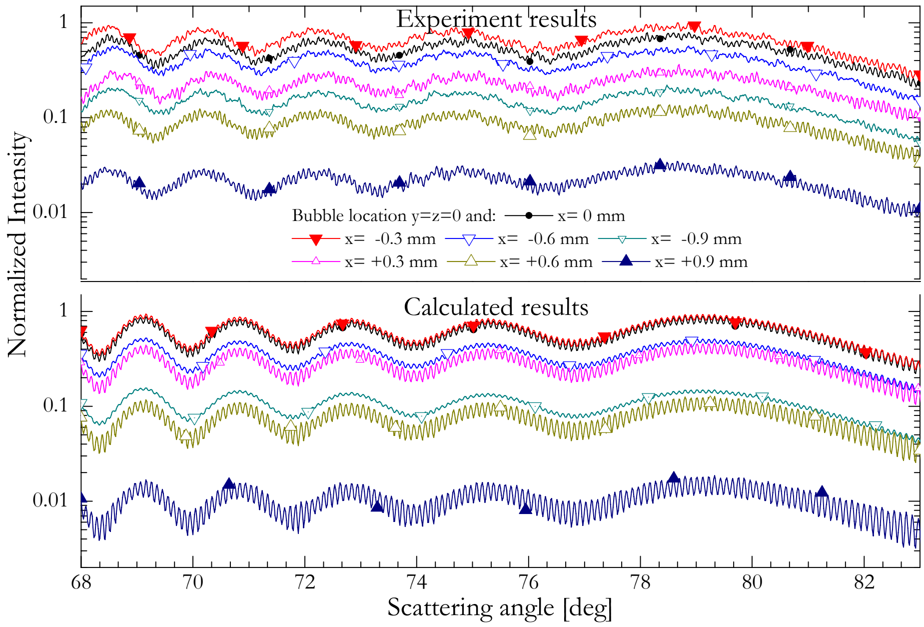

Figure 7.10 Comparison of experimental and numerical critical scattering diagrams averaged over 100 air-bubble in water with diameter 465µm, a laser beam diameter of 750µm and $\lambda = 0.532\mu m$.

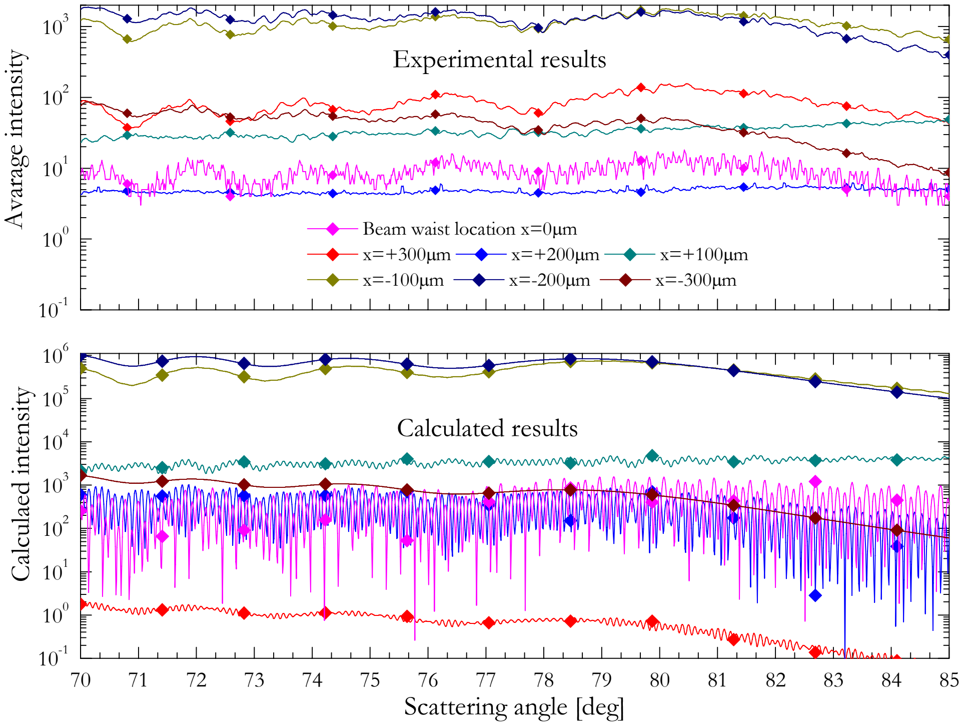

Figure 7.11 Same parameters as in Figure 7.10 but for a single bubble and a probe volume diameter of 75µm.

To conclude on that part let first point out this important result: bubbles can have rather random trajectories within the probe volume, their CSP can be complex and impossible to analyze individually (see Figure 7.12), if we average many of these CSP we get an average CSP that can be analyzed without any difficulty (see Figure 7.13). Indeed, all is like Gaussian beam effects compensate each other when integrating over a large number of bubbles and trajectories. It means that, these effects are totally negligible when we use the CARS technique as a spatial integrating technique (i.e. large laser beam).

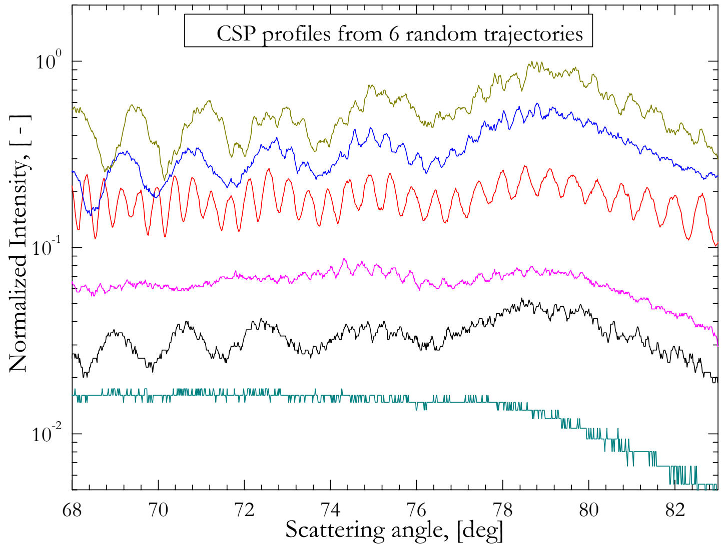

Figure 7.12 CSP intensity profiles for six random trajectories within the probe volume.

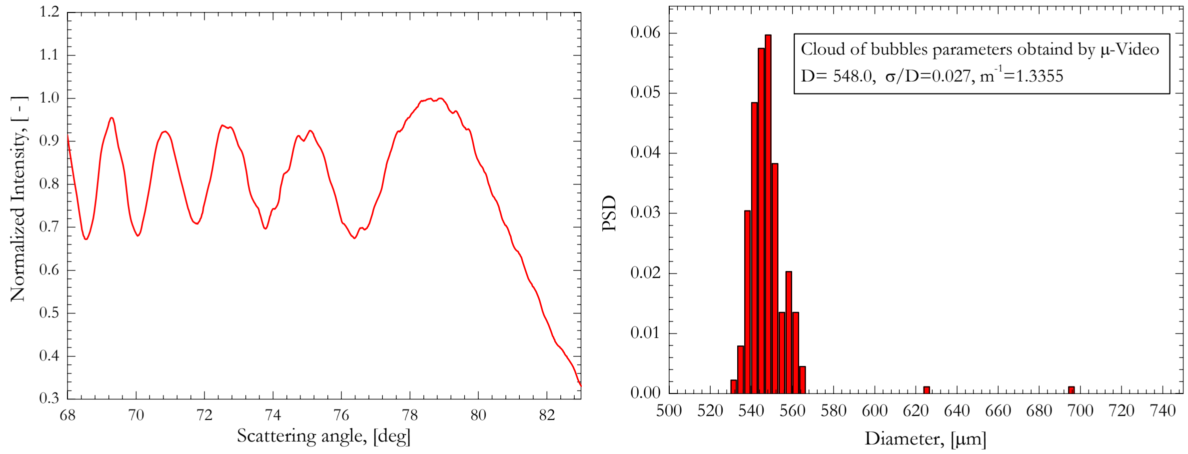

Figure 7.13 Mean CSP over 100 single bubbles and trajectories, size distribution obtained with the micro-video system.

	D [um]	σ/D [-]	m^{-1} [-]
Micro-Video / Abbe refract.	548,0	0,027	1,3355
Full-LSQ-LMT	523,0	0,025	1,3375
3points-LMT	456,0	0,030	1,3400

Table 7.1 Comparison of statistical results for 100 bubbles with random trajectories within the probe volume.

7.2 Spatial filter effects

7.2.1 Necessity and limit

In section §4.3 we explained that the collection optics of the CARS system requires an "optical diaphragm" or "spatial filter" (see Figure 7.15). In fact, the aperture of the collection optics is already limited by the clear aperture of all lenses. But, it is well known that to limit optical aberrations, barrel effects, etc. it is better to use only the center of lenses. Nevertheless, by doing this, we also reduce the useful angular range of the optical system. There is an additional and more constraining reason to integrate a spatial filter into the collection optics: it is to control the probe volume width. Indeed, the nominal probe volume of the CARS system is limited by the laser beam diameter but the collection optics aperture. Note that the effective probe volume size depends also of the laser beam power and the camera amplification settings. Without any spatial filter, the width of the nominal probe volume would be too large. Indeed, a large probe volume width means a lower spatial resolution of the system (which is not interesting from the fluid mechanics view point) and more optical aberrations related to bubble side locations within the probe volume. As an example, Figure 7.14 compares CSP images recorded when the spatial filter is fully opened and a stream of mono disperse air-bubbles is passing through the center of the probe volume, or on the edge of this one (large z, see Figure 7.1) . It is clear that in both cases the fringes are located at the same positions (absolute angular measurement) but that the intensity transmitted by the optics depends on the bubble location (CSP are weighted by the transmission of the collection optics).

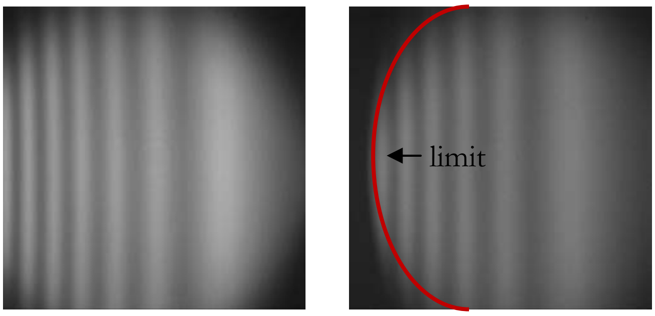

Figure 7.14 CSP images of a stream of mono disperse air-bubbles in water when the spatial filter is fully open: on the left, when bubbles pass through the center of the probe volume; on the right right, when they pass of the edge of the probe volume.

7.2.2 Experimental setup and results

7.2.2.1 Setup and procedure

To investigate the effect of the spatial filter aperture onto the CARS technique we consider three cases: 1st case, the spatial filter (optical diaphragm with round aperture) is fully open so that its clear aperture is of 23mm; 2nd case its clear aperture is reduced to 13mm; 3rd its clear aperture is only 6mm. The nominal laser beam diameter was of 15 mm.

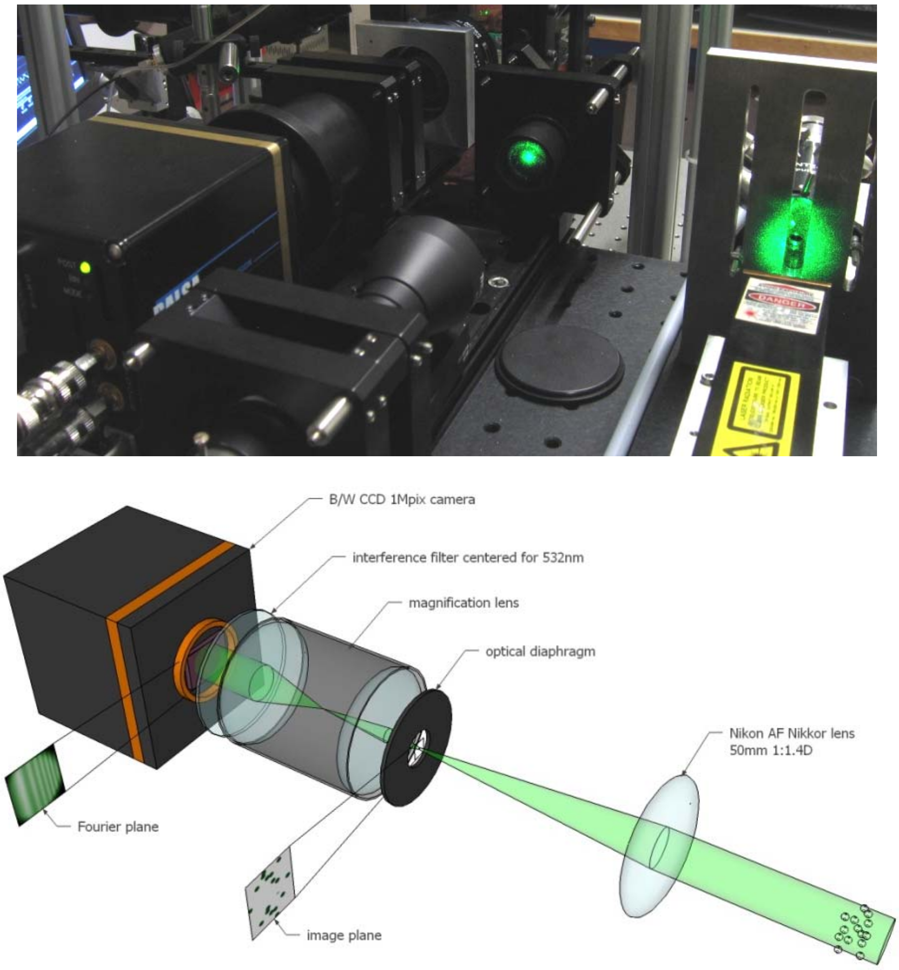

Figure 7.15 Image and schematic of the collection optics

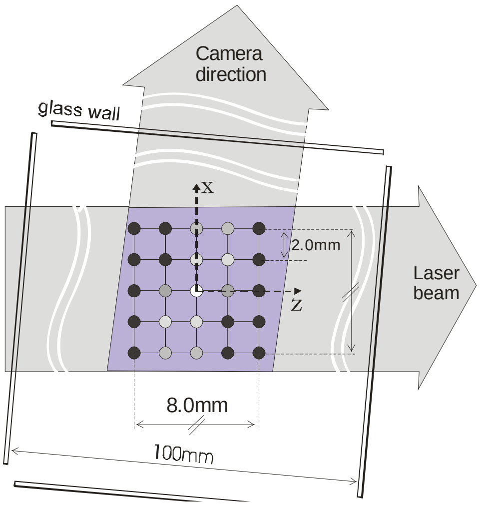

Figure 7.16 Cartesian mesh of the micro-displacement system used to localize the stream of monodisperse bubbles within the probe volume.

To generate well controlled stream of D=465µm air-water bubbles we have used the piezo-jet fixed onto the micro-displacement system (see § 7.1.2). With the latter system we create a Cartesian mesh of 8 x 8mm with steps of 2mm. Due to experimental constraint the mesh was parallel to the laser beam axis, making an angle of $\approx 14°$ with the collection optics optical axis, see Figure 6.16

7.2.2.2 Results

Figure 7.17 and Figure 7.18 show results obtained for case 1 (spatial filter fully open) and the 25 nodes of the probe volume's mesh. Figure 7.17 displays the CSP averaged over 100 bubbles. Figure 7.18 shows the corresponding intensity profiles. To simplify the understanding of these results let's point out that, as a first approximation, results in the same "column" (i.e. $\approx x - axis$) are mainly sensitive to the laser beam intensity profile whereas, results in the same "row" (i.e. $\approx z - axis$) are more sensitive to spatial filter effects. For this first case, we can already remark that the intensity of CSP change with locations of the bubble within the probe volume. In colons, CSP intensity profiles change but without significant modification in shape. In rows, the shape of the CSP intensity profiles change on the side ways. Indeed, when the bubbles are on the probe volume side $z > 0$ a part of the light they scatter at $\theta < \theta_c$ is blocked by the collection optics. In opposite, when the bubbles are located in the $z < 0$ side of the probe volume, it is the light scattered at $\theta > \theta_c$ that is blocked.

All these effects are much more pronounced for the second case (intermediate aperture), see Figure 7.19 and Figure 7.20 ; and the third case (small aperture), see Figure 7.21 and Figure 7.22. For the intermediate spatial filter aperture, the shape of the CSP is only "normal" for bubble positions corresponding to the interval $|\Delta z| \leq 4mm$. For the smallest spatial filter aperture, the CSP are almost invisible for $|\Delta z| \geq 6mm$, strongly perturbated for $|\Delta z| = 2mm$ and somewhat perturbated for $\Delta z \approx 0mm$.

Looking at the previous results one can be afraid about the influence of the disturbed CSP to CARS measurements. However, to conclude on that point, let first remember that, under real bubbly flow conditions, bubbles have random trajectories within the probe volume. It is the reason why, in Figure 7.23 to Figure 7.25, we compare for the three spatial filter apertures: the CSP obtained when bubbles are passing through the center of the probe volume with the average CSP obtained for all bubble positions in the probe volume (all CSP presented respectively in Figure 7.17 to Figure 7.19). The results are clear: the smaller is the spatial filter aperture, the smaller is the distortion of the averaged CSP. So it means that the spatial filter avoid excessive optical aberrations in the collection system and allows better measurements, see also Table 7.2.

	Bubble at the center			Average CSP/positions		
Spatial filter aperture [mm]	$\bar{D}$ $[\mu m]$	$\sigma / \bar{D}$ $[-]$	m $[-]$	$\bar{D}$ $[\mu m]$	$\sigma / \bar{D}$ $[-]$	m $[-]$
23	600	0,030	1,3350	612	0,030	1,335
13	614	0,010	1,3350	625	0,015	1,3345
6	604	0,010	1.3350	605	0,010	1,3350

Table 7.2 Effet of the spatial filter aperture onto CARS measurements.

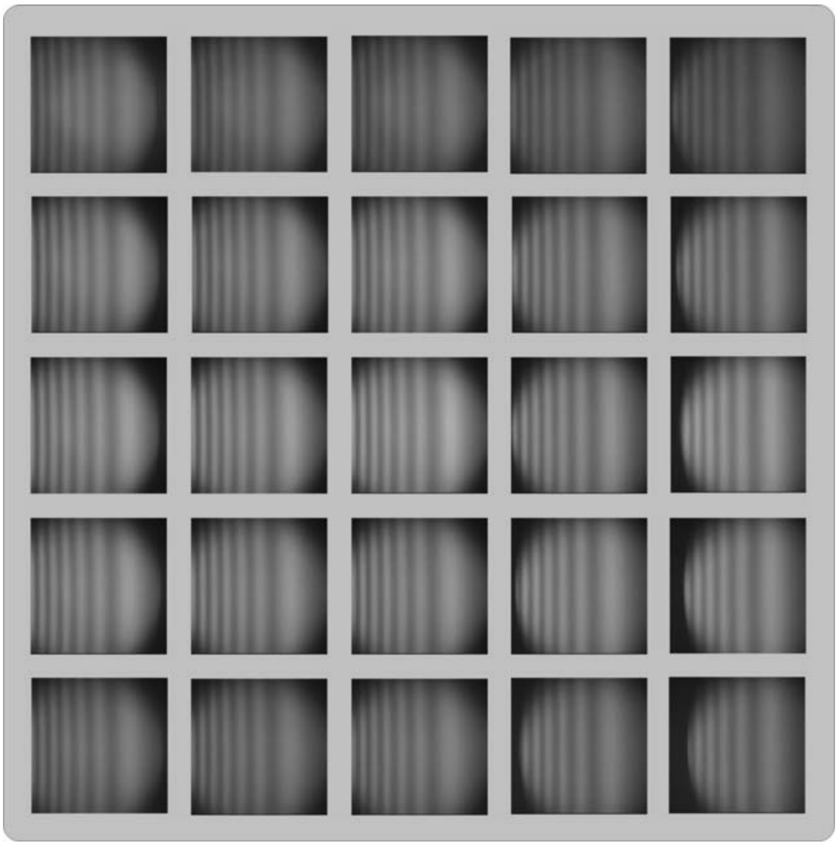

Figure 7.17 For full spatial filter aperture (1st case, 23 mm): recorded CSP for bubbles localized at the nodes of the spatial mesh of the probe volume.

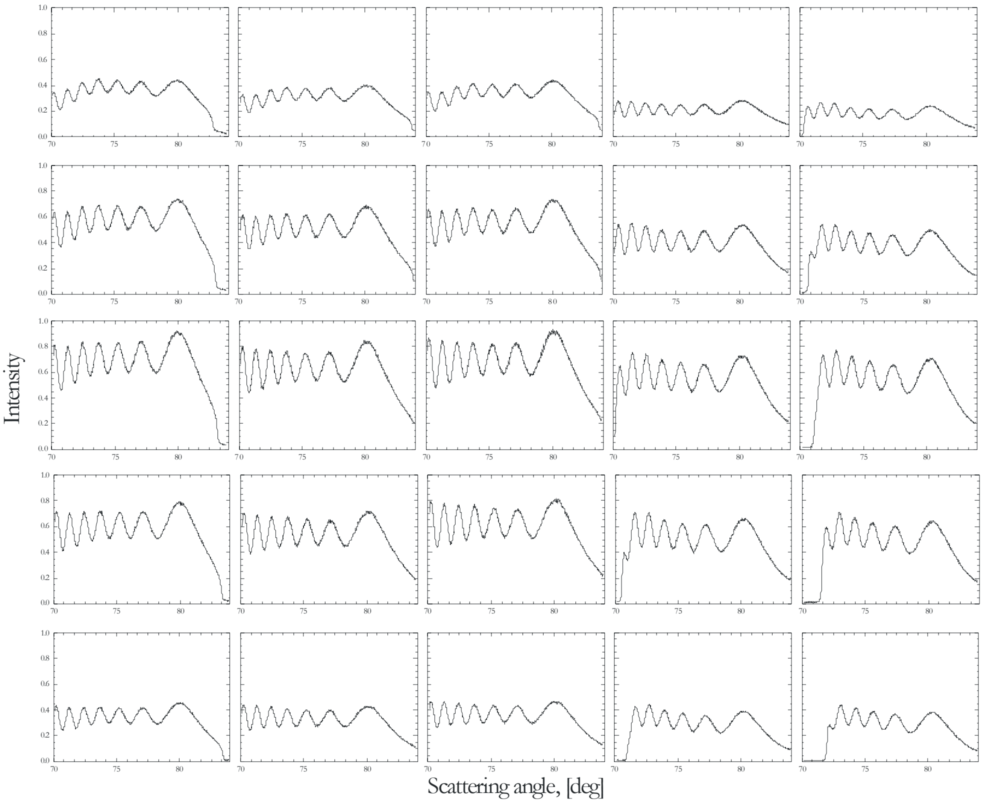

Figure 7.18 For full spatial filter aperture (1st case, 23 mm): intensity profiles for bubbles localized at the nodes of the spatial mesh of the probe volume.

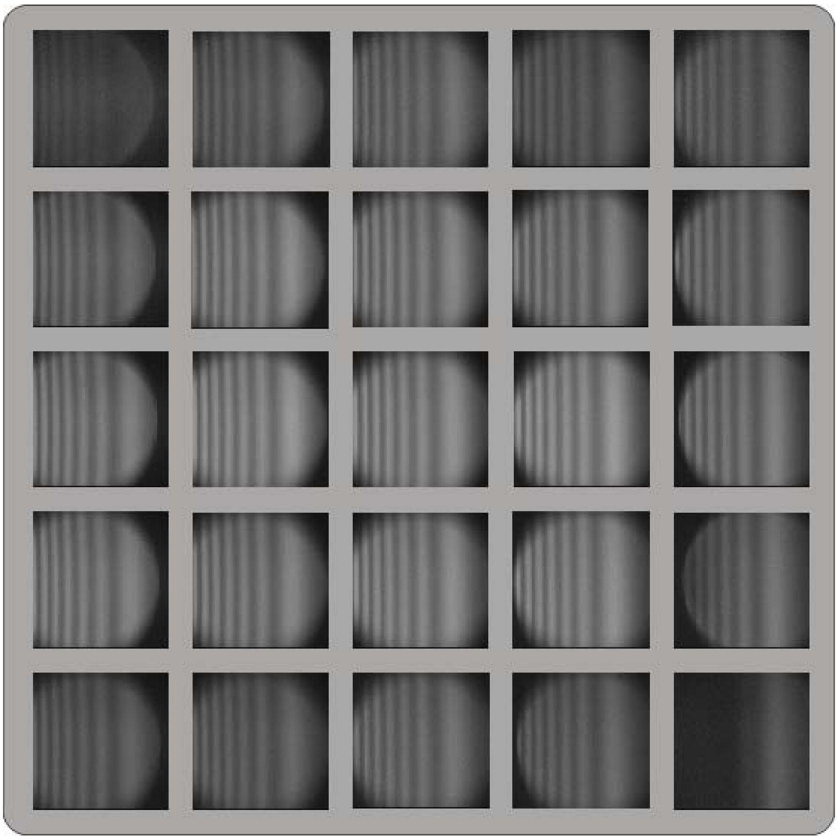

Figure 7.19 For intermediate spatial filter aperture (2nd case, 13 mm): recorded CSP for bubbles localized at the nodes of the spatial mesh of the probe volume.

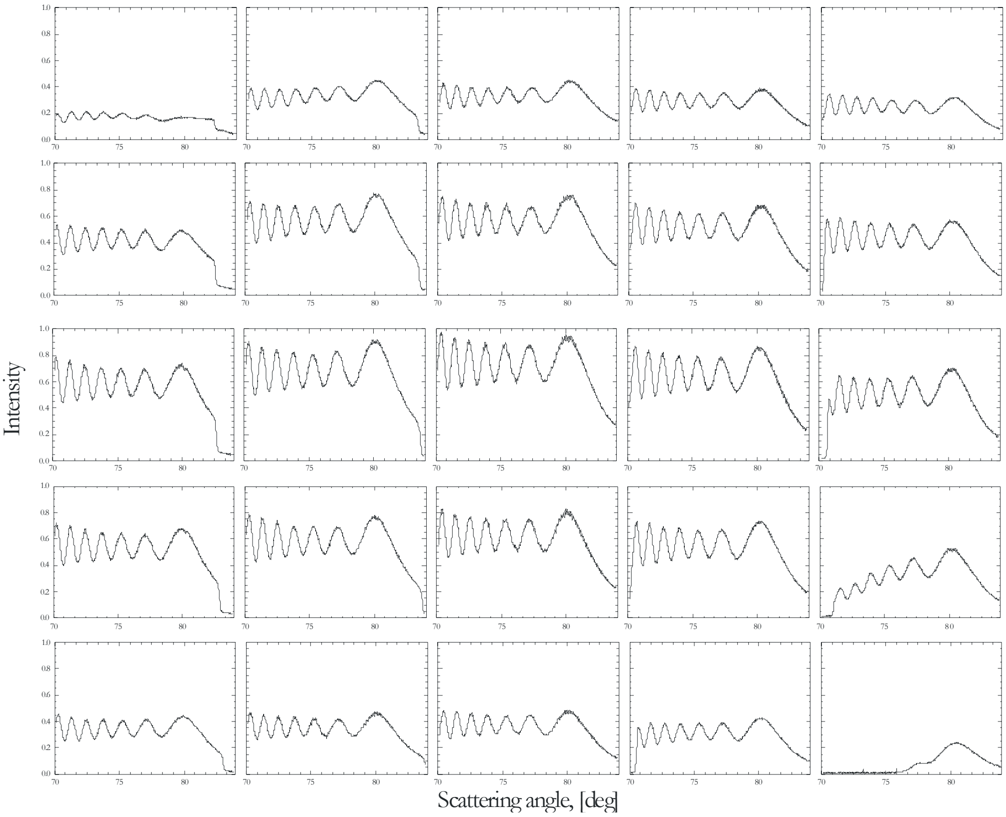

Figure 7.20 For fully open spatial filter (2nd case, 13 mm): intensity profiles for bubbles localized at the nodes of the spatial mesh of the probe volume.

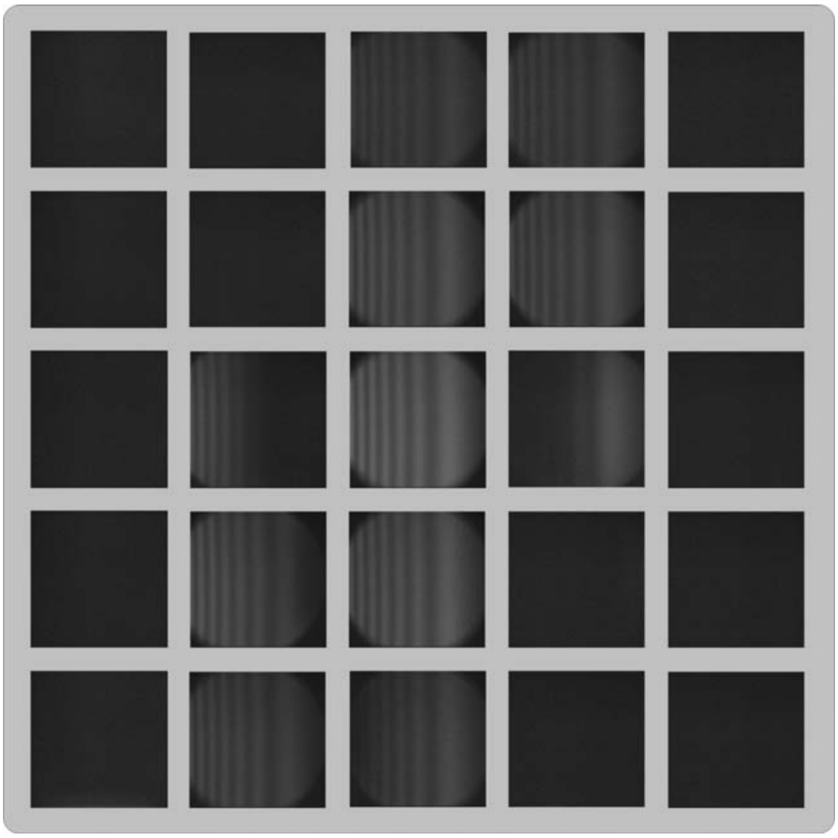

Figure 7.21 For reduced spatial filter aperture (3rd case, 6 mm): recorded CSP for bubbles localized at the nodes of the spatial mesh of the probe volume.

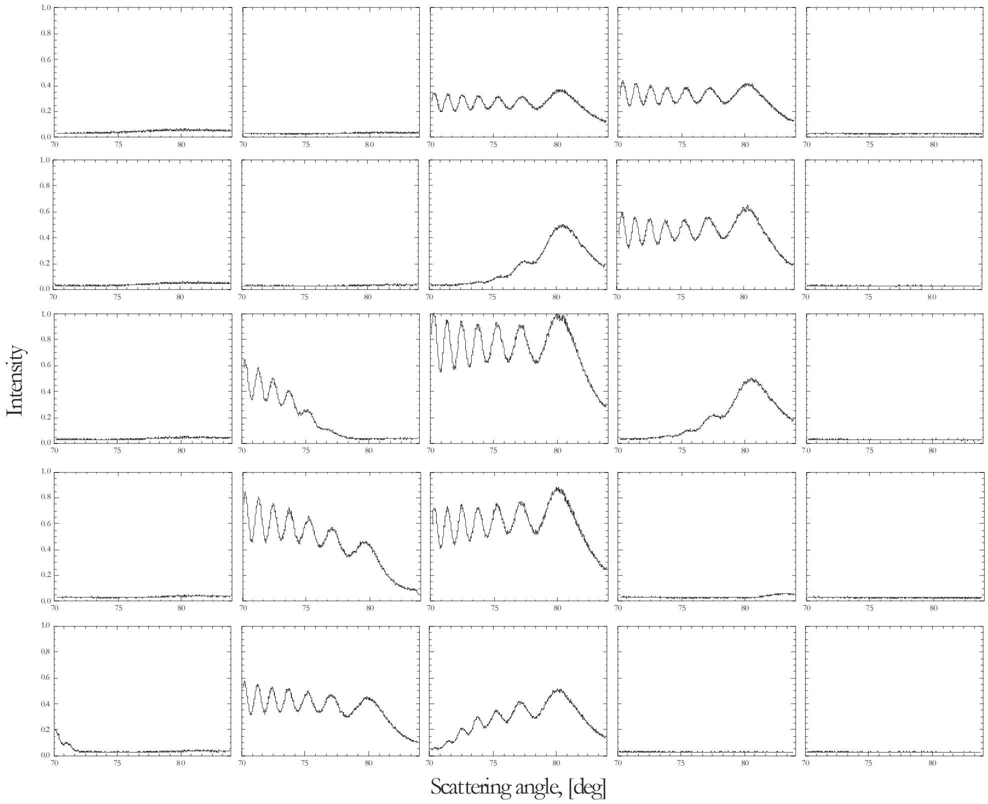

Figure 7.22 For reduced open spatial filter (3rd case, 6 mm): intensity profiles for bubbles localized at the nodes of the spatial mesh of the probe volume.

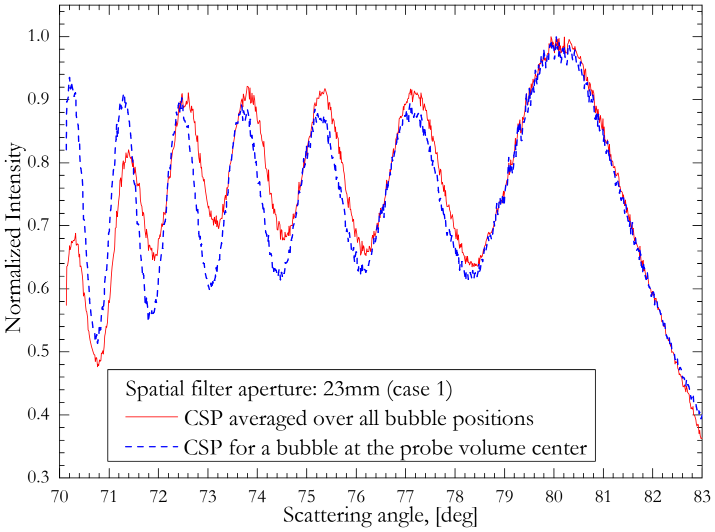

Figure 7.23 Comparison of CSP obtained when bubbles are passing through the center of the probe volume with average CSP obtained for all bubble positions in the probe volume, large spatial filter.

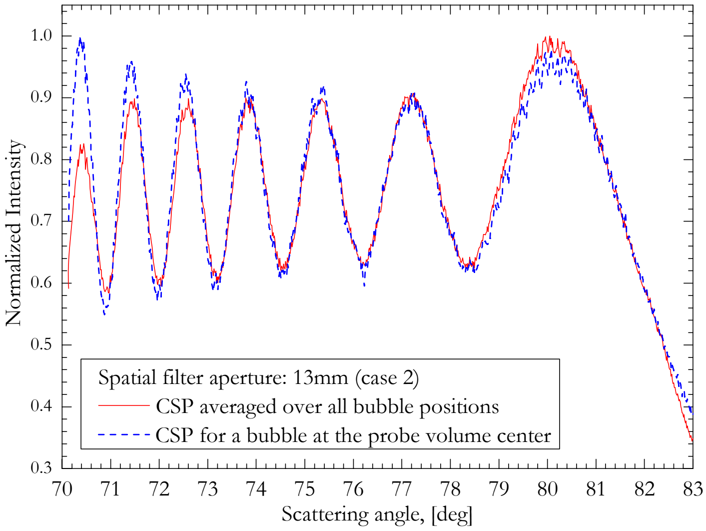

Figure 7.24 Like Figure 7.23 but an intermediate spatial filter aperture.

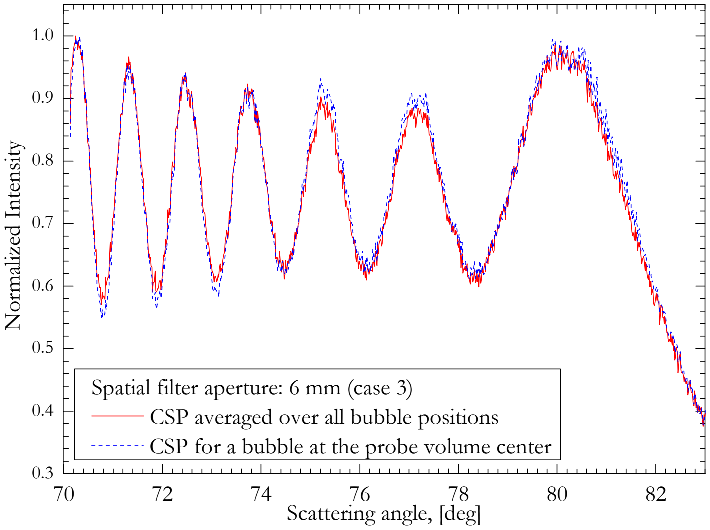

Figure 7.25 Like Figure 7.23 but for a small spatial filter aperture.

7.3 Conclusions

Gaussian beam and spatial filter effects weight the intensity of critical scattering diagrams. For highly focused laser beam and small spatial filter aperture, their effects are significant. Both effects can highly distort the CSP so that the latter cannot be analyzed with conventional inverse methods. With GLMT, Gaussian beam effects can be investigated numerically but, for spatial filter effects, we do not have the corresponding numerical tools.

Mixing numerical and experimental investigations we can nevertheless draw some conclusions on both effects:

- Gaussian beam or "trajectory" effects compensate each other for bubbles passing with random trajectories in the probe volume. If the bubbles are much smaller than the laser beam diameter, the CARS analyze is insensitive to Gaussian beam effects even for bubbles with a particular position within the probe volume.

- The intensity of the laser beam controls the width of the probe volume (i.e. its dimension along the collection optics optical axis, $\approx$ x-axis).

- The spatial filter controls the probe volume length (i.e. its dimension perpendicular to the collection optics optical axis, $\approx$ z-axis), but it produces distorted CSP when bubbles pass on the side ways of the probe volume.

- The distortions induced by the spatial filter are more or less symmetric in respect to the collection optics optical ($\approx$ x-axis). They cancel each other for bubbles with random trajectories within the probe volume. This is particularly true for the smaller spatial filter aperture. It is the reason why, for the measurements presented in other chapters, we have chosen an aperture width of 10 mm and we have got good results for real bubbly flows (see Chapter 5).

Chapter 8

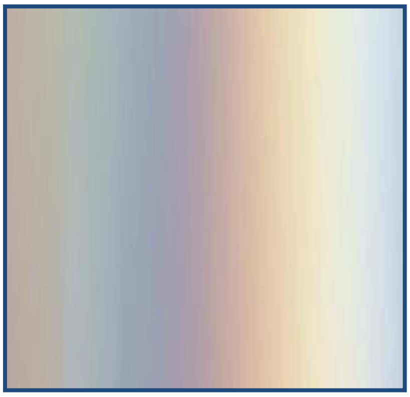

BOWS OF COLORS PRODUCED BY CRITICAL SCATTERING – A NATURAL PHENOMENA-

8.1 Introduction

According to geometrical optics the critical scattering angle $\theta_c = \pi - 2\sin^{-1}(m)$ depends only on the bubbles relative refractive index $m = m_b / m_s < 1$. It means that CSP are sensitive to the equation of dispersion of the materials that compose the bubbles and their surrounding medium. According to the physical optics approximation, the critical scattering is the result of the diffraction of reflected rays at the vicinity of the total reflection angle. For spherical bubbles, critical scattering produces fringes or "bows" that are axisymmetric with respect to the beam optical axis and with a large cone angle. On the other hand, we have mentioned in the introduction that there are great similarities between critical scattering, rainbow scattering and forward diffraction.

On the basis of these arguments and remarks, we can assume that bubbles could create bows of colors at the vicinity of the critical scattering angle. Then two questions come out: can we observe these bows of color in Nature ? Could we use them for some metrological applications ? In this last chapter, we try to answer both questions for air-bubbles in water, giving comparisons with rainbows produced by water droplets in air (as a symmetrical or reverse case)

8.2 Modeling of white-light scattering patterns

To investigate the dependency of critical scattering patterns (CSP) with the dispersion of bubble material as well as the spectral bandwidth of the input beam, we have used the Lorenz-Mie theory (LMT).

To predict the spectral irradiance of Sun, we use the Planck's law with a black body at T=5777°K:

$$I(\nu,T)=\frac{2h\nu^3}{c^2}\frac{1}{e^{\frac{h\nu}{kT}}-1} \tag{147}$$

where $h \approx 6.626\ 10^{-34}\,\mathrm{Js}$ is the Planck's constant, $c \approx 2.998\ 10^{8}\,\mathrm{m/s}$ is the speed of light in vacuum, $k = 1.381\ 10^{-23}\,\mathrm{J/K}$ is the Boltzmann's constant, ν the frequency of electromagnetic waves and T the temperature of the emitting source. The above irradiance will be used as an input function in the LMT to adjust the incident plane wave intensity for a specific wavelength, $\lambda = c\nu^{-1}$. Figure 8.1 shows the spectral emission of black bodies at different temperatures.

With thermal sources or large spectral bandwidth it is not possible to get a perfectly collimated beam over a long distance, so that we have to take into account the beam divergence. From Earth, it is usually admit that Sun's angular aperture is about $\sim 0.4^o$. This will be our divergence angle over all spectrum. Classically, the divergence of the incident beam will be threaded as a low path angular filter to be applied to the scattering diagrams. At the ground level, we consider the Sun light has an unpolarized.

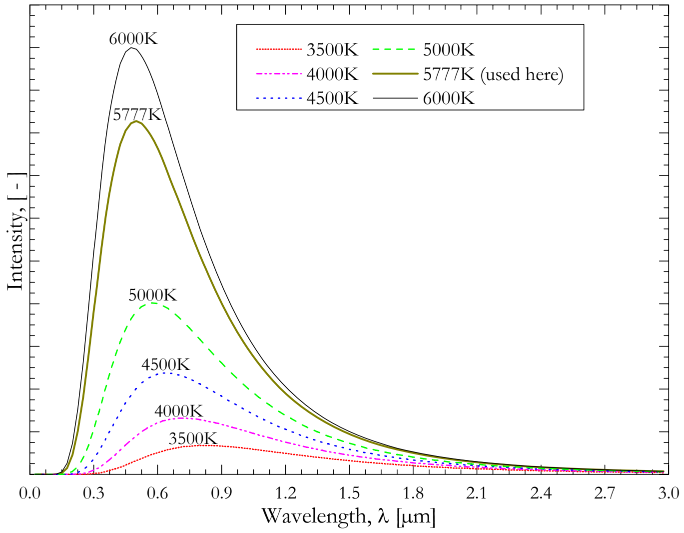

Figure 8.1 Spectral irradiance of the black body T=5777°K.

According to Birch K.P. et Downs M.J. (1994) refractive index for air is equal to

$$(n-1)_{tp}=\frac{(p/\mathrm{torr})\,(n-1)_s}{720{,}775} \times \frac{[1+(p/\mathrm{torr})\,(0{,}817-0{,}013\,3\ t/^\circ\mathrm{C})\ 10^{-6}]}{(1+0{,}003\,661\,0\ t/^\circ\mathrm{C})}. \tag{1'}$$

where

$$\left(\mathrm{m}_{air}-1\right)\times 10^{8} = 8342.54 + 2406147\left(130-\sigma^{2}\right)^{-1} + 15998\left(38.9-\sigma^{2}\right)^{-1} \tag{148}$$

where ($\sigma =$ k wave number in vacuum) $(m\text{-}1)_{tp}$ is a parameters that depends on air temperature and pressure. In the visible region (λ=405–705 nm) the following approximation is more convenient and gives a maximum discrepancy of only 1.4×10^{-8},

$$m_{air} - 1 = 0.0472326\left(173.3 - \sigma^2\right)^{-1} \tag{149}$$

For our conditions, we take a constant value for the refractive index $m_b \equiv m_{air} = 1.000237$. For the dispersion equation of water the things are more complicated. In fact there is many available data in the literature but they are not always totally consistent. In what follows, we use the data provided by Querry et al. (1991). Their spectral resolution is fine enough so that we do not need to interpolate them. Table 8.1 shows few values of the real and the imaginary parts of water's refractive index. The latter one is so small that it will be neglected in the next paragraphs. Figure 8.2 shows the equation of dispersion of water for T=24°C and pressure 1013,25hPa.

	Refractive index of water	
Wavelength [nm]	Real part	Imaginary part
299.9	1.371437	4.148E-9
444.6	1.344418	8.685E-10
590.2	1.333609	6.365E-9
734.5	1.327652	1.348E-7
879.0	1.324074	4.053E-7

Table 8.1 Water refractive index dependancy with wavelength

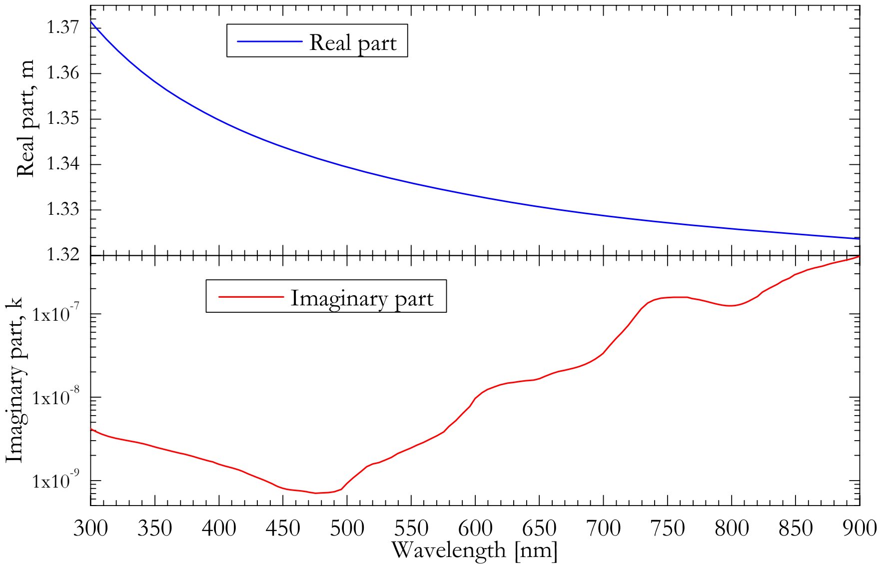

Figure 8.2 Evolution of the dispersion equation of pure water.

Our procedure to model white-light critical scattering patterns is the following one. For a given bubble size we calculate its CSP for a given wavelength and the corresponding refractive index. To take into account the beam divergence we filter out the CSP with a filter of angular width $\Delta\theta = \pm 0.2°$. We then repeat this operation for bubbles within the size range $D = 100 \sim 600\mu m$ with step $\Delta D = 5\mu m$, and the scattering angle range $\theta = 65 \sim 84°$ with step $\Delta\theta = 0.02°$. Figure 8.3 and Figure 8.4 show the diagrams respectively, for a collimated beam and a diverging beam.

Colors patterns are similar although, for the collimated beam finer structures are observed. The spacing of the colored fringes increases as far as we are getting closer to the critical scattering angle. These two diagrams exhibits a lot of similarities with the ones calculated by Lee (1998), for the rainbow.

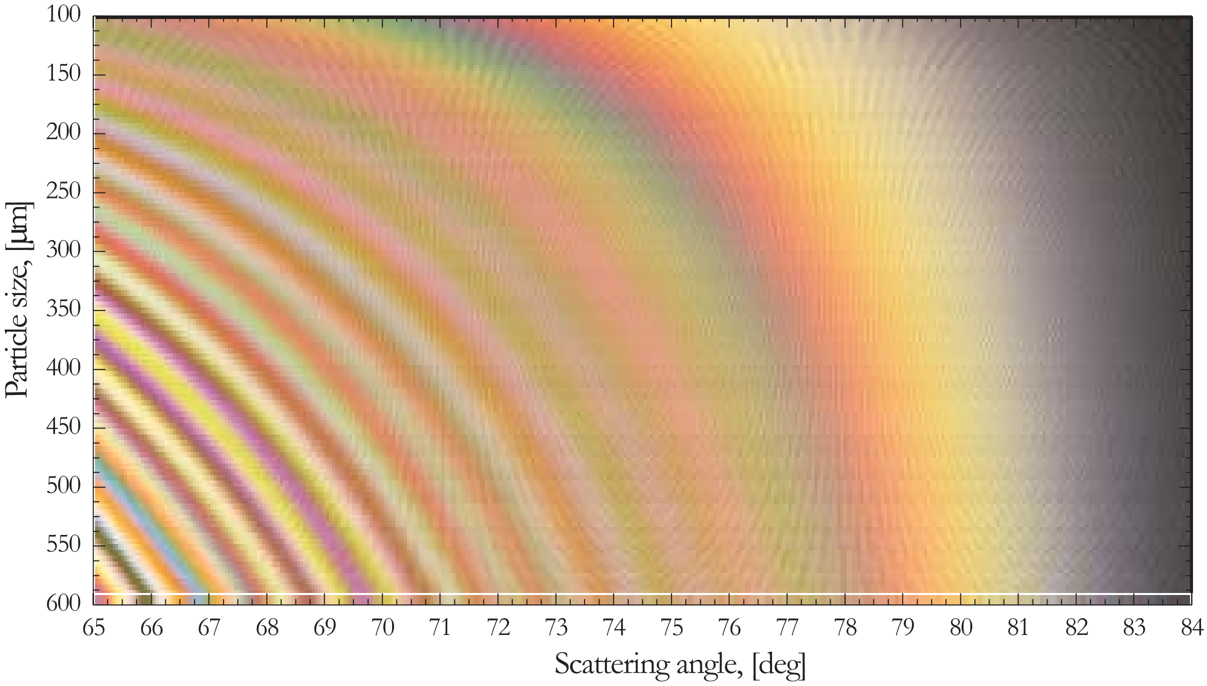

Figure 8.3 Simulation with LMTof the color intensity of the critical scattering diagrams produced by mono disperse air-bubbles in water, under a collimated white-light beam illumination.

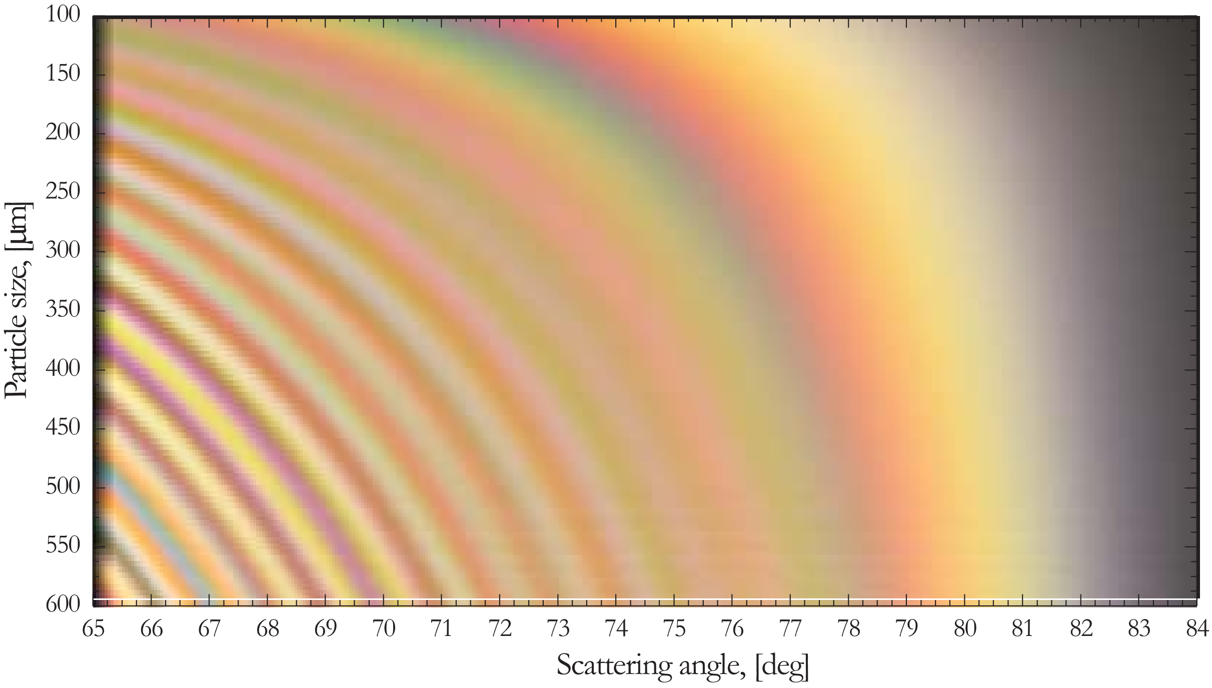

Figure 8.4 Same parameters as in Figure 8.3 but for a slightly diverging white-light beam illumination.

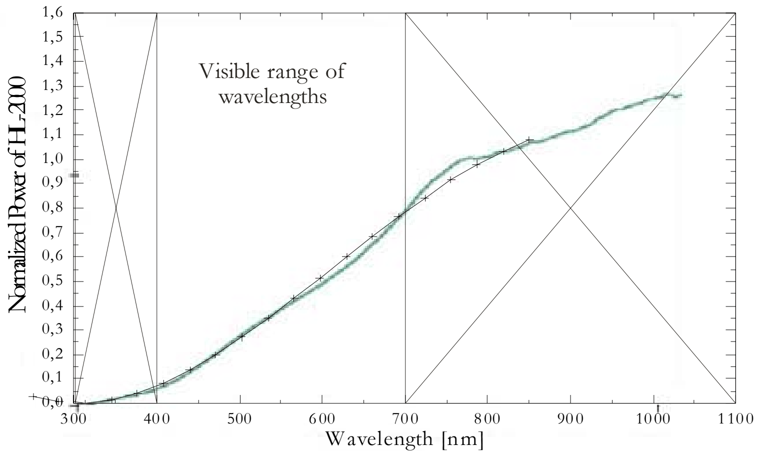

Figure 8.5 Emmission spectrum of the Microtek HL-2000 lamp (polynomial fit with symbols).

8.3 Preliminary experimental results

To observe critical bows of colors in laboratory environment we must use a wide spectra light beam. To do so, we have utilized an fiberized and stabilized halogen lamp from Ocean Optics (Microtek HL-2000). Figure 8.5 shows (in blue) the output spectrum of this thermal source. For computational efficiency reasons, we have fitted this spectrum with a third order polynomial function: $I(\lambda)=A+B_1\lambda+B_2\lambda^2+B_3\lambda^3$ with for the constants: $\mathrm{A}=1.0658009$, $\mathrm{B}_1=-0.0078540$, $\mathrm{B}_2=1.7128427\ 10^{-5}$ and $\mathrm{B}_3=-9.25925926\ 10^{-9}$. The piezo-jet was used to produce a cloud of monodisperse air bubbles in water, with $\overline{D}=420\mu m$ and $\sigma/\overline{D}=0.01$. To record the multi-wavelength CSP we have used a color CCD camera from "The Imaging Source" (see §4.5). The latter was equipped with a Nikkon camera lens in a Fourier configuration. The white balance of the camera was adjusted carefully using a color reference target.

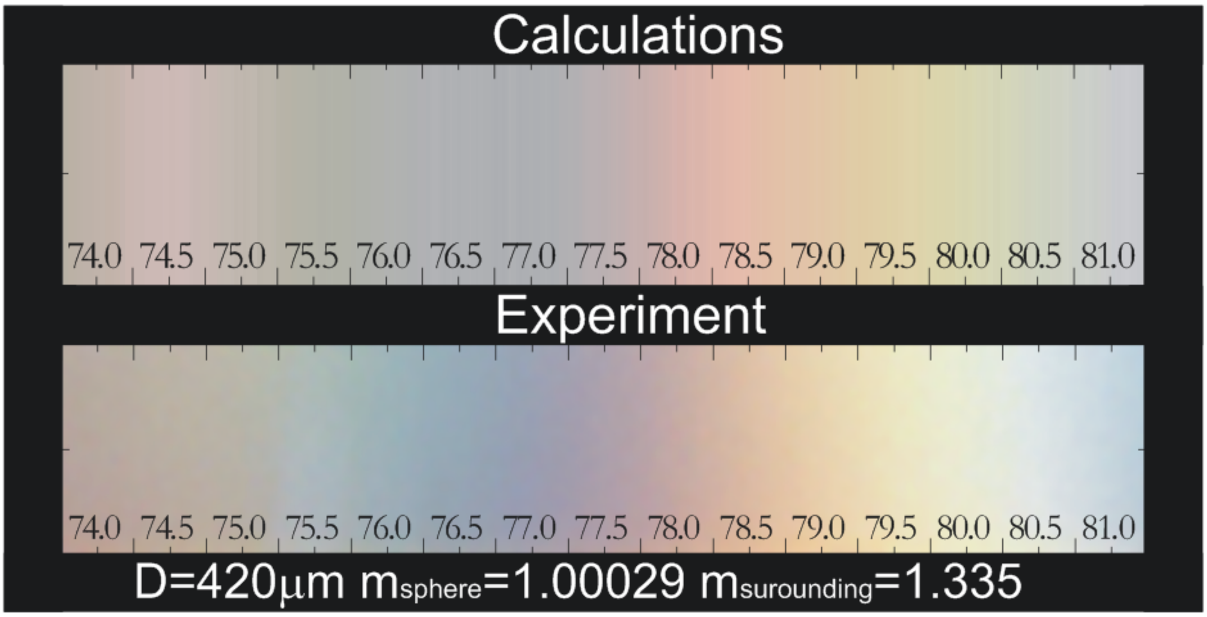

Figure 8.6 Critical bows of colors: numerical and experimental critical scattering patterns produced by monodisperse air-bubble in water lighted with a collimated white-light beam

8.4 Conclusion

In this chapter we have shown numerically that critical scattering phenomenon can generate bows of color in the same way that the rainbow does (e.g. Lee, 1998). This phenomenon has also been observed experimentally, however we did not have enough time to perform more detailed experiments and more specially, concerning the influence of the width of the bubble size distributions. However, from numerical results we can already conclude that bows produced by the critical scattering patterns are more spread angularly than the ones observed for the rainbow. It implies that colors are more difficult to distinguish. In addition, as for air-bubbles in water the critical angle is close to 90°, the fringes are less curved than those of the rainbow. Indeed, the bows produced by the critical scattering look like parallel fringes than circular ones. This is not detailed as, clearly, one of the main distinguishing property of the rainbow is the fringes curvature. On the other hand, we know that CSP are more sensitive to bubble sizes than the rainbow is sensitive to droplets diameter. As a consequence, for polydisperse bubble size distributions, the color of CSP should be more dumped by the size distribution width than the rainbow. In our opinion, if it can be observed, the critical scattering in Nature must be an underwater phenomenon. If true, it is expected to be sensitive to the refraction angle of Sun rays through the water surface. We have tried to observe this phenomenon in sea water, around midday, looking at the bubbles produced by the breaking of waves. But we did not succeed yet.

From the metrological point of view, it is obvious to conclude that additional colors could give us more information about the bubbles properties. When we are dealing with very polydisperse bubbles for instance, the CARS technique is limited by the CSP-visibility which tends to zero. With a second laser beam, with a different wavelength, this problem could be solved.

Chapter 9

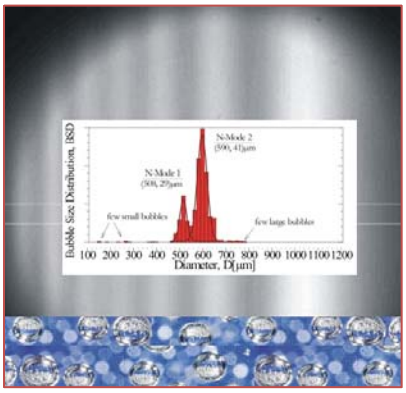

CONCLUSION AND PERSPECTIVES

This manuscript present the Ph. D work completed in "cotutelle" between the laboratory IUSTI UMR CNRS n° 6595 (Marseille, France) and the Chair of Electronics and Photonics (Wroclaw, Poland). The main objective of this work was to study the properties of the critical scattering pattern produced by a cloud of bubbles. Second, to propose a new optical method, based on this phenomenon, which allows inferring the bubble clouds properties (size distribution and refractive index) for fluid mechanics applications.

After an introduction, the first part of this manuscript concerns the development and the test of models and theories to predict the scattering of a single and spherical bubble. We have found that the Lorenz-Mie theory (LMT) is the only one which is sufficiently accurate for all aspects of the problem. The Debye and Complex Angular theories were considered as in adapted. The physical optics approximation (POA) from Marston (Marston 1979) has some interest for applications requiring fast calculations with limited computational resources (i.e. integrated sensor). In fact, from POA we can obtaine useful analytical relations that allow getting directly from the CSP the bubble mean size and refractive index (Onofri 1999a, Onofri et al. 2007a-b).

To model the scattering of a cloud of bubbles we have assumed a single scattering regime, so that the intensity profile is described by a Fredholm integral equation of the first kind. To access to the bubble clouds properties it is necessary to develop inverse methods. We have developed several of them. The best method is based on the resolution of the discretized Fredholm integral with a non negative least square method (NNLSQ). We have also developed methods based on some correlation estimator or fitting functions (LSQ, 3-points methods). Numerical studies were performed to tests, with success, the stability and resolution of these inverse methods, using LMT or POA as scattering theories.

To test all basic assumptions, as well as scattering models and inversion procedures, we have built up a complete optical and mechanical setup. The optical setup to record critical scattering patterns (CSP) is called “critical angle refractometry and sizing” (CARS) system. It allows recording the CSP produced by all bubbles within a probe volume of $\approx 1cm^3$. In this experiment, bubbles are produced by different injectors: piezo-jet on a micro-displacement system, assisted jet, porous injection system, etc. To validate the experimental results obtained with this new optical method we have built two additional optical sizing systems: a micro-video imaging system (MVIS) operating as a shadowgraphic system and an interferometric laser imaging droplet sizing system (ILIDS).

Our experimental results show clearly the accuracy of the models and the inverse methods we have developed, as well as the resolution and reliability of the CARS system. For all cases we have found a good agreement with reference techniques, for the bubbles mean size, size distribution width and refractive index (Onofri et al. 2009a, 2010). This was proven for several bubble/surrounding medium compositions: air/water, air/ethanol solution, water/silicon oil, etc. It is important to point out that, from these tests, it appears to us the CARS technique is more suitable for denser flows than conventional imaging techniques (MVIS, and ILIDS).

To further improve the CARS technique we have investigated various effects: bubbles non sphericity, Gaussian beam intensity profile and spatial filter effects. For the two latter cases, we have shown that for bubbles with random trajectories in the probe volume these effects are naturally compensated. However, for some particular flows, composed of a regular stream of bubbles, caution must be paid to centre the bubbles within the probe volume. For non sphericity, we have demonstrate that CSP of ellipsoid bubbles without tilt angle correspond to the ones of spherical bubbles with a diameter equal to the ellipsoid axis length in the scattering plane. For tilted ellipsoids, the measured diameter is a rather complex mixing between different radiuses of curvature of the ellipsoids surface, around the scattering plane. We have proposed two approaches to infer the equivalent spherical diameter of ellipsoids: from the analysis of the curvature of CSP fringes and to use some hydrodynamics assumptions. We have also studied the scattering of a white-light beam by a cloud of monodisperse bubbles. As a model of Sun light, with beam divergence, it was shown numerically that the CSP obtained under such conditions should exhibits colours that make the CSP quite similar to the rainbow observed in Nature. This was observed experimentally, but we did not have enough time to study this phenomenon for polydisperse bubble size distributions.

Perspectives for this work will be in the elimination of “ghost bubbles” generated sometimes by the inversion procedures, to improve the measurement of non spherical bubbles with a tilt angle, the use of several laser wavelengths to get more information on widely polydisperse size distributions, to access to the bubble concentration. However, we truly believe that CARS could be already used in its current state, or as an integrated sensor, for some fluid mechanics applications requiring a characterization of bubbles size distributions and composition.

10 ANNEX

Correction method for refraction effects at the walls

When the refractive index of the surrounding liquid is changing the refraction of the incident beam and the scattered light does the same. The Fourier optics of the CARS system measure the angle of the scattered rays in air, so the recorded CSP is biased by the refraction effects at the wall. The problem is solved with the calibration procedure, provided the liquid composition does not change during the experiment. If it changes, we have shown that it has not a severe influence on the size measurements but a slight effect on the measurement of bubbles refractive index. So I have developed a very simple model to compensate the aforementioned effects.

I develop a small ray tracing code to follows the rays paths in the cell. It uses the Snell-Descartes's laws at the cell glass windows and the critical scattering law onto the particle surface. Note that in this model we neglect the glass walls, that are considered to be thin and parallel (the rays are transmitted parallel to them self with a negligible displacement). For given refractive indices, see Figure 10.1, knowing the input angle θ_{i1} we can calculate easily the output angle θ_{o2}, with for the first refraction angle

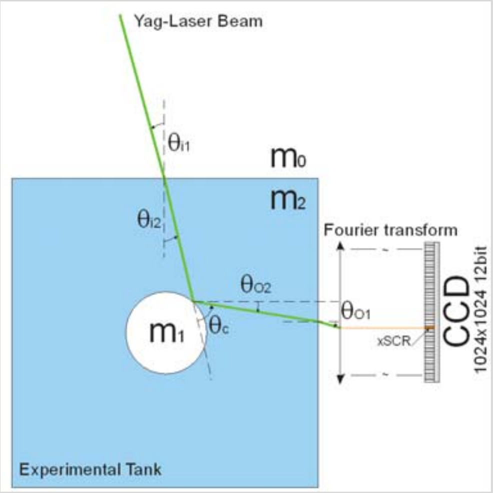

Figure 10.1 Ray tracing model of the ray paths from the laser to the CCD chip

$$\theta_{i2} = \sin^{-1}\left(m_0 / m_2 \sin\theta_{i1}\right) \tag{150}$$

And the critical angle

$$\theta_c = \sin^{-1}\left(m_1 / m_2\right) \tag{151}$$

The output ray refraction angle is

$$\theta_{o2} = 2\left(\theta_c - 45^o\right) - \theta_{i2} \tag{152}$$

Finally we get for the ray measured by the CARS system

$$\theta_{o1} = \sin^{-1}\left(\sin\left(\theta_{o2}\right) \cdot m_2 / m_0\right) \tag{153}$$

Changing the refractive index of the liquid we can see the displacement of the scattering beam onto the CCD chip. We did this calculation for two cases: a full calculation (as described above) and a calculation without refraction at the walls (i.e. $\theta_{o1} \equiv \theta_c$). The difference in displacement of the rays onto the CCD chip is took as the angular correction to add to CSP, see Figure 5.33.

11 REFERENCES

Airy GB (1838) On the intensity of light in the neighborhood of a caustic. Transactions of the Cambridge Philosophical Society 6:397-403

Albrecht H-E., Borys M, Damasche N, Tropea C (2003), Laser Doppler and phase Doppler measurement techniques; Springer-Verlag, Berlin

Barber P.W. and S.C. Hill (1989) Light Scattering by Particles: Computational Methods, World Scientific Publishing, NY.

Barbosa S., M. Krzysiek, M. Wozniak, F.R.A. Onofri (2010), Critical Angle Refractometry and Sizing technique for bubbly flows characterization: Particular effects, submitted for presentation in Proc. 15th Int. Symp on Appl. Laser Techniques to Fluid Mechanics, Lisbon, Portugal, July 5–8.

Barton J. P., D. R. Alexander, and S. A. Schaub (1988), Internal and near-surface electromagnetic fields for a spherical particle irradiated by a focused laser beam, J. Appl. Phys. (64):1632-

Birch K.P., Downs M.J. (1994) Correction to the Updated Edlén Equation for the Refractive Index of Air, Metrologia, 31(4), 315-316

Binek P., Mroczka J. (2007), Metoda Monte Carlo w opisie wielowarstwowych ośrodków dyspersyjnych, Kongres Metrologii 2007.

Bohren CF, Huffman DR (1998), Absorption and Scattering of Light by Small Particles, John Wiley & Sons, New-York

Bultynck H (1998) Développements de sondes laser Doppler miniatures pour la mesure de particules dans des écoulements réels complexes, Ph. D. thesis, University of Rouen, France

Celeta G.P., D'Annibale F., Di Marco P., Memoli G., Tomiyama A. (2007) Exp. Therm and Fluid Science. 31, 609-623

Chang SC, Jin JM, Jin J, Zhang S (1996) Computations of Special Functions, John Wiley & Sons, New-York

David J, Pereira F, Gharib M (2003) Applications of Defocusing DPIV to Bubbly Flow, Measurement, Particle & Particle System Characterization 20(3):193-198

Davis G. E., Scattering of light by an air bubble in water, J. Opt. Soc. Am., 45:572-581 (1955).

Dehaeck S. (2007), Development of Glare Pointm Shadow and Interferometric Planar Techniques for Gas Bubble Sizing, Ph.D. Thesis University of Gent, May 23.

Dhotre MT, Smith BL, Niceno B (2007) CFD simulation of bubbly flows: Random dispersion model, Chemical Engineering Science 62:7140-7150

Electrolysis (2008). Encyclopedia Britannica.

Fan L.S., Tsuchiya K. (1990), Bubble Wake Dynamics in Liquids and Liquid–Solid Suspensions, Butterworth–Heinemann, Oxford.

Fiedler-Ferrari N, Nussenzweig H.M., Wiscombe W.J. (1991), Theory of near-critical-angle scattering from acurved interface. Physical Review A 43:1005-1038

Hecht E. (1987) Optics, Addison Wesley.

Goodman JW (1996) Introduction to Fourier optics, McGraw-Hill, New York

Gouesbet G, Maheu B, Gréhan G (1988) Light scattering from a sphere arbitrarily located in a Gaussian beam, using a Bromwich formulation, J. Opt. Soc. Am. A 5:1427-1443.

Glover A.R., S.M. Skippon, and R.D. Boyle (1995), Interferometric laser imaging for droplet sizing: a method for droplet-size measurement in sparse spray systems, Applied Optics 34(36):8409-84.

Grace J. R., Wairegi T., and Nguyen T. H. (1976), Trans. Inst. Chem. Eng. 54, 167-173

Gréhan G., Onofri F., Girasole T. and Gouesbet G. (1994), Measurement of Bubbles by Phase Doppler Technique and Trajectory Ambiguity, Selected Papers from the 8th International Symposium Lisbon, Portugal, 11-14 July, (Eds. Adrian, R.J , Durao D.F.G, Heitor M.V), Springer, p. 290-302

Fdida N. (2008), Developpement d'un systeme de granulometrie par imagerie application aux sprays larges et heterogenes, Ph.D. Thesis from the University of Roue, 5 Dec.

Fiedler-Ferrari N., H. M. Nussenzweig (1987) Mie scattering near the critical angle, Part. and Part. Syst. Charact. 4:147-150.

Fiedler-Ferrari N. (1983)., Espalhamento de Mie na Vizinhanca do angulo critic , Ph. D. Thesis, University of São Paulo, Brazil.

Fowles G. R. (1975), Introduction to modern Optics, Holt, New York

Hess F. (1998), Planar Particle Image Analyzer, 9th. Int. Symp. Appl. of Laser Tech. to Fluid Mech., Lisbon (Portugal), paper 18.1.

Hovenac E.A. and Lock J.A. (1992) Assessing the contribution of surface waves and complex rays to far-field scattering by use of the Debye series, *J. Opt. Soc. Am. A* 9(5):781-795

ImagingSource (2007), http://www.theimagingsource.com.

Kawaguchi T., Y. Akasaka, M. Maeda, Size measurements of droplets and bubbles by advanced interferometric laser imaging technique (2002) Meas. Sci. Technol. 13(3):308-316

Koning G., Anders K., Frohn A. (1986), A new light-scattering technique to measure the diameter of periodically generated moving droplets, J. Aerosol Sci. 17(2):157-167

Langley D.S., Marston P.L. (1984), Critical scattering of laser light from bubbles in water: measurements, models, and application to sizing bubbles, Appl. Opt. 23:1044-1054

Lawson CL, Hanson RJ (1974) Solving Least Squares Problems, Englewood Cliffs (N.J.): Prentice-Hall

Lötsch H.K.V., Beam displacement at total reflection: the Goos-Hänchen effect, Optick 32 (1971).

Maeda M., T. Kawaguchi and K. Hishida (2000) Novel interferometric measurement of size and velocity distributions of spherical particles in fluid flows, Meas. Sci. Technol. 11 :13-18.

Malot H. et Blaisot J.B. (2000), Droplet Size distribution and Sphericity Measurements of Low-Density Sprays through Image Analysis. Part. Part. Syst. Charact., 17(4) :146-158

Marston P.L. (1979), Critical scattering angle by a bubble: physical optics approximation and observations, J. Opt. Soc. Am. 69(9):1205-1211

Marston P.L., D. L. Kingsbury (1981): Scattering by a bubble in water near the critical angle: interference effects, J. Opt. Soc. Am. 71(3):358-361

Massoli P., F. Beretta, A. D'Alessio, M. Lazzaro (1993), Temperature and size measurement of single transparent droplets by light scattering in the forward and rainbow regions, Appl. Opt. 32(18):3295-3301

Matrox Electronics Systems Ltd (1997), http://www.matrox.com/

Mie G. (1908) Beitrâge zur optik truber medien, speziell kolloidaler metallosungen, *Ann. Phys.* (25):377-452.

Mroczka J. (1991), Metrologiczne wykorzystywania światła rozproszonego do badań rozkładu wielkości cząstek w roztworach dyspersyjnych, Praca habilitacyjna, Wroclaw University of Technology.

Mroczka J.(2008), Problemy metrologii elektronicznej i fotonicznej. Praca Zbiorowa, Wrocław, Oficyna Wydawnicza. Wroclaw Uniwersity of Technology.

Naqwi A., F. Durst., X. Liu (1991) Extended Phase-Doppler system for characterization of multiphase-flows, Part. Part. Syst. Charat. 8:16-22

Nussenzveig H.M., Wiscombe W.J. (1980) Efficiency factors in Mie scattering, Phys. Rev. Lett. 34:1490-1494

Nussenzweig H. M. (1992) Diffraction effects in semiclassical scattering, Cambridge University Press, Cambridge

Lee Jr. R.L. (1998) Mie theory, Airy theory, and the natural rainbow, Applied Optics, 37(9):1506-1520

Oguz H. N. Prosperetti A. (1993), Dynamics of bubble growth and detachment from a needle, Johns Hopkins University, Baltimore, MD 2128, USA 28 May.

Onofri F, Gréhan G, Gouesbet G (1995) Electromagnetic scattering from a multilayered sphere located in an arbitrary beam, Applied Optics 34:7113-7124

Onofri F., Critical Angle Refractometry (1999a) For Simultaneous Measurement of Particles in Flow Size and Relative Refractive Index, Part. and Part. Syst. Charact. 16:119-127

Onofri F., L. Bergougnoux, J. Firpo, and J. Misguich-Ripault (1999b) Size, Velocity, and Concentration in Suspension Measurements of Spherical Droplets and Cylindrical Jets, Applied Optics 38(21): 4681-4690

Onofri F, Lenoble A, Bultynck B, Guéring P-H (2004) High-resolution laser diffractometry for the on-line sizing of small transparent fibres, Opt. Commun. 234:183-191

Onofri F, Krzysiek M, Mroczka J (2006a) Generalisation of the Critical Angle Refractometry for the characterisation of clouds of bubbles, In : Proceedings of the 13th Int. Symposium on Applications of Laser Techniques to Fluid Mechanics, Lisbon, June. Insituto Superior Técnico, Lisbon, 7.3.1.

Onofri F., Worms J., Krzysiek M., Mroczka J. (2006b) Généralisation de la technique de Granulométrie et Réfractometrie d'angle critique a la caractérisation de nuages de bulles, Congrès Francophone de Techniques Laser, CFTL 2006, 19 - 22 Sept., Toulouse, paper 24.

Onofri F, Krzysiek M, Mroczka J (2007a) Critical Angle Refractometry and Sizing for Bubbly Flow Characterization, Opt. Lett. 32:2070-2072.

Onofri F., Worms J., Krzysiek M., Mroczka J. (2007b) Critical Angle Scattering for Bubbly Flows Investigations, 8th International Congress on Optical Particle Characterization, 9-13 July, Karl-Franzens University Graz, Austria.

Onofri F., Krzysiek M., Mroczka J., Ren K.F., Radev S. (2008a) Collective critical angle scattering for bubble clouds characterization. In : Proceedings of the 14th International Symposium on Applications of Laser Techniques to Fluid Mechanics, Lisbon, July. Insituto Superior Técnico, Lisbon, 4.2.2.

Onofri F., Worms J., Krzysiek M., Mroczka J. (2008b), Caractérisation de nuages de bulles par analyse de la diffusion critique collective, *11ème Congrès Francophone de Techniques Laser (CFTL 2008, ISBN 2-905267-62-3)*, 16 - 19 Sept., Poitiers, France, paper 5.5, 8 pages.

Onofri F.R.A., M. Krzysiek, J. Mroczka, K-F. Ren, St. Radev, J-P. Bonnet (2009a), Optical characterization of bubbly flows with a near-critical-angle scattering technique, Exp. in Fluids 47(4):721-732

Onofri F., K.F. Ren and C. Grisolia (2009b), Development of an in situ ITER dust diagnostic based on extinction spectroscopy: dedicated light scattering models, Journal of Nuclear Materials, 390–391:1093–1096

Onofri F.R.A, M. Krzysiek, S. Barbosa, M.Wozniak, J. Mroczka, Y. Yuan, K-F Ren (2010a) Inverse near-critical-angle scattering as a tool to characterize bubble clouds, in Proc. SPIE Photonics West-LASE, 23-28 Jan., San Francisco, USA, paper 7588-12.

Okdale – Engineering (2006), DataFit 8.2 Software, http://www.oakdaleengr.com/

OriginLab (2003), Origin 7.5 Software, http://www.originlab.com/

Pajot O. and C.Mounaim-Rousselle (1998), Droplet Sizing by Interferometric Method Based On Mie Scattering in an I.C. Engine, 9th. Int. Symp. Applications of Laser Techniques to Fluid Mechanics, Lisbon (Portugal), paper 18.2

Pentland. A. P. (1987), A new sense for depth of field. IEEE Transactions on Pattern Analysis and Machine Intelligence, 9(4) :523

Querry, M. R., Wieliczka D. M., and Segelstein D. J. (1991) Water H_2O, in Handbook of Optical Constants of Solids II, Academic Press, pp. 1059-1077,

Qiu H.H., Hsu H.T. (2004) The impact of high order refraction on optical microbubble sizing in multiphase flows, Exp. in Fluids 26:100-107

Raffel, M., Willert, C.E. and Kompenhans (1998) J.: Particle Image Velocimetry - A Practical Guide. Springer-Verlag Berlin

Radev S, Onofri F, Tadrist L (2007) Sinuous instability of a viscous capillary jet injected into an immiscible non-viscous fluid, Part II: different forms and numerical analysis of the dispersion equation, J. Theor. Appl. Mech. 37(2):15-32

Ren K.F., Grehan G. and Gouesbet G. (1994), Evaluation of laser sheet beam shape coefficients in generalized Lorenz-Mie theory by using a localized approximation, J. Opt. Soc. Am. A 11(7):2072-2079

Ren K. F., Lebrun D., Özkul C., Kleitz A., Gouesbet G., et Gréhan G.(1996). On the Measurement of Particules by Imaging Methods : Theoretical and Experimental Aspects. Part. Part. Syst. Charact, 13 :156-164

Ren K.F., Grehan G. and Gouesbet G. (1997), Scattering of a Gaussian beam by an infinite cylinder in GLMT-framework, formulation and numerical results, J. Opt. Soc. Am. A 14(11):3014-3025

Ren K.F., Onofri F.R.A., Rozé C. and Girasole T. (2010), Vectorial Extended Geometrical Optics for scattering of a spheroid, accepted for presentation in Proc. Progress In Electromagnetics Research Symposium (PIERS), Cambridge, USA, 5 - 8 Jul.

Roth N., Anders K., and Frohn A. (1991) Simultaneous measurement of temperature and size of droplets in micrometer range, J. of Laser. Appl. 2,(1): 294-304

Sankar S. V., K. M. Ibrahim, D. H. Buermann, M. J. Fidrich, W. D. Bachalo (1993) An integrated Phase Doppler/Rainbow refractometer system for simultaneous measurement of droplet size, velocity, and refractive index, 3rd Int. Cong. on Optical Particle Sizing, Yokohama (Japan), 23-26th Aug., pp. 275-284

Sommerfeld M. (2003) Bubbly Flows: Analysis, Modelling, and Calculation, Springer-Verlag

Świrniak G., Mroczka J. (2008), Wybrane zagadnienia pomiaru średnicy włókna optycznego w procesie produkcji z wykorzystaniem światła laserowego, Problemy metrologii elektronicznej i fotonicznej. Praca Zbiorowa, Wrocław, Oficyna Wydawnicza. Wroclaw Uniwersity of Technology

Tomiyama A.,Yoshida S., Hosokawa S. (2001), Surface tension force dominant regime of single bubbles rising through stagnant liquid, UK-Japan Seminar on Multiphase Flow

Tadaki T., Maeda M. (1961) On the shape and velocity of single air bubbles rising in various liquids, Kagaku Kogaku 25, 254-264.

Twomey S. (1979). Introduction to the Mathematics in Remote Sensing and Indirect Measurement. Elsevier, New York.

Tryggvason G., Esmaeeli A., Lu J., Biswas S. (2006) Direct numerical simulations of gas/liquid multiphase flows, Fluid Dynamics Research 38:660–681

Van Beeck, J.P.A.J, Grosges T. , De Giorgi M.G (2003) Global rainbow thermometry assessed by Airy and Lorenz-Mie theories and compared with phase Doppler anemometry, App. Opt. 42(19): 4016 – 4022

Van de Hulst H.C (1957), Light Scattering by Small Particles, Dover Publications Inc., New York, Chapt.11& 12

Vanýsek P. (2007), Handbook of Chemistry and Physics: 88th Edition Section 5, Chemical Rubber Company

Vetrano M.R., van Beeck JPAJ., Riethmuller ML (2005), Assessment of refractive index gradients by standard rainbow thermometry, Appl. Opt., 44(34):7275-7281

Wiscombe W.J. (2006), NASA Goddard Space Flight Center, Greenbelt, USA , ftp://climate1.gsfc.nasa.gov/wiscombe/

Wooten, Frederick (1972)Optical Properties of Solids. New York City: Academic Press. pp. 49. ISBN 0127634509

Xu F., Ren K.F., Cai X., Gouesbet G., Grehan G. (2007) Generalized Lorenz-Mie theory for arbitrarily oriented, located and shaped beam scattering by a homogeneous spheroid, J. Opt. Soc. Am. A 24(1):119-131

Xu R. (2001) Particle characterization light scattering methods, Kluwer Academic Publishers, Miami

12 RÉSUMÉ EN FRANCAIS (EXTENDED ABSTRACT IN FRENCH LANGUAGE)

Ce manuscrit présente mes travaux de thèse, réalisés en “cotutelle” entre le laboratoire IUSTI, unité mixte de recherche du CNRS et de l’Université de Provence (France), et la Chaire de Métrologie Electronique et Photonique de l’Université Technologique de Wroclaw (Pologne). L'objectif principal de ce travail de recherche est d'étudier les propriétés des diagrammes de diffusion produits au voisinage de l’angle critique par des nuages de bulles. Puis en second lieu, de proposer et de tester les potentialités d’une méthode optique nouvelle, fondée sur l’analyse de la diffusion critique, qui permet de remonter aux caractéristiques granulométriques et à la composition du nuages de bulles et ceci, en vue d’applications possibles dans le domaine de la Mécanique des Fluides.

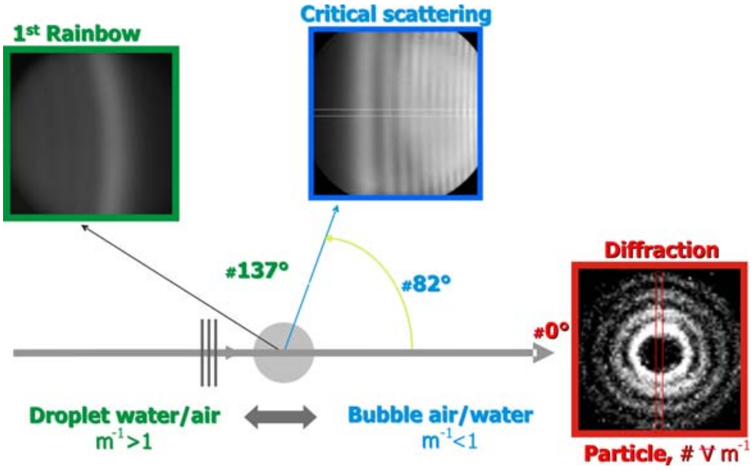

Figure F1. Schéma illustrant les grandes similarités qui existent entre les trois phénomènes de diffraction (ou pseudo-diffraction) que sont la diffraction vers l’avant, la diffusion dans les régions de l’angle de l’arc-en-ciel et de la diffusion critique (Onofri et al. 2008).

Après une introduction générale sur la nécessité de caractériser les écoulements à bulles, les avantages et les limites des techniques optiques actuellement disponibles, le 2nd chapitre porte sur le développement et le test de modèles et de théories pour prédire la diffusion de la lumière par une bulle sphérique unique. La diffusion critique y est présentée, dans le cadre de l’approximation d’optique physique (acronyme anglais : POA) de Marston (1979), comme un pseudo-phénomène de diffraction lié à l’existence d’une discontinuité dans le coefficient de réflexion des rayons réfléchis (notés p=0) au voisinage de l’angle critique. A partir de cette théorie nous avons montré que l’on peut dériver des équations analytiques, Eqs. (12)-(13), pour relier simplement la position angulaire des franges critiques au diamètre et à l’indice de réfraction relatif d’une bulle. Les études numériques ont cependant montré que la précision des prédictions de la POA, même en incluant la contribution des rayons réfractés (notés p=1), n’est pas suffisante pour toutes les applications (Onofri 1999a, Onofri et al. 2007a). La POA reste cependant intéressante si l’on envisage le développement d'un capteur intégré, aux capacités de calcul limitées. Nous montrons également dans ce chapitre que la théorie de Lorenz-Mie (acronyme anglais : LMT) est la seule à pouvoir modéliser de manière satisfaisante la diffusion critique. Contre toute attente, nous montrons en effet que les théories de Debye et du Moment Complexe Angulaire sont trop imprécises, tout en étant lourdes en termes de calculs. Afin de modéliser la diffusion d'un nuage de bulles, nous nous plaçons dans l'hypothèse d'un régime de diffusion simple, c.-à-d. un milieu optiquement dilué et sans diffusion multiple significative. Dans ce cadre, le profil d'intensité du diagramme de diffusion critique (acronyme anglais : CSP) est décrit par une équation intégrale de Fredholm de première espèce, voir l'Eq. (42). Ceci signifie que, à partir du profil d'intensité d'un CSP et pour accéder aux propriétés du nuage de bulles, il est nécessaire de développer des méthodes inverses. Dans ce chapitre, comme dans l'introduction, nous mettons en avant et pour la première fois les grandes similitudes qui existent entre la diffraction de Fraunhofer, le phénomène d'Arc-en-ciel (théorie D'Airy) et la diffusion critique, voir la Figure F1.

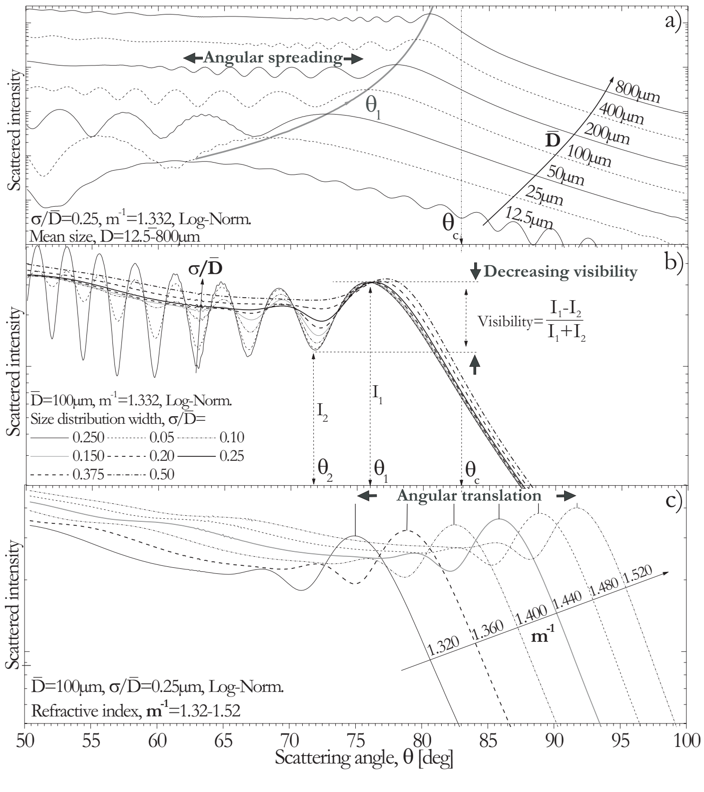

Figure F2 Résultats numériques obtenus avec la théorie de Lorenz-Mie pour un nuage de bulles d'air dans l'eau et dont on fait varier a) le diamètre moyen, b) la largeur de la distribution granulométrique et la composition (indice). Trois faits sont particulièrement remarquables: le diamètre moyen joue principalement sur l'étalement angulaire des diagrammes, la poly-disperion joue sur la visibilité des franges et l'indice de réfraction, sur la position angulaire globale des diagrammes.

Dans le $3^{ème}$ chapitre nous exposons le principe et testons numériquement (voir la Figure F2) les différentes techniques d'inversion développées au cours de ces trois années de thèse. La plus performante est basée sur la résolution d'une forme discrétisée de l'intégrale de Fredholm. Pour ce faire, nous utilisons une méthode de moindres carrés dont la contrainte unique est l'obtention de solutions non négatives (acronyme anglais : NNLSQ, Lawson and Hanson, 1974). Cette méthode ne nécessite pas d'hypothèse sur la forme des distributions granulométriques. Pour obtenir l'indice de réfraction, cette méthode algébrique minimise le résidu global obtenu pour différentes matrices de diffusion (noyau de l'intégrale de Fredholm calculé avec la LMT). Nous avons également développés des méthodes inverses basées sur un estimateur de corrélation entre CSP expérimentaux et théoriques (méthode LSQ voir l'Eq. (55)), ou sur la résolution analytique d'un système de trois équations empiriques (méthode 3-points, voir Eqs. (62) à (64)). Dans ce dernier cas, les équations décrivent la position et la visibilité des deux premières franges des CSP, en fonction du diamètre moyen et de son écart-type, de l'indice de réfraction des bulles. Les méthodes LSQ et 3-points nécessitent de poser un modèle de distribution granulométrique, nous avons choisi en l'occurrence celui d'une distribution Log-Normale.

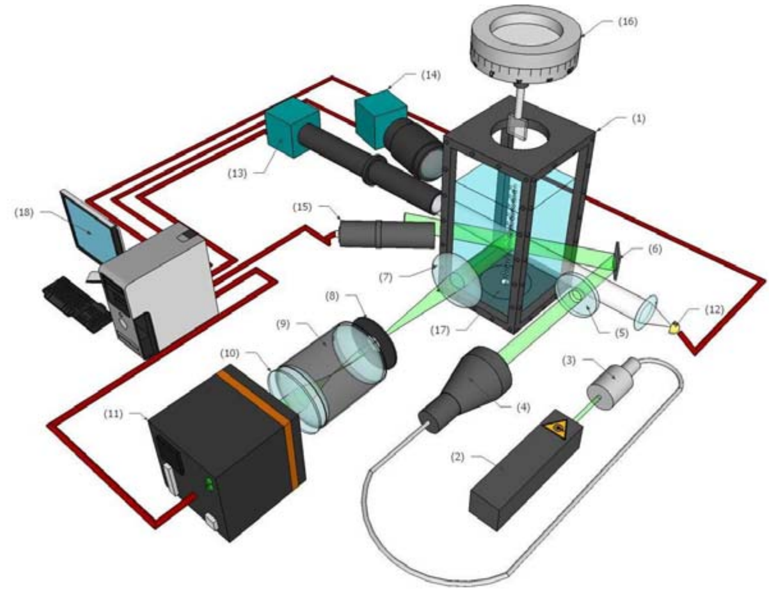

Figure F3 Schéma de principe de l'expérience réalisée étudier et valider le principe de la technique de granulométrie et réfractométrie de nuage de bulles par analyse de la diffusion critique.

Pour tester toutes les hypothèses faites, ainsi que les modèles de diffusion et les méthodes inverses, nous avons construit une expérience complète. Ces travaux d'instrumentation et de programmation sont détaillés dans le chapitre 4, voir à ce propos la figure F3. Le montage optique qui permet d'enregistrer les CSP est désigné comme système de « granulométrie et de réfractométrie par angle critique » (acronyme anglais : CARS). Il permet d'enregistrer le CSP produit par toutes les bulles contenues dans un volume de mesure de l'ordre de # 1cm^3. Dans cette expérience, les bulles sont produites par différents injecteurs: jet-piézoélectrique, injecteur assisté, milieu poreux et un système électrolytique multipoints. Afin de valider par comparaison les résultats expérimentaux obtenus avec la technique CARS, nous avons construit deux autres systèmes optiques: un système d'imagerie micro-vidéo à longue distance avec éclairement ombroscopique et un système d'imagerie interférométrique par défaut de mise au point (acronyme anglais : ILIDS).

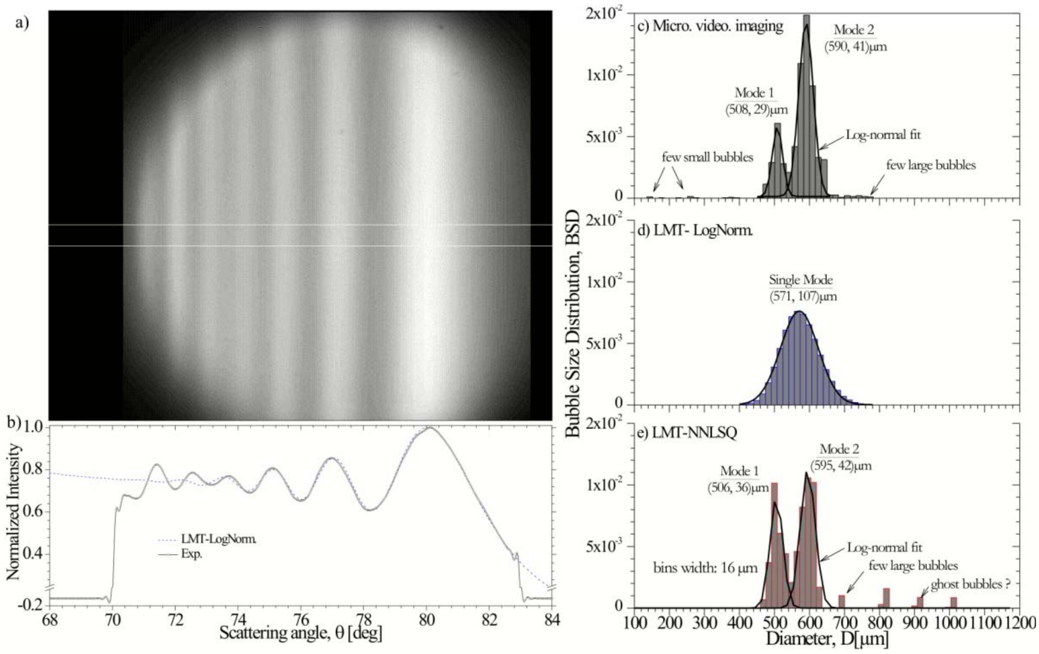

Figure F4 Exemple de résultats expérimentaux types: a) image dans le champ lointain des arcs de diffusion critique ; b) Profil expérimental et profil théorique reconstruit ; c) histogramme des tailles de bulles mesurées par imagerie micro-video ; d) même histogramme mais obtenu avec la technique CARS et une inversion par corrélation et e) idem mais avec la méthode d'inversion algébrique.

Pour produire des bulles de différentes compositions, nous avons utilisés différents couples de fluides pour la bulle et le milieu environnant : air/eau, air/solution d'éthanol, eau/huile de silicone, etc. Les résultats obtenus pour des bulles sphériques sont comparés et discutés dans le chapitre 5, voir la figure F4. Pour tous les cas considérés, nous avons trouvé un bon accord avec les techniques de référence, pour les diamètres moyens, la largeur des distributions granulométriques et l'indice de réfraction (Onofri et al. 2009). De cette étude il ressort également que la technique CARS semble pouvoir caractériser des milieux dont la concentration en bulles est supérieure à celles que peuvent traiter les techniques d'imagerie conventionnelles, mais sans pouvoir mesurer cette concentration.

Le chapitre 6 traite de la mesure des bulles non sphériques. La technique CARS déduit le diamètre des bulles d'une mesure de la courbure locale des bulles au voisinage du paramètre d'impact des rayons réfléchis à l'angle critique. Dans le cas d'une bulle ellipsoïdale non inclinée (grand axe orienté suivant l'axe optique de la détection du système CARS), la mesure restituée correspond à celui de la sphère de même rayon de courbure. La quantité mesurée est donc précisément définie mais elle ne rend pas compte du rayon de courbure de la bulle suivant son petit axe. Le volume de la bulle est de ce fait surestimé. Nous proposons dans ce chapitre deux méthodes de correction pour cet effet: l'une est basée sur l'analyse de la courbure des franges des

CSP et l'autre, sur l'utilisation d'une corrélation entre ellipticité et nombre de Tadaki. La deuxième méthode pourrait apporter une correction appréciable. Pour les ellipsoïdes inclinés de manière aléatoire, la mesure CARS rend compte d'un rayon de courbure intermédiaire. Dans le chapitre 7 nous étudions l'influence sur la forme des CSP de deux phénomènes : le profil d'intensité du faisceau laser, supposé gaussien, et les effets liés à la présence d'un filtre spatial au niveau de l'optique de collection. La conclusion sur ces deux effets est que, globalement, ceux-ci s'auto-compensent lorsque les bulles ont des trajectoires aléatoires, c.-à-d. que les bulles sont équi-réparties dans le volume de mesure. Pour les écoulements naturels, classiques, ces effets peuvent donc être négligés. Cependant, si l'écoulement est fortement non symétrique au niveau du volume de mesure, ou si les bulles ne passent que d'un côté du volume de mesure, les CSP peuvent apparaître déformés. L'ajustement du diamètre du filtre spatial peut contribuer à résoudre ce problème, mais ce dernier doit être envisagé.

Le chapitre 8 présente des travaux préliminaires sur la possibilité d'observer et d'utiliser des arcs de couleurs avec la diffusion critique, à l'image des arcs-en-ciel produit par les gouttes. Nos simulations numériques montrent qu'il est possible d'observer ces arcs-critiques, mais que ceux-ci sont plus étalés angulairement que les arcs-en-ciel. Une expérience préliminaire, avec un faisceau polychromatique collimaté, a permis de confirmer que cela est effectivement possible. Cependant, l'observabilité de ce phénomène dans la Nature nous semble délicate du fait qu'il faille l'observer dans l'eau (la mer par exemple), de la nécessité d'avoir une surface libre parfaitement lisse (c-a-d des bulles sans vagues, et pas qui ne soient pas trop poly-disperses) pour ne pas trop perturber les rayons solaires qui pénètrent la couche d'eau chargée en bulles.

Les perspectives de ce travail portent notamment sur l'élimination des "bulles fantômes" (bruit numérique) qui sont générées parfois par les techniques inverses, l'amélioration de la mesure des bulles non sphériques, l'utilisation de plusieurs longueurs d'onde laser pour obtenir plus d'informations sur les écoulements très poly-disperses, etc. Au-delà de ces améliorations possibles, nous sommes toutefois intimement convaincus que dans son état actuel, ou sous la forme d'un capteur intégré, cette technique pourrait d'ores et déjà permettre l'étude d'écoulements nécessitant une caractérisation de la taille et de la compostion des bulles. D'un point de vue plus théorique, les perspectives envisagées pour ce travail portent sur la théorie de Debye, une généralisation de l'approximation d'optique physique à des particules non sphériques, une modélisation plus complète du système optique.

Mots clefs :

Réflexion totale, diffusion de la lumière, théorie de Lorenz-Mie, optique physique, problèmes inverses, bulles, granulométrie, indice de réfraction, composition, écoulements multiphasiques.

13 ABSTRAKT PO POLSKU (EXTENDED ABSTRACT IN POLISH LANGUAGE)

„Problem odwrotny do scharakteryzowania układów cząstek przez inwersję modelu dla krytycznego kąta rozproszonego”

Światło jest potężnym narzędziem do badania zarówno prostych jak i skomplikowanych układów cząstek. Można je zaobserwować w naturalnych zjawiskach i przemysłowych procesach (wymiana ciepła, kawitacja, przepływ erytrocytów we krwi czy system redukcji oporu wody w transporcie wodnym). Dlatego pomiar parametrów cząstek jest dla nauki bardzo ważny.

Szereg metod pomiarowych zostało zaprojektowanych pod kątem charakterystyki wielkości pojedynczej cząstki, np. fazowa interferometria dopplerowska, PDI (ang. *Phase Doppler Interferometry*), technika rozproszenia w kącie krytycznym, a inne w celu charakterystyki układów cząstek w opisie rozkładu ich wielkości, np. anemometria laserowa w analizie pól prędkości, PIV (ang. *Particle Image Velocimetry*) czy PTV (ang. *Particle Tracking Velocimetry*), dyfraktometria, mikroskopia, a także klasyczne metody przetwarzania obrazów).

Niektóre z metod umożliwiają jednoczesny pomiar wielu wielkości fizycznych. Dla przykładu, anemometria PIV pozwala na pomiar rozkładu wielkości układu cząstek i prędkości pojedynczych obiektów rozpraszających światło (David i in. 2003).

Żadna z powyższych metod nie jest w stanie mierzyć kompozycji układów cząstek oraz otaczającego go medium. Współczynnik załamania światła jest kluczowym badaniem do scharakteryzowania układów cząstek czy przepływów wielofazowych.

W pracy autor wskazuje na podobieństwa trzech zjawisk dla rozproszenia światła: dyfrakcji, tęczy i krytycznego kąta.

Zarówno dyfrakcji jak i tęczy zostało poświęcone wiele uwagi, która zaowocowała publikacjami i pracami naukowymi(Van de Huslt 1957, Mroczka J. 1991, Bohren and Huffman 1998). W odróżnieniu od tych dwóch przykładów, zjawisko rozproszenia światła dla krytycznego kąta załamania nie doczekało się jeszcze gruntownej analizy.

Głównym celem niniejszej pracy było zbadanie właściwości światła rozproszonego na cząstkach w kącie krytycznym. Zaproponowano metodę pomiarową, wykorzystującą rozwiązanie problemu odwrotnego w eksperymencie z rozpraszaniem światła przez cząstki w kącie krytycznym. Metoda ta, w drodze pomiaru pośredniego, umożliwia uzyskanie informacji o właściwościach mierzonych cząstek, takich jak średnia wielkość oraz kompozycja (pomiar względnego współczynnika załamania światła). Zaproponowana technika pomiarowa wykorzystuje monochromatyczne, spolaryzowane, koherentne promieniowanie laserowe i umożliwia prowadzenie pomiarów w czasie rzeczywistym.

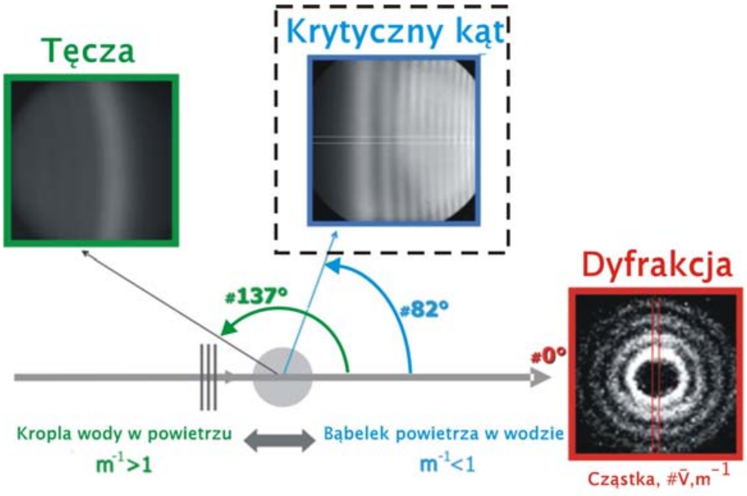

Rysunek P1. Schemat ilustrujący trzy zjawiska: dyfrakcji, rozproszenie światła w regionie tęczy i krytycznego kąta załamania.

Rozdział pierwszy poświęcony jest ogólnemu wprowadzeniu oraz analizie potrzeby charakterystyki przepływu cząstek, korzyści i ograniczeń technik optycznych aktualnie stosowanych.

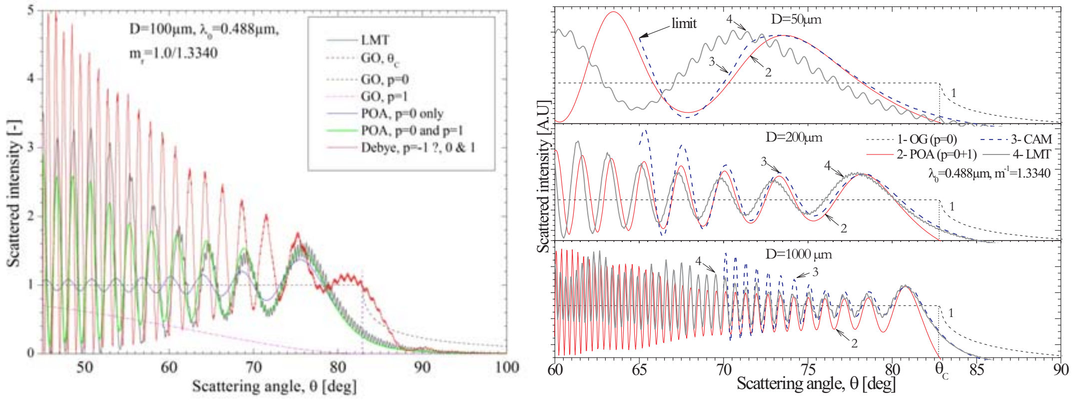

Rysunek P3 Wykresy przedstawiające profil rozproszenia światła na sferycznej cząstce dla krytycznego kata załamania opisany przez różne teorie.

W rozdziale drugim skoncentrowano się na rozwoju i testowaniu modeli oraz teorii aproksymacji rozproszenia światła na pojedynczej cząstce sferycznej. Rozproszenie światła dla rejonu kąta krytycznego został opisany z wykorzystaniem aproksymacji według fizyki optycznej (ang. Physical Optics Approximation, skrót: POA) a zaprezentowany przez Marstona (1979) jako zjawisko dyfrakcji związane z występowaniem nieciągłości we współczynniku odbicia w rejonie kąta krytycznego (opisywanych w literaturze jako p=0). Dzięki tej teorii pokazano, że jest możliwe wyprowadzenie analitycznego równania ukazującego ten związek (Onofri 1999, patrz wzory P1, P2).

$$m_{\upsilon\kappa} = \sin\left[\left(\pi - \theta_\upsilon - \Omega_{\upsilon\kappa}\right)/2\right] \qquad \text{(P1)}$$

$$a_{\upsilon\kappa} = \lambda_0 m_{\upsilon\kappa} \frac{\omega_\upsilon^2 + \omega_\kappa^2 - 2\omega_\upsilon\omega_\kappa \cos\Delta_{\upsilon\kappa}}{\sin^2\left(\Delta_{\upsilon\kappa}\right)\sin\left[\left(\theta_\upsilon - \Omega_{\upsilon\kappa}\right)/2\right]} \qquad \text{(P2)}$$

W nieskomplikowanym opisie przedstawiono zależność położenia kątowego w rejonie krytycznego kąta i relatywnego współczynnika załamania światła (dla $m^{-1}>1$) dla cząstek sferycznych. Analiza numeryczna pokazała jednak, iż aproksymacja POA nawet zawierająca w swoim opisie promienie załamane (oznaczone p=1) nie jest wystarczająca dla wszystkich aplikacji (Onofri 1998, Onofri i in. 2007). POA jest interesującą teorią, jeśli weźmie się pod uwagę rozwój zintegrowanych czujników i przetworników.

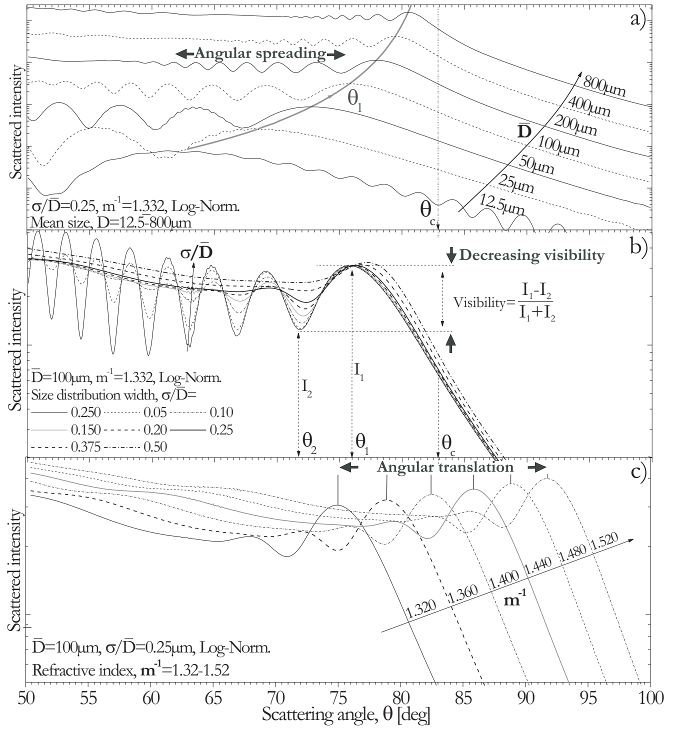

Rysunek P4 Wyniki dla teorii Lorenz-Mie dla grupy cząstek powietrza w wodzie dla zmiennych parametrów: a) wielkości cząstek, b) szerokość rozkładu dystrybucji wielkości i c) kompozycji (relatywny współczynnik załamania światła). Trzy główne cechy są znaczące: średnica jest głównie odpowiedzialna za kątowe „rozciąganie" profilu, szerokość dystrybucji wielkości wpływa na kontrast maksimów funkcji, a współczynnik załamania światła za zmianę położenia kątowego profilu.

W tym rozdziale wykazaliśmy również, że teoria Lorenza-Mie (skrót z ang. LMT) jako jedyna jest w stanie w sposób zadowalający opisać rozproszenie światła w rejonie kąta krytycznego. Przedstawiono, iż inne modele rozproszenia światła jak teoria Debye'go i CAM (ang. *Complex Angular Momentum*) dostarczają zbyt ogólnego opisu zjawiska rozpraszania.

W dalszym etapie pracy zdefiniowano podstawowe kryteria dla grupy cząstek do zamodelowania przez rozproszenie światła: średnia wielkość cząstki, optycznie rozcieńczone bez zwielokrotnionych rozproszeń. W tym kontekście, profil pola rozproszonego CSP (ang. *Critical*

Scattering Patern) jest opisany przez równanie całkowe Fredholma pierwszego rodzaju (patrz wzór P5).

$$I_t\left(\theta,m,\lambda_0\right)=N\int_{D_{\min}}^{D_{\max}} I\left(\theta,D,m,\lambda_0\right)f\left(D\right)dD \qquad \text{(P5)}$$

Opis całkowy przedstawia pole rozproszone na grupie cząstek jako sumę rozproszonego światła przez poszczególne cząstki dla założonego rozkładu wielkości.

Oznacza to, że z profilu intensywność CSP i opisywanych przez niego właściwości grupy cząstek, koniecznym było opracowanie metod odwrotnych, co zostało ujęte w rozdziale trzecim. Wykazano szereg podobieństw między dyfrakcją, zjawiskiem tęczy (według modelu Airy) oraz rozproszeniem światła dla krytycznego kąta załamania (rys. P1.)

Rozdział trzeci został poświęcony zasadom różnych technik inwersji oraz analizie wyników eksperymentów opracowanych w ramach pracy. Najlepsze wyniki uzyskano wykorzystując dyskretną formę funkcji całkowej Fredholma. Problem odwrotny dla tego przypadku bazuje na metodzie najmniejszych kwadratów z ograniczeniem dla nie ujemnych rozwiązań (ang. *Non Negative Least-SQuare problem*, ang. skrót: *NNLSQ*) (Lawson i Hanson, 1974). Metoda ta nie wymaga żadnych założeń dotyczących funkcji rozkładu wielkości cząstek.

Dla wyznaczenia współczynnika załamania światła, zminimalizowano algebraicznie wynik macierzy uzyskanych dla różnych funkcji rokładu wielkości (jądra funkcji całkowej Fredholma obliczanej dla teori Lorenza-Mie). Stworzono rozwiązania oparte na metodzie odwrotnej obliczającej korelację pomiędzy profilem eksperymentalnym i teoretycznym CSP (metoda najmniejszych kwadratów, ang. *Least-Square method*, ang. skrót: *LSQ*), lub korelację dla trzch charakterystycznych punktów profilu eksperymantalnego i teoretycznego (patrz wzór P6).

$$\Gamma^2=\alpha\left[\bar{\theta}_1^{Th}\left(\bar{D},\sigma_D,m\right)-\bar{\theta}_1^{Exp}\right]^2+\beta\left[\Delta\bar{\theta}_{12}^{Th}\left(\bar{D},\sigma_D,m\right)-\Delta\bar{\theta}_{12}^{Exp}\right]^2+\gamma\left[\bar{V}_{12,13}^{Th}\left(\bar{D},\sigma_D,m\right)-\bar{V}_{12,13}^{Exp}\right]^2 \qquad \text{(P6)}$$

dla układu trzech równań empirycznych (metoda 3-punktowa)

$$\theta_1(\bar{D},m,\sigma_D)=\left(\frac{a_1-b_1}{1-\bar{D}^{c_1}}+b_1\right)\left(f_1\sigma_D/\bar{D}+g_1\right)+d_1m+e_1+h_1\sigma/\bar{D}+i_1 \qquad \text{(P7)}$$

$$\theta_2(\bar{D},m,\sigma_D)=\left(\frac{a_2-b_2}{1-\bar{D}^{c_2}}+b_2\right)\left(f_2\sigma_D/\bar{D}+g_2\right)+d_2m+e_2+h_2\sigma/\bar{D}+i_2 \qquad \text{(P8)}$$

$$V(\bar{D},m,\sigma_D)=\left(\frac{a_3-b_3}{1-\bar{D}^{c_3}}+b_3\right)\left(f_3\sigma/\bar{D}+g_3\right)+d_3m+e_3+\frac{h_3}{1+\left(\frac{\bar{D}}{i_3}\right)^{j_3}}+k_3 \qquad \text{(P9)}$$

W ostatnim przypadku, równania opisujące położenie i kontrast pierwszych maksimów profilu CSP (patrz wzory P7-P9) bazują na podstawie wartości średniej i odchyleniu standardowemu wielkości cząstek oraz względnemu współczynnikowi załamania światła. Metody LSQ i 3-punktowa muszą być zdefiniowane dla danego modelu rozkładu wielkości. Dla potrzeb analiz wybrany został rozkład logarytmiczno-normalny.

Aby przetestować wszystkie hipotezy i modele dla rozproszenia światła w rejonie krytycznego kąta załamania oraz metod odwrotnych, zbudowano układ eksperymentalny, Rys.P10.

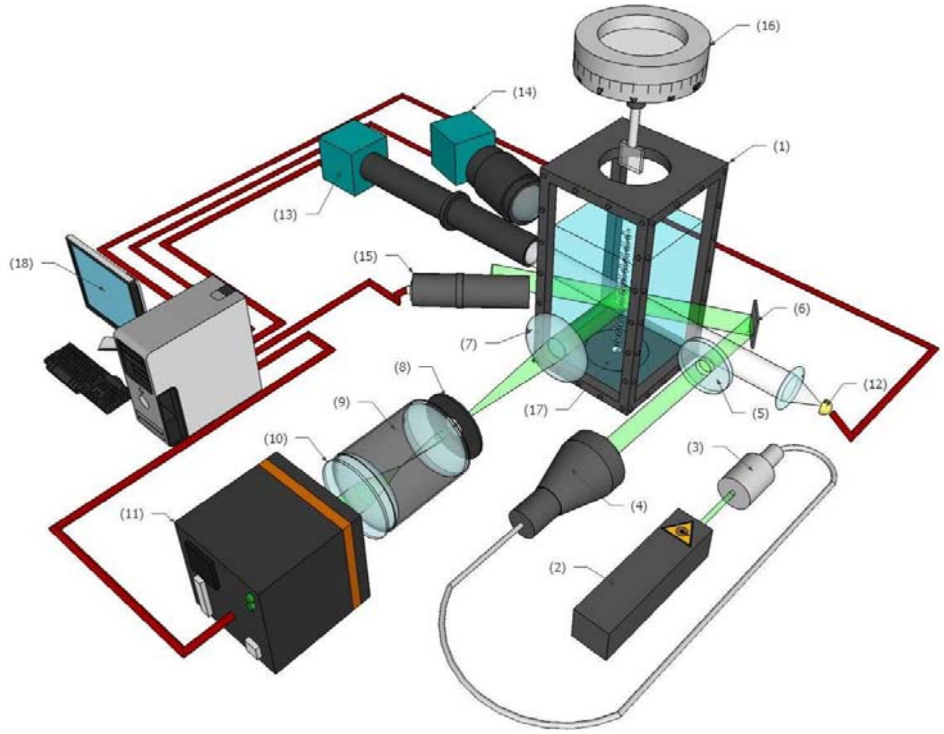

Rysunek P10: Schemat układu eksperymentalnego: (1) obiekt pomiarowy, (2) Laser YAG 50mW , (3) światłowód. (4) expander wiązki laserowej, (6) lustro, (7) obiektyw Nikon AF NIKKOR 50mm 1:1.4D , (8) przysłona, (9) soczewka, (10) filtr interferencyjny dla długości światła 532nm, (11) kamera czarno-biała CCD 1Mpix 12bits, (12) stroboskop, (13) kamera z trybem makro, (14) system pomiaru interferometrycznego (ILIDS) – kamera Imaging System CCD B/W z obiektywem Nikon AF NIKKOR 35-80mm 1:4-5.6D, (15) fotodetektor, (16) silnik krokowy, (17) dysze generujące cząstki sferyczne, (18) komputer

Zaprojektowany instrument badawczy jak i oprogramowanie umożliwiające analizę wyników pomiaru zostały opisane szczegółowo w rozdziale czwartym. Układ optyczny, który pozwala na rejestrowanie CSP został nazwany CARS (ang. *Critical Angle Refractometry Sizing*). Rejestruje on CSP tworzone przez grupę cząstek znajdujących się w przestrzeni pomiarowej o objętości około 1cm^3. W eksperymencie tym, cząstki (sferyczne bąbelki powietrza) są produkowane przez różne dysze.

Do porównania wyników uzyskanych w sposób doświadczalny przez CARS, stworzono dwa dodatkowe systemy optyczne: system rejestracji obrazu w trybie makro oraz interferometryczny układ pomiarowy ILIDS (ang. *Interferometric Laser Imaging Droplet Sizing*).

Wytworzenie cząstek dla różnych kompozycji (wielu współczynników załamania światła) wymagało wykorzystania różnych par cieczy dla cząstki i otaczającego ją środowiska:

powietrze/woda, powietrze/roztwór etanolu, woda/olej silikonowy, itp.. Wyniki uzyskane dla sferycznych cząstek zostały porównane i omówione w rozdziale piątym. Dla wszystkich przypadków otrzymano dobre wyniki dla podstawowych parametrów grupy cząstek: średniej wielkości, szerokość rozkładów wielkości i współczynnika załamania światła (Onofri i in., 2009).

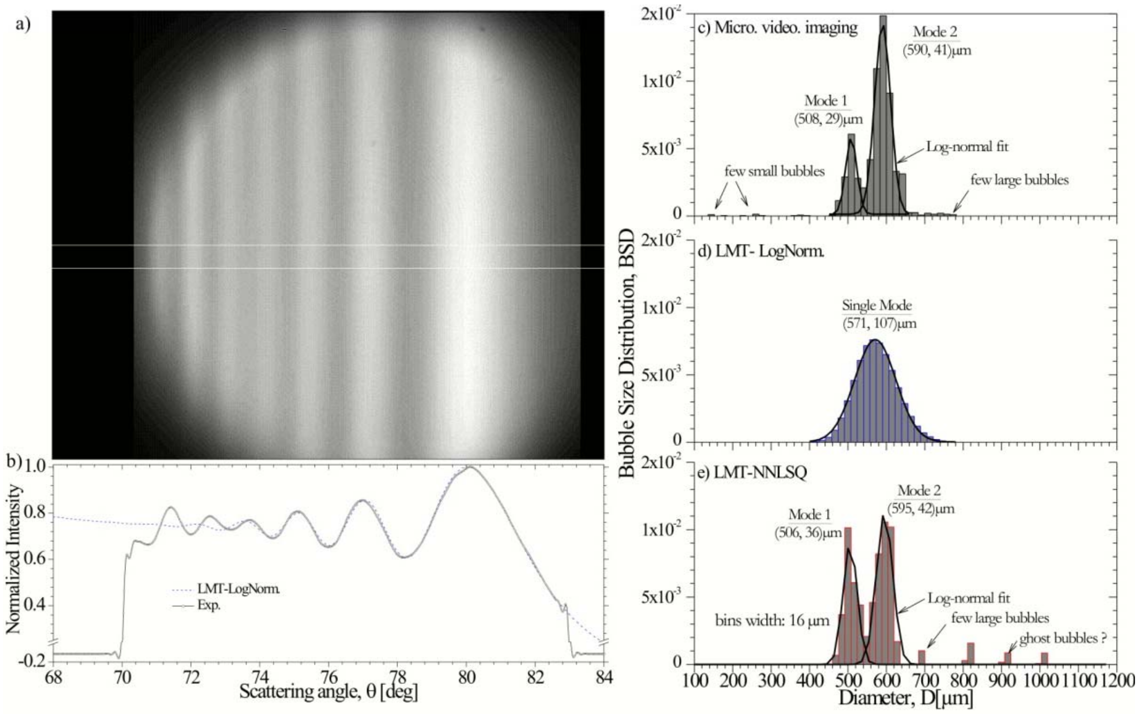

Rysunek P10 Przykład wyników doświadczeń: a) obraz rozproszenia światła dla kąta krytycznego (CSP) b) eksperymentalny i teoretyczny profil CSP c) histogram wielkości cząstek zmierzony przez układ w trybie makro d) histogram uzyskany przez metodę odwrotną dla CARS, e) wynik dla algebraicznej metody odwrotnej LMT-NNLSQ.

Przeprowadzone badania dowodzą, że przy użyciu techniki CARS możliwa jest charakterystyka środowiska, w których zagęszczenie cząstek jest znacznie większe, dla których analiza metodami klasycznymi nie jest już możliwa.

W rozdziale szóstym przedyskutowano problematykę cząstek elipycznych. Technika CARS daje wynik średnicy cząstki poprzez pomiar lokalnej krzywizny w rejonie kąta krytycznego. W przypadku cząstki eliptycznej, dla której wielkość wzdłuż jej osi poziomej jest położona w płaszczyźnie układu optycznego CARS, wynik układu będzie odpowiadał sferze dla tej wielkości elipsy. Wielkość cząstki zostanie wiec przeestymowana. W celu korekcji tego efektu zaproponowano dwie metody korekcji tego efektu: jeden oparty jest na analizie krzywizny profilu CSP i inne rozważania bazujące na hydrodynamicznym podejściu poprzez stosowanie korelacji między eliptycznością a wartością wielkością bezwymiarowej liczby Tadaki. Drugi sposób zapewnia znaczne poprawienie wyniku. Dla losowo rozmieszczonych elipsoid system CARS mierzy średni promień krzywizny.

W rozdziale siódmym został zbadano wpływ dwóch zjawisk na kształt CSP: profil intensywności wiązki laserowej dla rozkładu Gaussa i efektów związanych z obecnością przysłony w układzie optycznym. Oba efekty naturalnie się kompensują dla losowo rozmieszczonych cząstek w układzie pomiarowym. Dla naturalnych przepływów efekty te mogą być pominięte. Przy przepływie, który jest bardzo niesymetryczny lub jego cząstki znajdują się z jednej strony układu pomiarowego, profil CSP może być zniekształcony, przez co wynik pomiaru może być obarczony większym błędem. Dostosowanie średnicy przestrzennego filtru pomogło rozwiązać ten problem.

Rozdział ósmy przedstawia wstępne prace i analizy dla możliwości obserwowania i wykorzystania kolorowych łuków dla rozproszenia światła w rejonie krytycznego kąta, podobnie jak dla tęczy stworzonej przez krople wody w powietrzu. Symulacje numeryczne pokazują, że możliwa jest obserwacja różnobarwnych łuków, lecz kąt występowania tego zjawiska jest bardziej zbliżony do kąta 90 stopni niż w przypadku zjawiska tęczy (rys. P1). Wstępny eksperyment potwierdził możliwość obserwacji tego efektu przez rozproszenie światła białego na sferycznych cząstkach tej samej wielkości. Obserwacja tego zjawiska w przyrodzie jest bardzo utrudniona ze względu na fakt, iż może być zaobserwowana pod wodą (np. w morzu). Powierzchnia wody musi być przy tym płaska i gładka (tzn. bez pęcherzyków, zanieczyszczeń i fal), aby nie zniekształcić trajektorii dla równoległej wiązki promieni słonecznych przechodzących przez tę powierzchnię.

Perspektywa dalszych prac obejmuje: wyeliminowanie niedogodnych błędów w problemie odwrotnym LMT-NNLSQ (wynikających z szumu numerycznego), rozwinięcie opisu dla sferycznej cząstki, przez użycie wielu długości fali lasera dzięki temu będzie możliwe uzyskanie większej ilości informacji na temat przepływów cząstek o różnych współczynnikach załamania światła.

W opinii autora pracy, technika ta może pozwolić na badania przepływów wymagających charakterystyki wielkości i kompozycji sferycznych cząstek biorąc pod uwagę obecny stan zintegrowanych czujników. Ze strony teoretycznej perspektywy prac należy przeprowadzić dokładnej analizy teorii Debye'go (ze względy na problem tej teorii w opisie rozproszenia światła dla tego rejonu i cząstek dla którego względny współczynnik światła $m^{-1}>1$), uogólnienie teorii POA dla cząstek sferycznych oraz dokładniejsze zamodelowanie układu optycznego.

Słowa kluczowe:

kąt krytyczny, rozpraszanie światła, teoria Lorenza-Mie, aproksymacja według optyki fizycznej, problem odwrotny, bąbelki, pomiar wielkości, refraktometria, kompozycja, przepływy wielofazowe

14 SHORT ABSTRACT AND KEYWORDS

This Ph. D. work deals with the scattering of light by a cloud of bubbles (i.e. particles with relative refractive index below unit) near the critical-scattering-angle. Under a single scattering assumption, a critical scattering pattern (CSP) can be accurately modeled with the Lorenz-Mie theory and a Fredholm integral of the first kind. A CSP is basically composed of several bows that are very similar to those observed in the forward diffraction zone and the rainbow region. By measuring the angular spreading, the visibility and the global position of these bows it is possible to deduce the bubbles mean size, polydispersion and mean refractive index (i.e. composition). We have developed several inverse methods and experiments to recover these properties, demonstrating the validity of what can be called the "Critical-Angle Refractometry and Sizing" (CARS) technique. Various effects like the laser Gaussian intensity profile or the laser beam spectrum width have also been studied. This new optical particle characterization technique is thought to be a useful tool to study real bubbly flows as well as for laboratory experiments requiring bubbles material recognition.

Keywords:

Critical-angle, light scattering, Lorenz-Mie theory, physical optics approximation, inverse problem, bubble, sizing, refractometry, composition, multiphase flows.